IMPERIAL COLLEGE LONDON

ADVANCES IN POTENTIAL DROP TECHNIQUES FOR NON-DESTRUCTIVE TESTING

by

Giuseppe Sposito

A thesis submitted to Imperial College London for the degree of

Doctor of Philosophy

Non-Destructive Testing Group
Department of Mechanical Engineering
Imperial College London
London SW7 2AZ

January 2009

Abstract

In the field of Non-Destructive Testing, Potential Drop (PD) techniques have been used for decades, especially in the petrochemical and power generation industries, for monitoring crack growth and wall thickness variations due to corrosion and/or erosion in pipes, pressure vessels and other structures.

Inspection is carried out by injecting currents in the specimen to be tested and measuring the arising electrical potential difference between two or more electrodes placed on its surface. The presence of a defect generally increases the resistance and hence the measured voltage drop; inversion of these data can give information on the size and shape of the defect.

However, while the principle underlying these techniques is relatively simple, some difficulties have been encountered in their practical applications. Many commercial systems based on PD methods, for instance, require the injection of very large currents in order to obtain sufficiently large signals; doubts have been raised on the stability of these methods to variations in the contact resistance between the electrodes and the inspected material. The present work aims to show that some of these problems can be easily overcome, and to evaluate the capabilities of PD techniques for crack sizing and corrosion mapping.

After a brief review of the advantages, disadvantages and applications of the main electromagnetic methods for Non-Destructive Testing, an experimental setup for Potential Drop measurements which was developed for this work and which uses small alternating currents (AC) is described. The setup is benchmarked against existing PD systems and then used to validate a model that allows AC PD simulations to be run with a commercial Finite Element code. The results of both numerical simulations and experimental measurements are used to investigate the possibility of sizing defects of complex geometry by repeating the analysis at several different frequencies over a broad range, and of reconstructing the depth profile of surface-breaking defects without the need for assumptions on their shape. Subsequently, the

accuracy to which it is possible to obtain maps of corrosion/erosion on the far surface of an inspected structure is discussed, and results obtained with an array probe that employs a novel arrangement of electrodes are presented. Finally, conclusions are drawn and suggestions for further research are made.

Acknowledgements

I would like to sincerely thank my supervisor Prof. Peter Cawley for his excellent guidance throughout this work. I am very grateful to him and to Prof. Mike Lowe for giving me the opportunity to be part of their Non-Destructive Testing group, which struck me from the beginning not only as a team providing a lively and stimulating research environment, but also as 'a bunch of friends'. I would therefore like to extend my thanks to Matt, Jake, Bu-Byoung, Marco, Daniel, Fred, Ken, Prabhu, Tino, Tom, Pierre and all the other colleagues with whom I enjoyed sharing time both at College and outside.

I am profoundly indebted to Prof. Peter B. Nagy of the University of Cincinnati for his invaluable help with the experimental part of this thesis, for his precious advice and for the patience shown in our many long and useful discussions.

I would also like to acknowledge Mr. David Tomlin for his help in manufacturing the probes for the experiments, and the Research Centre of Non-Destructive Evaluation (RCNDE) for funding this project.

Finally, a heartfelt thank goes to Mr. and Mrs. Martin and Sarah Weise, who made me feel at home here in London; to Verena for standing by me and renewing my enthusiasm; and of course to my parents Angela and Antonino, who have always supported and encouraged me — even though far away — and to whom I wish to dedicate this work.

Contents

List of Figures

List of Tables

Chapter 1

Introduction

1.1 Motivation

The primary goal of Non-Destructive Testing (NDT) is the detection and evaluation of flaws that may compromise the functionality of a structure; wherever possible, the inspection is carried out while maintaining the structure in service. This is extremely attractive for a vast number of applications, ranging from civil engineering (*e.g.* health monitoring of bridges and railways) to the petrochemical and power generation industries (*e.g.* inspection of pipelines, storage tanks, pressure vessels, etc.), where NDT is important not only in order to guarantee safe operation of the tested structure, but also to assess its remaining life or the need for a replacement, and to dramatically reduce direct and indirect costs such as those associated with plant outage. In this context, it is of crucial importance to be able to monitor the growth of defects such as cracks or corrosion, and to estimate their size as accurately as possible.

In the framework of the Research Centre for Non-Destructive Evaluation (RCNDE) [1], an organisation that encompasses several British universities as well as companies operating in diverse sectors of engineering, the need was identified for the improvement of existing NDT techniques with respect to their ability to monitor and characterise defects, *i.e.* to provide as much information as possible about the

size, shape and morphology of flaws. While extensive work has been done on inspection techniques involving ultrasound (see for example [2–7]), relatively less research has been conducted on electromagnetic methods for NDT, which represent the focus of the present study.

In particular, a literature survey showed that techniques such as Direct Current Potential Drop (DCPD) and Alternating Current Potential Drop (ACPD), based on the injection of currents in the structure to be tested and on the measurement of the resulting voltage difference between two or more points on its surface, offered the possibility for further development thanks also to the recent advances in electronics, which can help overcome some difficulties that have been encountered in applications of these techniques in the field.

One objective of this work is therefore to show how such problems can be alleviated and to address additional concerns about the practical deployment of Potential Drop techniques. The principal aim of the present research, however, is to assess the capabilities of these techniques for accurate characterisation of surface-breaking defects of more or less complex geometry and for the quantitative evaluation of corrosion/erosion on the surface opposite to that accessible for inspection. In order to reach these goals, an essential part of this project was to gain a better understanding of the physical principles on which the inspection techniques are based, with particular reference to the interaction between the currents injected in the material and any defects present.

1.2 Thesis outline

The structure of this thesis broadly follows the chronological sequence in which research was undertaken for this work.

In order to understand how Potential Drop techniques relate to other electromagnetic methods for Non-Destructive Testing, the most commonly used of these are reviewed in Chapter 2: the basic principles and the main advantages, disadvantages

and practical applications of each technique are discussed, and reference is made to the relevant literature.

Chapter 3 describes a low-current experimental setup for Potential Drop measurements that was developed for this project. The main characteristics of the instrumentation used are presented, and an explanation is given of how these contribute to overcome the difficulties associated with the measurement of such small signals.

The setup was benchmarked against commercially available DCPD systems which have been successfully used for industrial applications: the results of these tests, reported in Chapter 4, show the stability of Potential Drop measurements with respect to some problems commonly encountered when employing these techniques in the field.

Chapter 5 presents the results of an early investigation aimed at assessing the feasibility of combining DCPD and ACPD into a new technique called Potential Drop Spectroscopy: this consists in repeating the measurements at several different frequencies over a broad range, in order to obtain more information on the geometry of a defect.

A new, simple model for three-dimensional numerical simulations of ACPD measurements with a Finite Element code is presented in Chapter 6: frequency-related effects are taken into account by appropriately modifying the geometry of the modelled structure; a DC analysis can then be performed, thus reducing the computational power required. This solves the direct problem of determining the response of a probe to defects of given shape and size.

The inverse problem of reconstructing the depth profile of a surface-breaking defect from values of potential drop measured across its width is considered in Chapter 7: notches of various depths and shapes are evaluated both numerically and experimentally. It is also shown that the quality of the reconstruction can be improved by using a simple technique for synthetic focusing of the injected currents.

Chapter 8 explores the possibility of producing maps of corrosion/erosion on the far

side of an inspected structure using an array probe for the injection of currents and the measurement of voltage differences at multiple locations.

Finally, the findings of the present thesis are summarised in Chapter 9, where conclusions are drawn and guidelines for future work are suggested.

Chapter 2

A review of electromagnetic methods for Non-Destructive Testing

2.1 Introduction

Electromagnetic methods for Non-Destructive Testing (NDT) have their roots in early experiments conducted in the 19^{th} century, but only in the last decades of the 20^{th} century did they start enjoying extensive application. Progress in electronics has allowed the development of more efficient probes, while new techniques and new approaches for improving the sensitivity and resolution of such techniques have been found. At the same time, the enormous advances in computer science have proved very useful not only in analysing larger amounts of ever more accurate test data, but also in paving the way to a better, deeper understanding of the underlying physical processes, which is essential if test results are to be correctly interpreted and the maximum information available to be obtained. Theoretical and experimental studies have therefore been performed, and today numerical simulations are used to design new probes, find the optimum parameter choice for each test, and rapidly predict the test performance.

Several different techniques for electromagnetic NDT have been developed; all of them share the same physical basis and can be described by Maxwell's equations. Nevertheless, each technique has its own range of application, although most of them require the tested material to be a fairly good electrical conductor. A brief review of the fundamentals of the most widely used techniques will be made in this Chapter, although this survey cannot claim to be exhaustive.

2.2 Eddy Current Testing (EC)

Eddy Current testing is arguably the most widely used electromagnetic technique; its main applications range from thickness measurements of metallic plates or insulating coatings to the detection of surface-breaking cracks or discontinuities; conductivity measurements are another important application, since they allow identification of metallic alloys [8]. This inspection method offers low-cost, high-speed testing of metallic materials; no direct coupling is required.

Conventional EC testing is based on the fact that, when a coil excited by an alternating current is brought in proximity to an electrically conducting material, the impedance measured at the terminals of the coil changes. The magnetic field associated with the current flowing in the coil (primary field) generates eddy currents within the conducting specimen; according to Lenz's law, the direction of the induced currents, and of the secondary magnetic field created by these currents, is such as to oppose the change in the primary field, as sketched in Fig. 2.1. This causes a decrease in the flux linkage associated with the coil, and therefore a decrease in the coil inductance if the test material is non-magnetic, whereas the higher permeability of ferromagnetic materials generally accounts for increases in the coil inductance. Accompanying this change in inductance is usually an increase in resistance, due to the eddy current losses incurred within the specimen.

This technique is highly sensitive to flaws or discontinuities on the surface of the inspected material, but much less to deep-buried defects. This is because eddy currents, like all alternating currents, tend to flow primarily close to the surface

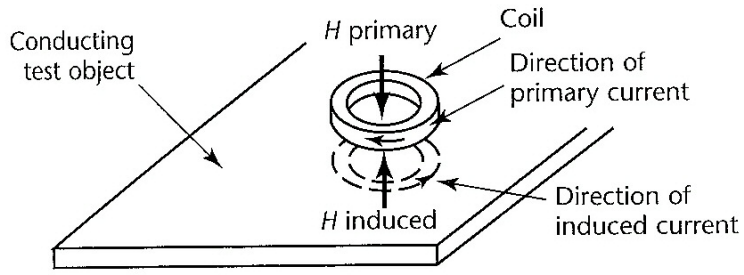

Figure 2.1: *Schematic of Eddy Current testing, showing opposing induced currents and magnetic field [9].*

of the specimen (a phenomenon known as *skin effect*) and their density decays exponentially with depth in the material [10]. For the same reason, the sensitivity to laminar discontinuities lying below the surface, parallel to the induced currents, is also limited.

A measure of the depth to which eddy currents penetrate the material is given by the standard penetration depth, or skin depth, defined as

$$\delta = \frac{1}{\sqrt{\pi f \sigma \mu}}, \tag{2.1}$$

where f is the frequency of the current in the exciting coil, σ is the electrical conductivity of the material and μ its absolute magnetic permeability. At a depth δ in the material the eddy current density has decayed by a factor e compared to its surface value. Test object properties that affect eddy currents therefore include conductivity and permeability, as well as geometry (shape); discontinuities can be revealed to the extent that they alter the path of electrical currents and therefore cause a change in the measured impedance.

In general, only materials with significant electrical conductivity can be examined by means of eddy current techniques, although thickness measurements of insulating coatings on conducting materials can be carried out by measuring the so-called lift-off, *i.e.* the distance between the coil and the surface of the object being analysed [10]. The permeability of the material strongly affects the signal; the analysis of the response of non-magnetic metals is more straightforward than it is the case for ferromagnetic materials. For the latter, the effects of thermal or mechanical process-

ing (which affect the magnetic permeability as well as several other properties of the material) can be detected, but magnetic anomalies produced by handling, welding, cold-working or prior magnetisation can interfere with interpretation of the material properties [8]. For this reason, ferromagnetic materials are sometimes brought to saturation prior to inspection, so that they behave like non-ferromagnetic materials and variations in permeability do not affect the eddy current coil response [11]. Other factors such as the shape and size of the coil, together with the frequency of the current, also determine the penetration and lateral spread of the eddy currents.

For the visualisation of the results of an EC inspection, it is customary to plot the terminal impedance of the probe on a complex plane, referred to as the impedance plane, after normalisation with respect to the inductance of the empty coil. As frequency is raised, the standard penetration depth decreases but higher eddy currents are induced, which cause the point representing the coil impedance on the complex plane to move clockwise tracing a semi-circumference in the first quadrant, as shown in Fig. 2.2*a*. A local increase in the conductivity of the specimen has a similar effect, whereas an increase in permeability moves the point upwards. If the distance

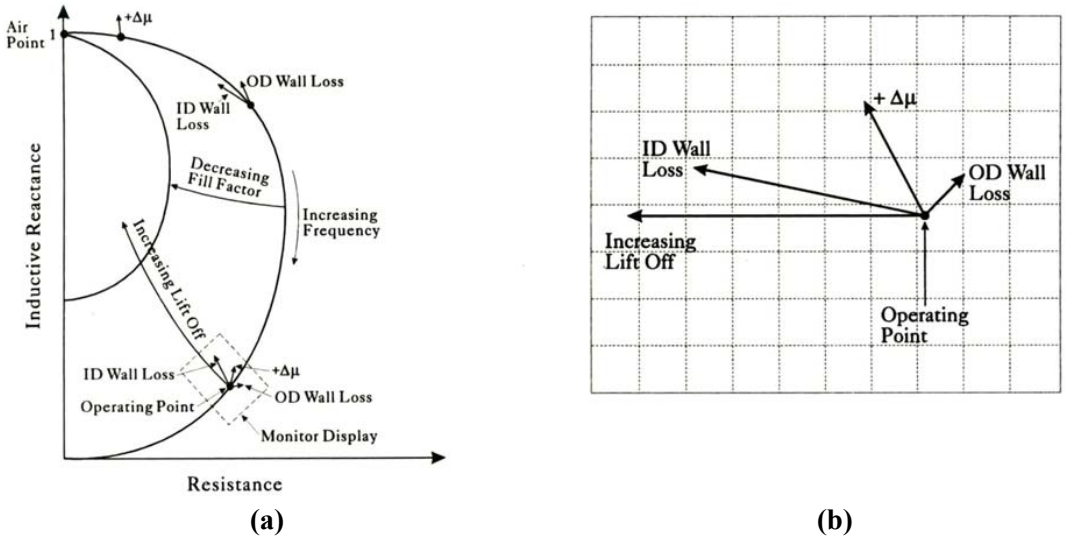

Figure 2.2: *(a) Typical impedance plane diagram for an eddy current probe in a non-ferromagnetic tube. (b) Rotated zoomed region of the impedance plane diagram, often used as monitor display, showing well separated traces for different responses [12].*

between the probe and the conducting material increases, for instance because of a loss of metal on the surface of the specimen, the point moves towards the inside of the impedance trajectory. Surface-breaking cracks can force the eddy-currents deeper into the material, and a phase shift results [9].

The operating frequency must be carefully chosen to give the maximum angular separation between signals arising from real defects and spurious signals such as those caused by lift-off. An example of good separation is shown in Fig. 2.2*b*. Frequencies used for Eddy Current testing range between 5 Hz and 10 MHz [9, 10], but the vast majority of commercially available probes have nominal working frequencies between 50 kHz and 4 MHz.

2.3 Pulsed Eddy Current method (PEC)

In the Pulsed Eddy Current method, broadband signals such as pulses or square waves are used to excite the coil, as opposed to the continuous sinusoidal wave used in conventional Eddy Current inspection. PEC can be considered to be a recent extension of Eddy Current testing, as it relies on the same basic principles: the transient current in the coil induces transient eddy currents in the test piece. For this reason, this technique is sometimes referred to as Transient Eddy Current.

Thanks to the relationship between a single transient field and multiple continuous-wave fields at different frequencies, by means of a Laplace or Fourier transform, one PEC measurement is equivalent to several measurements conducted at different frequencies with a conventional technique, as shown in [13]. The Pulsed Eddy Current method has therefore the advantage of being faster and cheaper. This technique also allows the detection, and to some extent the localisation, of hidden corrosion even in multilayer structures [14–16].

Unlike conventional Eddy Current techniques, the signal in PEC testing is not detected on the same coil used for the excitation; instead, the quantity measured is often the voltage across a resistor on the detecting coil, which can be plotted as a

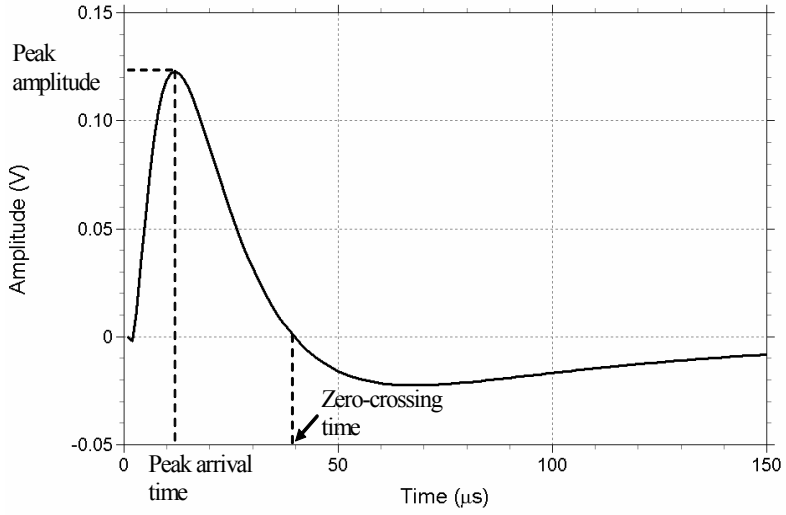

Figure 2.3: *Typical response of a detecting coil in Pulsed Eddy Current testing, plotted as a function of time [15].*

function of time [13] or of both time and frequency [17]. Signals are usually obtained by subtraction of a reference, and they are characterised by peak amplitude, peak arrival time and zero-crossing time [18]: an example is shown in Fig. 2.3.

2.4 Remote Field Eddy Current method (RFEC)

Internal inspection of ferromagnetic tubes can be problematic with conventional Eddy Current techniques, because very low frequencies are needed in order to achieve a complete penetration of the currents through thick walls, and sensitivity is dramatically reduced. The Remote Field Eddy Current technique alleviates these difficulties, since it allows through-penetration of thick-walled pipes and it is equally sensitive to internal and external discontinuities — although this means that it is not possible to determine whether the defect is on the inner or the outer surface [19].

The operating principle is somewhat different from the conventional Eddy Current method. A large part of the magnetic field induced by an exciting coil internal to the pipe penetrates the wall of the tube and is guided preferentially along the outside of the pipe, as shown schematically in Fig. 2.4. Eddy currents following circular

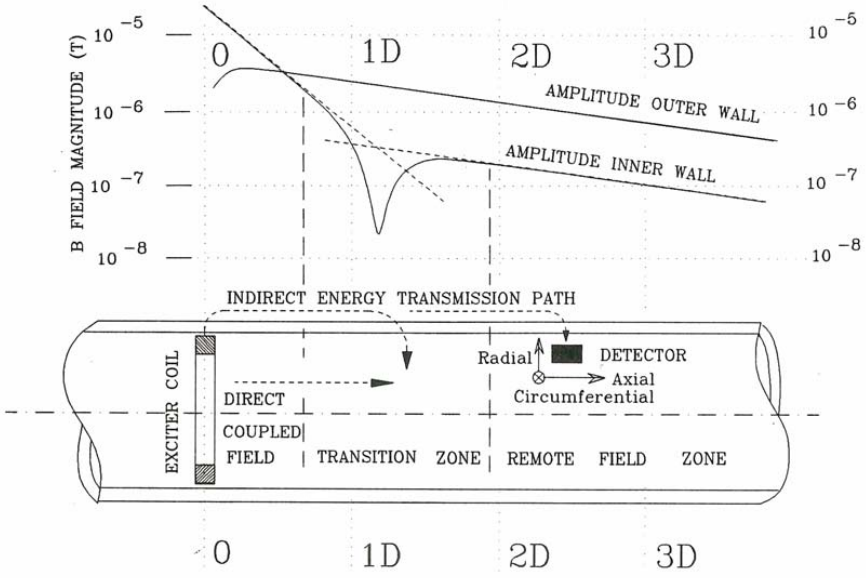

Figure 2.4: *Schematic of Remote Field Eddy Current testing, showing profiles of the magnetic flux field inside and outside the pipe [12].*

paths concentric with the axis of the tube flow within the tube wall and set up a reverse magnetic field, which strongly attenuates the part of the field remaining in the internal volume of the pipe. At a distance of two pipe diameters the direct field has almost vanished, and the signal sensed by the detector coil is predominantly due to the magnetic field diffusing back inward from the outside, slightly attenuated and phase-shifted by the double passage through the tube wall. Anomalies anywhere in this indirect path cause changes in the magnitude and phase of the received signal, and can therefore be used to detect defects [12, 20]. It must be stressed that, unlike conventional Eddy Current techniques, RFEC testing is much more sensitive to circumferential defects, such as metal loss due to corrosion or erosion, than to axial defects. This is because axial cracks introduce only a small discontinuity in the path of the magnetic field, so that the variations in the effective permeability are not significant; circumferential cracks, on the other hand, can be detected as they interrupt the lines of magnetic flux [21].

In the passage through the tube wall, the attenuation of the magnetic field is approximately exponential, whereas the phase shift increases linearly with the thickness of the wall: this allows the determination of the depth of metal loss. However, quanti-

tative measurements rely on calibration on reference tubes, so that any differences between these and the tubes tested (for example in terms of impurities, machining tolerances, heat treatments and magnetic history) can affect the reliability of the signal analysis [19,21]. Frequencies used in RFEC typically range between 40 Hz and a few kHz, the lower being used for very thick-walled tubes or highly ferromagnetic materials so that the ratio of skin depth to wall thickness is not too small [21].

2.5 Magnetic Flux Leakage detection (MFL)

Magnetic Flux Leakage detection is one of the most used techniques to test steel products, since it provides a quick and relatively inexpensive way to assess the integrity of materials with high magnetic permeability.

This method is based on the fact that, at high levels of induction (*i.e.* in the upper-right part of the magnetisation curve, where permeability $\mu = dB/dH$ is decreasing: with reference to Fig. 2.5, the part of the magnetisation curve between points A and B), a discontinuity in a ferromagnetic material forces the magnetic field to leak out of the tested specimen in proximity of the defect [22]. The field at the outside surface of the material can then be detected by coils, Hall probes or other sensors, or even visually in the so-called Magnetic Particle Inspection (MPI). This latter technique is an application of MFL and it is particularly suitable for the detection of surface defects, whose presence is revealed by an accumulation of magnetic particles trapped in the leakage field of the cracks [23].

Two basic models, with several variants, are used to describe the theory for MFL and to predict results analytically in relatively simple geometries, or numerically in more practical cases. In the first approach, the leakage fields of surface-breaking cracks are modelled by dipoles whose orientation is opposed to that of the magnetic domains in the material [24]; in the second, the crack is modelled as an air gap in a magnetic circuit [25].

In the practical deployment of this technique, the part to be tested is usually mag-

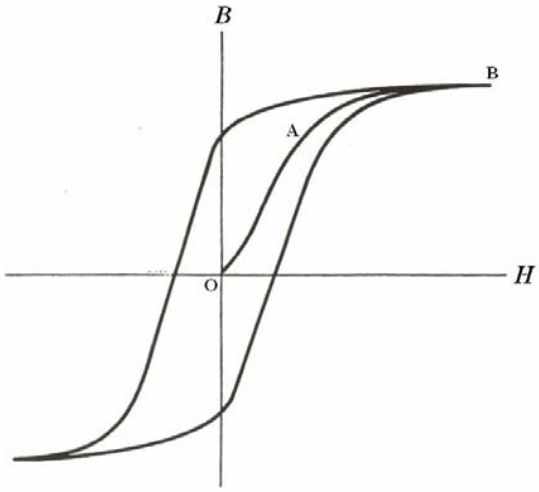

Figure 2.5: *Magnetisation curve and hysteresis loop for a typical ferromagnetic material.*

netised by applying a direct current to its ends; alternating currents at 50-60 Hz are sometimes used to detect imperfections on the outside surface, but they are unsuitable if defects lying below the surface are to be detected [22]. Electromagnetic yokes can also be used to magnetise the specimen by induction, as is commonly done with MFL 'pigs' in pipelines or MFL scanners for testing of oil storage tanks [26]. Inspection is often carried out in an active magnetic field (*i.e.* while currents are applied to magnetise the part), though the piece can also be brought close to saturation and then inspected in the resulting residual magnetic field [27].

2.6 Direct Current Potential Drop technique (DCPD)

The Direct Current Potential Drop method is among the oldest electromagnetic techniques for non-destructive testing, having been used for decades to measure thickness and estimate crack depth on plates and to monitor crack initiation and propagation in laboratory tests [28–31]. Among its main advantages are the capability to measure hidden cracks and the possibility of full automation of the monitoring;

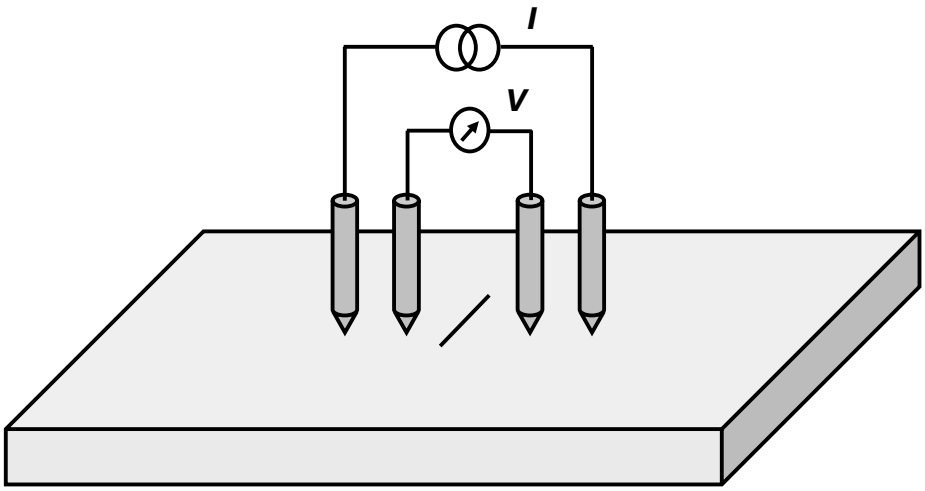

Figure 2.6: *Schematic of probe for Direct (or Alternating) Current Potential Drop testing.*

on the other hand, the need for good electrical contacts makes this technique unsuitable for scanning for defects, as the probe would be damaged if dragged over the surface.

In this simple technique, electrical DC currents are injected into a conducting specimen through one pair of electrodes, while a second pair straddles the crack (or a small monitoring area where crack initiation is expected), as shown in Fig. 2.6. The injecting electrodes should be positioned at a sufficient distance to ensure field uniformity in the inspection area. As the length or depth of the crack increases (or a new crack is initiated), the cross-sectional area of the specimen is reduced; this causes an increase in resistance and ultimately in the potential difference measured between the electrodes straddling the crack. The amplitude of the measured voltage depends not only on the properties of the inspected specimen, such as conductivity and geometry, but also on several other factors including the distance between the measuring electrodes. Disturbances like changes in temperature, lack of stability of the input currents or other undesirable changes in instrumentation can be almost eliminated — and measurement accuracy improved — by comparing the signal with a reference ('baseline') obtained on the same specimen in a defect-free area [28].

The measured voltage is also proportional to the intensity of the input current; in order to achieve measurable potential drops, many implementations of DCPD, both commercial (*e.g.* the systems developed by CorrOcean [32] and Rowan Technologies [33], described in Chapter 4, or the system by Matelect [34]) and in the research field (see for example [35, 36]), use very large currents, in some cases up to 200 A. However, today it is possible to measure reliably voltages of the order of a few nV, and the signal-to-noise ratio (SNR) can be improved in several different ways, so that, as will be shown in the present work, much lower currents can be used.

2.7 Alternating Current Potential Drop technique (ACPD)

In principle, the Alternating Current Potential Drop technique is very similar to DCPD, the main difference being the use of alternating currents instead of direct currents. However, apart from the induction effects arising in the measurement circuit, the injection of an AC current means that, because of the so-called skin effect mentioned in Section 2.2, the current is forced to flow in a thin layer below the surface and therefore 'sees' a smaller effective cross-section; as a consequence, sufficiently high potential differences can be generated by relatively low currents (< 1 A) [37–39]. The skin depth calculated from Eq. 2.1 is typically a few mm for most metals (*e.g.* $\delta = 10.5$ mm for stainless steel SS304 at 1 kHz) and even less for ferromagnetic materials in the frequency range commonly used: this goes up to about 10 kHz, as the impedance of the measuring circuit introduces errors that increase proportionally with frequency [39].

The presence of an electrically insulating defect such as a crack forces currents to flow around and below it, as showed in Fig. 2.7, and the longer current path results in a higher resistance and therefore in a higher potential drop between the electrodes. This allows the crack depth to be estimated, as will be discussed in Chapter 7.

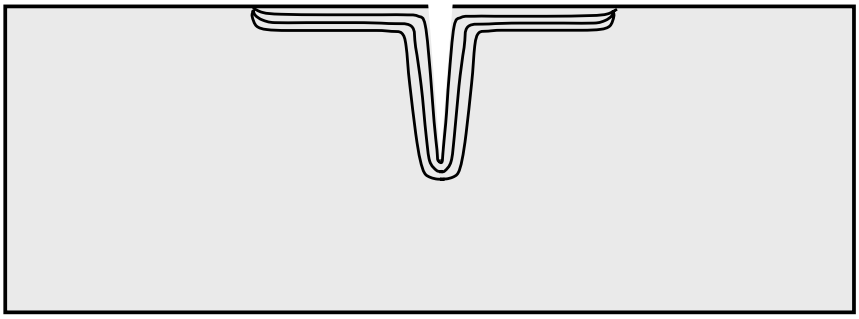

Figure 2.7: *Qualitative representation of the current path in the presence of a defect in Alternating Current Potential Drop testing.*

Measured potential differences can also be compared with theoretical results derived for the two extreme cases of thin-skin and thick-skin fields in simple geometries (see for example [40, 41]); it has even been suggested that for industrial applications it might be worthwhile choosing the input current frequency to fit one of the parameter sets for which theoretical results exist, not only in order to avoid calibration, but also to allow straightforward crack sizing by means of simple formulae or computed look-up tables [42]. Increasing the skin depth, though, means that the voltage readings and the sensitivity to changes in crack depth are both reduced; on the other hand, it gives the opportunity to determine the presence of subsurface flaws.

It should be mentioned at this point that, as is the case for DCPD, this technique is not ideal for crack detection because of its requirement of good electrical contacts, but it has been applied for many decades to monitor crack growth, especially in the petrochemical and power generation industries [43–46]. More recently, Bowler and co-workers [39, 47] obtained an analytical expression for the electrical potential created by the injection of alternating currents through two electrodes on a metal plate, and showed that their formula can be used to estimate accurately the conductivity or permeability of a non-cracked specimen of known thickness, or vice versa.

2.8 Alternating Current Field Measurement (ACFM)

The Alternating Current Field Measurement technique was developed to combine the ability of ACPD to size cracks without the need for calibration with the ability of Eddy Current techniques to work without electrical contact. The latter is achieved by inducing (rather than injecting) uniform currents on the surface of the inspected specimen and by measuring the magnetic field above the surface (instead of the surface voltage).

Fig. 2.8 shows the coordinate system conventionally used in ACFM: the direction of the induced current is designated as the y axis, whereas the direction of the associated magnetic flux density B, orthogonal to the electric field and parallel to the surface of the specimen, is assigned as the x axis; the direction normal to the surface is the z axis. A discontinuity is best detected when its largest dimension is along the x direction, orthogonal to the current [49]. The current is then partly diverted away from the deepest area and tends to concentrate near the ends of the surface-breaking crack, thus producing changes in the magnetic field components along the discontinuity, as shown in Fig. 2.9. In particular, small peaks are created in B_x by the concentration of current lines at the edges of the crack, and a broad dip

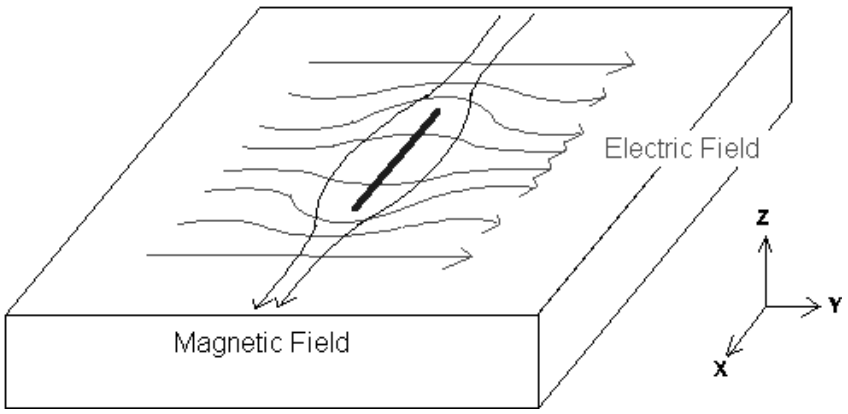

Figure 2.8: *Field directions and coordinate system conventionally used in Alternating Current Field Measurement [48].*

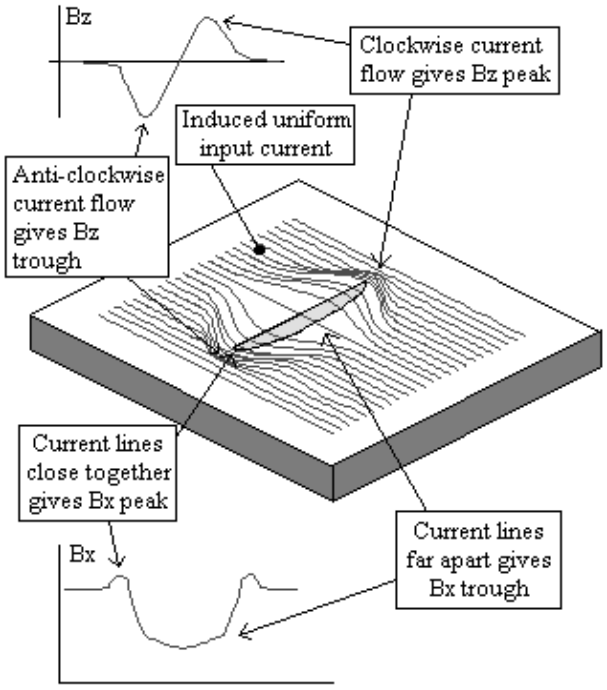

Figure 2.9: *Qualitative explanation of the effects of a surface-breaking discontinuity on the magnetic field [48].*

is produced between them with the minimum value attained at the deepest point of the discontinuity; this allows an estimation of the crack depth, because the deeper the discontinuity, the larger the amplitude of the B_x trough. At the same time, a non-zero component of the magnetic flux density normal to the surface is produced by the clockwise and anticlockwise flow of the current lines around the ends of the crack; the negative and positive peaks in B_z coincide roughly with the ends of the discontinuity, and the distance between them can therefore give an estimation of the crack length [49]. In order to make the readings independent of the probe speed, it is customary to plot B_x measurements versus B_z, forming what is known as a butterfly plot because of its shape: in this kind of representation, the presence of a discontinuity on the scanned surface is indicated by a loop vaguely resembling a butterfly. An example is given in Fig. 2.10.

As for ACPD, the sizing capability relies on theoretical modelling of the expected probe measurements. The mathematical models developed so far are based on semi-elliptical defects, with a maximum depth usually not larger than half the length

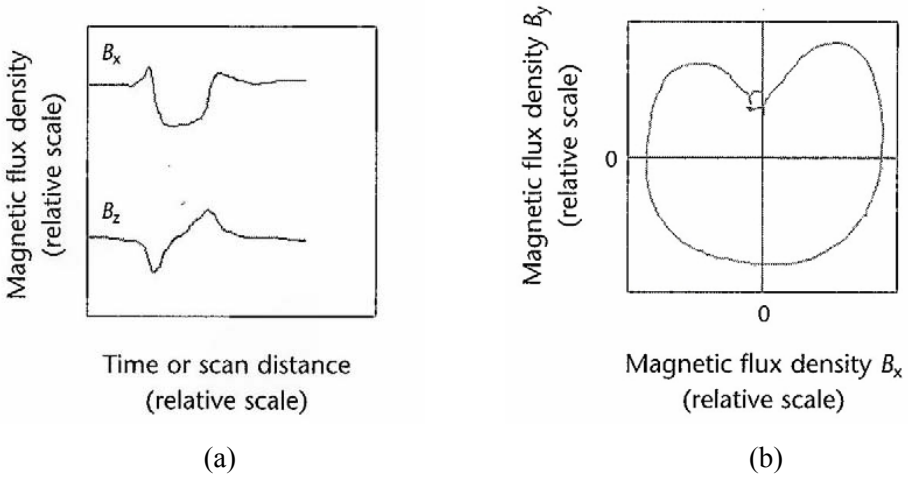

Figure 2.10: *(a) Typical signals from a discontinuity in Alternating Current Field Measurement. (b) The same signals combined to form a butterfly plot [49].*

of the crack [50]; if the shape of the real defect deviates from a semi-ellipse, the predictions of these models can be affected by significant errors. Furthermore, the models are based on isolated flaws, and therefore they do not lend themselves well to the study of clustered defects, which are typical for example of stress corrosion cracking: laboratory and on-site tests on pipes and storage tanks have shown that, while detection of these defects is good, improvements are needed in order to achieve accurate sizing [51, 52].

Apart from the possibility of sizing cracks without requiring calibration, one of the main differences between the conventional Eddy Current technique and ACFM is that in the latter a uniform input field, generally induced by larger coils, is used for inspection. The currents are then forced to flow further down the face of a crack, thus allowing sizing of cracks up to 20-30 mm deep, much more than the maximum depth sensitivity of Eddy Current testing [49]; if deeper penetration is required, Potential Drop techniques are more suitable thanks to the direct injection of currents. Another important advantage of ACFM is the small influence of lift-off on signals, due to the fact that the intensity of a uniform input field decays less rapidly with distance from the inducing coil: this technique is therefore suitable for testing rusty surfaces or structures covered with coatings up to 5 mm thick [52, 53].

On the other hand, using a larger coil means that ACFM has a lower sensitivity to small discontinuities at the normal operating frequencies (about 5 kHz); higher frequencies and smaller detection coils can improve sensitivity but noise increases [54]. Sensitivity to shallow defects is also reduced by the presence of thick or conductive coatings. Another disadvantage related to the larger size of the induction coil is that, because the currents spread out further, spurious signals are obtained from nearby geometry changes such as plate edges. A third, important disadvantage is the fact that the signal from a defect depends on the orientation of the discontinuity, and signals obtained from defects not aligned with the scanning direction of the probe need careful evaluation [49, 53].

ACFM can be used to test all metals, regardless of their magnetic permeability, which however does strongly affect the output field. This technique has proved suitable for underwater inspection [54, 55] and on-site testing of large welded structures [51, 56, 57].

2.9 Conclusions

From a survey of the literature on electromagnetic methods for Non-Destructive Testing it emerged that Potential Drop techniques (DCPD and ACPD) offer the possibility for further development, thanks to the availability of theoretical models of the underlying physical principles and especially to the recent progress in electronics and computational capabilities. Potential Drop techniques have been introduced only briefly here to show their relationship with other electromagnetic NDT methods, but they will be discussed in more detail in the rest of this thesis. In particular, a low-current experimental setup developed for the present work is described in Chapter 3, while in Chapter 4 some of the main concerns regarding practical applications of PD techniques are addressed; advances in modelling and defect characterisation are discussed in the remaining Chapters.

Chapter 3

Experimental setup for Potential Drop measurements

3.1 Introduction

This Chapter gives a description of an experimental setup for Potential Drop measurements developed with the assistance of Prof. Peter B. Nagy of the University of Cincinnati and used throughout the present work. The system is capable of injecting alternating currents (AC) of frequency variable between 0.1 Hz and over 10 kHz: at the lower end of this spectrum the skin depth calculated with Eq. 2.1 would typically be much larger than the thickness of the tested structure for most materials, and therefore, in many ways, the system effectively behaves as if direct currents (DC) were injected.

As discussed in the previous Chapter, Potential Drop systems using AC generally require the injection of currents of smaller intensity than those needed in DC-based systems: this is because the skin depth effect, which forces currents to flow only in a small layer under the surface, causes voltage drops which are larger and therefore easier to measure. Laboratory and commercially available ACPD systems (see for example [34, 37, 44, 58–61]) typically operate at frequencies between 300 Hz and a few kHz and often inject currents of 1 A or less. However, thanks to the state-of-

the-art instrumentation used in the setup developed for the present work, currents of the order of magnitude of 100 mA or less are sufficient in most cases even in the quasi-DC regime.

The probe used initially was based on the simplest configuration commonly used for Potential Drop measurements [28], shown in the schematic of Fig. 2.6 and consisting of two pairs of electrodes: one is used to inject currents in the specimen to be tested, while the other measures the voltage drop. Array probes with multiple electrode pairs were used later in this study, requiring the addition of multiplexers and other instruments. These changes to the setup will be discussed in the relevant Chapters; here a description will be given of the basic instrumentation.

A block diagram of the experimental setup is shown in Fig. 3.1 and the devices used are listed in Table 3.1; the working principle of the system can be briefly described as follows.

The signal coming from a function generator passes through a differential output amplifier, whose purpose is to ensure that the currents injected into the material through the first pair of electrodes of the probe are of equal amplitude and opposite sign. The function generator which drives the current electrodes is in fact a voltage

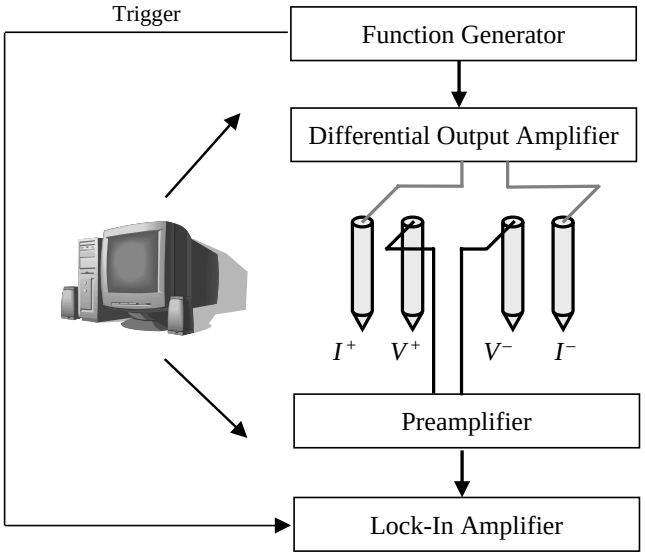

Figure 3.1: *Block diagram of the Potential Drop measurement system.*

Table 3.1: *Instruments used in the Potential Drop measurement system.*

Function Generator	Stanford Research DS335 Synthesized Function Generator *(not necessary if using the SR830 Lock-In Amplifier)*
Differential Output Amplifier	Texas Instruments THS4141 Evaluation Module *or* Stanford Research SIM983 Scaling Amplifiers
Preamplifier	Stanford Research SR552 Bipolar Preamplifier *or* Stanford Research SR554 Transformer Preamplifier
Lock-In Amplifier	Stanford Research SR530 Lock-In Amplifier *or* Stanford Research SR830 Lock-In Amplifier

source; however, since the loading impedances expected (about 0.1 Ω) are much smaller than its output resistance (50 Ω), it effectively behaves as a current source, and as such it will often be referred to for brevity in the remainder of this work. The voltage measured at the second pair of probe electrodes is fed through a preamplifier and then read with a lock-in amplifier. The measurements can be automated by using a computer to operate all the instrumentation through a routine written in LabVIEW, a popular software used to control electronic devices remotely. A detailed description of the electronics used in this experimental setup is beyond the scope of the present work, but the most relevant characteristics of the various instruments, as well as the rationale behind their choice, will be discussed later in this Chapter.

In order to do this, it is helpful to briefly describe first the equivalent electrical circuit of the measurement system. The simplified circuit is shown in Fig. 3.2, where R_{gH} and R_{gL} indicate the output resistances of the generator, R_{IH}, R_{IL}, R_{VH} and R_{VL} are the contact resistances between the four electrodes of the probe and the inspected material, while R_H, R_x and R_L are the resistances encountered by the current flowing in the specimen; in particular, R_x is the resistance in the path

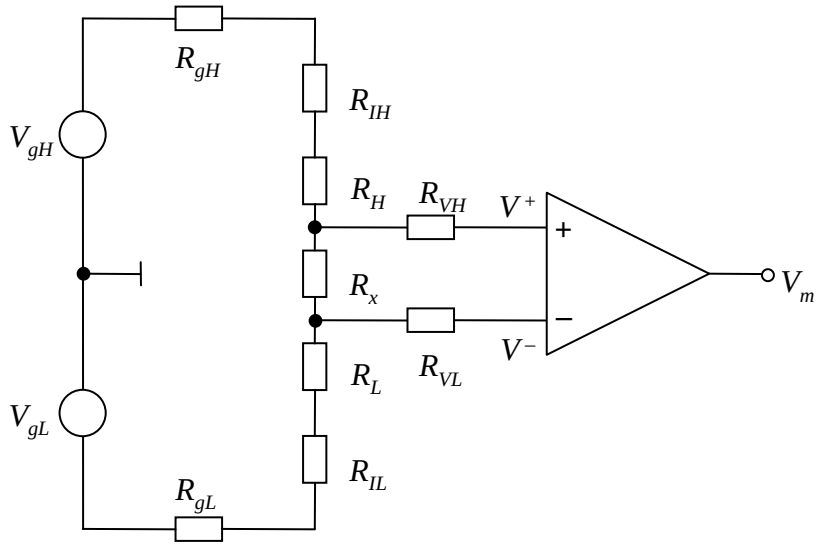

Figure 3.2: *Simplified equivalent electrical circuit of the Potential Drop measurement system.*

between the two internal electrodes, across which the voltage drop is measured, whereas R_H and R_L are the resistances between either of the injecting electrodes and its adjacent voltage electrode.

Assuming that the output of the amplifier is simply proportional to the difference between the input signals V^+ and V^-, and neglecting the loading effect of the input impedance of the amplifier itself (typically 10–100 MΩ), the measured signal V_m can be expressed as

$$V_m = (V^+ - V^-)\, G = \\ = (V_{gH} - V_{gL}) \frac{R_x}{R_{gH} + R_{IH} + R_H + R_x + R_L + R_{IL} + R_{gL}} G, \tag{3.1}$$

where G is the gain of the differential amplifier. The output impedances of the generator $R_{gH} \approx R_{gL} \approx 50\ \Omega$ are much larger than either the contact resistances $R_{IH} \approx R_{IL} \approx R_{VH} \approx R_{VL} \approx$ 10–100 mΩ or the intrinsic resistances of the material $R_x \approx R_H \approx R_L \approx$ 1–10 $\mu\Omega$. Therefore, substituting $V_{gH} \approx -V_{gL} \approx V_g$ and $R_{gH} \approx R_{gL} \approx R_g$ in Eq. 3.1, the measured voltage can be approximated as

$$V_m \approx V_g \frac{R_x}{R_g} G. \tag{3.2}$$

It should be mentioned here that, while the quantity measured in Potential Drop

tests is in fact a voltage difference, it is not uncommon to present the results of such measurements in the form of a *transfer resistance*. This is defined as the ratio R between the voltage difference $(V^+ - V^-)$ between the sensing electrodes and the nominal injected current $I_g = \dfrac{V_g}{R_g}$. Hence from Eq. 3.2 follows

$$R \approx R_x. \tag{3.3}$$

Note that the transfer resistance R does not coincide exactly with the 'real' resistance R_x encountered by the currents flowing in the material. This is because the very simple expressions of Eqs. 3.2 and 3.3 are based on the assumption that the system is perfectly symmetric, and in particular that the amplifier is an ideal differential amplifier; corrections must be made to take into account the asymmetries of a real system, as will be discussed in the following Section.

It should also be noted that, while it would be possible in theory to use one single pair of electrodes for both current injection and voltage sampling, as is done in common ohmmeters, this solution is not generally employed in practice for Potential Drop measurements because it would introduce substantial errors. If using one pair, the equivalent electrical circuit of Fig. 3.2 would be modified into the apparently simpler circuit of Fig. 3.3, where R_{VH} and R_{VL} now indicate the contact resistances of the

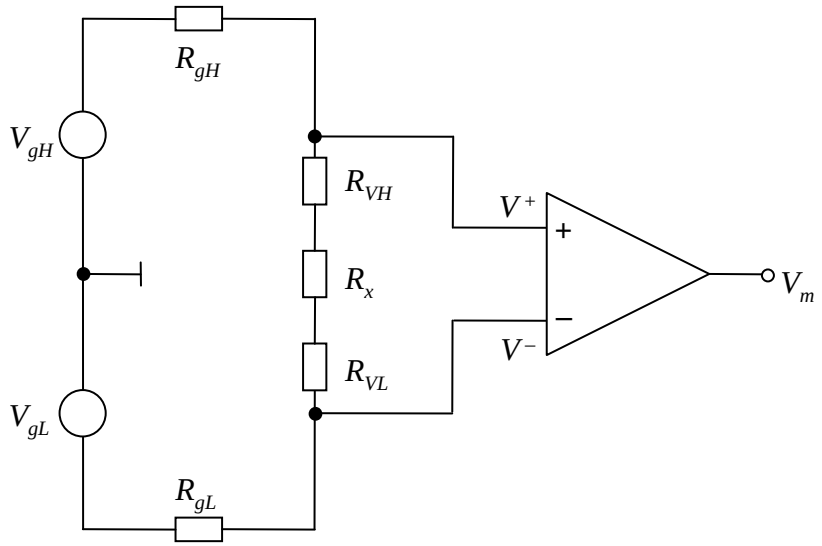

Figure 3.3: *Simplified equivalent electrical circuit of a system using only one pair of electrodes for both current injection and voltage measurement.*

only two electrodes. The current flowing through these resistances is the same that is injected in the specimen; as a consequence, the voltage drop across them, which also appears as a difference between the inputs of the amplifier, must be taken into account, and the measured signal V_m is given by

$$V_m = (V^+ - V^-)\ G = (V_{gH} - V_{gL})\frac{R_{VH} + R_x + R_{VL}}{R_{gH} + R_{VH} + R_x + R_{VL} + R_{gL}}G. \tag{3.4}$$

Because of the large differences between the various resistances, as discussed above, Eq. 3.4 can be approximated as

$$V_m \approx V_g\frac{R_{VH} + R_{VL}}{R_g}G, \tag{3.5}$$

which shows how the measured voltage would be proportional to the contact resistances of the electrodes and effectively independent of the much smaller sought resistance R_x in the material being tested.

3.2 Notes on the Common Mode Rejection Ratio (CMRR)

The output V_m of a real amplifier is not simply proportional to the difference between the two input signals V^+ and V^-, as the instrument inevitably exhibits less than perfectly symmetric transfer properties and amplifies the two inputs by slightly different factors G^+ and G^- respectively. It is therefore more correct to write

$$V_m = V^+G^+ - V^-G^- = (V^+ - V^-)G_d + \frac{V^+ + V^-}{2}G_c, \tag{3.6}$$

where $G_d = \dfrac{G^+ + G^-}{2}$ is the differential gain and $G_c = G^+ - G^-$ is called the common mode gain. This formulation shows that the output of a real amplifier has an additional component proportional to the average (common) input signal. To take this into account, Eq. 3.1 must be amended as follows:

$$\begin{aligned} V_m = (V_{gH} - V_{gL})&\frac{R_x}{R_{gH} + R_{IH} + R_H + R_x + R_L + R_{IL} + R_{gL}}G_d + \\ &+ \frac{1}{2}\frac{V_{gH}(R_x + R_L + R_{IL} + R_{gL}) + V_{gL}(R_x + R_H + R_{IH} + R_{gH})}{R_{gH} + R_{IH} + R_H + R_x + R_L + R_{IL} + R_{gL}}G_c; \end{aligned} \tag{3.7}$$

with the usual approximations, this can be re-written as

$$V_m \approx V_g \frac{R_x}{R_g} G_d + V_g \frac{R_{IL} - R_{IH}}{4R_g} G_c. \tag{3.8}$$

In this equation, the first term of the sum represents the true differential signal $V_{m,d}$ as would be obtained with an ideal amplifier, while the second term is the common mode signal $V_{m,CM}$.

The ratio between the differential and the common mode gains is known as the Common Mode Rejection Ratio (CMRR) and is an important characteristic of an amplifier:

$$\text{CMRR} = \frac{G_d}{G_c}. \tag{3.9}$$

Introducing this quantity in Eq. 3.8 yields

$$V_m \approx V_g \frac{R_x}{R_g} G_d \left(1 + \frac{\Delta R_I}{4R_x \text{CMRR}}\right); \tag{3.10}$$

similarly, the expression of transfer resistance of Eq. 3.3 becomes

$$R \approx R_x \left(1 + \frac{\Delta R_I}{4R_x \text{CMRR}}\right). \tag{3.11}$$

The common mode signal, and thus the error in the measured voltage, is therefore mainly due to the difference between the contact resistances of the two injection electrodes, $\Delta R_I = R_{IL} - R_{IH}$; since these resistances are much (about 10000 times) larger than the sought material resistance R_x, this effect is not negligible. If the contact resistances differ by as much as 50%, even a relatively high CMRR = 100 dB (*i.e.* $G_d/G_c = 100000$) could be insufficient to suppress the corresponding variation in the potential drop, and as a consequence the measurement could be affected by an error of a few percent.

3.2.1 Investigation on the effects of variations in contact resistance

The following experiment illustrates how inevitable variations in the contact resistance can severely compromise the accuracy of the measurements if the Common Mode Rejection Ratio is not sufficiently high.

The injection electrodes of the probe, at a distance $2a = 20$ mm from each other, were driven differentially by $V_{gH} - V_{gL} = 10\ \mathrm{V_{pp}} = 3.54$ V, and therefore the current was $I = 35.4$ mA; the sensing electrodes were located between the current electrodes at a distance $2b = 10$ mm from each other. As will be shown in the following Section, the CMRR of the system is lowest if none of the preamplifiers mentioned in Table 3.1 is used; therefore, in order to underline the consequences of an insufficient common mode rejection, the voltage measured was fed directly to a SR530 lock-in amplifier, whose CMRR at the frequency used for the test ($f = 4$ Hz) was found experimentally to be about 85 dB (see Fig. 3.7).

The probe was positioned on 50 different randomly chosen locations on a 50-mm thick block of 304 stainless steel with a clean but roughly machined surface. At each point both the differential and the common mode signal were measured, the latter being given with very good approximation by the voltage at either of the sensing electrodes. The differential measurement was repeated at each location after switching the input channels of the lock-in amplifier. This is because, as shown by Eq. 3.10, the measured 'differential' signal actually contains a significant common mode component which is not affected by switching the inputs, as opposed to the truly differential component, which changes sign. Thus, rewriting Eq. 3.10, the first measurement gives

$$V_m^{(1)} \approx V_g \frac{R_x}{R_g} G_d \left(1 + \frac{\Delta R_I}{4 R_x \mathrm{CMRR}}\right), \tag{3.12}$$

whereas a second measurement, taken after reversing the input channels, gives

$$V_m^{(2)} \approx V_g \frac{R_x}{R_g} G_d \left(-1 + \frac{\Delta R_I}{4 R_x \mathrm{CMRR}}\right). \tag{3.13}$$

The two values $V_m^{(1)}$ and $-V_m^{(2)}$ of the 'differential' signal measured before and after switching are plotted in Fig. 3.4 versus the common mode voltage measured at the same location. It can be seen that the larger the common mode signal, due to the difference ΔR_I between the contact resistances of the injecting electrodes, the more the two measured 'differential' values diverge from each other and from the true differential signal $V_m = 1.17\ \mu$V, as predicted by Eq. 3.12 and Eq. 3.13; whether the

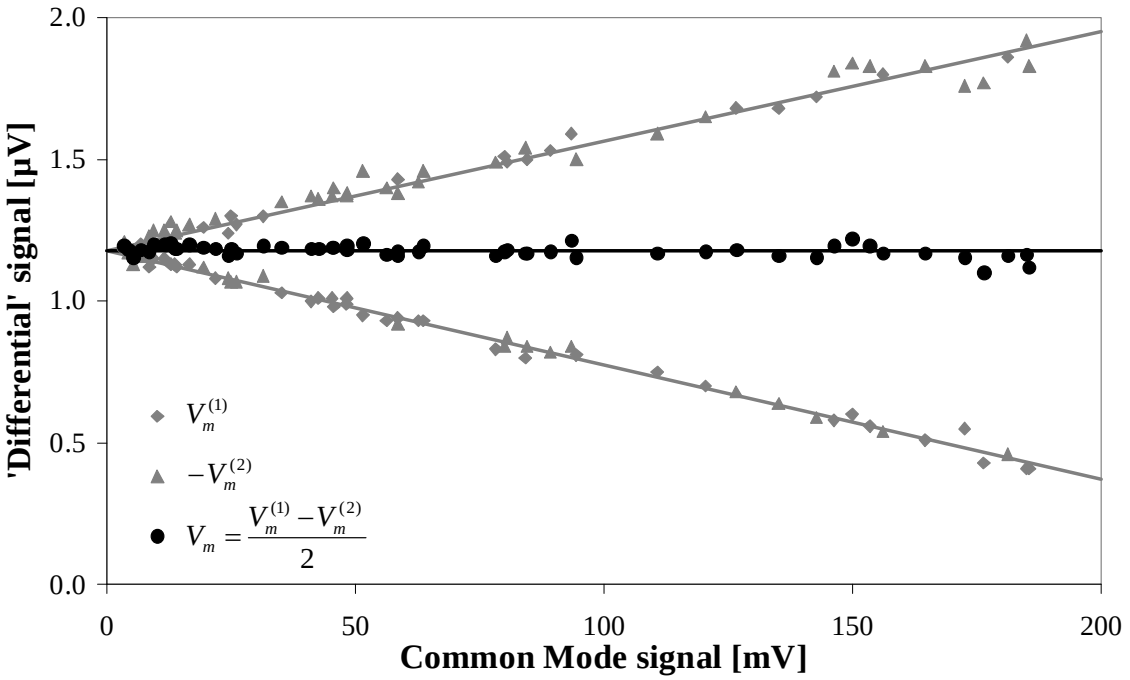

Figure 3.4: *Measured 'differential' signals $V_m^{(1)}$ and $-V_m^{(2)}$ for two different input channel polarities and true differential signal V_m versus the common mode signal at 50 randomly chosen locations on a 50-mm thick SS304 block with roughly machined surface (see text for details).*

higher value is obtained at the first or at the second measurement depends on the sign of the randomly changing difference ΔR_I.

However, if the two measured 'differential' signals are subtracted from each other, the spurious common mode components cancel out (within the accuracy of the measurements):

$$\begin{aligned} V_m &= \frac{V_m^{(1)} - V_m^{(2)}}{2} \approx \\ &\approx \frac{1}{2}\left[V_g \frac{R_x}{R_g} G_d \left(1 + \frac{\Delta R_I}{4R_x \mathrm{CMRR}}\right) - V_g \frac{R_x}{R_g} G_d \left(-1 + \frac{\Delta R_I}{4R_x \mathrm{CMRR}}\right)\right] \approx \\ &\approx V_g \frac{R_x}{R_g} G_d. \end{aligned} \tag{3.14}$$

The values of the true differential signal thus obtained for each location are also plotted in Fig. 3.4: it can be seen that they are independent of the amplitude of the common mode signal, at least in the range explored in this test (the measured

signals differed by as much as 50% from the true differential signal). The residual spurious common mode component, responsible for the oscillations in the differential signal V_m, does not exceed 0.03 μV, and is therefore reduced by more than one order of magnitude (about 30 dB).

To sum up, the results of this experiment show that the effective CMRR of the system can be increased with a very simple procedure which consists in taking a differential measurement of potential drop a first time, then inverting the input channels of the preamplifier (this can be easily done either by manually switching the cables, or with a 2-way multiplexer, maybe remotely controlled) and repeating the measurement, and finally subtracting the two values from each other. This expedient, which has been utilised also by other authors [39], can be considered as the simplest method of reducing measurement variations due to imperfect contact resistances, and has been applied for all measurements throughout the present study, except when the measurement speed was of concern in multiple-channel experiments and the system CMRR was sufficiently high (thanks to the special transformer-coupled preamplifier) to neglect this problem.

3.3 Notes on the instruments used

3.3.1 Preamplifiers

As discussed in the previous Section, a high Common Mode Rejection Ratio is required in order to recover the signal of interest, especially if the contact between one of the injecting electrodes and the surface of the specimen being tested is of poor quality. High values of CMRR can be reached by introducing a preamplifier in the measuring system.

The Stanford Research SR552 Bipolar Preamplifier has a CMRR which exceeds 100 dB at 100 Hz (this means that the differential part of the signal is amplified by a factor 10^5 times higher than the common signal) and degrades by 20 dB per

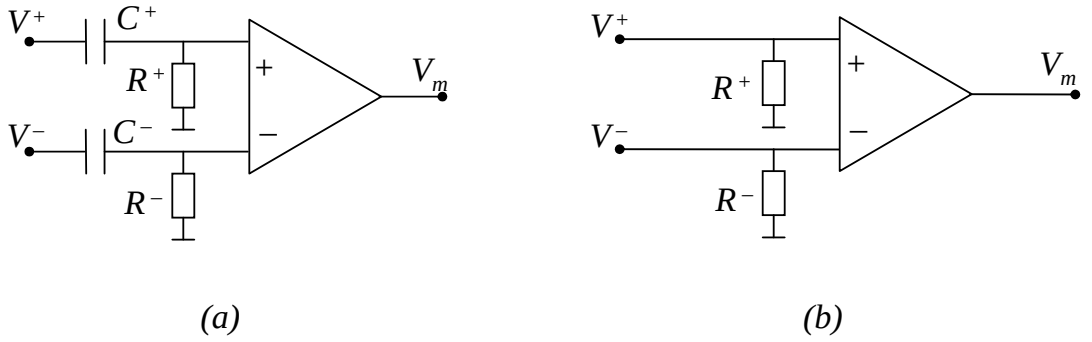

Figure 3.5: *Schematic of (a) AC-coupled and (b) DC-coupled differential amplifiers.*

decade above 1 kHz because of frequency-dependent symmetry effects. However, it is important to note that, as supplied by the manufacturer, this preamplifier is AC-coupled and therefore its CMRR decreases also at low frequencies because of similar asymmetries in the coupling. In order to understand this, let us consider the schematic of a generic AC-coupled amplifier shown in Fig. 3.5*a*. The AC coupling is also known as high-pass filter, since the capacitors C^+ and C^- let through only high-frequency components of the signal while stopping direct currents and attenuating low-frequency components; the gain of an ideal AC-coupled amplifier then decreases by 20 dB/decade below the so-called cut-off frequency $f_0 = (2\pi RC)^{-1}$. Inevitable differences between the capacitors (and to a smaller extent between the resistors) in a real amplifier lead to two different cut-off frequencies f_0^+ and f_0^-, so that the gains G^+ and G^- do not decrease simultaneously, as illustrated in Fig. 3.6; ultimately, this contributes to increasing the common mode signal. The qualitative plot in Fig. 3.6 highlights the two main sources of a common mode signal, namely (1) the difference between the gains G^+ and G^- of the two inputs and (2) the difference between the cut-off frequencies f_0^+ and f_0^-.

The SR552 preamplifier used in the present work was modified by short-circuiting its internal capacitors in order to make it DC-coupled (see the schematic of Fig. 3.5*b*): the device exhibits then a constant gain (and hence CMRR) at low frequencies, whereas its high-frequency behaviour is not affected. With careful optimisation it was possible to achieve a CMRR of over 120 dB for all frequencies up to 1 kHz, as shown in Fig. 3.7. The Common Mode Rejection Ratio of an amplifier, defined in

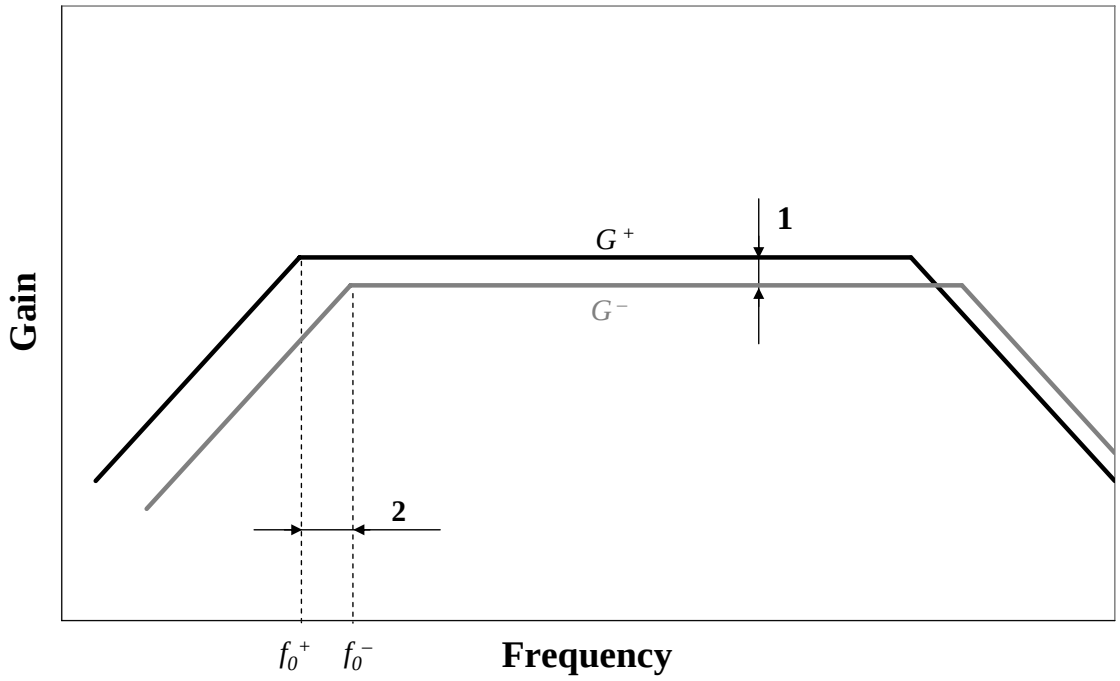

Figure 3.6: *Gains of the two inputs of an AC-coupled amplifier as a function of frequency.*

the previous Section as the ratio between the differential gain and the common mode gain, can be easily measured by feeding a low-voltage (*e.g.* 0.1 V) signal directly from the function generator to both input channels of the amplifier: the ratio between the amplitudes of the input signal and of the resulting 'differential' signal read on the amplifier gives the CMRR.

Another characteristic of the SR552 preamplifier, particularly important at higher frequencies, is its small voltage noise: 1.4 nV/$\sqrt{\text{Hz}}$ at 1 kHz, according to the specifications. However, the lowest level of voltage noise (only 0.1 nV/$\sqrt{\text{Hz}}$ at 1 kHz) is exhibited by the Stanford Research SR554 Transformer Preamplifier, which combines a passive transformer having a turn ratio of 100 with an amplifier whose gain is 5.00; this results in a total gain of 500. As shown in Fig. 3.7, this instrument has an extremely high Common Mode Rejection Ratio (over 160 dB below 10 Hz), although its performance degrades rapidly with increasing frequency not only because of the capacitive coupling between the primary and secondary windings, but also because at very low and high frequency the gain is reduced. In fact, the gain of the SR554 preamplifier, unlike that of the other instruments used in this setup, depends

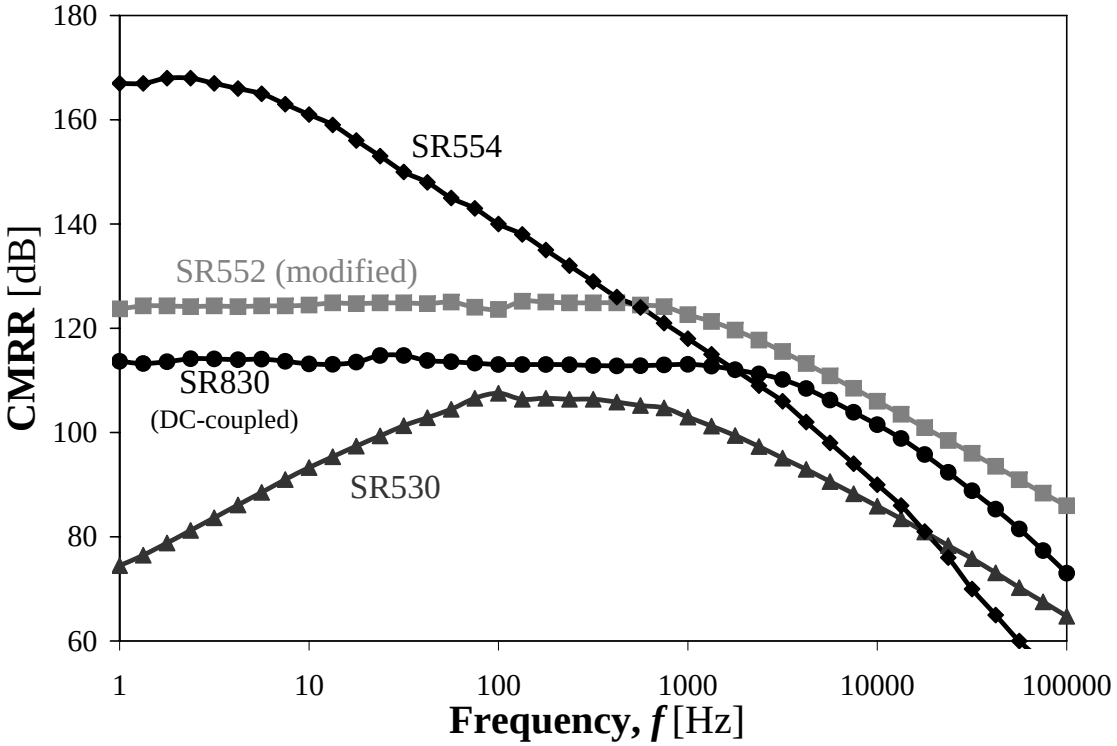

Figure 3.7: *Common Mode Rejection Ratio measured as a function of frequency for the amplifiers and preamplifiers used in the setup.*

Table 3.2: *Summary of the main specifications of the preamplifiers used in the setup.*

	SR552 Bipolar Preamp.	SR554 Transformer Preamp.
Input impedance	100 kΩ	0.5 Ω
Voltage noise	2.5 nV/$\sqrt{\text{Hz}}$ at 10 Hz 1.6 nV/$\sqrt{\text{Hz}}$ at 100 Hz 1.4 nV/$\sqrt{\text{Hz}}$ at 1 kHz	0.12 nV/$\sqrt{\text{Hz}}$ at 10 Hz 0.10 nV/$\sqrt{\text{Hz}}$ at 100 Hz 0.10 nV/$\sqrt{\text{Hz}}$ at 1 kHz
Gain	100	500
Frequency range (for 2% gain accuracy)	DC – 100 kHz (after modification)	1 Hz – 10 kHz
Output impedance	600 Ω	< 1.0 Ω

on the source impedance, which in the case of Potential Drop measurements will be given by the contact resistances between the voltage electrodes and the inspected material; as the source impedance increases, the frequency range over which the gain is constant at its maximum value (and therefore the CMRR is highest) narrows considerably. However, for the typical values of contact resistance expected in PD measurements, the gain of this device is practically constant between 1 Hz and 1 kHz, and the CMRR still exceeds 140 dB up to 100 Hz; this makes the SR554 the preamplifier of choice for tests at frequencies up to about 1 kHz.

The main specifications of both preamplifiers are summarised in Table 3.2.

3.3.2 Lock-in amplifiers

A lock-in amplifier has the capability of recovering small signals from strong noise. This feature, particularly important in Potential Drop applications where the signals of interest can often be smaller than 1 μV, is achieved by supplying the lock-in amplifier with a reference voltage (trigger) having the same frequency and a fixed phase relationship to the signal to be measured; the instrument will then be able to effectively tune a filter with a very narrow bandwidth to the frequency of the signal, thus rejecting most of the noise. In the first part of this study the Stanford Research SR530 Lock-In Amplifier was used, and the reference voltage was provided by the same function generator used to generate the signal for the inspection. At a later stage the SR530 was replaced by the more advanced Stanford Research SR830 Lock-In Amplifier, which has an internal oscillator capable of generating the signal: the function generator can then be eliminated from the system, and the trigger is taken internally from the amplifier itself.

In order to explain in more detail the working principle of a lock-in amplifier, let us consider a generic sinusoidal input signal $V_i = A_i \cos(\omega_i t + \varphi)$, where φ is an arbitrary phase shift with respect to a reference signal $V_r = A_r \cos \omega_r t$; if the same source is used for both signals, the two frequencies will obviously coincide, but the calculations will be developed initially for the more general case $\omega_i \neq \omega_r$. At the

heart of the lock-in amplifier is a phase-sensitive detector, also called mixer, which multiplies the input and reference signals with each other; its output is therefore

$$V_{mix} = V_i V_r = A_i A_r \cos(\omega_i t + \varphi) \cos \omega_r t = \\ = \frac{A_i A_r}{2} \cos(\omega_i t - \omega_r t + \varphi) + \frac{A_i A_r}{2} \cos(\omega_i t + \omega_r t + \varphi). \tag{3.15}$$

The mixer is followed by a low-pass filter which will in general reject both components; however, if $\omega_i = \omega_r$, then a DC signal

$$V_X = \frac{A_i A_r}{2} \cos \varphi \tag{3.16}$$

will pass undisturbed through the filter. The output of the lock-in amplifier will thus be proportional to the input, but subject to variations if the phase shift φ between the input and the reference signals varies. In order to remove this latter effect, most lock-in amplifiers use a second mixer identical to the first one but driven by a reference signal phase-shifted by 90°. The output from this second mixer is

$$V'_{mix} = V_i V'_r = A_i A_r \cos(\omega_i t + \varphi) \sin \omega_r t = \\ = \frac{A_i A_r}{2} \sin(\omega_r t - \omega_i t - \varphi) + \frac{A_i A_r}{2} \sin(\omega_i t + \omega_r t + \varphi), \tag{3.17}$$

which reduces to

$$V_Y = -\frac{A_i A_r}{2} \sin \varphi \tag{3.18}$$

if $\omega_i = \omega_r$. The outputs of the two mixers represent the components of a vector of magnitude

$$V_o = \sqrt{V_X^2 + V_Y^2} = \frac{A_i A_r}{\sqrt{2}}. \tag{3.19}$$

Since the amplitude A_r of the reference signal is usually known, Eq. 3.19 gives a measure of the amplitude of the input signal independent of its phase shift with respect to the reference.

Any spurious signal (noise) at a generic frequency $\omega_i \neq \omega_r$ will be filtered out, as discussed above. In practice, components at frequencies very close to ω_r will also pass through the filter with little attenuation; however, it can be shown that the

Table 3.3: *Summary of the main specifications of the lock-in amplifiers used in the setup.*

	SR530 Lock-In Amplifier	SR830 Lock-In Amplifier
Input impedance	100 MΩ	10 MΩ
Voltage noise	7 nV/$\sqrt{\text{Hz}}$ at 1 kHz	6 nV/$\sqrt{\text{Hz}}$ at 1 kHz
Full scale sensitivity	100 nV – 500 mV	2 nV – 1 V
Frequency range	0.5 Hz – 100 kHz	1 mHz – 100 kHz

bandwidth of the low-pass filter is inversely proportional to the time over which the signal is integrated, so that, by using sufficiently long time constants (typically a few seconds for the applications presented in this work), it is possible to restrict the effective bandwidth to a fraction of a Hz.

The Common Mode Rejection Ratio of both the SR530 and the SR830 lock-in amplifiers was measured experimentally and is shown in Fig. 3.7. Note that the SR830 offers the possibility of switching between AC and DC coupling, but for the sake of clarity only the values measured when the DC coupling was selected have been plotted in Fig. 3.7; if the AC coupling is used instead, the CMRR decreases at low frequency in a similar fashion as for the SR530, which is an AC-coupled amplifier. Although the CMRR of both instruments is relatively high, the advantage given by the use of either the SR552 Bipolar Preamplifier or the SR554 Transformer Preamplifier is evident.

A summary of the other main specifications of both the lock-in amplifiers used in the present work is given in Table 3.3.

3.3.3 Differential output amplifiers

The role of the differential output amplifier in the setup of Fig. 3.1 is to reduce the common mode signal by increasing the symmetry of the system. It can be easily shown that, if no differential output amplifier were used and the probe received

the excitation signal directly from the function generator ($V_{gL} = 0$, $R_{gL} = 0$ with reference to the schematic in Fig. 3.2), the differential component of the measured signal would not change, whereas the common mode signal would increase to

$$V_{m,CM} = \frac{1}{2} V_g \frac{R_x + 2R_L + 2R_{IL}}{R_g + R_{IH} + R_H + R_x + R_L + R_{IL}} G_c, \tag{3.20}$$

where V_g and R_g have been used instead of V_{gH} and R_{gH}. Because of the large differences between the various resistances, as discussed above, Eq. 3.20 can be approximated as

$$V_{m,CM} \approx V_g \frac{R_{IL}}{R_g} G_c. \tag{3.21}$$

The common mode signal would then be proportional to the value of the contact resistances, rather than to their difference.

The instrument initially used in the setup was a Texas Instruments THS4141 Evaluation Module, a fully-differential amplifier (this means that the same device can be used both as a differential input amplifier and as a differential output amplifier), driven by an external two-channel power supply. The default gain of this amplifier is ± 1.

This device was later replaced by a pair of Stanford Research SIM983 Scaling Amplifiers, whose gain can be varied between ± 0.01 and ± 19.99 in steps of 0.01. The gain of each of the two SIM983 amplifiers can be adjusted separately if necessary, thus allowing further, fine corrections to the symmetry of the system if the common mode signal happens to be too high due to the poor quality of the contact between one of the injecting electrodes and the inspected surface.

3.4 Conclusions

An experimental setup for Potential Drop measurements was developed, and the main characteristics of the instruments used have been presented. In particular, the role of the Common Mode Rejection Ratio has been discussed, and it has been shown that high values of CMRR are required in order to recover the signal of interest;

furthermore, the effect of variations in the contact resistance between the electrodes and the surface of the inspected material has been analysed, and it has been shown that by simply repeating a measurement after switching the input channels of the preamplifier it is possible to further improve the quality of the data. Thanks to the very high effective CMRR that can thus be achieved and to the capability of the lock-in amplifier to measure accurately signals as small as 2 nV even in the presence of strong noise, it is possible to inject currents of much smaller amplitude than those required in most existing Potential Drop systems.

Results obtained with this experimental setup will be presented in the remainder of this work. In particular, the next Chapter will describe some benchmark tests that were run to compare the performance of this setup with that of commercially available DCPD systems.

Chapter 4

Benchmarking against commercial PD systems

4.1 Introduction

As mentioned in the previous Chapter, the experimental setup for Potential Drop measurements developed for the present work, which will be referred to in the following as the 'Imperial' system, was designed to operate with currents of about 100 mA even in the quasi-DC regime; in contrast, the order of magnitude of the currents required by commercially available DPCD systems and by other laboratory setups developed in the past is often 10–100 A [32,33,35,36,62]. In order to compare the performance of some of these systems, a simple benchmark test was devised to evaluate their stability with respect to various issues that may arise when employing Potential Drop techniques in the field.

In this Chapter, after a brief description of two commercial DCPD systems that have been used for industrial applications and a discussion of some of the technical difficulties that monitoring schemes based on the Potential Drop method are commonly thought to suffer from, the test procedure will be described and the results obtained with the selected commercial systems and with the Imperial setup will be presented and discussed.

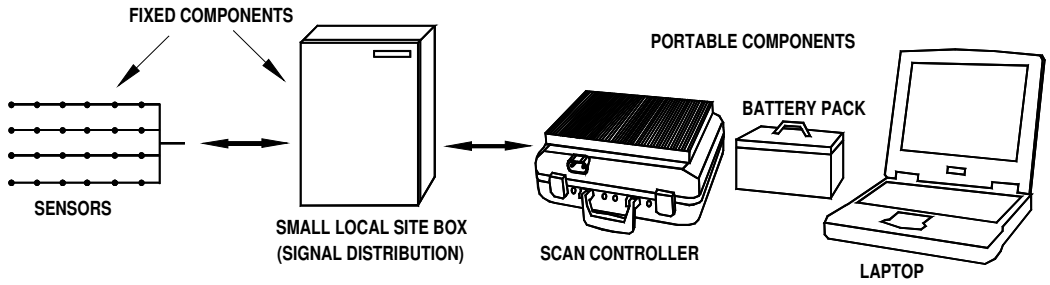

Figure 4.1: *Schematic of the Portable Electrical Resistance system developed by Rowan Technologies Ltd. [33].*

4.2 Commercial DCPD systems used for the test

4.2.1 System developed by Rowan Technologies Ltd.

The first commercial system considered in this study is the Portable Electrical Resistance system developed and patented by Rowan Technologies Ltd. [33], in the following referred to simply as Rowan system; a schematic is given in Fig. 4.1.

The probe consists of an array of equally-spaced nickel alloy electrodes welded onto the surface to be monitored. Four horizontally, vertically or diagonally consecutive electrodes are used at a time for the injection of direct currents of intensity between 10 and 70 A and the measurement of the electrical resistance; the measurements are repeated sequentially to cover all combinations of adjacent electrodes in the array. A second electrode welded in the proximity of each sensing location has the function of monitoring the local temperature, which allows variations in electrical conductivity due to temperature changes to be taken into account. While electrodes and cables are fixed, the multiplexing system that controls the measurement sequence and the battery pack that supplies the power needed are portable and can be moved to different monitoring locations.

A fixed scanner system also developed by Rowan Technologies Ltd. and based on the same technology has been used in the power industry for continuous on-line monitoring of boiler wall corrosion [63, 64] and circumferential crack growth [65].

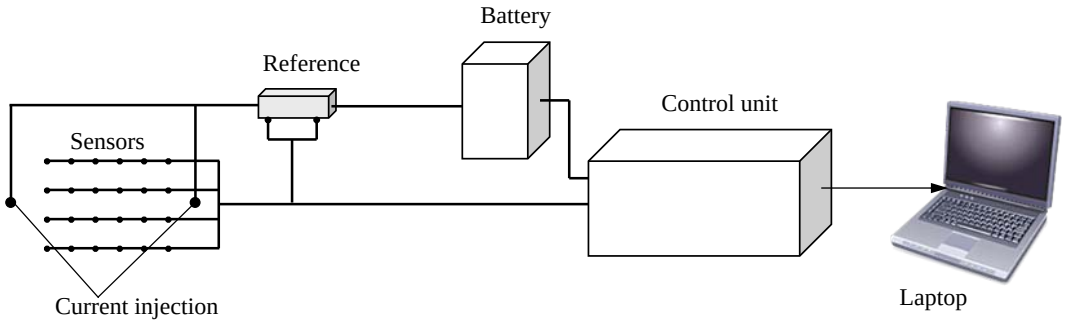

Figure 4.2: *Schematic of the FSM Portable system developed by CorrOcean.*

4.2.2 System developed by CorrOcean

The second commercial system against which the Imperial setup was tested is the FSM Portable system developed by CorrOcean (now Roxar) [32], which will be referred to as CorrOcean system. This setup also employs an array of equispaced electrodes to measure the voltages in the area to be tested, but the current injection points are external to the inspection area (see the schematic of Fig. 4.2).

The voltage differences between horizontally adjacent electrodes only (*i.e.* in the direction of the main current flow) are measured sequentially and divided by the voltage measured on a reference sample which is electrically connected in series with the injecting electrodes. The need for a reference arises from the difficulty in controlling with sufficient precision the intensity of the injected current, which can be as high as 350 A: by scaling each measurement to the voltage read at the same time between two fixed points on the reference sample, the uncertainty associated with the current is effectively eliminated. The reference can also compensate for variations in electrical conductivity due to small changes in temperature. The amplitude of the injected currents is chosen for each case so as to produce a voltage drop large enough for the instrument to read it with sufficient accuracy: it is recommended that the potential drop between any two measuring electrodes be at least 100 μV.

It should be mentioned that the array probe can consist of either permanently attached electrodes, as in the Rowan Technologies system, or spring-loaded pins which are pushed against the area to be inspected, as in the Imperial setup. In

both cases the current feeder, the battery pack and the logging system are portable, although rather bulky; the very large currents injected require cables of considerable diameter.

The acronym FSM stands for Field Signature Method. The name derives from the fact that before the actual measurements a 'signature' is acquired on an uncorroded part of the structure to be tested; this signature is then used as a further reference (baseline) for the estimation of corrosion depth. The CorrOcean system has been used especially in the oil industry for on-line monitoring of corrosion in pipelines, both buried and submerged [66,67], and in power plants for the inspection of welded pipes [68].

4.3 Concerns in practical applications of Potential Drop techniques

Among the difficulties that have been encountered during the years in the applications of Potential Drop techniques in the field, industrial partners in the Research Centre for Non-Destructive Evaluation (RCNDE) have drawn particular attention to the effects of:

1. variations in contact resistance between the electrodes and the inspected material;
2. stray current loops that often develop in large grounded structures;
3. shunt currents that can be created if an electric contact is established between two or more points on the tested structure;
4. variations in the electrical conductivity of the inspected material due to changes in temperature.

The first problem obviously does not arise if the electrodes used for the measurements are permanently or semi-permanently attached (*e.g.* welded or clamped) to

the inspection area, as is the case for the Rowan system. If using a movable probe, as in the Imperial setup, it is possible to greatly reduce the effect of variable contact resistances on the measured signal by using amplifiers with a very high Common Mode Rejection Ratio, as discussed in the previous Chapter. This issue was therefore not considered in the benchmark test.

Increasing the effective CMRR of the system also contributes to reduce the effects of stray current loops that can develop in grounded structures. Ideally, the currents $I_{gH} = \dfrac{V_{gH}}{R_{gH}}$ and $I_{gL} = \dfrac{V_{gL}}{R_{gL}}$ injected in the specimen (see the equivalent electrical circuit of Fig. 3.2) have exactly equal amplitude I_g and opposite sign (for alternating currents, this means that their phase difference is 180°): in this case, the resulting current distribution in the tested structure will not extend beyond a limited region of size about twice the distance between the injecting electrodes, as shown in Appendix A. However, an imbalance may be caused by asymmetries in the driving system such as differences in the output resistances R_{gH} and R_{gL} of the generator. This situation is illustrated in Fig. 4.3: if the dipole formed by the two injected currents I_{gH} and I_{gL} is not ideal, some of the current lines from the positive pole will not close on the negative pole; instead, across an arbitrary closed surface S around the dipole there will be a net current density j, which for the conservation

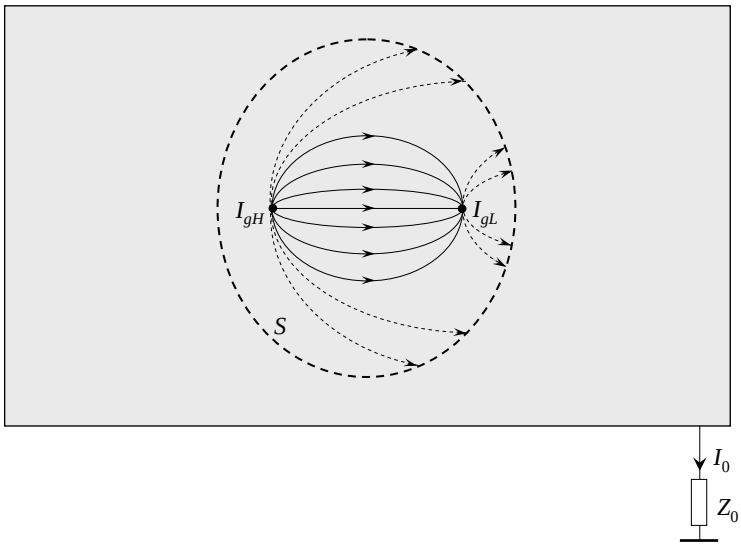

Figure 4.3: *Illustration of the formation of a ground loop from a non-ideal dipole source.*

of electrical charges will be given by

$$\int_S j \, \mathrm{d}S = I_{gH} + I_{gL}. \tag{4.1}$$

Similarly, for the conservation of charges in the remainder of the structure (*i.e.* beyond the volume enclosed by the surface S), there will be a ground current I_0 given by

$$I_0 = \int_S j \, \mathrm{d}S = I_{gH} + I_{gL}. \tag{4.2}$$

If the tested structure is connected to ground through an impedance Z_0, then the common mode voltage measured at the sensing electrodes is increased by $I_0 Z_0$: note that, from Eq. 4.2, I_0 can be effectively considered as the common mode current of the generator. It should be mentioned that this problem arises only if both the driving system and the structure being inspected are separately grounded, as is often the case in the field because of health and safety requirements on large structures. In laboratory tests, however, the specimens are usually electrically insulated ($Z_0 = \infty$), so $I_0 = 0$ which forces the condition $I_{gH} = -I_{gL} = I_g$ even if the driving system *per se* is not entirely symmetric.

Independent of the grounding of the structure, shunt currents can develop if the currents injected are offered an alternative path, *e.g.* in the presence of a 'short circuit' between two or more locations in the inspection area. In this case, part of the current will flow via the shunt, rather than between the electrodes of the probe, and this will result in a smaller measured voltage. The extent to which the measurements can be affected was evaluated in the benchmark test.

Finally, the inherent dependence of a material's electrical conductivity on temperature needs to be taken into account in any long-term monitoring applications of Potential Drop techniques. For many austenitic stainless steels, for example, a temperature increase of 10 °C is sufficient to cause the electrical resistivity, and hence the voltage measured between the electrodes, to increase by about 1% [69]. These variations, although very significant, can be easily compensated for with a simple algorithm, as will be shown in the following Section.

4.4 Test procedure and results

The test procedure devised to compare the performance of the experimental setup described in Chapter 3 and of the commercial systems developed by Rowan Technologies and CorrOcean addresses all the issues presented in the previous Section, with the exception of the variation in contact resistance.

The specimen used for the test is a bar of stainless steel 450 mm long, 55 mm wide and 6 mm thick. The two pairs of electrodes needed for measuring voltage and temperature with the system developed by Rowan Technologies were provided by the company itself and welded on the testpiece (TIG welding) about 125 mm from one end, as shown schematically in Fig. 4.4; the separation between the voltage electrodes is about 25 mm and was chosen so as to have an electrical resistance of around 40 $\mu\Omega$, since the scanner by Rowan Technologies was optimised for measurements between 5 and 166 $\mu\Omega$. The same voltage electrodes were also used as the sensing pair for the CorrOcean and the Imperial systems; connections were made using crocodile clips.

During the tests with the Imperial setup or with the system developed by Corr-

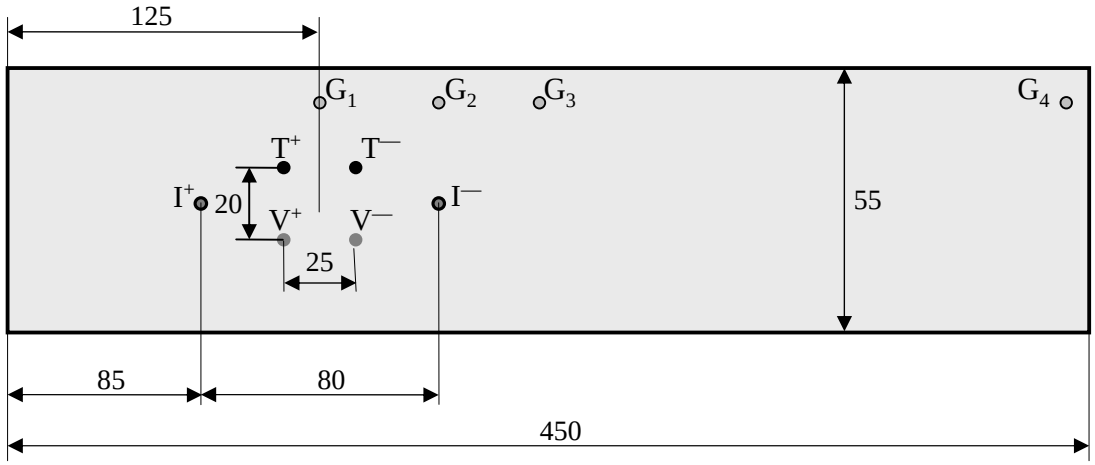

Figure 4.4: *Schematic of the SS304 specimen used for the test, viewed from the top (drawing not in scale). Currents are injected at* I^+ *and* I^-*, voltages measured between* V^+ *and* V^-*, and temperatures monitored at* T^+ *and* T^-*; points* G_1 *through* G_4 *indicate the locations where a cable was attached to connect the testpiece to ground in the first part of the test.*

Ocean, the temperature was monitored using a K-type thermocouple attached on the specimen in proximity of the test area, and recorded using a Pico TC-08 USB Data Logger.

Currents were injected in all cases through copper cables clamped onto the specimen via a bolt, washer and nut on either side of the electrodes (points I^+ and I^- in Fig. 4.4). The CorrOcean and Rowan systems required the injection of direct currents as high as 20 and 38 A, respectively, whereas low-frequency ($f = 4$ Hz) alternating currents of intensity as low as 130 mA were injected with the Imperial setup.

The measurements were controlled via computer, using a LabVIEW routine to operate the instruments in the Imperial setup or dedicated software developed by each the two companies for their respective systems. Resistance and temperature were recorded every 10 s during the tests with the Rowan and Imperial setups, whereas much longer intervals (a few minutes) between two consecutive measurements were necessary when using the CorrOcean system, because of the recovery time needed by the battery that generates the currents for the inspection.

4.4.1 Effect of grounding

The first part of the test evaluated the stability of PD measurements with respect to grounding: the transfer resistance between the sensing electrodes was measured first with the specimen electrically insulated, then after connecting the testpiece to ground by means of a copper cable with crocodile connectors. The grounding cable was attached to a few different positions along the bar, both within the inspection area (between the electrodes, as in point G_1 in the schematic of Fig. 4.4, or close to one of the current injection points, as in G_2 in the same figure) and outside it (first at a small distance, point G_3, then at the opposite end of the specimen, G_4).

Resistance and temperature values measured with the Rowan system are reported in Fig. 4.5, which shows that grounding at any location does not significantly affect the resistance measured between the electrodes. The overall slight increasing trend

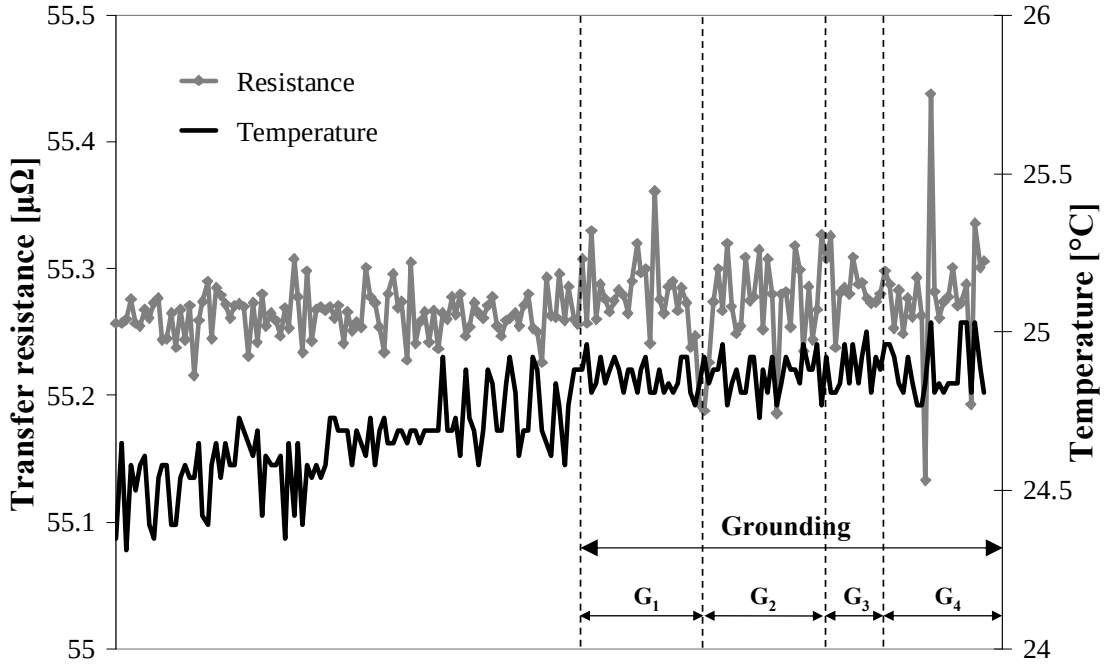

Figure 4.5: *Results with the Rowan system showing no significant change when grounding at different positions (*G_1 *through* G_4*).*

of the resistance is due to the small but perceivable increase in temperature recorded during the test, as no algorithm for thermal compensation was applied to the data at this stage (this will be done later in this Chapter, when the effect of temperature is discussed). Even without taking into account the temperature rise, the difference between the average values of resistance measured before and after grounding (55.26 and 55.28 $\mu\Omega$, respectively) is one order of magnitude smaller than the maximum random oscillation observed, which is about ± 0.2 $\mu\Omega$. It should be mentioned that the values of transfer resistance returned by the Rowan system were higher than expected; the reasons for this are not entirely clear, and unfortunately it was not possible to access the raw data.

The values of resistance measured with the Imperial setup are plotted in Fig. 4.6 together with the temperature registered by the thermocouple; again, the data presented here have not been corrected for temperature variations (see Section 4.5 for the values after thermal compensation). The fluctuations in the values recorded do not exceed ± 0.04 $\mu\Omega$, and there is no sign of a clear correlation between measured resistance and grounding, as the change in the average resistance is only 0.01 $\mu\Omega$.

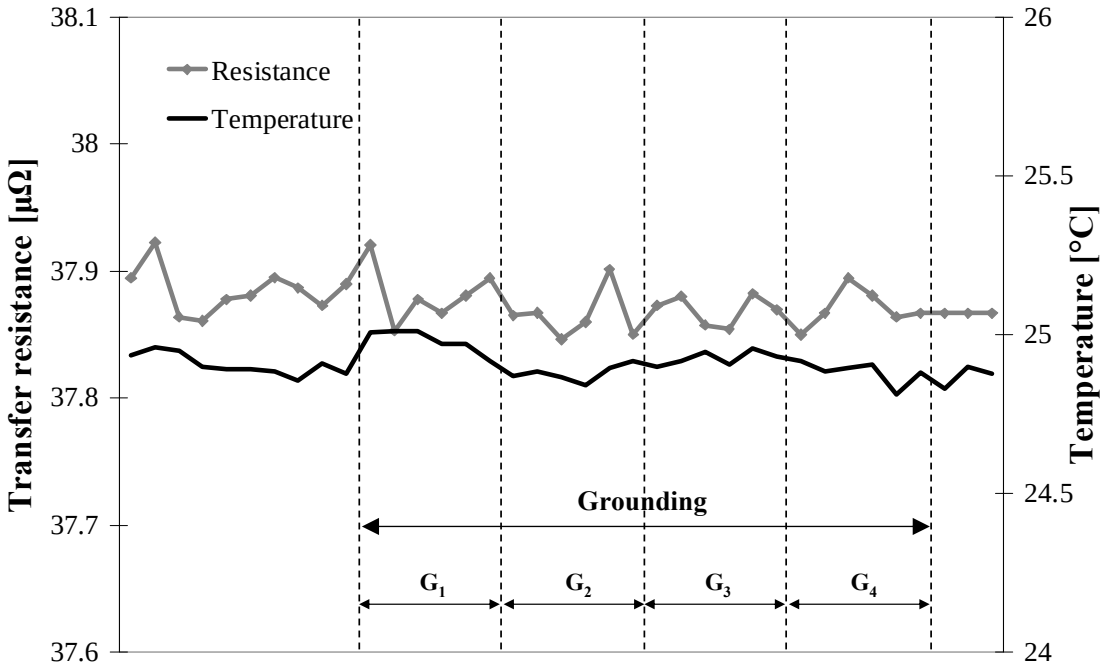

Figure 4.6: *Results with the Imperial system also showing no significant change when grounding at different positions.*

With reference to the discrepancy between the values of transfer resistance measured by the Rowan and Imperial systems, it should be mentioned that the latter was calibrated by taking measurements on large undamaged plates of stainless steel 304 of various thicknesses (ranging from 50 μm to 50 mm) and comparing the measured values against the predictions of an analytical formula available in the literature [70]. This test, discussed in more detail in Chapter 5, shows very good agreement between experimental and theoretical results; this suggests that the values obtained with the Imperial setup in the benchmark tests presented in the present Chapter are correct.

Finally, the results obtained with the CorrOcean system are reported in Fig. 4.7. In this case, the quantity on the y axis of the graph is the ratio between the potential drops ΔV and ΔV_{ref} measured on the testpiece and on the reference sample, respectively. The amount of data collected is considerably smaller because of the long waiting time needed between two measurements, as mentioned earlier; the grounding was therefore only applied at points G_1 and G_4 (see Fig. 4.4). As was the case for the resistances measured with the other two systems, however, the ratio $\Delta V/\Delta V_{ref}$ is not significantly affected by grounding (change of 0.01%), and the deviation of

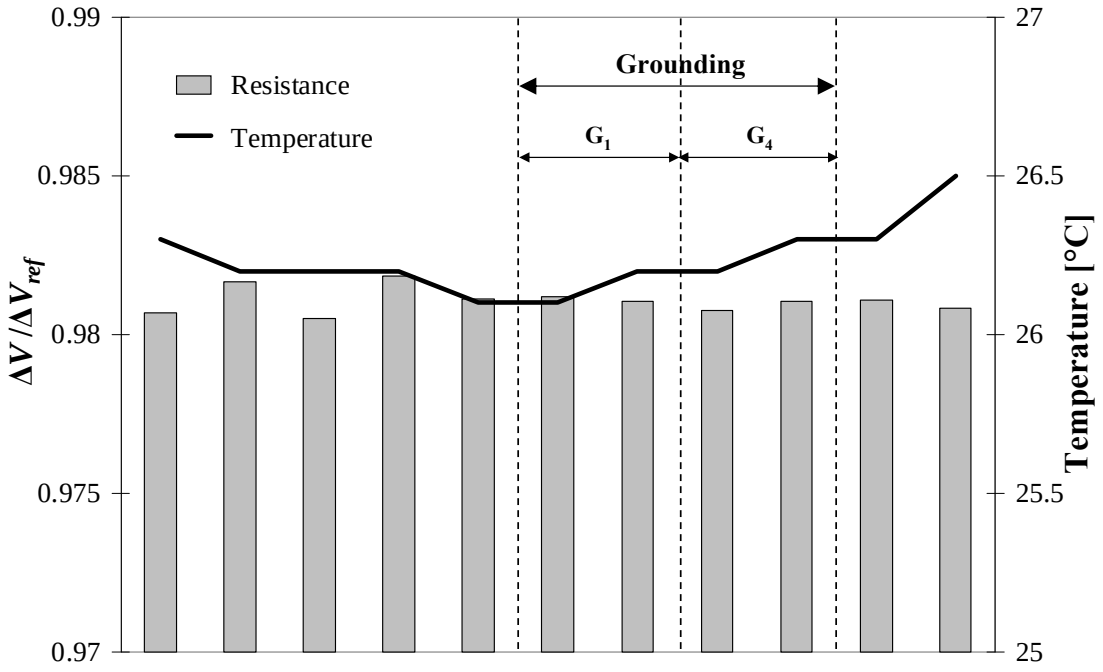

Figure 4.7: *Results with the CorrOcean system: bars indicate the ratio $\Delta V/\Delta V_{ref}$, line indicates the temperature. Again, no significant change when grounding is applied.*

any measurement from the average is no more than $\pm 0.1\%$.

4.4.2 Effect of shunt

The second part of the benchmark test addressed the issue of shunt currents. A 3-mm diameter, 500-mm long copper cable was attached to the specimen using crocodile connectors at two locations close to the current injection points (see Fig. 4.8), with the aim of creating a shunt and forming an alternative path for the currents.

Fig. 4.9 shows the values of transfer resistance and temperature as measured by the Rowan system with and without the shunt. It can be seen that the resistance measured decreases by about 0.6% (from 55.41 to 55.08 $\mu\Omega$ on average) when currents can flow via the shunt; note this change is significantly larger than either the random fluctuations in the data or the variation due to the slow temperature increase recorded during the test. The change introduced by the shunt appears more clearly once temperature compensation has been applied (see Fig. 4.17).

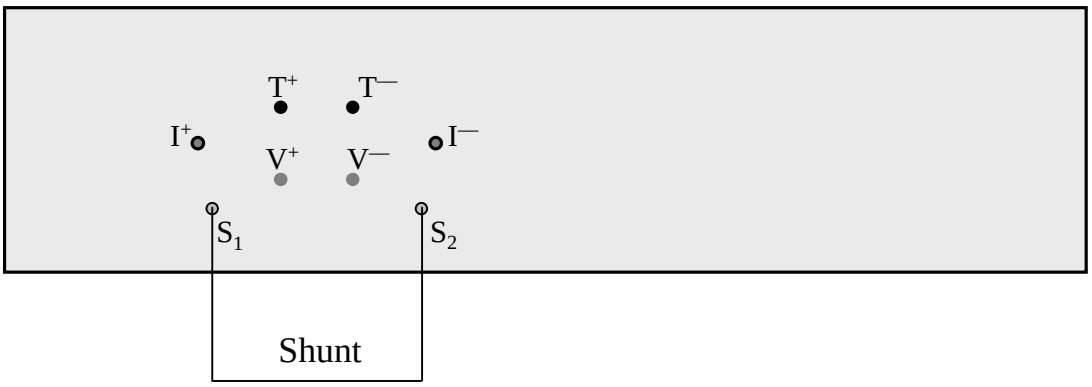

Figure 4.8: *Schematic of the testpiece (drawing not in scale) highlighting the locations where a cable was attached to create a shunt.*

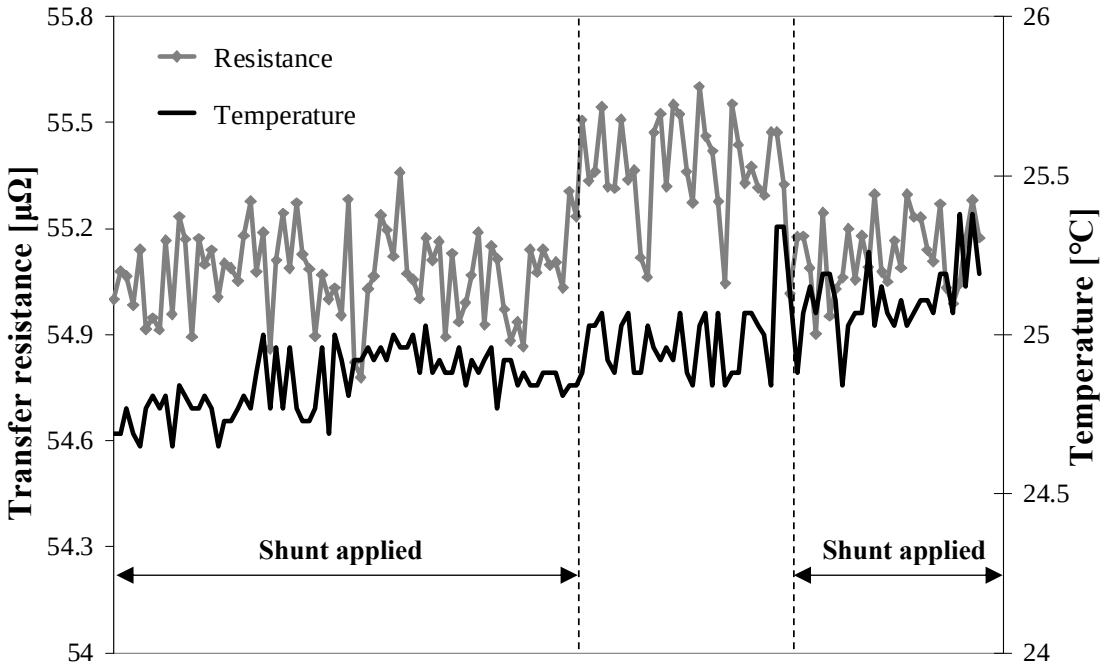

Figure 4.9: *Results with the Rowan system showing a reduction in transfer resistance of about 0.6% when a shunt is created via the cable.*

After this test it was realised that the contact resistance between the specimen and the crocodile connectors could be a limiting factor that reduced the effectiveness of the shunt. When repeating the test with the Imperial setup it was therefore decided to retain the shunt via the copper cable for comparison purposes, but to additionally simulate the 'short circuit' effect by clamping the specimen onto a mild steel plate, as shown in the schematic of Fig. 4.10. In practical situations, a similar scenario

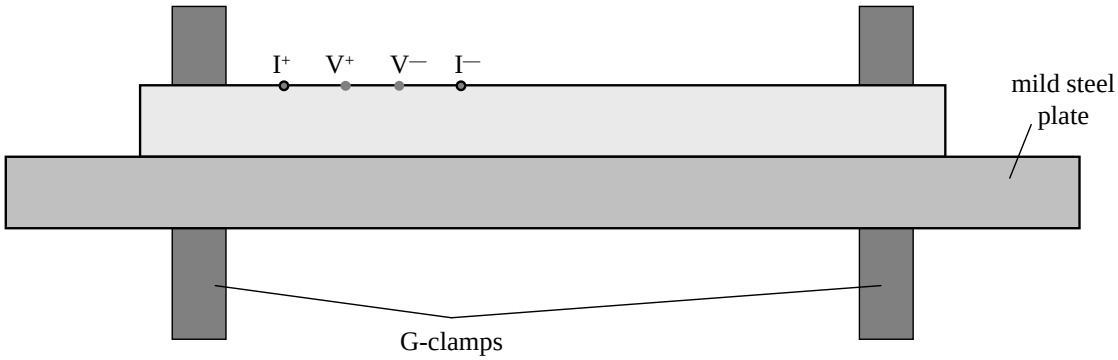

Figure 4.10: *Schematic of the testpiece clamped against a mild steel plate to create a shunt.*

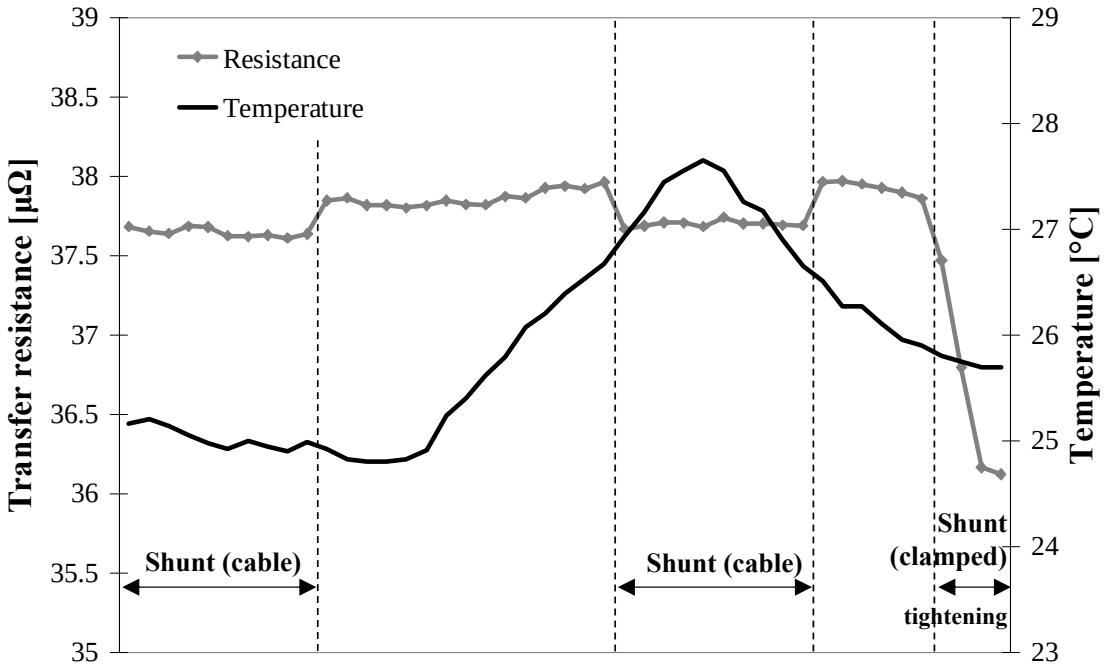

Figure 4.11: *Results with the Imperial system showing a reduction in transfer resistance of about 0.6% when a shunt is created via the cable and of up to 5% when the specimen is clamped on the mild steel plate.*

can occur for instance if a shunt is formed via the supports of a pipe.

The results obtained with the Imperial setup are shown in Fig. 4.11. The decrease in transfer resistance observed when the copper cable is used to create a shunt is very similar to that recorded with the Rowan system (reduction of about 0.6%, from 37.88 to 37.67 $\mu\Omega$). However, the variations produced when the specimen is clamped

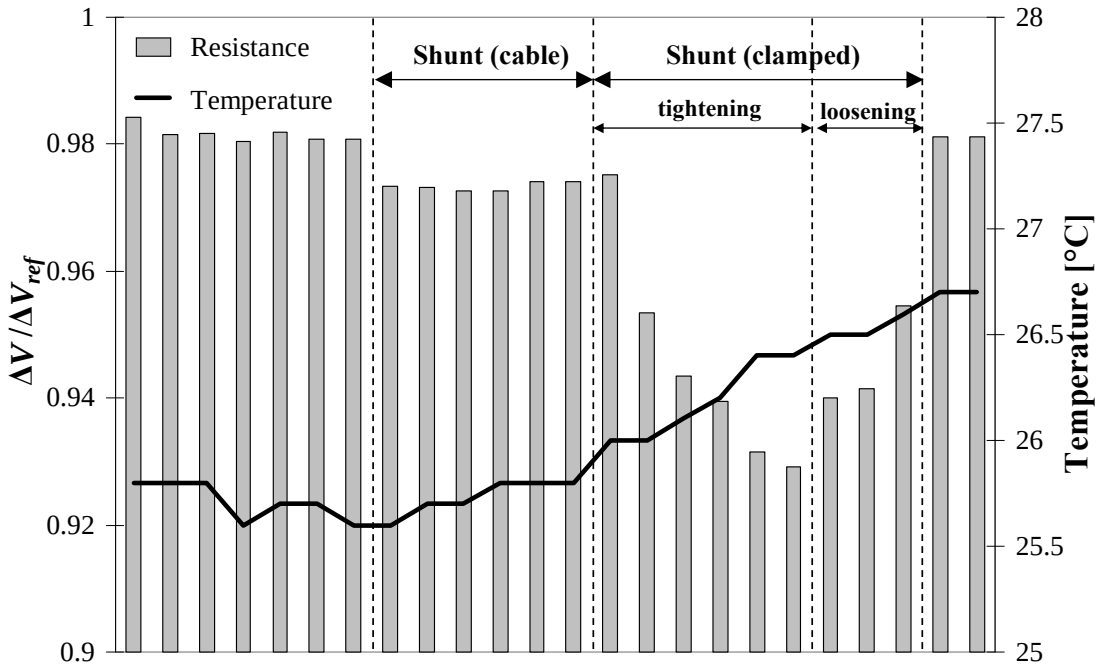

Figure 4.12: *Results with CorrOcean system showing a reduction of about 0.8% when a shunt is created via the cable and of up to 5% when the specimen is clamped on the mild steel plate.*

to the mild steel plate can reach about 5%, with larger decreases corresponding to a better quality of the contact (the clamps were progressively tightened before each measurement). While such change is certainly significant, it should be borne in mind that it was obtained under particularly harsh circumstances that are unlikely to occur in practice in applications of PD techniques in the field.

A similar procedure was followed when repeating the test with the system developed by CorrOcean. The results, shown in Fig. 4.12, are very similar to those obtained with the Imperial setup: when using the copper cable to create a shunt, the decrease in the voltage ratio $\Delta V/\Delta V_{ref}$ is about 0.8%, but the change reaches up to 5% when clamping the mild steel plate more and more tightly.

4.4.3 Effect of temperature

The objective of the third and last part of the benchmark test was to study the response of the systems to changes in resistance caused by temperature variations.

In the case of the Rowan system, the specimen was quickly heated using a heat gun against the surface opposite to that on which the electrodes are welded, until the local temperature measured by the instrument reached 70 °C; then the specimen was allowed to cool down naturally in air. The version of the controlling software used for this test did not include an algorithm for thermal compensation; however, a common and very simple way of compensating for small temperature changes is to assume a linear relationship between resistance and temperature, such as given by

$$R = R_0 + \beta(T - T_0), \tag{4.3}$$

where the average resistance and temperature measured before heating the specimen can be used as the reference values R_0 and T_0, respectively, and the thermal coefficient β can be estimated so as to best fit the experimental data; the temperature effect can then be cancelled out of the measured resistance R_m to give the 'compensated' resistance R_c:

$$R_c = R_m - \beta(T - T_0). \tag{4.4}$$

The values of resistance and temperature recorded during the experiment are plotted in Fig. 4.13 together with the compensated resistance; it can be seen that the simple thermal compensation algorithm is effective provided that temperature does not vary too quickly. If the measured resistance is plotted as a function of temperature for the cooling phase of the test, the graph of Fig. 4.14 is obtained, which shows a clear linear relationship for temperatures up to about 65 °C: the experimental values lie with good approximation on a straight line defined by Eq. 4.3, where $R_0 = 55.199$ $\mu\Omega$, $T_0 = 24.19$ °C (average resistance and temperature measured before heating) and $\beta = 0.071$ $\mu\Omega/°C$.

A different procedure was followed when repeating the test with the Imperial setup. In this case the specimen was placed in a Gallenkamp Plus II oven and its temperature monitored with a thermocouple attached in proximity of the inspection area, while the temperature of the oven was increased slowly in intervals of 1 °C. The resistance and temperature recorded are plotted in Fig. 4.15 together with the 'cor-

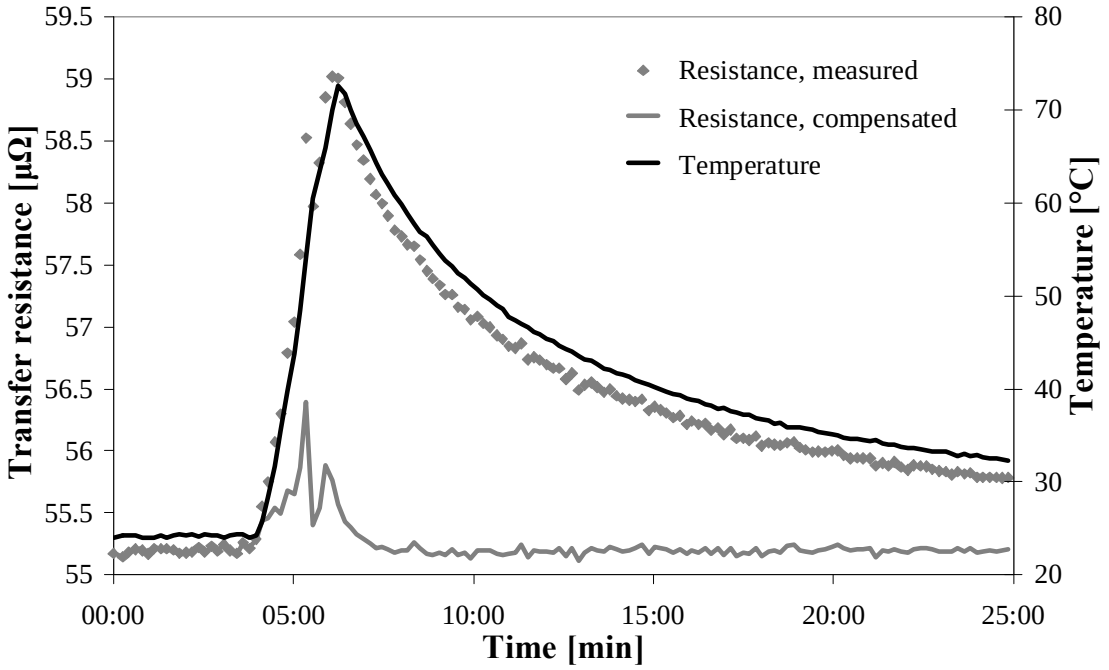

Figure 4.13: *Results with the Rowan system showing variation of measured resistance with temperature and thermal compensation with Eq. 4.4.*

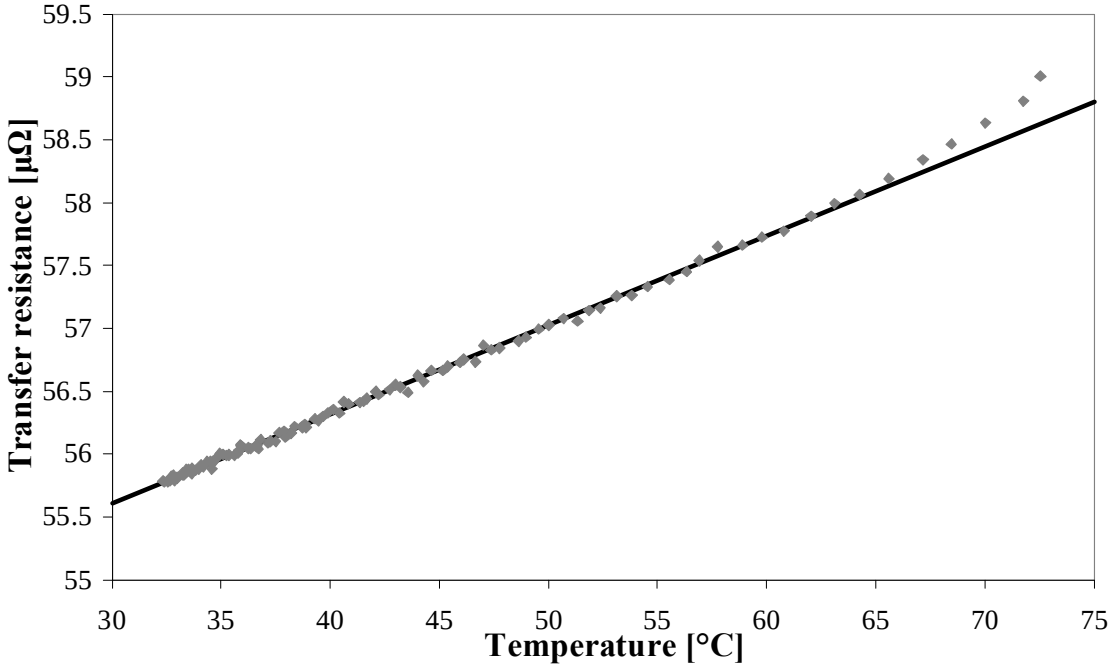

Figure 4.14: *Resistance as a function of temperature, measured with the Rowan system during the cooling phase of the experiment (symbols) and calculated with the linear approximation of Eq. 4.3 (line).*

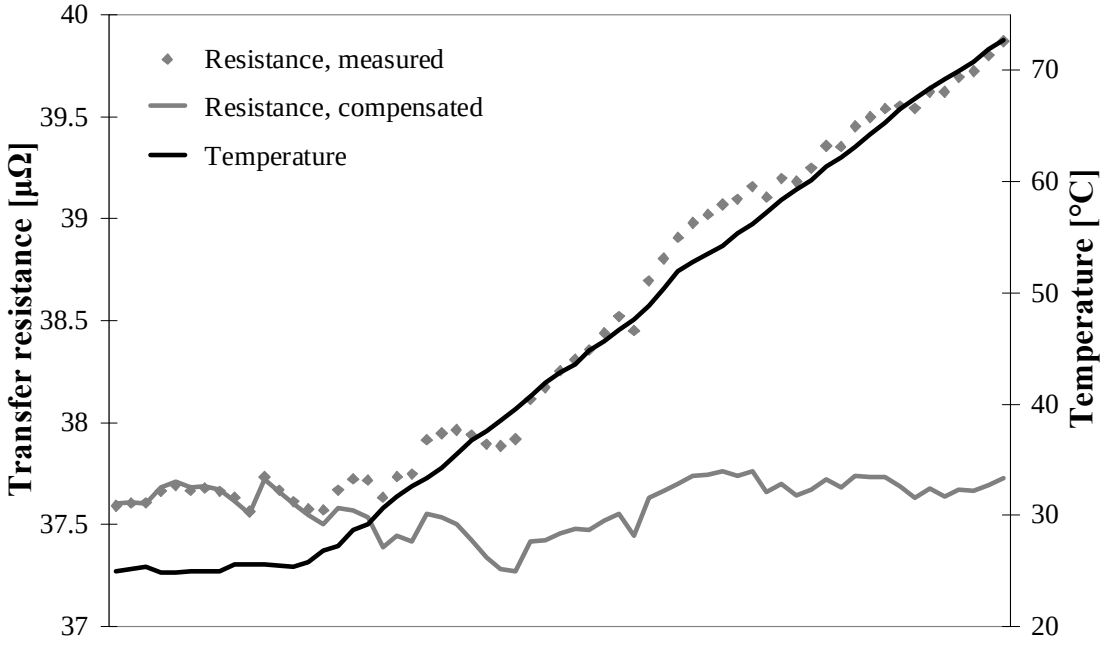

Figure 4.15: *Results with the Imperial system showing variation of measured resistance with temperature and thermal compensation with Eq. 4.4.*

rected' resistance obtained with the simple compensation algorithm of Eq. 4.4. The fluctuations in the results are most likely due to a degradation of the Common Mode Rejection Ratio of the SR552 preamplifier used in the experiment: as discussed in Chapter 3, this instrument was modified to make it DC-coupled and needs periodic fine-tuning of its delicate balance.

The values of transfer resistance measured during the experiment are plotted as a function of temperature in Fig. 4.16: the general linear trend seen with the Rowan system is confirmed, although the data are noisier, as observed earlier. The parameters of the best-fitting line are $R_0 = 37.639\ \mu\Omega$, $T_0 = 25.24\ ^\circ\mathrm{C}$ and $\beta = 0.046\ \mu\Omega/^\circ\mathrm{C}$: the difference between this value of the thermal coefficient β and that calculated from the data obtained with the Rowan setup is a consequence of the different value of transfer resistance registered by the two instruments (as mentioned earlier, the values obtained with the Imperial setup are likely to be more correct).

It was not possible to perform this test with the system developed by CorrOcean: the possibility of using a heating gun and then letting the specimen cool freely in

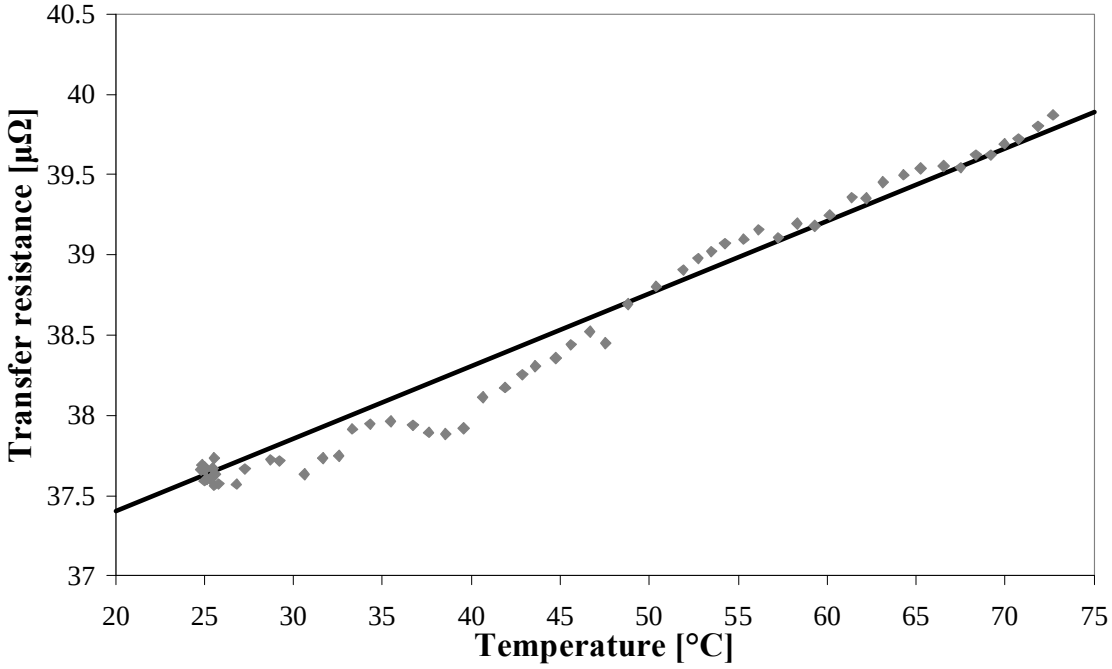

Figure 4.16: *Resistance as a function of temperature, measured with the Imperial system during the experiment (symbols) and calculated with the linear approximation of Eq. 4.3 (line).*

air, as done for the Rowan system, is ruled out because of the long recovery time of the instrument between two measurements, while the size of the cables hindered the feasibility of a test with the specimen placed in an oven, even neglecting the considerable time that would be necessary in this case to acquire a significant amount of data.

4.5 Discussion and conclusions

It is interesting to compare the amplitude of the changes in resistance introduced by each of the effects considered in the test. Fig. 4.17 shows the values of transfer resistance as a function of temperature obtained in the first part of the test, with and without the specimen connected to ground, using the Rowan system: almost all these values lie within a relatively narrow region (deviations of less than 0.2%) around a line defined by Eq. 4.3, where the reference values $R_0 = 55.263\ \mu\Omega$ and

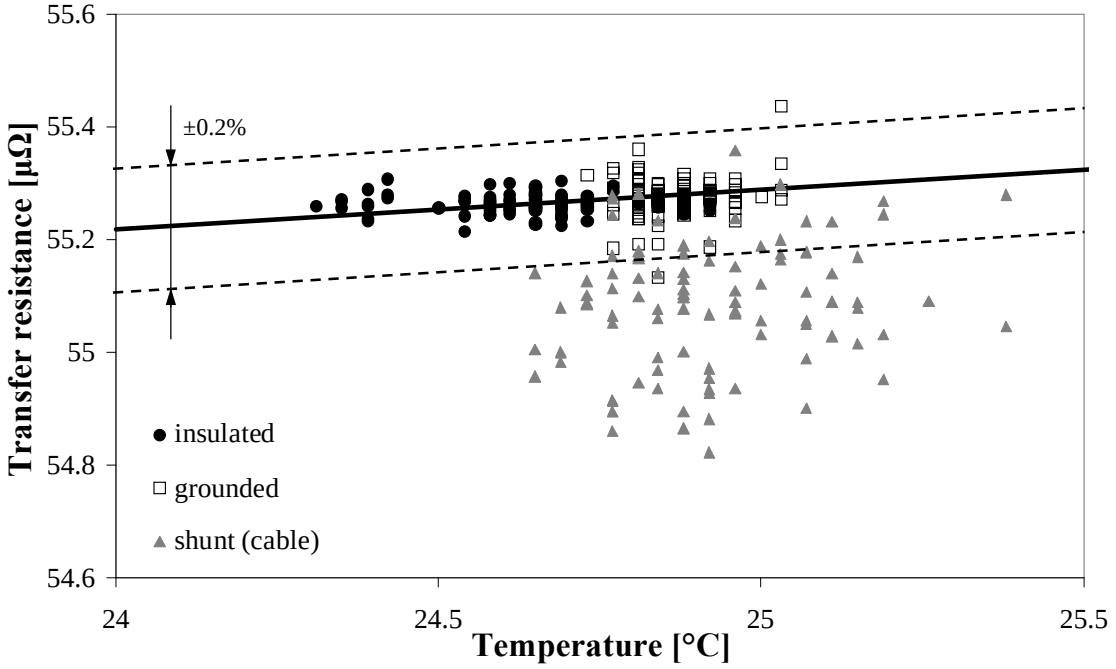

Figure 4.17: *Summary of the results with the Rowan system.*

$T_0 = 24.64$ °C were calculated by averaging the resistance and temperature measured before connecting the testpiece to ground, and the thermal coefficient calculated in the previous Section was used ($\beta = 0.071$ $\mu\Omega/$°C). Fig. 4.17 also shows that, if the data obtained after creating a shunt are plotted on the same graph, they fall mostly outside the previous region, although they are noticeably more scattered.

The same conclusions can be drawn from the data collected with the Imperial setup, which are summarised in Fig. 4.18. In this case, the best-fitting line for the resistance measured on the electrically insulated specimen is given by Eq. 4.3 where $R_0 = 37.882$ $\mu\Omega$, $T_0 = 25.39$ °C and $\beta = 0.046$ $\mu\Omega/$°C. All measurements taken when the specimen was electrically insulated or connected to ground deviate by no more than 0.2% from this line, whereas the values measured when the shunt was applied are clearly separated from the rest, the largest reductions in resistance being measured when the specimen was clamped on a mild steel plate.

Only a much smaller amount of data could be taken with the CorrOcean system: this is due to difficulties in operating the instrument, and in particular to the necessarily long interval between two measurements (it should also be mentioned that some of

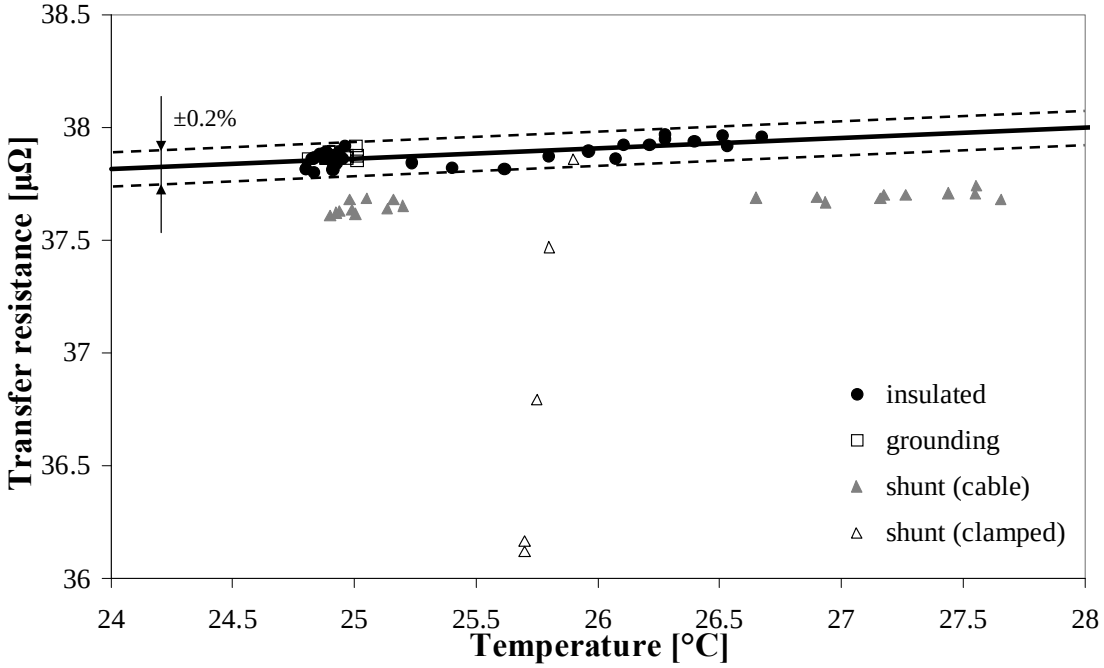

Figure 4.18: *Summary of the results with the Imperial system.*

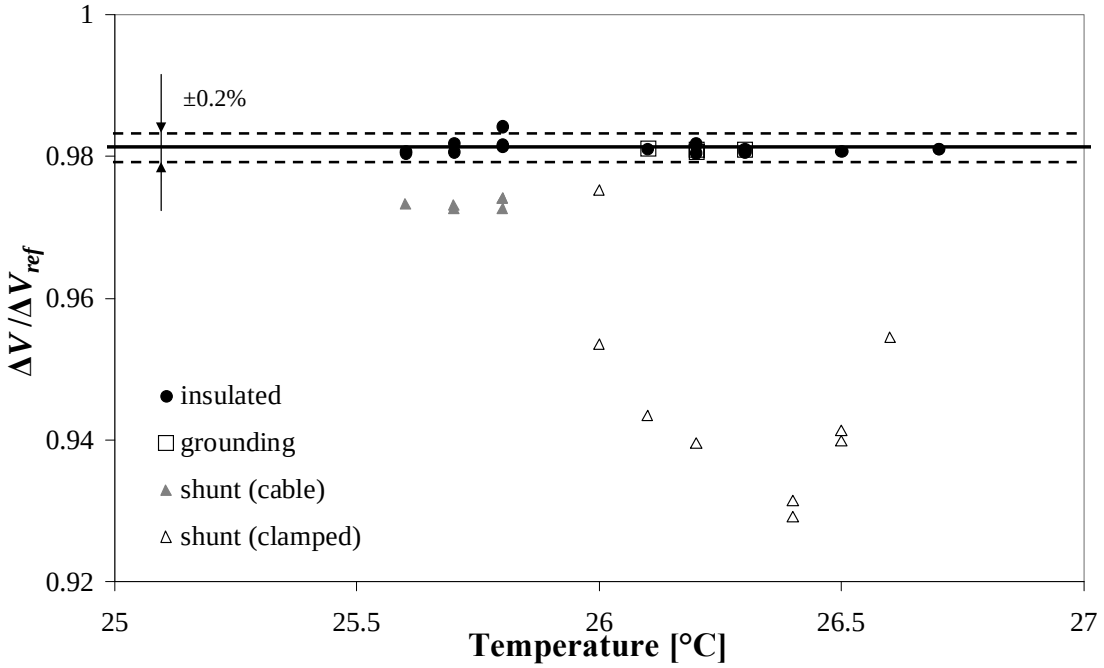

Figure 4.19: *Summary of the results with the CorrOcean system.*

the data collected had to be discarded because the current generated by the battery was not sufficiently high, or because errors occurred in the system). Nevertheless, Fig. 4.19 shows that it is still possible to identify the same behaviour observed with the other two systems. The solid line in the graph indicates in this case the average value of the ratio $\Delta V/\Delta V_{ref}$ measured on the insulated specimen. The only correction for temperature variations taken into account is that inherent in the system, through the reference sample.

In conclusion, the main outcome of this benchmark test is that the performance of the low-current setup for Potential Drop measurements described in Chapter 3 is comparable to that of commercially available DCPD systems which have been successfully used for industrial applications but require the injection of much larger currents.

Furthermore, this study showed that Potential Drop measurements in general are not significantly affected by stray currents loops which can develop in grounded structures. If a shunt is formed between two points of the structure close to the inspection area, a decrease in the measured transfer resistance can be observed; however, this depends strongly on the quality of the electrical contacts, and the reduction in the signal is significant only if the contacts are very good, which is unlikely to occur in practice. Finally, in long-term monitoring applications, and in general in the presence of temperature variations, it is essential to compensate for the corresponding changes in the resistivity of the tested material, but this can be done satisfactorily even by using a very simple algorithm, at least when the thermal variations are slow and limited to a few tens of °C.

Chapter 5

Potential Drop Spectroscopy

5.1 Introduction

This Chapter reports the results of an investigation conducted at an early stage of this research, aimed to evaluate the possibility of combining the principles of Direct and Alternating Current Potential Drop techniques for the study of surface-breaking defects of complex geometry.

Such defects are commonly encountered for example in the power generation industry, where branched defects due to stress corrosion cracking are often found [71–73], or in the railway industry, where gauge corner cracking is a problem of major concern [74–76]. While electromagnetic non-destructive methods such as conventional eddy current techniques can easily detect flaws of this kind [75, 77], they sometimes fail to give an accurate estimate of their depth because of the complicated shape of the defects themselves [78, 79].

In order to assess the integrity of a structure or to estimate its remaining service life, it would be very valuable to be able to define the envelope of a complex defect (see the schematic of Fig. 5.1), as this would facilitate the determination of its maximum depth d_{max}, which is usually a key parameter in integrity calculations. At the same time, however, knowledge of the defect morphology can be important

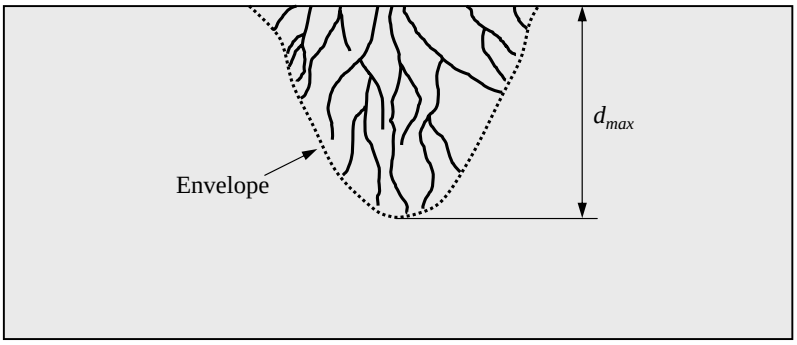

Figure 5.1: *Schematic of a branched defect, highlighting its envelope (dotted line) and maximum depth.*

when calculating stress concentration, as there is some evidence that the presence of branching reduces the stress intensity around the defect [80].

For ease of reference, let us recall here the standard depth of penetration (or skin depth) of an alternating current induced or injected in a material, which was defined in Chapter 2:

$$\delta = \frac{1}{\sqrt{\pi f \sigma \mu}}. \tag{5.1}$$

The quantities appearing in this formula are the frequency f of the current and the electrical conductivity σ and absolute magnetic permeability μ of the material. At high frequency, the penetration depth δ is relatively small, and in the presence of branched defects currents would tend to flow around each of the single branches of the crack. As a consequence, techniques involving the use of high-frequency currents, such as ACPD or ACFM, would give information on the total length of the crack profile rather than on its maximum depth, and therefore they may not give an accurate estimate of the depth of complex defects [51, 52]. On the other hand, if very low-frequency or indeed direct currents are injected, as in DCPD, they would flow more deeply and form an envelope around the defect seen as a whole, as they would follow a similar path whether the defect is a simple crack or has multiple branches.

Potential Drop Spectroscopy combines these existing techniques by repeating the measurement of voltage difference between the sensing electrodes at different frequencies over a wide range; this offers the advantage of obtaining information on

both the overall size and the complexity of the defect.

5.2 Preliminary tests

In order to gain some insight on how the results of Potential Drop measurements can vary with frequency, and thus to evaluate the applicability of the PD Spectroscopy technique, preliminary tests were run on plates of stainless steel 304 ($\mu_r = 1$, $\sigma \approx 1.45 \cdot 10^6\ \Omega^{-1}\mathrm{m}^{-1}$) of various thicknesses ranging between 50 μm and 50 mm. Measurements were taken with the setup described in Chapter 3, using an in-line four-point probe in which currents are injected through the two external electrodes, separated by $2a = 20$ mm, and the voltage drop is measured across the two internal electrodes, which are $2b = 10$ mm apart: a simple schematic is given in Fig. 5.2. A current meter was used to monitor the intensity of the injected currents, which was 37.2 mA.

Since an AC voltage was used to generate the signal for the inspection, the potential drop measured at the sensing electrodes is defined not only by its amplitude, but also by its phase: in other words, it is a complex quantity with both a real and an imaginary component. The latter is very small at low frequency (it must be zero if direct currents are injected) and tends to be equal to the real component at high frequencies [47]. Throughout the present work, however, only the real part of the

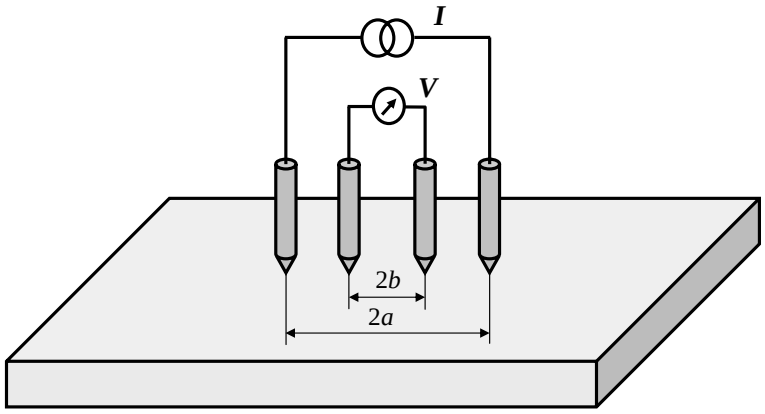

Figure 5.2: *Schematic of probe used for the tests.*

signal was considered for the analysis, because in experimental measurements the imaginary component, while containing some information on the properties of the tested material, is affected by significant errors due to the inductive pickup of the probe. As shown in [39], the loop inevitably formed by the measuring circuit gives rise to a purely inductive signal, proportional to the inspection frequency, which can be even larger than the 'good' signal due to the impedance of the material.

The transfer resistance (as the real part of the transfer impedance will henceforth be referred to for simplicity) was measured on the various plates over a broad range of frequencies, from 1 Hz to 100 kHz; the results are plotted in Fig. 5.3. Since the penetration depth calculated with Eq. 5.1 is larger than the thickness of most of the tested plates even at high frequency (δ = 1.3 mm at 100 kHz), the transfer resistance measured on those plates does not vary with frequency, and the values are inversely proportional to the thickness, in accordance with Ohm's law. For specimens thicker than the spacing $2a$ between the injecting electrodes, however,

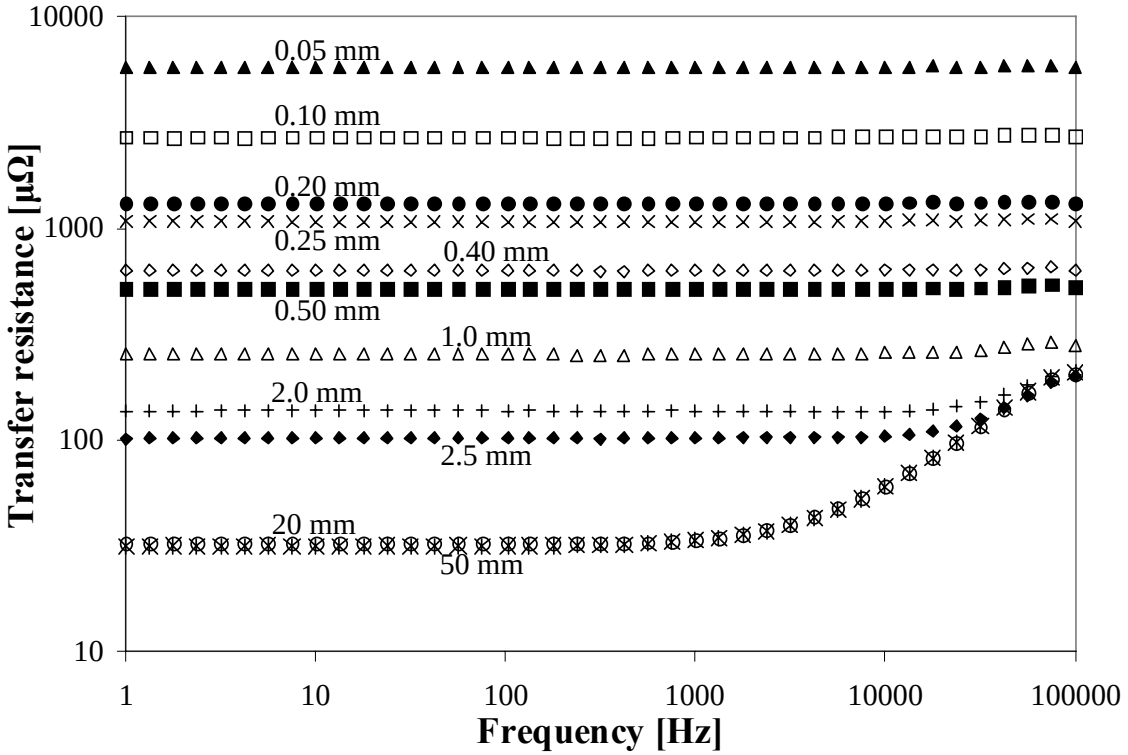

Figure 5.3: *Transfer resistance between the sensing electrodes measured as a function of frequency on plates of SS304 of various thicknesses.*

the latter becomes the limiting factor that determines how deeply currents can flow in the material: this explains why the voltage drop measured on a 50-mm thick plate is almost equal to that on a 20-mm plate. On the other hand, it can be noticed that at high frequencies, when the penetration depth is smaller than the plate thickness, the resistance increases with frequency and is independent of the thickness of the specimen: this is because the effective cross section 'seen' by the currents is reduced, as they are forced to flow in a shallower layer below the surface.

It should be mentioned that in ferromagnetic materials, or in metals with higher electrical conductivity, the skin depth at a given frequency would be smaller, even by orders of magnitude, and therefore the frequency-dependent increase in transfer resistance would be observed in thinner plates and at lower frequencies.

With reference to the data of Fig. 5.3, it is interesting to plot the low-frequency values of transfer resistance as a function of thickness, as in Fig. 5.4: they fall on a curve given by an analytical formula recently derived by Bowler [70] under the assumption that DC currents are injected on an infinite plate of uniform thickness

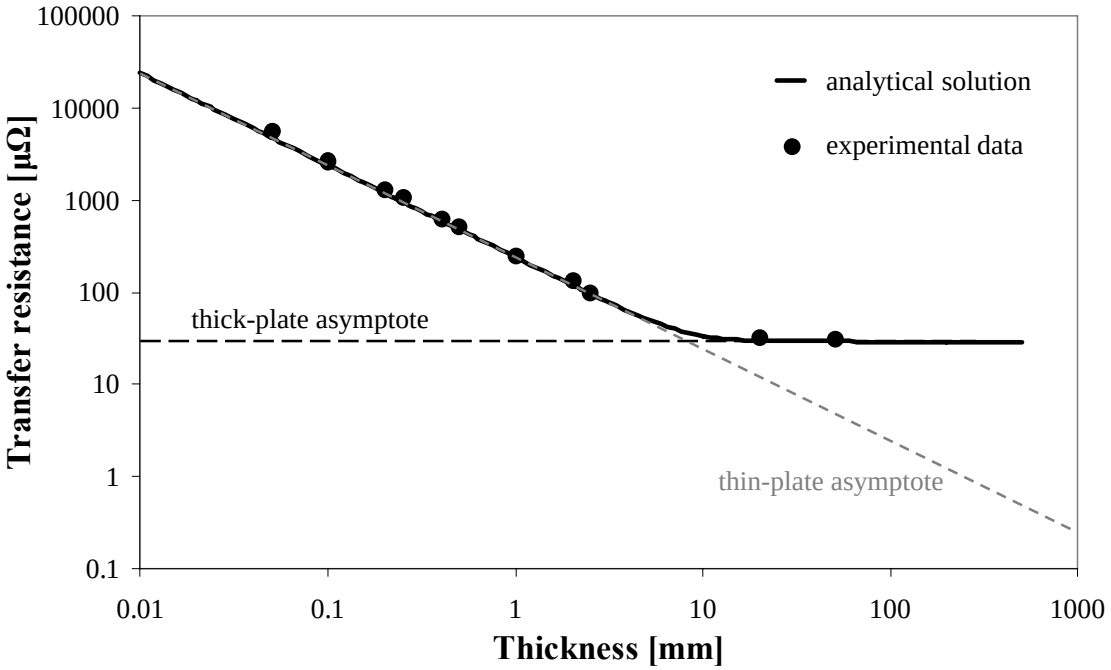

Figure 5.4: *Transfer resistance measured at $f = 10$ Hz on SS304 plates of various thicknesses (from Fig. 5.3; symbols) and calculated with Eq. 5.2 (solid line).*

t and conductivity σ:

$$R = \frac{1}{\pi\sigma} \sum_{n=0}^{\infty} \epsilon_n \left[\frac{1}{\sqrt{(a-b)^2 + (2nt)^2}} - \frac{1}{\sqrt{(a+b)^2 + (2nt)^2}} \right], \tag{5.2}$$

where $\epsilon_0 = 1$ and $\epsilon_n = 2$ for $n \neq 0$. In practice, this formula holds with very good approximation when very low-frequency currents (so that $\delta > t$) are injected at locations sufficiently far from the edges of the plate, as was the case in this test. Eq. 5.2, together with its two asymptotic values for thin and thick plates, will be discussed in more detail in Chapter 8.

5.3 Geometry of the test cases

Numerical simulations with a Finite Element (FE) code and experimental tests were run on cases with simple geometry to study the changes in the flow of currents introduced not only by varying the frequency, but also by the presence of surface-breaking defects.

A 300-mm long, 140-mm wide, 38-mm thick block of ferritic steel was used for the experiments (see Fig. 5.5). Three 10-mm deep, 0.5-mm wide notches were machined across its width, using Electrical Discharge Machining (EDM); two of the notches are

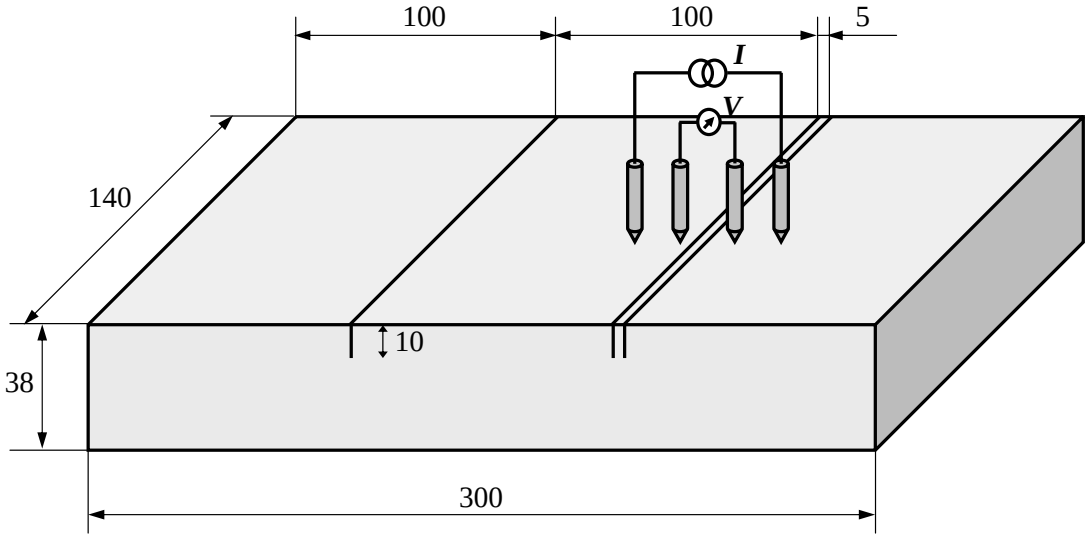

Figure 5.5: *Geometry of the ferritic block used for the experimental tests.*

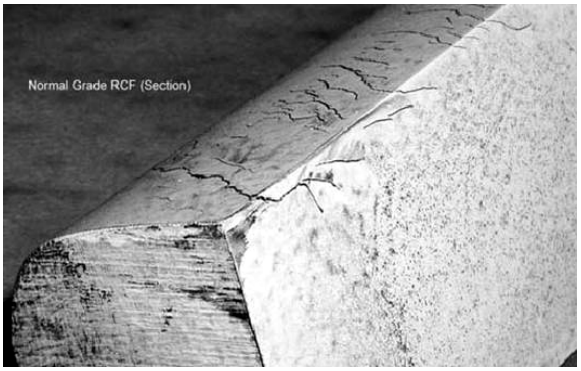

Figure 5.6: *Photograph of a section of railhead showing multiple parallel cracks [74].*

separated by only 5 mm, thus simulating a very simple defect of 'complex' geometry that will be referred to as a 'double notch' in the following, whereas the remaining notch is well apart from the others and represents a 'single notch'. While the double notch certainly cannot simulate complicated, branched defects such as those due to stress corrosion cracking, it can still be considered representative of a type of defect commonly encountered in railheads, where multiple parallel cracks are often generated by rolling contact fatigue: the photograph of Fig. 5.6 shows an example.

It should be mentioned that a two-dimensional model had to be used for the numerical simulations, because of the heavy computational demand of a fully 3-D model: this problem was addressed at a later stage of the present study and will be discussed in the next Chapter. As a consequence, it will only be possible to draw a qualitative comparison between the results of the numerical simulations and of the experiments.

Three different geometries were used for the FE analyses, simulating the cases of a block of ferritic steel ($\sigma = 5.0 \cdot 10^6\ \Omega^{-1}\mathrm{m}^{-1}$, $\mu_r = 100$) with no notches, a block with a single 5-mm deep, 0.2-mm wide notch, and a block with a double notch (two notches 5 mm apart from each other), respectively. All three blocks are 100 mm long and 40 mm thick, and the distances between the electrodes of the simulated probe are identical to those of the probe used for the experiments: this means that the spacing between the injecting electrodes was set to $2a = 20$ mm and the separation between the sensing electrodes was $2b = 10$ mm.

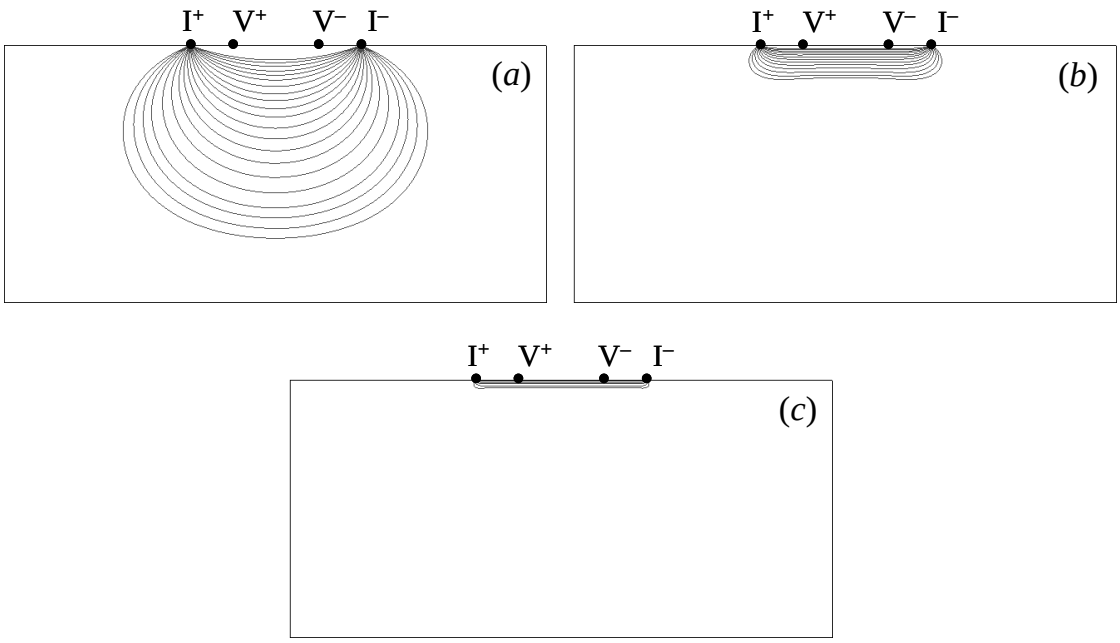

Figure 5.7: *FE predictions of current streamlines in a block of ferritic steel with no notches at (a) 0.1 Hz, (b) 50 Hz and (c) 1 kHz. Points* I^+, I^-, V^+ *and* V^- *indicate the location of the probe electrodes.*

5.4 Results of the numerical simulations

The commercial code Femlab (now Comsol Multiphysics) was used to run Finite Element analyses on the three geometries described in the previous Section. Fig. 5.7 shows the current streamlines predicted for the case of a block with no notches at three different frequencies ($f = 0.1$ Hz, 50 Hz and 1 kHz). It can be noticed that, while currents flow deeply in the material at very low frequency, they are forced into a shallower layer as frequency increases: for the three examples given in Fig. 5.7, the skin depth calculated with Eq. 5.1 is 71 mm, 3.18 mm and 0.71 mm, respectively (the first value is only theoretical, since the actual penetration depth is limited by the distance between the injecting electrodes).

The presence of a defect alters the path of the currents, as illustrated by Fig. 5.8: currents flow around the notch and, as they are squeezed towards the surface at higher frequencies, they tend to follow more closely the profile of the notch. This highlights the two different principles on which DCPD and ACPD are based: in the

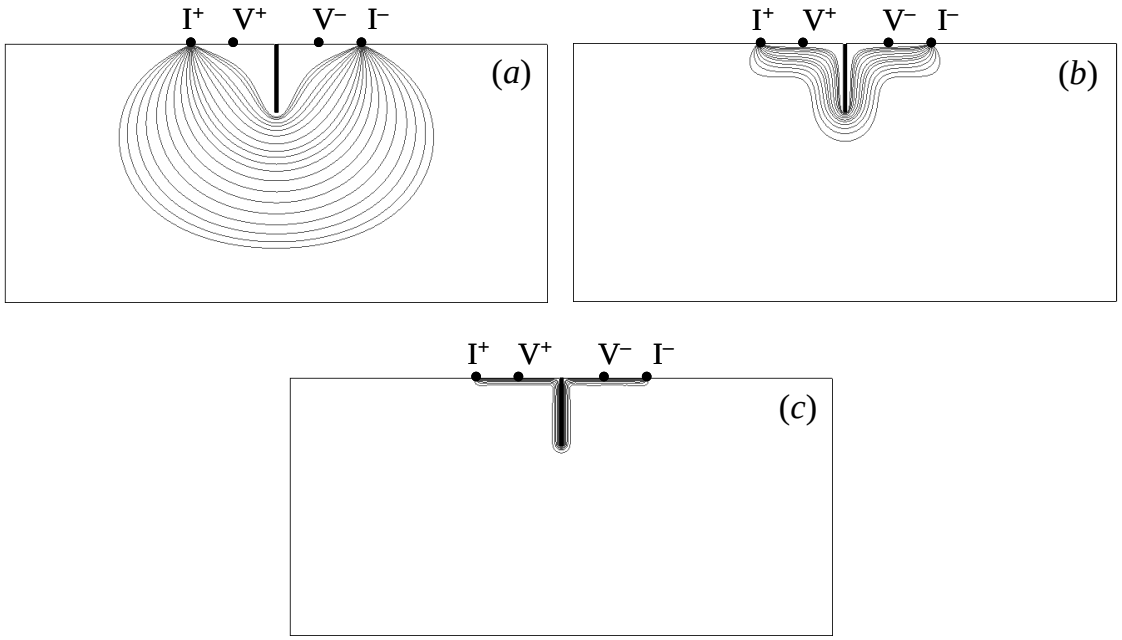

Figure 5.8: *FE predictions of current streamlines in a block of ferritic steel with a single 5-mm deep notch at (a) 0.1 Hz, (b) 50 Hz and (c) 1 kHz.*

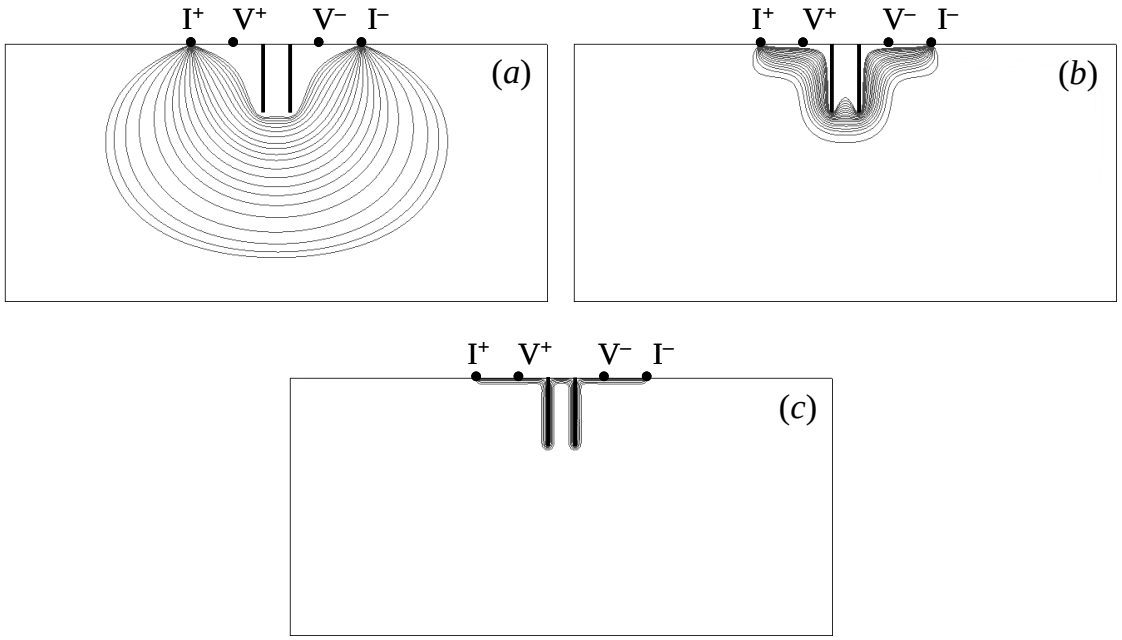

Figure 5.9: *FE predictions of current streamlines in a block of ferritic steel with a double 5-mm deep notch at (a) 0.1 Hz, (b) 50 Hz and (c) 1 kHz.*

DC or quasi-DC regime, where the skin depth δ calculated with Eq. 5.1 would be greater than — or at least comparable to — the thickness t of the tested structure (as in Fig. 5.8a), the increase in transfer resistance measured in the presence of a defect is mainly due to a reduction in the cross section of the material; at high frequency ($\delta \ll t$), instead, the increase in resistance produced by a defect is due to an increase in the length of the path of the currents (as in Fig. 5.8c).

It is very interesting to observe how the current streamlines change with frequency in the case of a block with a double notch. Fig. 5.9 shows that at very low frequency they form an envelope around the two notches 'seen' as one defect, then they start to penetrate in between the notches, and at relatively high frequency they follow closely the profile of each of the two notches.

If the transfer resistance R between the two sensing electrodes is plotted as a function of frequency for the three cases examined, as in Fig. 5.10, it can be seen that it stays constant over the lower end of the spectrum: as noted earlier, this is due to the fact that the skin depth at very low frequencies would be much greater than the thickness of the specimen, which therefore represents the controlling parameter together with the spacing between the electrodes. Note that this quasi-DC regime ends at a much lower frequency than was the case for the SS304 plates of Fig. 5.3, because of the higher conductivity and much higher permeability of ferritic steel. As the penetration depth becomes smaller at higher frequencies, the effective cross section 'seen' by the currents is reduced, and the resistance — or equivalently the potential drop — increases proportionally to $\sqrt{f}$ for the case of a block with no notches (baseline).

In the presence of notches, however, the increase is slightly more rapid, as appears more clearly in Fig. 5.11, which is obtained by dividing the values of transfer resistance calculated for the case of a block with a single or a double notch by the values calculated on the baseline. The additional increase in resistance (*i.e.* on top of that due to the reduction in the effective cross section) is due to the increasing length with frequency of the current streamlines, as these are forced to follow more tightly the defect profile; in particular, the ratio between the values for the block with a

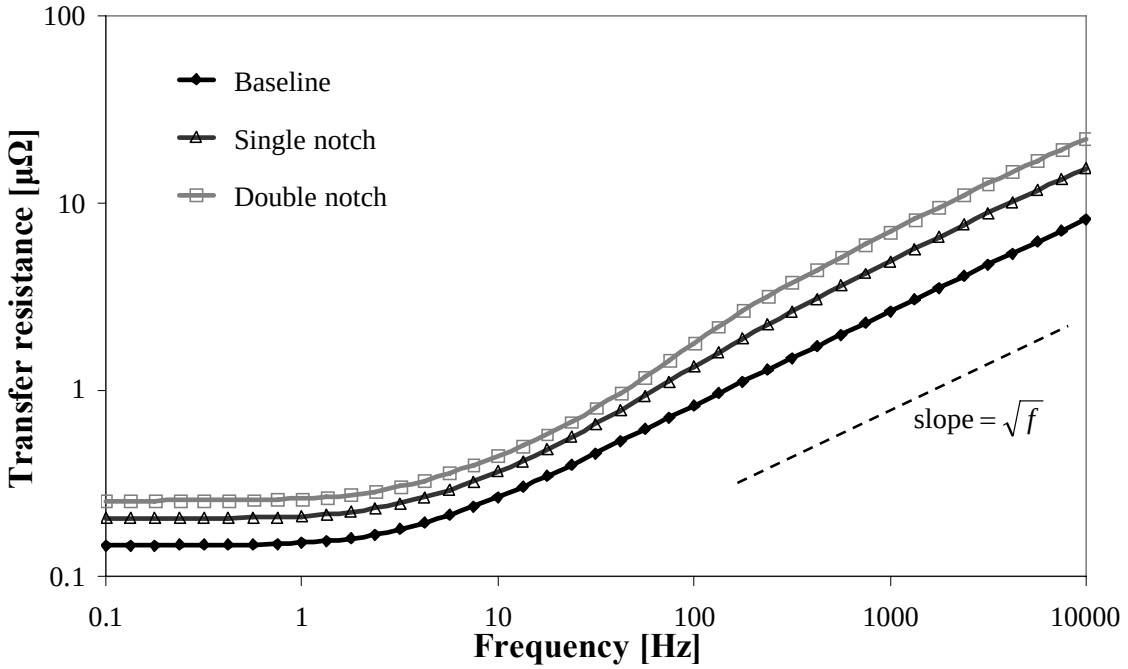

Figure 5.10: *Transfer resistance in ferritic steel blocks as a function of frequency, calculated with a 2-D FE model.*

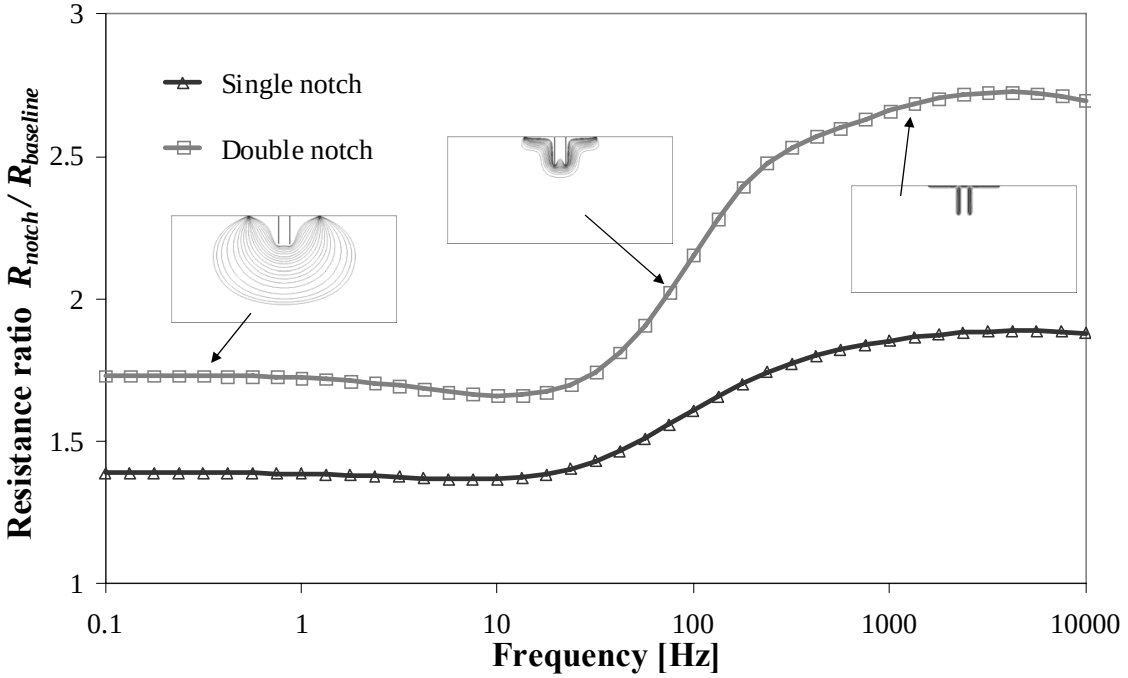

Figure 5.11: *Ratios between the transfer resistance for a ferritic steel block with either a single or a double notch and a block with no notches (baseline), calculated with a 2-D FE model.*

double notch and the block with no notches shows a sharp increase in the frequency range where currents start to flow between the two notches.

At very high frequency the resistance ratio approaches an asymptotic value which can be quickly estimated following a simple suggestion by Dover *et al.* [58]. They observed that if a uniform current of sufficiently high frequency is applied orthogonally to an infinitely long notch of uniform depth $d \gg \delta$, then the potential difference between two points at a fixed distance Δ on the surface will be proportional to the distance 'travelled' by the current between those two points, so that the voltage measured will be

$$V_0 \propto \Delta \tag{5.3}$$

if both measuring points are on the same side of the defect, or

$$V \propto (\Delta + 2d) \tag{5.4}$$

if they straddle the notch. In the tests considered in this Section $\Delta = 2b = 10$ mm and $d = 5$ mm, so the predicted asymptotic value of the resistance ratio would be 2.0 for the single notch and 3.0 for the double notch (which at sufficiently high frequency can be treated as two isolated notches, as shown by Fig. 5.9*c*). The values obtained with the FE simulations are slightly lower (see Fig. 5.11), but this is thought to be due to an insufficient mesh density; the necessary refinements would cause the memory required for the simulations to exceed the resources available. This problem can be overcome by reducing the geometry of the model used in the simulations, as will be explained in the next Chapter.

Note that, if the notch depth were unknown, it would be straightforward to estimate it from high-frequency potential drop measurements. In fact, from Eqs. 5.3 and 5.4 follows immediately

$$d = \frac{\Delta}{2} \frac{V - V_0}{V_0} \ . \tag{5.5}$$

This is the so-called one-dimensional estimate, used as a first guess in many algorithms for crack depth sizing (see for example [81, 82]), as will be discussed in Chapter 7. It should be noted here that if the probe straddles more than one defect

(as in the case of a double notch), or indeed a branched crack, the estimated depth calculated with Eq. 5.5 would be erroneous.

In all cases considered so far the probe was exactly centred with respect to the notches; however, it should be observed that the voltage drop between the sensing electrodes can vary if the probe is moved laterally. Mirshekar-Syahkal *et al.* [83] showed that the potential drop at high frequency is almost independent of the probe position as long as the voltage electrodes straddle the defect, whereas at low frequency it increases considerably as the distance between one of the voltage electrodes and the notch decreases. This is shown in Fig. 5.12, where the transfer resistance at three different frequencies (and scaled to the respective baseline values) on a block with a single 5-mm deep notch is plotted as a function of the lateral displacement of a probe with separations $2a = 20$ mm between the current electrodes and $2b = 10$ mm between the voltage electrodes. It can be observed that, when both voltage electrodes are on the same side of the defect (in the case of Fig. 5.12,

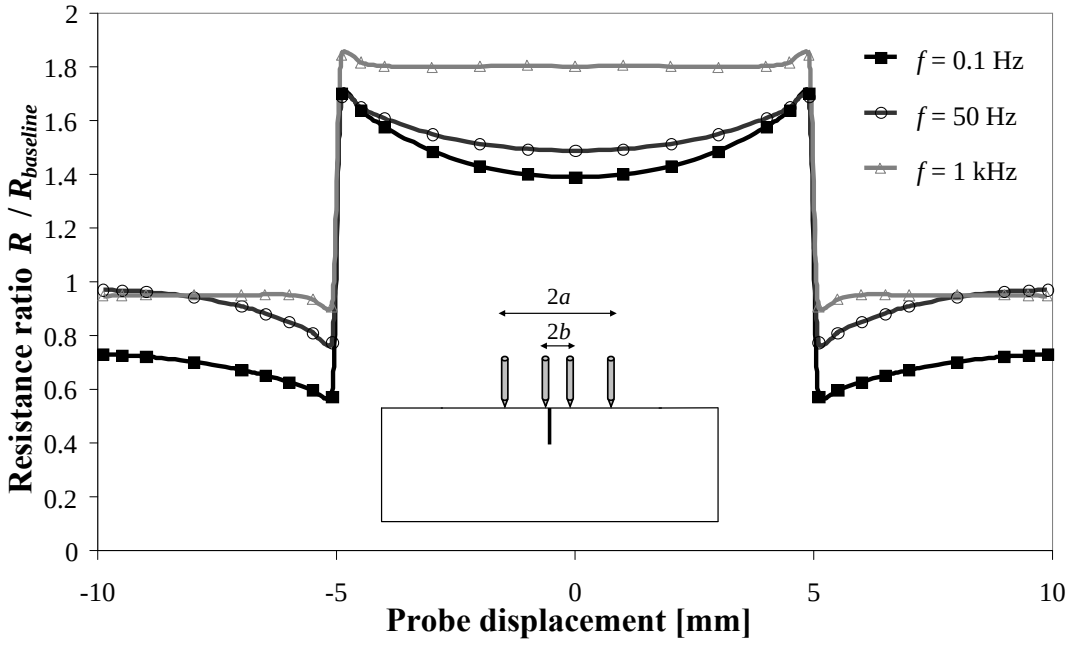

Figure 5.12: *Ratios between the transfer resistance for a ferritic steel block with a single 5-mm deep notch and a block with no notches (baseline), calculated with a 2-D FE model, as a function of probe displacement with respect to the defect. The insert shows the schematic of a probe with electrode separations* $2a = 20$ *mm and* $2b = 10$ *mm, displaced by 4 mm.*

when the displacement is larger than $b = 5$ mm), the potential drop, or equivalently the transfer resistance, falls to values smaller than those which would be obtained on an intact specimen (baseline). The resulting sharp peak was exploited in previous works (see for example [40, 44, 46, 81]) for sizing defects of uniform depth, as the voltage measured when the inner electrodes are just straddling the defect was compared to the value obtained when the voltage electrodes are just both past the notch: this results in larger ratios and therefore enhances the sensitivity of the measurements, but a high degree of accuracy is required in positioning the probe. Throughout the present work, instead, all measurements were taken with the probe centred with respect to the defect being studied, unless otherwise stated, and the values thus obtained were compared to those measured either on an intact specimen or at sufficiently large distance from the defect.

Finally, it should be observed that while the results shown here can provide useful qualitative information on the distribution of currents in the material as a function of frequency, two-dimensional analyses cannot be used in practice for the study of real defects. This is not only because the current source in 2D simulations is assumed to be along an infinite line instead of being concentrated on a single point, but also because any defect is assumed to be infinitely long, and as a consequence currents can only flow below it but not around its extremities.

5.5 Experimental results

Measurements were taken on the block of ferritic steel shown in Fig. 5.5; the probe was positioned first in the central area with no defects (baseline), then straddling the single notch and finally across the double notch. The results are plotted in Fig. 5.13: the qualitative agreement with the results of the numerical simulations plotted in Fig. 5.10 is very good. Because of the relatively small penetration depth, it would have been necessary to extend the study to frequencies below 1 Hz in order to obtain the flat region of the curves, but such low frequencies were out of the working range of the instrumentation used. At higher frequencies, on the other hand, the increase

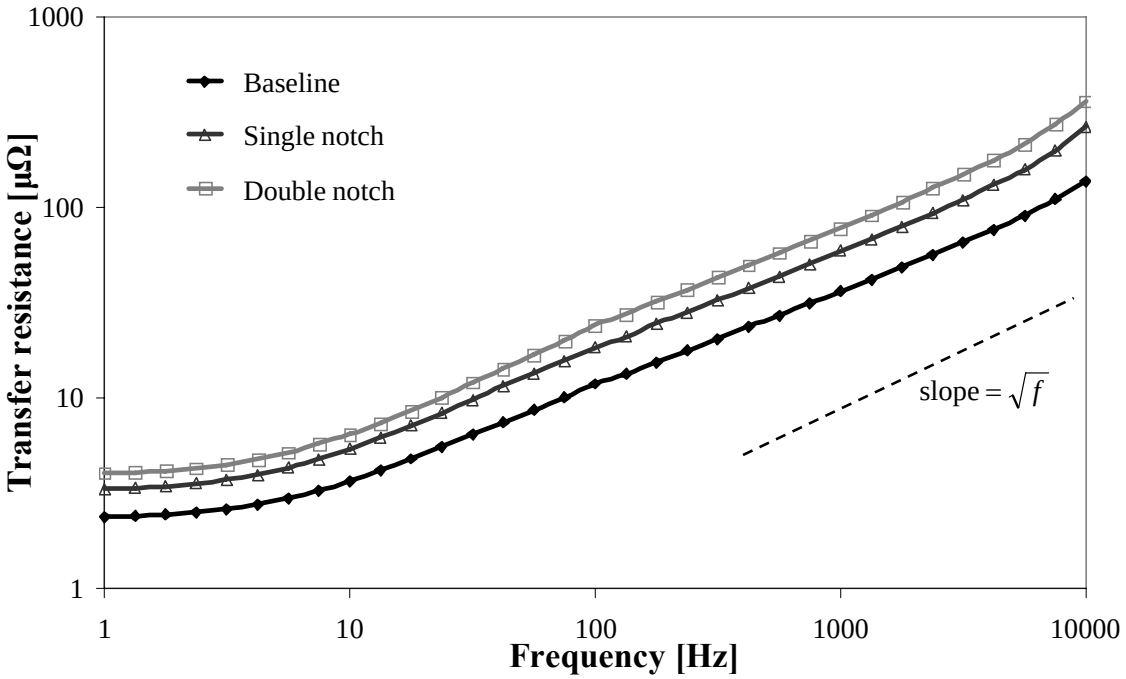

Figure 5.13: *Transfer resistance at different locations on a ferritic steel block as a function of frequency, measured experimentally.*

in resistance is approximately proportional to $\sqrt{f}$, since the effective cross section seen by the currents is determined by the standard penetration depth.

The ratios between the three curves in Fig. 5.13 are given in Fig. 5.14, which is obtained by dividing the values measured for either the single or the double notch by the baseline measurements. This chart exhibits some similarities to the analogous graph obtained with the FE simulations (Fig. 5.11), at least for frequencies up to about 1 kHz: the ratio for the double notch shows a significant increase at intermediate frequencies because the current path becomes longer as currents start to penetrate in between the two notches. However, it should be observed that the values reached by the resistance ratios for both the single and the double notch are considerably lower than those which would be predicted using Eqs. 5.3 and 5.4; on the other hand, the validity of applying the one-dimensional estimate to this case is debatable since one of the assumptions on which it is based, namely the uniformity of the electric field in the inspection area, is probably not satisfied given the relatively small separation of the injecting electrodes ($2a = 20$ mm). It should also be borne in mind that a quantitative comparison between the experimental and numerical

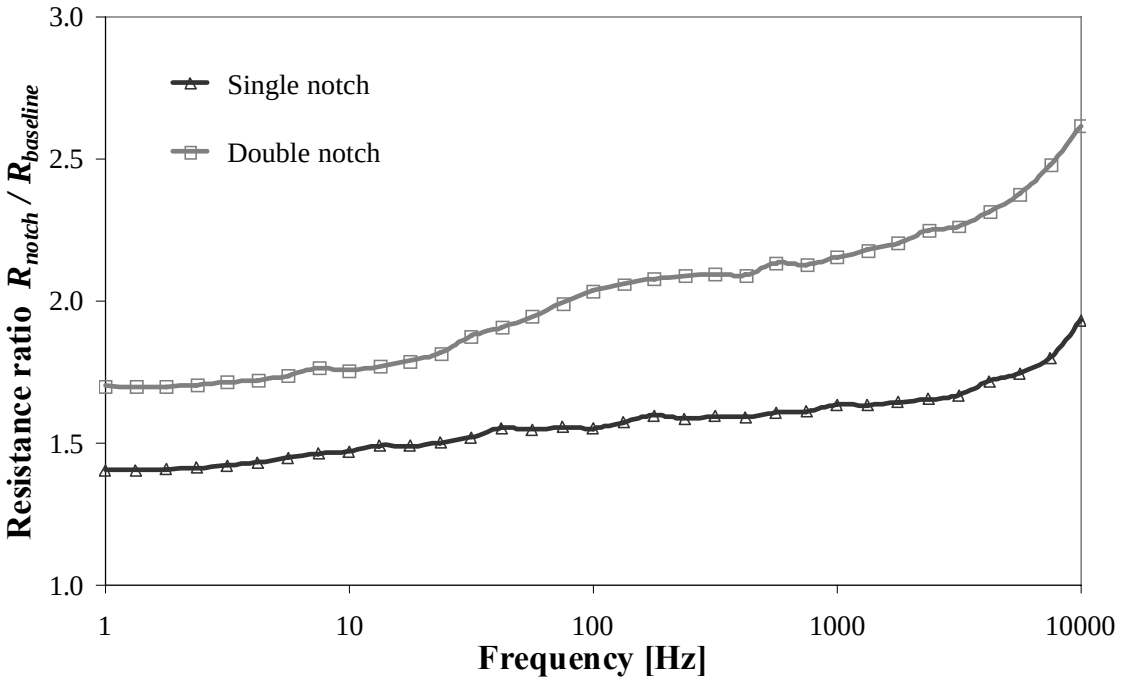

Figure 5.14: *Ratios between the transfer resistance measured across either a single or a double notch and on an area with no notches (baseline), on a block of ferritic steel.*

data is not possible because the two-dimensional FE analyses assume a line source for the currents, whereas a point source is used in the experiments.

Furthermore, Fig. 5.14 shows that, contrary to the predictions of the FE model, the resistance ratios for the experimental data increase again above 1 kHz; in fact, the curves become steeper as frequency increases towards the upper limit of the tested range. A possible reason for this is the inductive effect of the notches, due to their finite width (0.5 mm): as discussed in [84], when the probe straddles an open notch it picks up an additional, parasitic voltage produced by the flux of the time-varying magnetic field generated by the alternating current, according to Faraday's law. This effect is proportional to frequency and to the notch width and depth.

5.6 Discussion and conclusions

A multi-frequency approach for Potential Drop testing was considered in this Chapter. Simple numerical simulations with a commercial Finite Element code were used

to study how varying the frequency modifies the path of currents flowing in the inspected material, both on intact specimens and in the presence of surface-breaking defects: in particular, it was shown that as frequency increases, currents tend to follow more tightly the profile of a notch (or crack). In theory, this could be exploited by repeating the measurements over a broad spectrum of frequencies to obtain more information on the defect's geometry; however, it was realised that the practical implementation of this technique poses several challenges.

For non-ferromagnetic materials with relatively low electrical conductivity, such as stainless steels, frequencies of the order of 1 MHz could be needed (depending on the thickness of the tested structure) to achieve a sufficiently small penetration depth; however, the undesired inductive signal which inevitably arises from non-closed defects and from the measurement circuit itself practically limits the frequency range for the inspection to a few tens of kHz, as has been acknowledged in the literature (see for example [39, 84, 85]).

More importantly, the results of the tests presented in this Chapter suggest that sizing of even the simplest defects (infinitely long notches of uniform depth) may not be straightforward, and that a few issues need to be addressed before trying to evaluate defects of more realistic geometries. In particular, if the length of a defect is finite, currents can flow not only below the defect, but also around its extremities: this can only be taken into account by three-dimensional models. It was therefore necessary to develop a strategy to overcome the limitations imposed in practice by existing commercial Finite Element codes, whose requirements in terms of computational power for the fully 3-D simulation of ACPD measurements exceed the resources commonly available today; this is the subject of the next Chapter.

Experimentally, one way of accounting for the finite length of defects is to measure the potential drop at multiple locations; the same approach could then be used for the study of defects of non-uniform depth. This will be investigated in Chapter 7.

Chapter 6

Finite Element model for three-dimensional ACPD calculations

6.1 Introduction

Fully three-dimensional numerical simulations of ACPD analyses cannot be run easily on existing commercial Finite-Element (FE) codes. For instance, Abaqus, one of the most popular FE packages, does not solve AC problems, whereas Comsol Multiphysics, while accounting for alternating currents, is in practice limited to two-dimensional geometries because of heavy memory requirements. From initial simulations with Comsol it was found that, in order to obtain accurate results, the layer of material corresponding to the first standard penetration depth δ must be described by a minimum of 8 four-noded elements in the direction orthogonal to the surface. At high frequencies the thickness of this layer can be very small, especially for ferromagnetic or highly conductive materials (for example, the skin depth at 1 kHz for a mild steel of the type used in the experiments described in this Chapter is $\delta = 0.6$ mm); it should also be borne in mind that the element size in directions parallel to the surface cannot be much bigger, since elements with a large aspect

ratio are likely to cause numerical errors, and that for similar reasons any coarsening of the mesh with increasing distance from the surface must be gradual. All of this means that a fully three-dimensional model can require several million elements, a number that exceeds the computational capabilities commonly available today.

However, in this Chapter it will be shown that the results of AC problems can be reproduced with fair accuracy by modelling the injection of DC currents into a specimen of appropriately modified geometry. The use of direct currents means that the model will not be able to predict the imaginary component of the AC signal; however, as discussed in Chapter 5, this is in practice affected by errors due to the inductive pickup of the measuring circuit and has therefore been discarded in the analysis of the results throughout the present work.

6.2 Reduced-thickness model

In order to illustrate this approximate model, let us consider a specimen of thickness $T > \delta$. Bearing in mind that the standard penetration depth δ is defined as the depth in the material at which the current density has decayed by a factor of e compared to its surface value, a little physical insight suggests that regions of the specimen sufficiently far from the electrodes could be neglected in the analysis, because any currents flowing in those regions would be very small. The computational domain can therefore be reduced to a layer of thickness $t < T$ just below the surface, as shown in Fig. 6.1 where the shadowed area represents the part of the specimen 'cut out' of the domain; in doing this, any features such as surface-breaking defects (*e.g.* the crack of depth d in Fig. 6.1) must be taken into account as they alter the path of currents by pushing them more deeply into the material. It is important to note that the layer of reduced thickness t should run along the entire surface of the specimen, including lateral and bottom surfaces; this is especially relevant for specimens with a length or width comparable to their thickness, or when the electrodes are placed close to an edge, since in these cases the fraction of currents flowing along those surfaces may not be negligible.

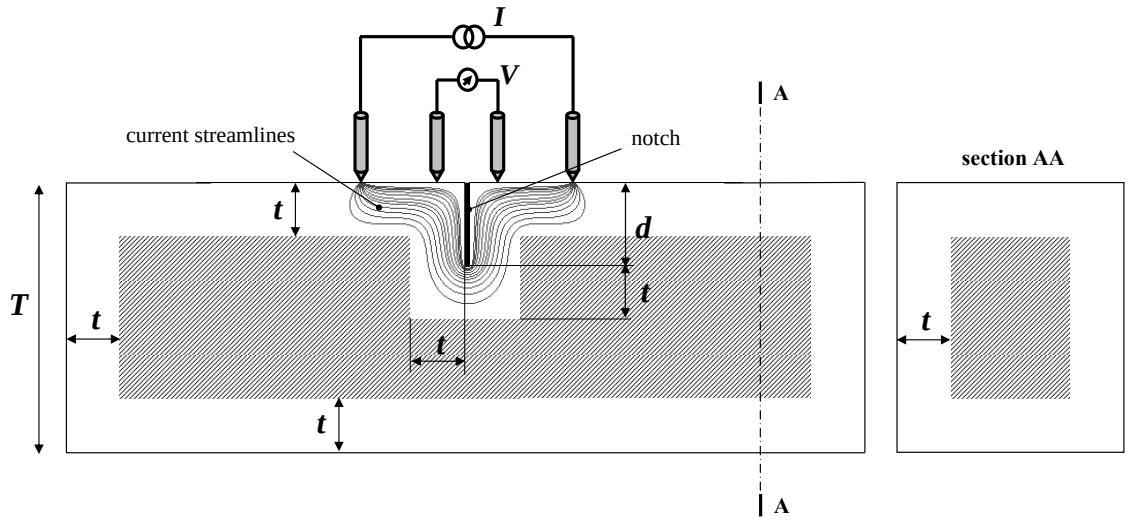

Figure 6.1: *Illustration of the approximate FE model for 3D ACPD simulations. Only a layer of thickness t under the surface of the specimen and around any surface-breaking features is considered in the analysis.*

If direct currents are now injected in this modified geometry, the shape of the domain itself will force them to follow a path similar to that of alternating currents in the original geometry.

It is worth mentioning at this point that, as the standard penetration depth is a function of the frequency of the injected currents, the thickness t of the approximate model will also depend on frequency. Indeed, from two-dimensional numerical simulations run both on Comsol Multiphysics (AC analyses on the full geometry and DC analyses on the approximate model) and on Abaqus (DC only) it was found that choosing a reduced thickness equal to the standard penetration depth ($t = \delta$) gives almost exactly the same results as the AC simulations. This is shown in Fig. 6.2 where the ratio between the potential drop $V_{DC,\,t}$ calculated with DC analyses on the reduced-thickness model and the potential drop $V_{AC,\,T}$ (or more precisely its real part) calculated with an AC analysis on the full geometry is plotted as a function of the reduced thickness t expressed in units of skin depth.

It is not a casual coincidence that this ratio becomes equal to 1 for $t \approx \delta$. If a direct current of intensity I is injected in an undamaged plate of thickness t (whose value is yet to be determined), it will spread through the entire thickness; at a sufficient

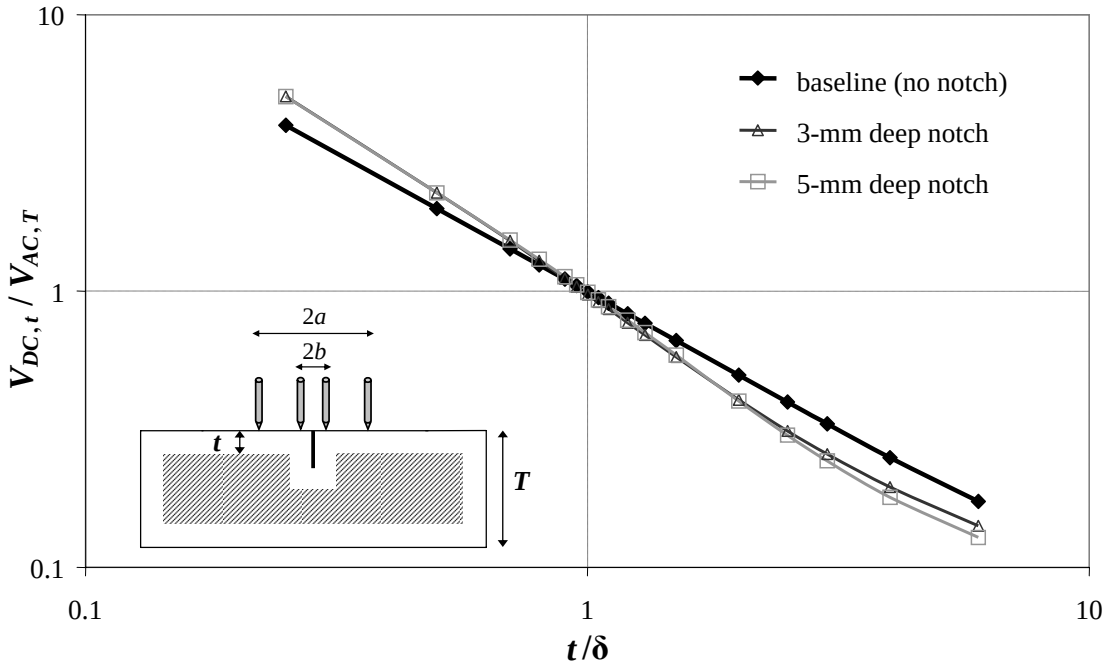

Figure 6.2: *Ratio between the DC potential drop for the reduced-thickness model and the AC potential drop on the full geometry, as a function of the ratio between the reduced thickness t and the skin depth δ. Values obtained for a 200-mm long, 30-mm thick block of mild steel AISI 1020 ($\sigma = 5.3 \cdot 10^6\ \Omega^{-1}m^{-1}$, $\mu_r = 120$) at $f = 100$ Hz ($\delta = 2.00$ mm) with probe spacings $2a = 30$ mm and $2b = 10$ mm; notch width 0.2 mm.*

distance $\varrho \geq t$ (measured on the surface) from the injecting electrode, the current will flow across the whole section of the plate, so that the current density can be calculated simply as

$$J_{DC} = \frac{I}{2\pi\varrho t}. \tag{6.1}$$

In the case of an alternating current, instead, the skin effect must be taken into account. Bowler [86] showed that, at a sufficient distance from the injecting point, the current density for the injection of an alternating current of intensity I in a half-space is

$$J_{AC} = -ik\frac{I}{2\pi\varrho}\mathrm{e}^{ikz}, \tag{6.2}$$

where i is the imaginary unit, z is the depth and $k = \sqrt{i\omega\mu\sigma} = \dfrac{1+i}{\delta}$. It is now required that in the reduced-thickness model the current density on the surface be

equal to that for the AC case in the full geometry, or more exactly to its real part:

$$J_{DC} = \Re[J_{AC}(z = 0)]; \tag{6.3}$$

the imaginary component cannot obviously be taken into account with a DC model. Substituting the expressions of J_{DC} and J_{AC} in Eq. 6.3 gives

$$\frac{I}{2\pi\varrho t} = \Re\left[\frac{1-i}{\delta}\frac{I}{2\pi\varrho}\right] = \frac{I}{2\pi\varrho\delta}, \tag{6.4}$$

from which immediately follows

$$t = \delta : \tag{6.5}$$

this is therefore the value of reduced thickness to be chosen in the model.

It should be noted that Eq. 6.1 is valid under the assumption that the direct current can penetrate through the entire thickness t: this is only possible if the distance between the points of injection and extraction of the current (*i.e.* the separation $2a$ between the current electrodes) is at least twice the thickness t. This will be discussed in more detail later in this Section. On the other hand, Eq. 6.2 is strictly valid only for a half-space; in the case of a plate of finite thickness T this expression must be replaced by

$$J_{AC} = -ik\frac{I}{2\pi\varrho}\lim_{N\to\infty}\left[\sum_{n=0}^{N-1}\left(\mathrm{e}^{ik(z+2nT)} + \mathrm{e}^{-ik[z-2(n+1)T]}\right) + \mathrm{e}^{ik(z+2NT)}\right], \tag{6.6}$$

as calculated in [87]. Substituting this and Eq. 6.1 in Eq. 6.3 yields after a few passages

$$\frac{I}{2\pi\varrho t} = \Re\left[\frac{1-i}{\delta}\frac{I}{2\pi\varrho}\left(1 + \frac{2}{\mathrm{e}^{\frac{1-i}{\delta}2T} - 1}\right)\right], \tag{6.7}$$

from which

$$t = \delta \cdot \frac{1}{\Re\left[(1-i)\left(1 + \dfrac{2}{\mathrm{e}^{(1-i)\frac{2T}{\delta}} - 1}\right)\right]}. \tag{6.8}$$

This expression, which therefore includes a correction factor that is function of the thickness T of the plate, can be evaluated numerically and is plotted in Fig. 6.3, where both t and T have been scaled to the standard penetration depth δ for generality. It can be observed that, in addition to the asymptote $t = \delta$ for thick plates

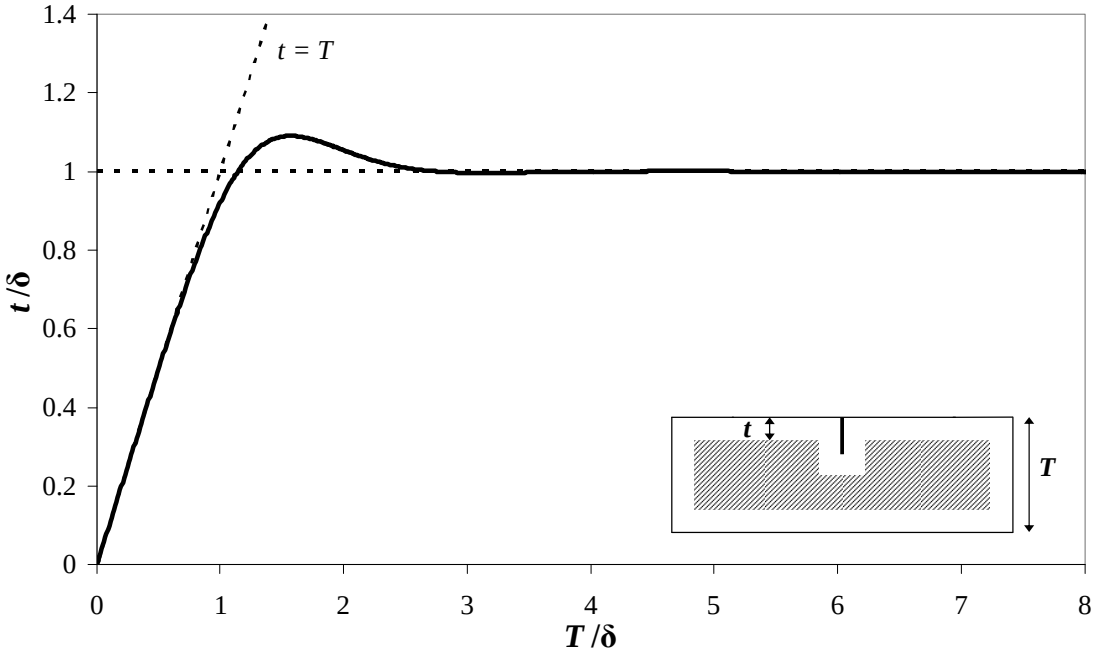

Figure 6.3: *Reduced thickness t to be used in the FE model as a function of the full thickness T of the plate, both expressed as a ratio to the skin depth δ.*

($T \gg \delta$), Eq. 6.8 has another asymptote $t = T$ for plates which are very thin compared to the skin depth ($T \ll \delta$), as can be expected if one considers that in those cases alternating currents would penetrate through the entire thickness of the material just as direct currents would.

Note that in deriving the expressions for t no assumptions were made on the presence of defects in the tested specimen, so that Eq. 6.8 and its approximation for thick plates, Eq. 6.5, are of general validity. A confirmation of this can be found in Fig. 6.2, where the presence of cracks of different depths is shown to have no influence on the optimal value of reduced thickness t. However, it is interesting to note that the voltage drop $V_{DC,t}$ calculated with the reduced-thickness model decreases more rapidly with increasing t in the presence of notches. In order to understand this, let us consider the illustration of Fig. 6.4, which shows the current streamlines in the area close to the notch for two different values of t. As the thickness t increases, the potential drop diminishes not only because of the increase in the cross section 'seen' by the currents (which explains the exact inverse proportionality for the baseline case, *i.e.* for the undamaged block), but also because the perturbation introduced

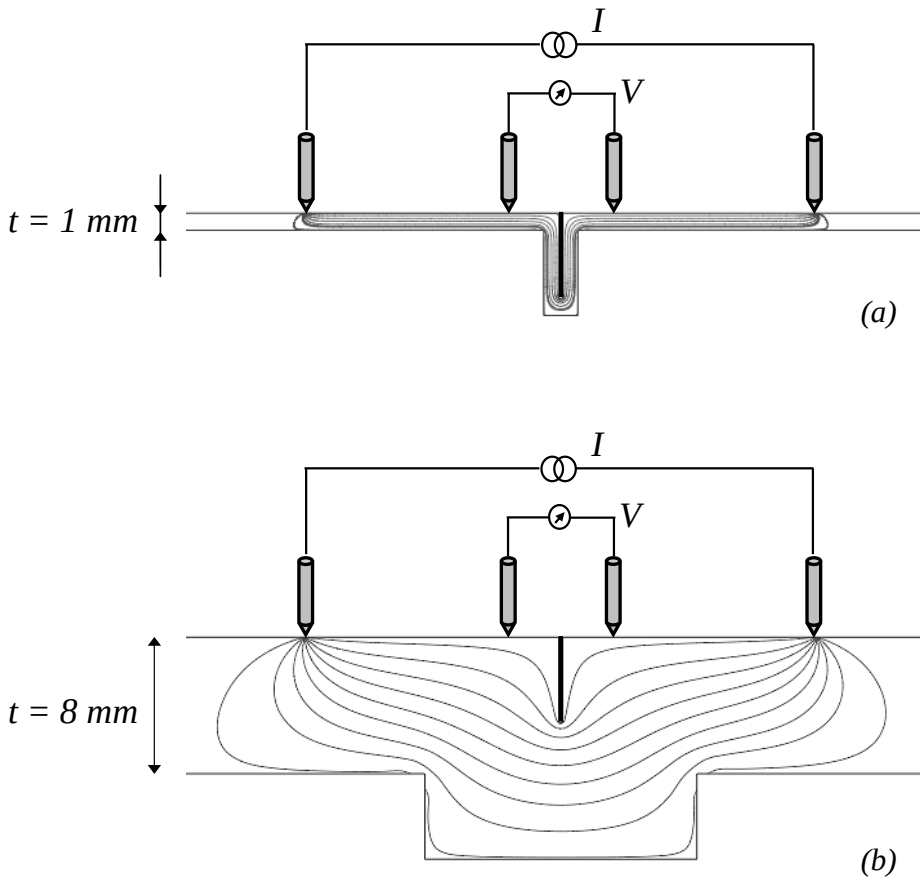

Figure 6.4: *Current streamlines in the area around a 5-mm deep notch in a block of mild steel AISI 1020, calculated with the FE model with two different values of reduced thickness, t.*

by the defect in terms of alteration of the current path becomes less pronounced.

A higher-frequency case is considered in Fig. 6.5: again it is found that the results of the AC analysis can be reproduced by a DC analysis with the reduced-thickness model, choosing $t \approx \delta$. In this case the values of the ratio calculated for the baseline and for a 3-mm deep notch differ only for relatively large values of t/δ. This is because the skin depth at this frequency ($\delta = 0.20$ mm) is much smaller than the depth of the notch, and as a consequence currents are already forced to closely follow the defect profile for $t \approx \delta$; further decreasing the thickness t only modifies the effective cross section, but not the current path. On the other hand, as the thickness t is increased and becomes larger than the notch depth, the effect of the presence of a defect on the distribution of currents becomes smaller and therefore

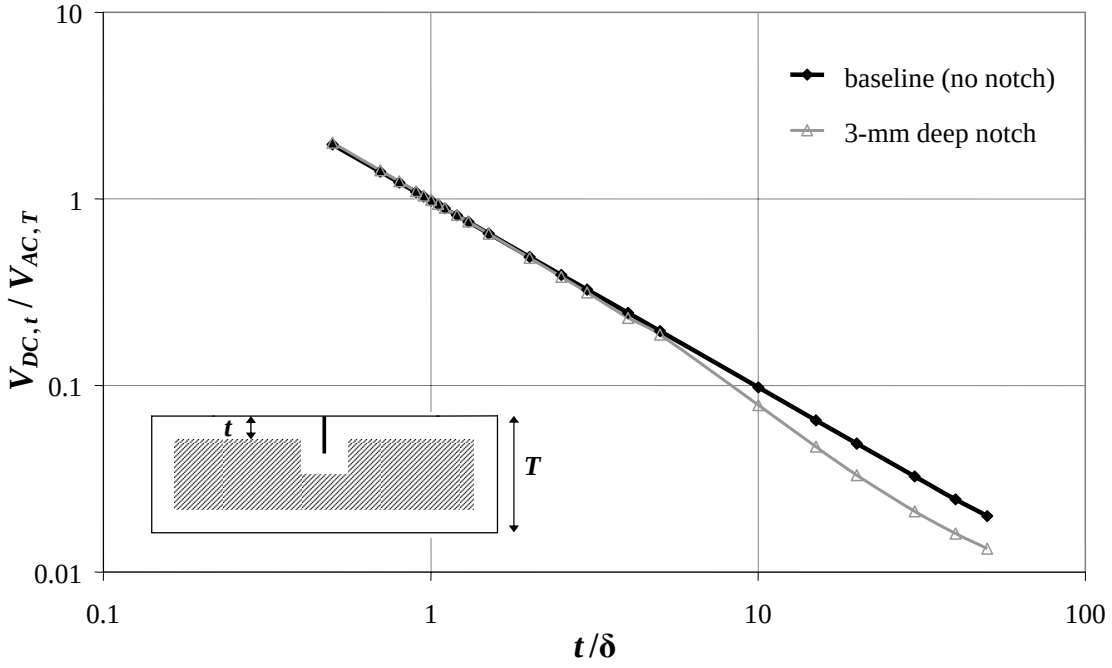

Figure 6.5: *Ratio between the DC potential drop for the reduced-thickness model and the AC potential drop on the full geometry, as a function of the ratio between the reduced thickness t and the skin depth δ. Values obtained for the same block of Fig. 6.2 but at a higher frequency, $f = 10$ kHz ($\delta = 0.20$ mm).*

the potential drop decreases more rapidly, as explained before.

The other parameters that intervene in the calculation of the standard penetration depth δ (see Eq. 2.1) and hence of the reduced thickness t are the electrical conductivity σ and the magnetic permeability μ of the inspected material. Conductivity varies by as much as two orders of magnitude for metals and metallic alloys, whereas the permeability of ferromagnetic materials can be several orders of magnitude bigger than that of para- or diamagnetic materials; as a consequence, the skin depth at a given frequency also varies significantly between different materials. The thickness t of the reduced model needs to be modified accordingly: in any case the results of the AC problem can be reproduced by a DC analysis on a model with $t \approx \delta$. As an example, the ratio $V_{DC,t}/V_{AC,T}$ as a function of t/δ is plotted in Fig. 6.6 for a different material (aluminium, instead of mild steel).

In practical deployments of Potential Drop techniques the spacings between the

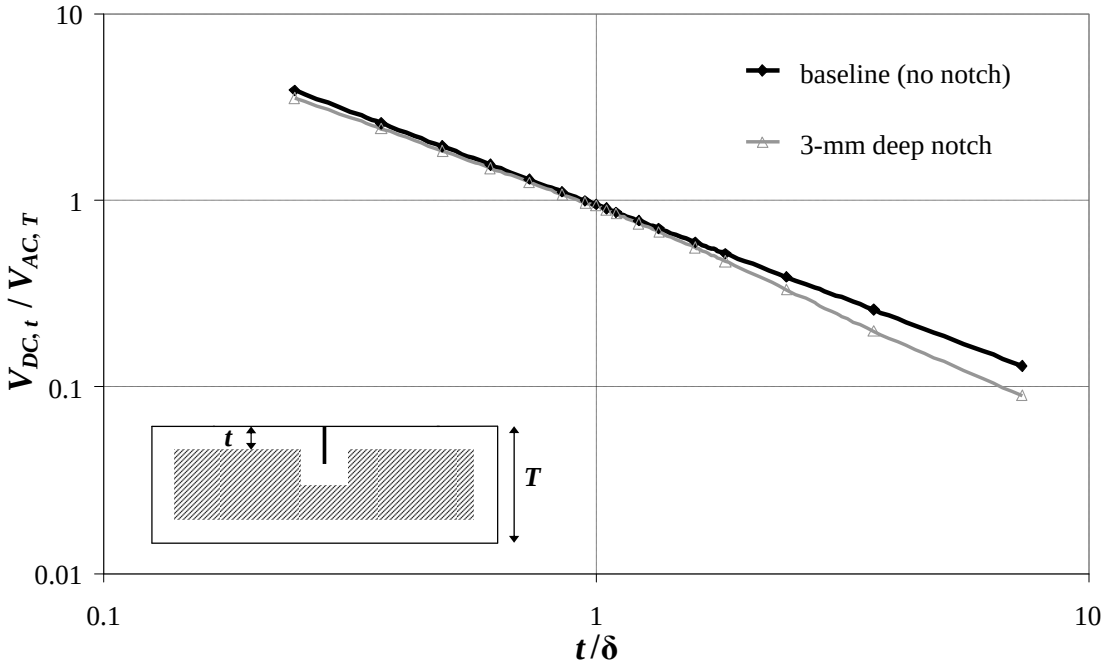

Figure 6.6: *Ratio between the DC potential drop for the reduced-thickness model and the AC potential drop on the full geometry, as a function of the ratio between the reduced thickness t and the skin depth δ. Values obtained for a 200-mm long, 30-mm thick block of aluminium ($\sigma = 3.77 \cdot 10^7\ \Omega^{-1}m^{-1}$, $\mu_r = 1$) at $f = 10$ kHz ($\delta = 0.82$ mm) with probe spacings $2a = 30$ mm and $2b = 10$ mm; notch width 0.2 mm.*

electrodes of the probe are often varied depending on the application (*e.g.* thickness gauging, crack sizing, conductivity measurement, etc.) and on factors such as the accuracy and sensitivity required or the size of the area to be tested [28, 62]. It was mentioned earlier that, in order to ensure that direct currents penetrate through the entire thickness t of the reduced model as postulated in Eq. 6.1, it is required that the spacing between the injecting electrodes be $2a \geq 2t$; this condition is often readily satisfied in most practical applications. Fig. 6.7 shows that the value of reduced thickness to be chosen in the FE model is not significantly affected by the probe geometry even in the limiting case $2a = 2t$: the flattening of the curve for $t \gg a$ in this case is due to the fact that the penetration of current in the material is limited by the spacing between the injecting electrodes, so that further increases in thickness would have no influence on the voltage measured either in the AC or in the DC regime.

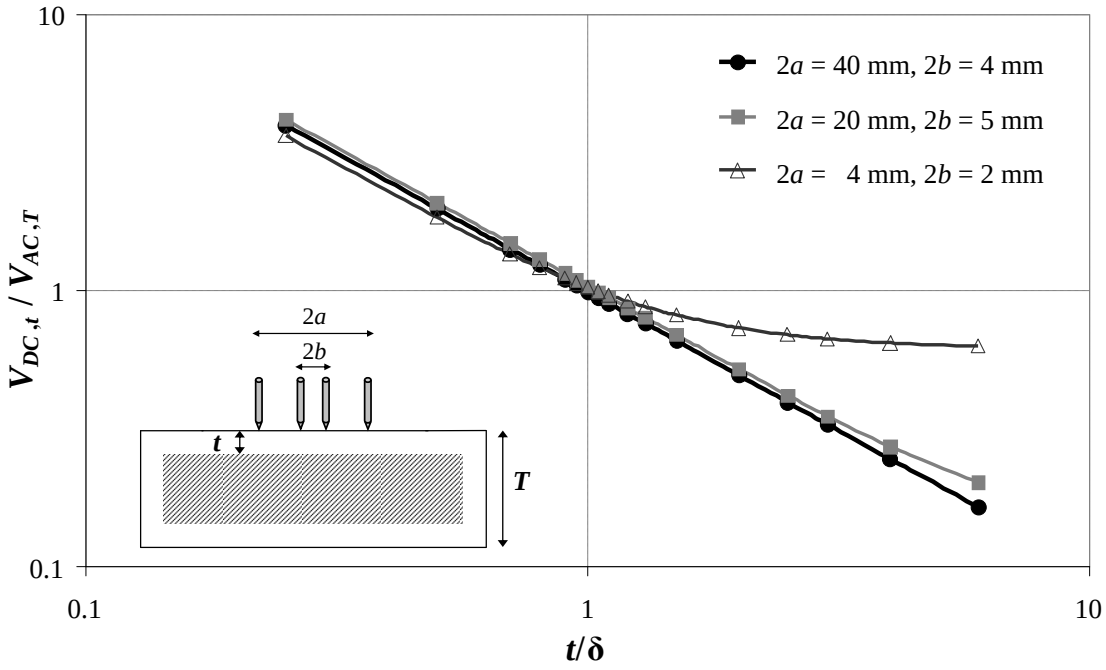

Figure 6.7: *Ratio between the DC potential drop for the reduced-thickness model and the AC potential drop on the full geometry, as a function of the ratio between the reduced thickness t and the skin depth δ. Values obtained at $f = 100$ Hz for the same block of Fig. 6.2 but with three different probe geometries.*

Finally, it is worth mentioning that, although in all cases considered so far the probe was exactly centred with respect to any notches, the relative position of the probe and of the defect also has no influence on the optimal value of t. This is shown in Fig. 6.8, where the ratio $V_{DC,t}/V_{AC,T}$ as a function of t/δ is plotted both for the case in which the two inner electrodes are at the same distance $b = 5$ mm from a 3-mm deep notch and for the case in which the probe is displaced laterally so that one of the two inner electrodes is only 0.5 mm from the defect (see insert in Fig. 6.8); note that the latter value is smaller than the skin depth at the inspection frequency, $\delta = 2$ mm. The case in which both electrodes are on the same side of the defect has not been considered here as it is of little interest in practical applications of the PD techniques.

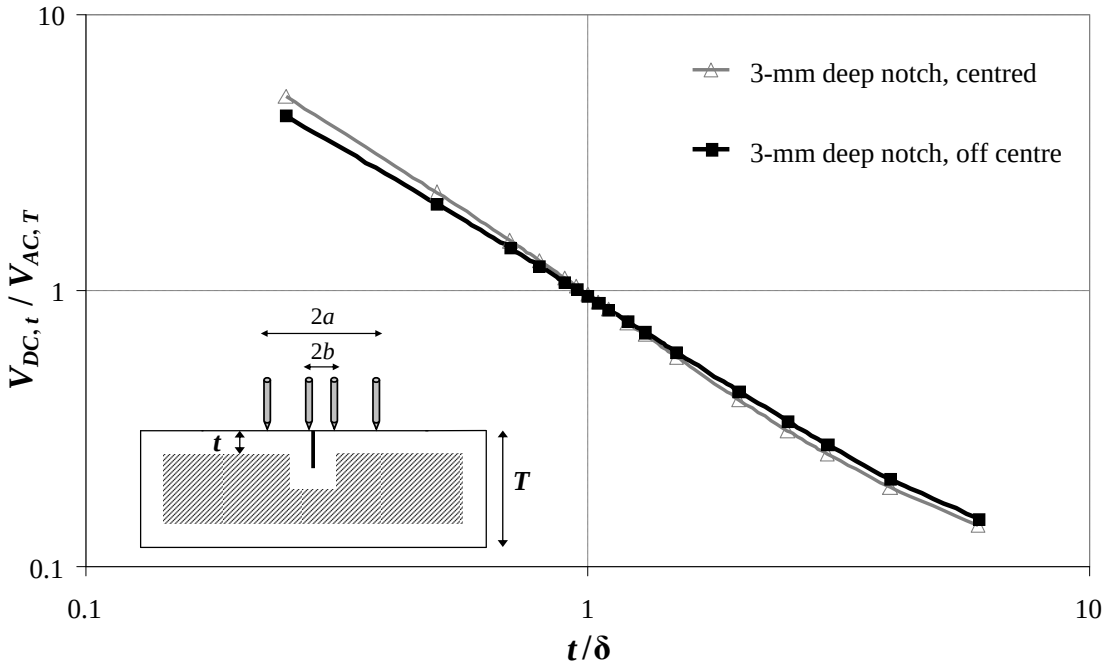

Figure 6.8: *Ratio between the DC potential drop for the reduced-thickness model and the AC potential drop on the full geometry, as a function of the ratio between the reduced thickness t and the skin depth δ. Values obtained at $f = 100$ Hz for the same block of Fig. 6.2 but for two different positions of the probe with respect to the notch. The insert refers to the case in which the probe is off centre.*

6.3 Experimental validation of the model

Tests were run on specimens of simple geometry to validate the approximate model just described; the results of the xperiments were compared with those of three-dimensional numerical simulations run with the commercial FE code Abaqus.

Four 300-mm long, 18-mm wide, 16-mm thick bars of mild steel AISI 1020 were used for the tests. Each bar had a 0.5-mm wide notch machined across its width using electrical discharge machining (EDM); the depth of the notches d ranged from 1 mm to 5 mm. The probe, attached to the setup described in Chapter 3, consisted of four small spring-loaded pins, aligned orthogonally to the notch; currents were injected through the two outer electrodes, which were 35 mm apart, while the voltage drop was measured across the two inner electrodes, separated by 25 mm.

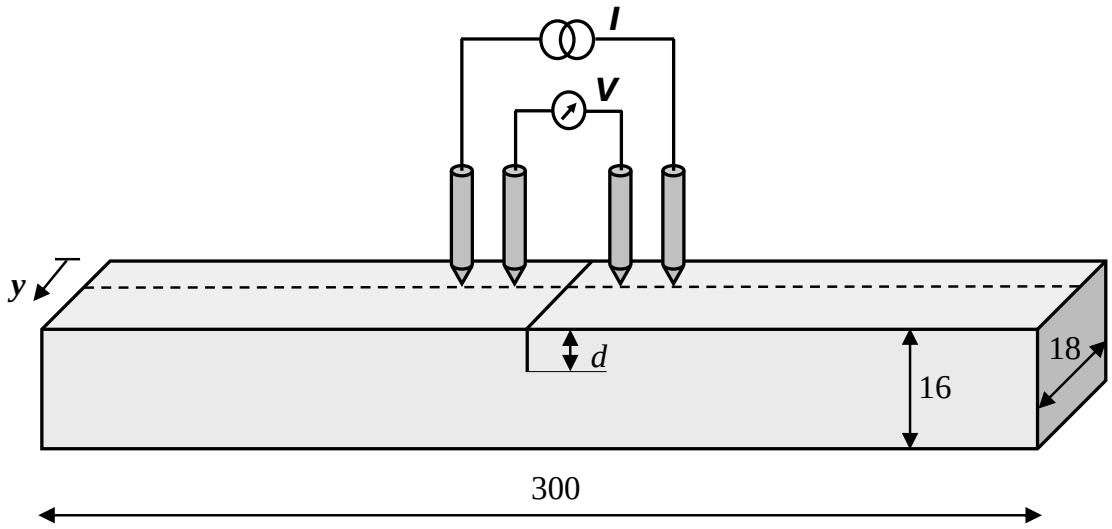

Figure 6.9: *Schematic of the probe and bars used in the tests.*

The tests were run over a range of frequencies between 1 Hz and 1 kHz. The value of electrical conductivity used in the FE analyses was $\sigma = 5.3 \cdot 10^6\ \Omega^{-1}\mathrm{m}^{-1}$; the permeability value is not known with precision for ferromagnetic materials as it is influenced by factors such as the past magnetic history of the material and the thermal and mechanical treatments the specimen has undergone; the value used in the present work ($\mu_r = 120$) falls in the range typical for low-carbon steels [88].

Data were taken initially on one of the bars in an area far from the notch, so as to have a set of reference values ('baseline'). The probe was positioned at first with the four pins aligned on the centreline, then moved along the width of the bar towards one of the edges. The test was then repeated with the probe straddling each of the notches, as shown in the schematic of Fig. 6.9.

As an example, the results obtained both numerically and experimentally for the baseline and for a 5-mm deep notch are reported in Fig. 6.10 and Fig. 6.11 for $f = 1$ Hz and $f = 1$ kHz, respectively. The graphs show the transfer resistance measured at the voltage electrodes as a function of the distance y of the pins from the edge of the specimen (so that $y = 9$ mm represents the case in which the probe is positioned on the centreline of the bar). It should be noted that at 1 Hz the standard penetration depth calculated according to Eq. 2.1 would be larger than

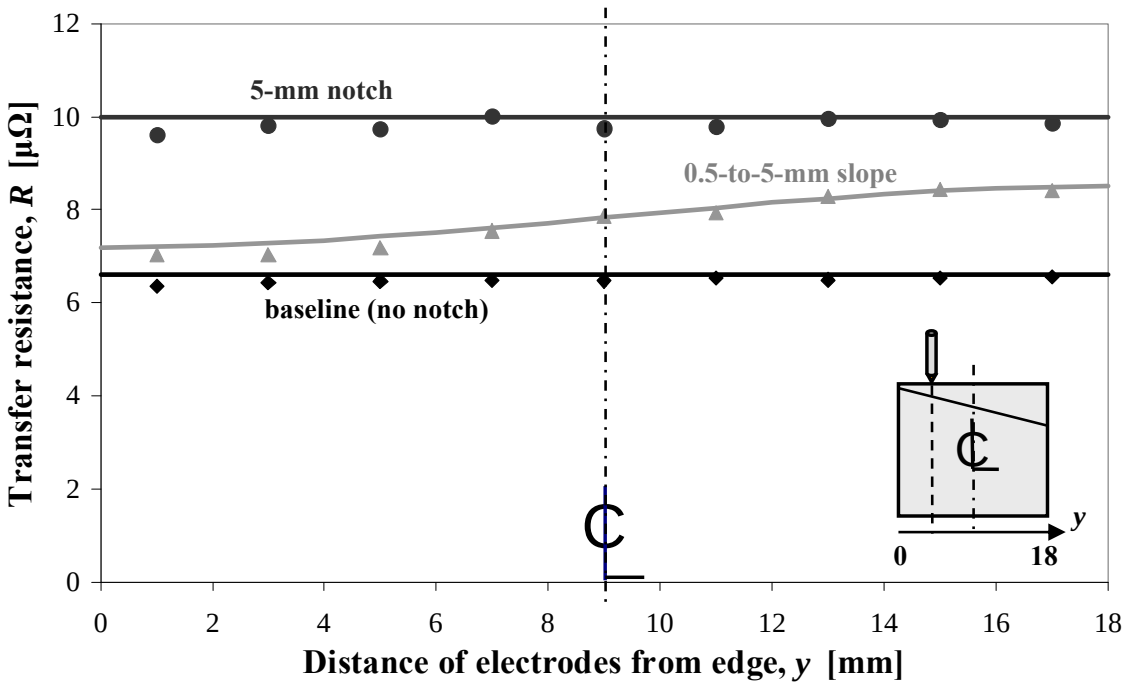

Figure 6.10: *Transfer resistance measured at $f = 1$ Hz calculated with the FE model (lines) and measured experimentally (symbols) on bars of mild steel. The insert shows a schematic lateral view of the probe placed at a generic position y from the edge of the specimen.*

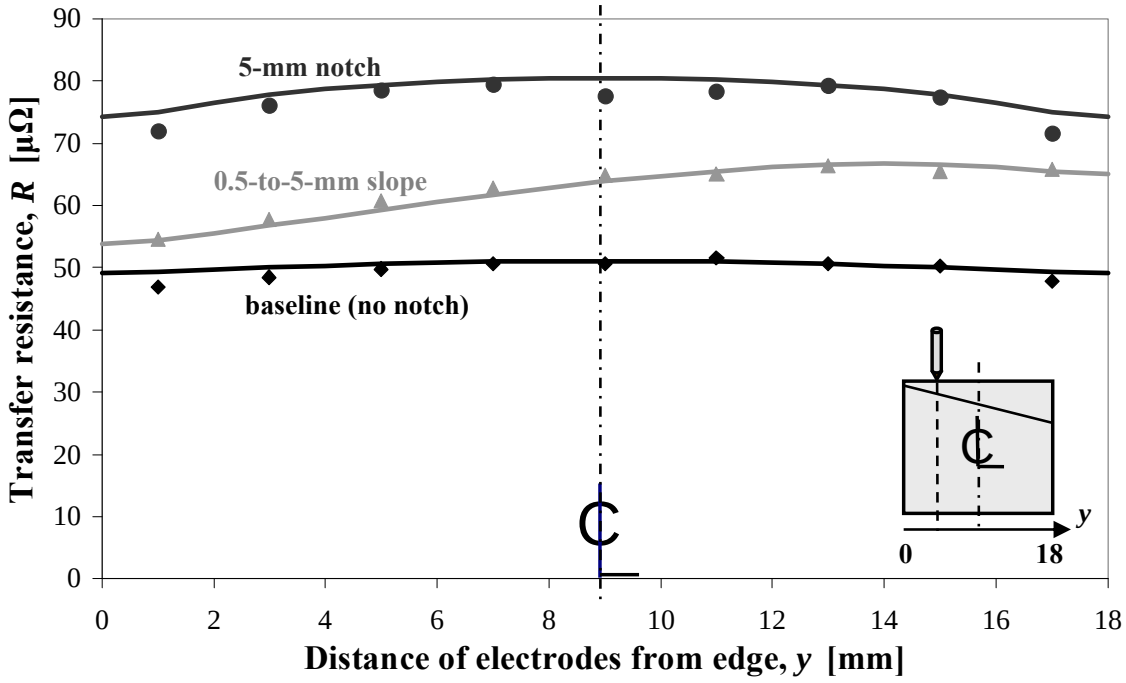

Figure 6.11: *Transfer resistance measured at $f = 1$ kHz calculated with the FE model (lines) and measured experimentally (symbols) on bars of mild steel.*

the thickness of the specimen, and therefore the geometry of the model for the FE analysis coincides with the real geometry of the bar: the model thus effectively represents the DC case. For higher frequencies, on the other hand, the geometry of the model was modified as discussed in the previous Section, assuming $t = \delta$ (*e.g.* $t = 0.631$ mm at 1 kHz).

It can be seen that the values predicted by the FE simulations are in very good agreement with those measured experimentally, both at low and high frequency. The model also predicts satisfactorily the increase in transfer resistance as the probe is moved closer to the edge of the specimen: this effect is much more pronounced at low frequencies (see Fig. 6.10) because the lateral spreading of currents decreases with increasing frequency in a similar fashion to the standard penetration depth; a quantitative analysis of this 'edge effect' is presented in Appendix A.

6.4 Conclusions

A simple approximate method for modelling three-dimensional ACPD problems using a commercial FE code was developed. Modifying the geometry of the tested specimen prior to the analysis allows accurate prediction of the results of ACPD measurements by simulating the injection of DC currents: in particular, it was shown that the thickness of the specimen in the model should be reduced to about the standard penetration depth δ if the latter is smaller. This is independent of the probe geometry and position (with the proviso that the separation between the injecting electrodes be at least twice the reduced thickness) and of the presence of defects. The model was validated on specimens of simple geometry with notches of various known depths, and excellent agreement was found with the experimental results.

Chapter 7

Depth profiling of surface-breaking cracks

7.1 Introduction

Estimating the shape and size of a defect is a problem of major interest in many industrial applications, since the depth of a crack is often a key parameter in calculations of structural integrity. One of the simplest formulae for the determination of the maximum depth of a surface-breaking defect by using Potential Drop techniques is probably the so-called one-dimensional estimate by Dover *et al.* [58], presented in Chapter 5 and recalled here for ease of reference:

$$d = \frac{\Delta}{2} \frac{V - V_0}{V_0} \ . \tag{7.1}$$

This estimate only applies for infinitely long defects whose depth d is much larger than the skin depth δ of the current flowing in the material. Michael *et al.* [40] noted that, for a rectangular notch of finite length $L = 3d$, Eq. 7.1 underestimates the depth by at least 30%.

Most previous work on the inverse problem of using values of transfer resistance measured at a number of different locations to reconstruct the depth profile of an unknown defect have either used the one-dimensional estimate as a first guess in an

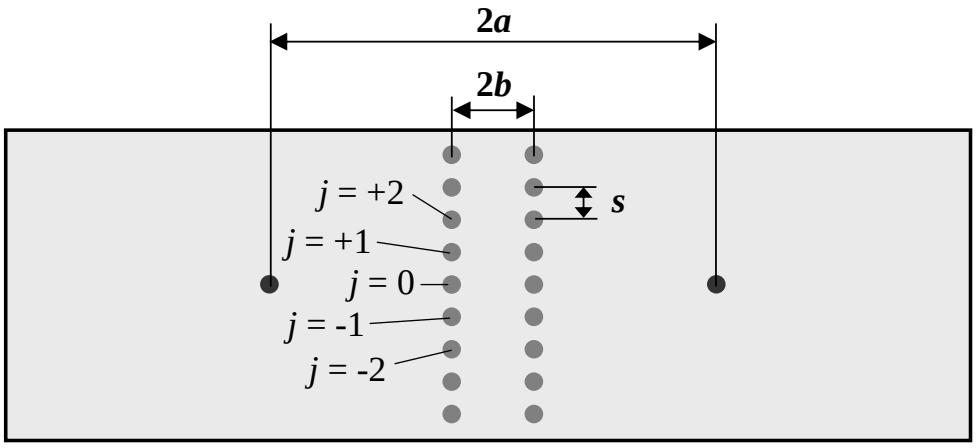

Figure 7.1: *Geometry of linear array probe.*

iterative algorithm [81, 82], or assumed *a priori* knowledge of the defect shape [40, 89, 90], or even made use of parameters to be evaluated heuristically [91]. PD crack gauges are commercially available that assume the defect has a semi-circular form. However, this assumption is not always correct. This Chapter reports the results of a study aimed at developing an inversion technique of more general validity.

7.2 Design and testing of a linear array probe

7.2.1 Guidelines for the design

Potential Drop measurements are usually done with a simple four-point probe like the one used so far in this work, which employs one pair of electrodes to inject currents in the specimen to be tested and a second pair to measure the resulting voltage difference between two points. However, using an array probe in which multiple pairs of sensing electrodes are connected to a multiplexer would give the advantage of taking data at several positions along the width of the specimen without having to move the probe; furthermore, keeping the injecting electrodes fixed, instead of moving them in line with the sensing electrodes, would ensure better uniformity of the distribution of currents — and hence of the potential field — in the measuring area in the presence of edges.

For the present study a linear array probe like the one shown in the schematic of Fig. 7.1 was manufactured. The distance $2a$ between the outer electrodes must be sufficient to ensure that, if current is injected through them, the resulting distribution across the measurement pins is fairly uniform. A compromise has to be reached on the spacing $2b$ between the lines of inner electrodes: reducing this distance increases the sensitivity to flaws, since the fractional increase in resistance due to a defect is roughly proportional to the defect depth as a fraction of the electrode spacing (in the one-dimensional estimate this is assumed to be valid exactly, see Eq. 5.4); but, on the other hand, it also amplifies the effects of the inevitable errors and uncertainties in pin positioning in the practical deployment of the probe. After running a series of numerical simulations with the FE model presented in Chapter 6, the values chosen were $2a = 60$ mm and $2b = 10$ mm, respectively; the spacing between any two of the 9 adjacent pairs in the lines of inner electrodes was set at $s = 2$ mm.

The probe thus designed was then calibrated by taking several sets of data on a 500-mm long, 300-mm wide, 2.5-mm thick SS304 plate. Stainless steel is a homogeneous material, at least from the point of view of its electromagnetic properties, and therefore the response of each sensing pair of the probe should be independent of the position, as long as the probe is placed sufficiently far from the edges of the plate. This allows a 'signature' of the probe to be acquired and any errors due to the non-uniformity of the current distribution and to unavoidable imperfections in the making of the probe (*e.g.* tolerances on the spacing between the sensing electrodes) to be significantly reduced.

It should be noted at this point that swapping the roles of the electrodes used for injection and measurement would yield the same results: Maxwell's reciprocity theorem states that 'the relationship between an oscillating current and the resulting electric field is unchanged if one interchanges the points where the current is placed and where the field is measured' (see *e.g.* [92, 93]). In fact, since it is much more practical to multiplex the sizeable input currents (∼130 mA) than the very small measured voltages (order of 1 μV), when running the tests it was decided to measure

the voltage across the two outer electrodes of Fig. 7.1 and inject current across pairs of inner electrodes on opposite sides of the defect position in turn.

7.2.2 Modifications to the experimental setup

A multiplexer was then added to the setup described in Chapter 3. In particular, a battery of three Stanford Research SIM925 octal four-wire multiplexers was used for these tests. In its original configuration, each of these instruments acts as a switch that connects one of eight four-wire input channels to one four-wire output; there is also a bypass channel which allows cascading of multiple instruments. However, it is also possible to use the SIM925 as a demultiplexer which performs the reverse operation of connecting one input to one of eight output channels: this latter operating mode was exploited in this case, so that the currents coming from the scaling amplifiers could be switched between the pairs of injecting electrodes. In order to allow switching the polarity of currents between the two electrodes of each pair (which contributes to reducing the CMRR, as explained in Chapter 3), two channels are needed for each injecting pair, so that a total of 18 channels is required for the probe used.

7.2.3 Preliminary tests

The probe was tested on the same mild steel bars used in the experiments to validate the FE model (see Chapter 6); in fact, the tests reported in this Section also represent part of the validation process. An additional specimen of identical material and dimensions was also used, on which a 'sloped notch' was machined; the depth of this notch increased constantly along the width of the bar, going from 0.5 mm to 5 mm (these values are measured at the edges). Data were taken over a range of frequencies between 1 Hz and 1 kHz.

Fig. 7.2 shows a comparison between the data collected experimentally at $f = 1$ Hz and the predictions of the FE model with a fully DC analysis, for the three cases of

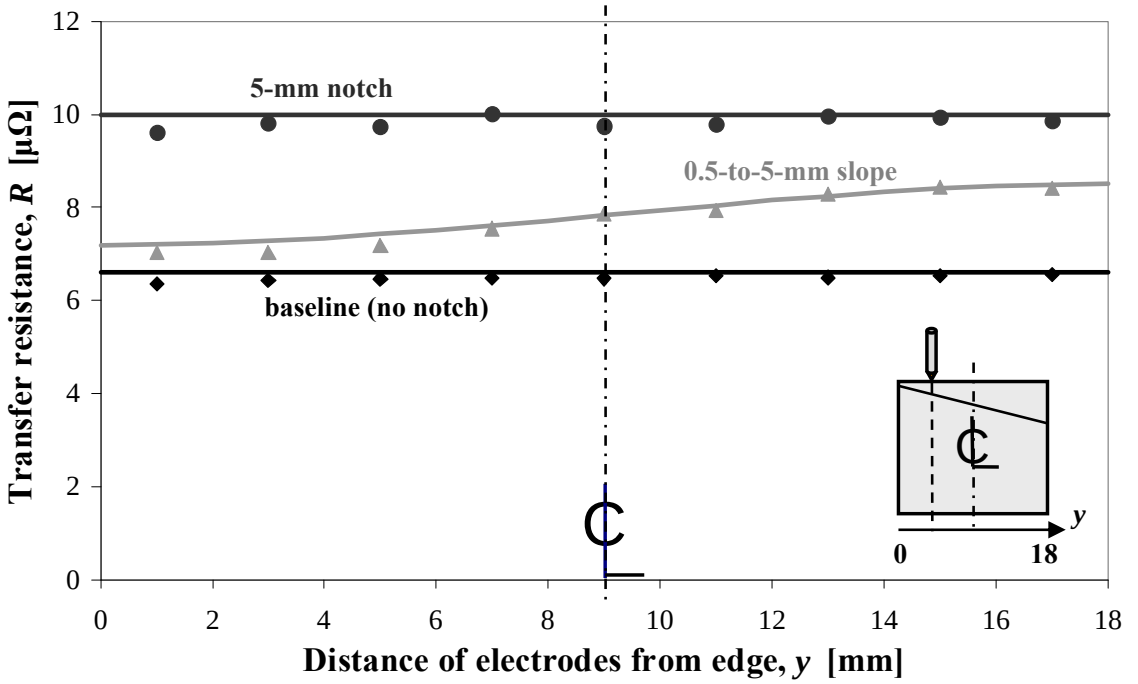

Figure 7.2: *Transfer resistance measured at $f = 1$ Hz calculated with the FE model (lines) and measured experimentally with a linear array probe (symbols) on bars of mild steel. The insert shows a schematic lateral view of one of the inner electrodes at a generic position y on the specimen with a sloped notch.*

the probe positioned in an area with no notches (baseline) or straddling either the sloped notch or a notch with a constant depth of 5 mm: the measured or calculated transfer resistance is plotted as a function of the distance y of the injecting (inner) electrode pair from the edge of the specimen (for the bar with a sloped notch, $y = 0$ was chosen on the shallower side, so that the notch depth increases with y, as shown in the insert of Fig. 7.2). Fig. 7.3 shows the values of transfer resistance measured for the same specimens at $f = 1$ kHz, compared with those predicted by the FE model in which a reduced thickness $t = \delta_{(1\,\mathrm{kHz})} = 0.631$ mm was assumed. Both the DC and the AC cases show a very good agreement between the numerical and the experimental results for each of the specimens.

A comparison of Figs. 7.2 and 7.3 with Figs. 6.10 and 6.11 shows that the values of transfer resistance measured with the linear array probe are not only lower because of the smaller distance $2b$ between the inner electrodes, but also more uniform across the width of each specimen because the outer electrodes are kept fixed. The increase

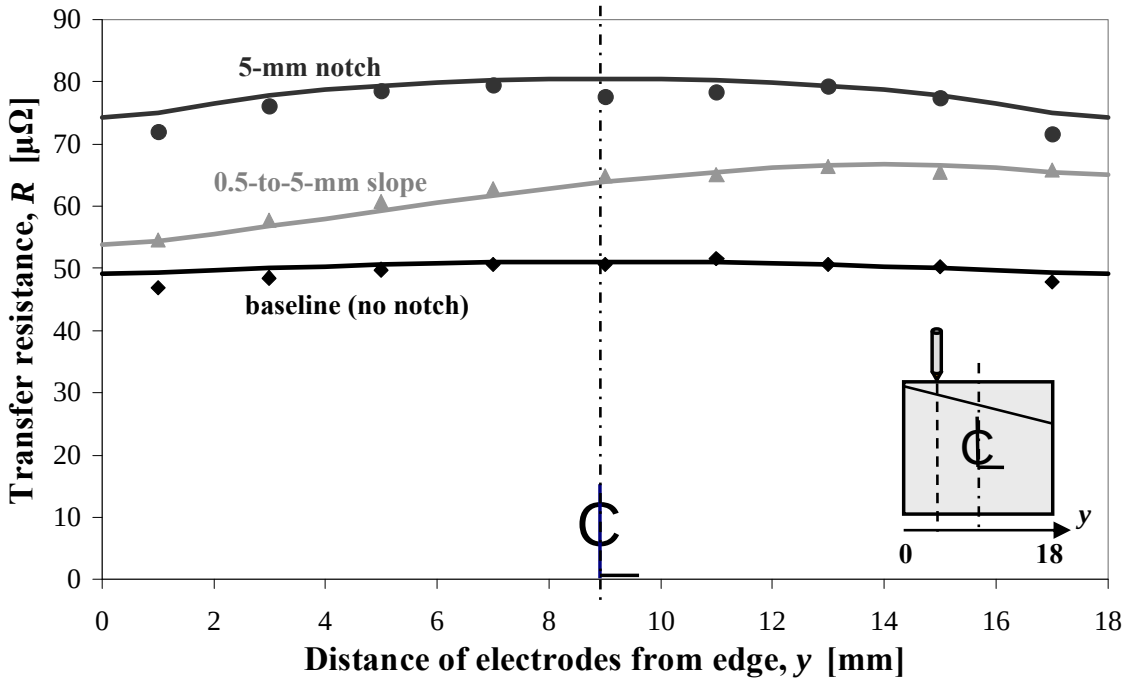

Figure 7.3: *Transfer resistance measured at $f = 1$ kHz calculated with the FE model (lines) and measured experimentally with a linear array probe (symbols) on bars of mild steel.*

in sensitivity resulting from the reduction of the spacing $2b$ between the inner pairs is also evident.

If the values of transfer resistance measured on the baseline are subtracted from those measured across the notches, the graphs of Fig. 7.4 and Fig. 7.5 are obtained for $f = 1$ Hz and $f = 1$ kHz, respectively: these values thus represent the additional transfer resistance introduced by a defect. The increasing depth of the sloped notch can be clearly identified from the data, but it can also be seen that its depth cannot simply be estimated from the resistance measured at a given point, since the maximum resistance measured is less than that on the uniform 5-mm deep notch. This under- or overestimation is due to the averaging effect caused by the lateral spreading of the currents, and it is less pronounced at higher frequencies.

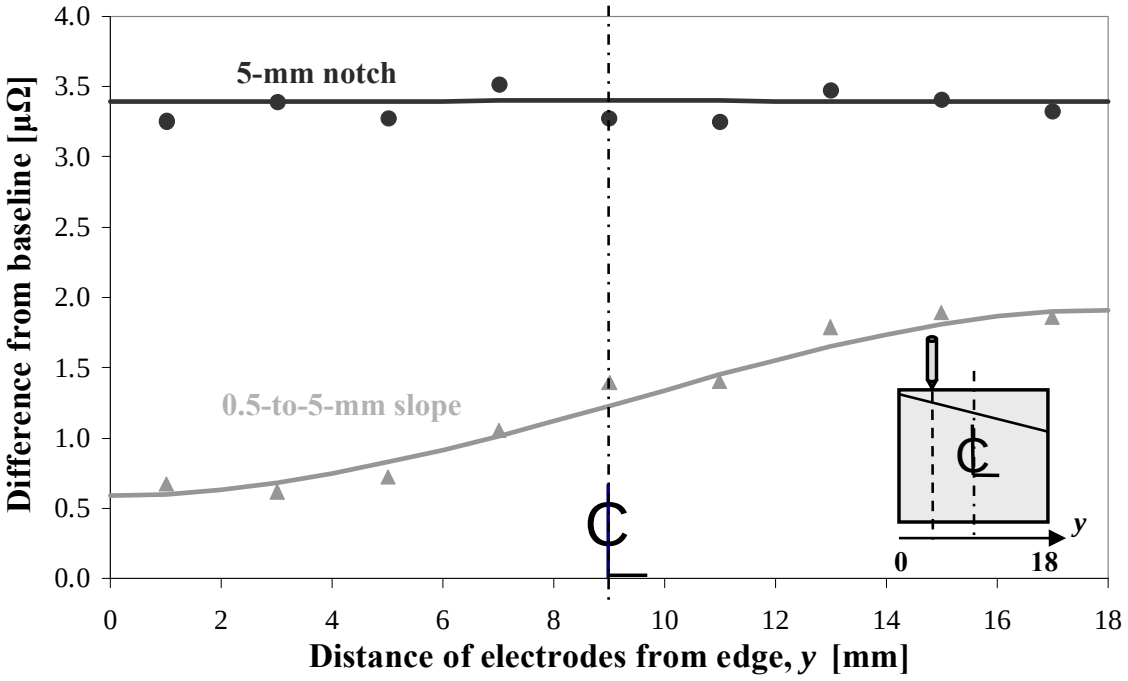

Figure 7.4: *Increase in transfer resistance due to the presence of a notch for the case of Fig. 7.2 ($f = 1$ Hz): predictions of the FE model (lines) and experimental values (symbols).*

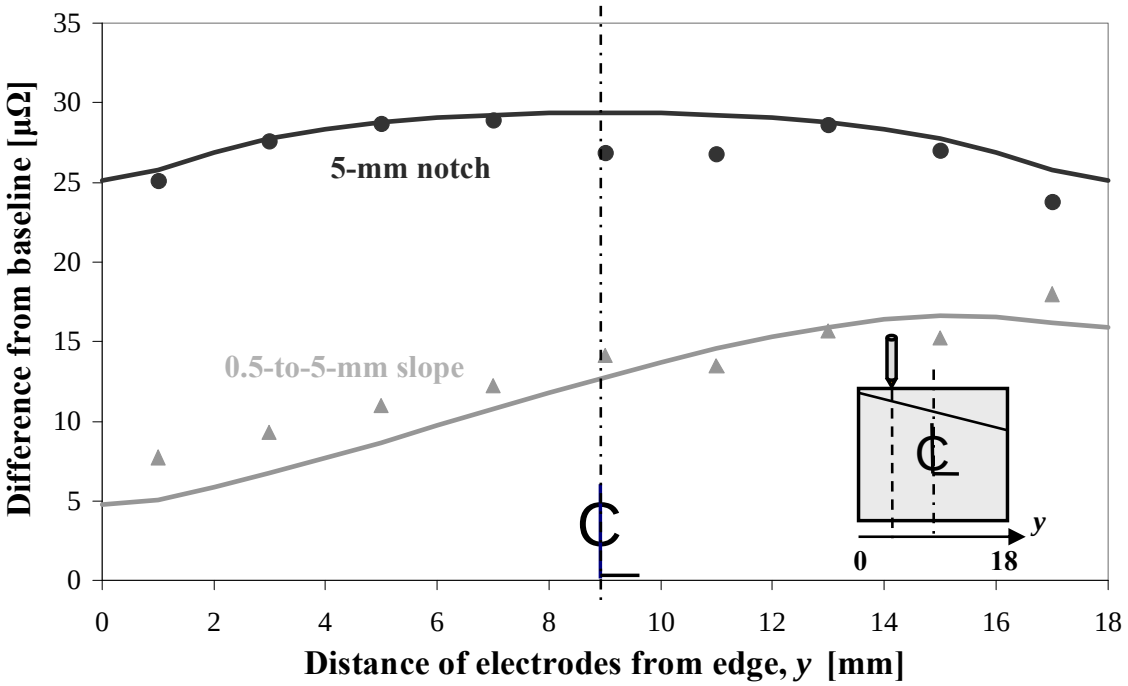

Figure 7.5: *Increase in transfer resistance due to the presence of a notch for the case of Fig. 7.3 ($f = 1$ kHz): predictions of the FE model (lines) and experimental values (symbols).*

7.3 Focusing

The thin line in Fig. 7.6 shows the current distribution across the centreline of the array probe when a unit DC current I_0 is injected between the two central electrodes on a plate with no defects (refer to Appendix B for a mathematical derivation): the wide lateral spread of current is what causes the averaging effect that 'smears' rapid variations in the depth profile of a defect.

In ultrasonic testing, similar problems are routinely solved by employing a focused probe or by using an array probe with delay laws adjusted to give a focus [94, 95]. Similarly, the reciprocal array of Fig. 7.1 gives the possibility of producing 'focused' currents. If a negative current was applied to the pairs of electrodes $j = \pm 1$ in Fig. 7.1 adjacent to the central pair ($j = 0$) which was driven with the positive current that yielded the thin-line distribution of Fig. 7.6, it would be expected that

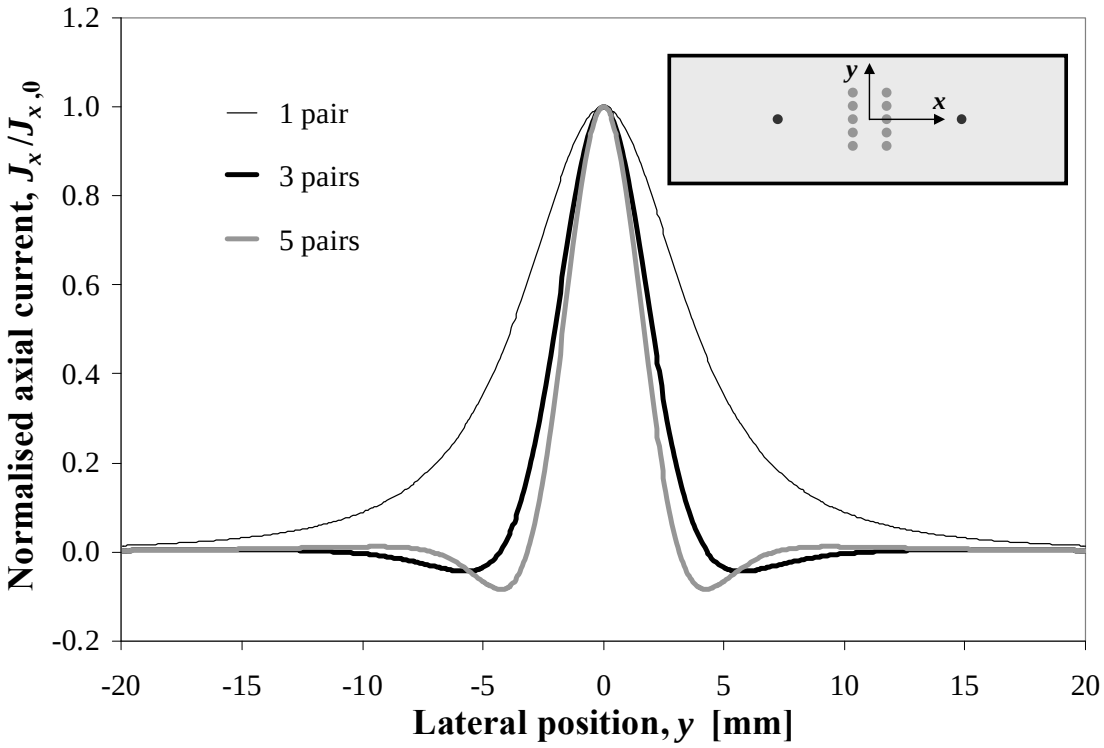

Figure 7.6: *Current distribution along the centreline ($x = 0$) of the array probe for focusing with 1, 3 and 5 pairs of electrodes, optimised for DC. The values are scaled to the current density reached at $y = 0$ in each case.*

part of the wide lobe could be cancelled out, thus 'squeezing' the current into the centre of the array. The thick black and grey curves of Fig. 7.6 show the resulting current distribution if this concept is applied to three and five pairs of electrodes, respectively: the peak is considerably narrower, as desired.

The optimum weightings of currents applied to the pairs are different depending on the number of pairs used, and they are also a (weak) function of frequency. The distributions shown in Fig. 7.6 are for low frequency (DC) and are obtained by injecting $I_{\pm1} = -0.44$ at the electrode pairs $j = \pm1$ for 3-pair focusing, or $I_{\pm1} = -0.57$ at $j = \pm1$ and $I_{\pm2} = +0.10$ at $j = \pm2$ for five pairs. These values, scaled to the positive unit current I_0 injected at the central pair, are obtained by minimising the value of the integral

$$\int \left| \frac{J_x(y)}{J_x(0)} \right| \mathrm{d}y \tag{7.2}$$

where J_x is the axial current density at the centreline of the array, as plotted in Fig. 7.6, and the integral is calculated over the centreline along the entire width of the specimen.

In practice the focusing was done synthetically, with a procedure analogous to SAFT (Synthetic Aperture Focusing Technique), commonly used in ultrasound and radar (see for example [94–96]). Measurements were taken by applying the same current to each electrode pair in turn, and the focused results were computed later by combining the weighted data, so that the total transfer resistance R is given by

$$R = \sum_j \frac{I_j}{I_0} R_j \tag{7.3}$$

where R_j is the transfer resistance measured for each electrode pair (with j varying for example between -2 and $+2$ in the case of focusing with five pairs).

This worked well on data calculated with the FE model. However, when applied to experimental data, focusing introduced so much scatter that the data became unusable for the purpose of reconstructing the depth profile of a defect: an example of this will be shown in the next Section (see Fig. 7.15). It was realised that this was due to the reduction in the total current caused by focusing. The values plotted

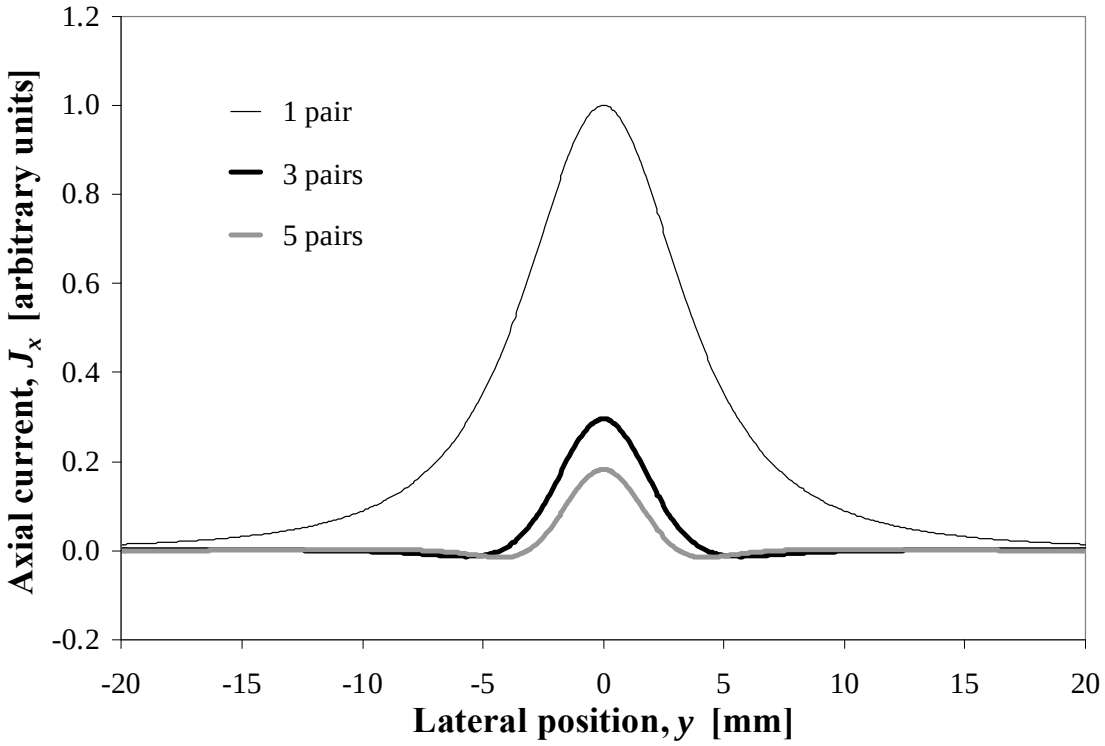

Figure 7.7: *Current distribution along the centreline of the array probe for focusing with 1, 3 and 5 pairs of electrodes, optimised for DC.*

in Fig. 7.6 are in fact *normalised* current densities, *i.e.* they have been scaled to the value reached at the centre of the array ($y = 0$) in each case; if the values are *not* scaled, as in Fig. 7.7, it becomes apparent that the reduction of the lateral spreading has been obtained at the price of a simultaneous significant decrease in the total current flowing in the area of inspection. Associated with this is a pronounced reduction in the amplitude of the measured signal: by substituting the values of the weighting factors in Eq. 7.3, it is found that the total transfer resistance decreases to about 12% of its 'pre-focusing' value if using three pairs, and to only about 6% (a loss of more than 20 dB) if using five pairs. As a consequence, the effects of the unaltered level of noise in the measurements become much more pronounced.

This problem can be overcome by modifying the geometry of the probe. Bringing the inner lines of electrodes closer to each other contributes to narrowing the peak in the current distribution: Fig. 7.8 shows the DC distribution for one, three and five electrode pairs when the distance $2b$ between the lines of injection pins is reduced to

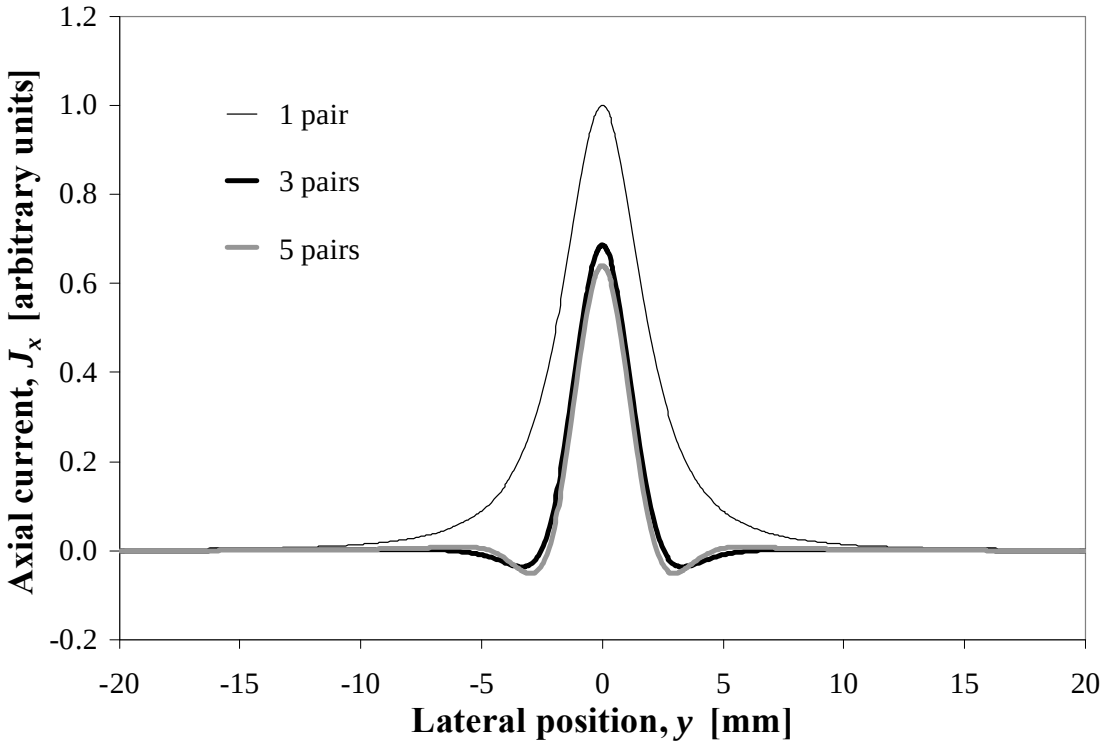

Figure 7.8: *Current distribution along the centreline of an array probe with reduced spacing between the lines of inner electrodes ($2b = 5$ mm), for focusing with 1, 3 and 5 pairs of electrodes, optimised for DC.*

5 mm, a value for which the noise associated with the uncertainties in pin spacing was found to be still acceptable. An important advantage offered by this reduced spacing is that the decrease in peak amplitude introduced by focusing is less pronounced: using three or five pairs of electrodes, current at the centre is over 60% of the value for one pair. Corresponding to this, the optimum weightings of currents applied to adjacent pairs, reported in Table 7.1, are also more favourable: the total amplitude of the focused signal, calculated with Eq. 7.3, is still about 30% of the 'pre-focusing' value even for five pairs.

Another modifiable probe parameter is the spacing s between two consecutive electrode pairs. It is intuitive that reducing this distance would produce an even sharper focusing of currents, but again the price to be paid would be a significant reduction in the amplitude of the signal. Fig. 7.9 shows the DC current distribution that would be obtained for three different values of s while keeping $2b = 5$ mm fixed.

Table 7.1: *Optimum weightings of currents applied to electrode pairs of a linear array probe with $2a = 60$ mm, $2b = 5$ mm and $s = 2$ mm, for low-frequency measurements.*

	I_0	$I_{\pm1}$	$I_{\pm2}$
1 pair (no focusing)	1.00	0	0
3 pairs	1.00	-0.33	0
5 pairs	1.00	-0.39	0.04

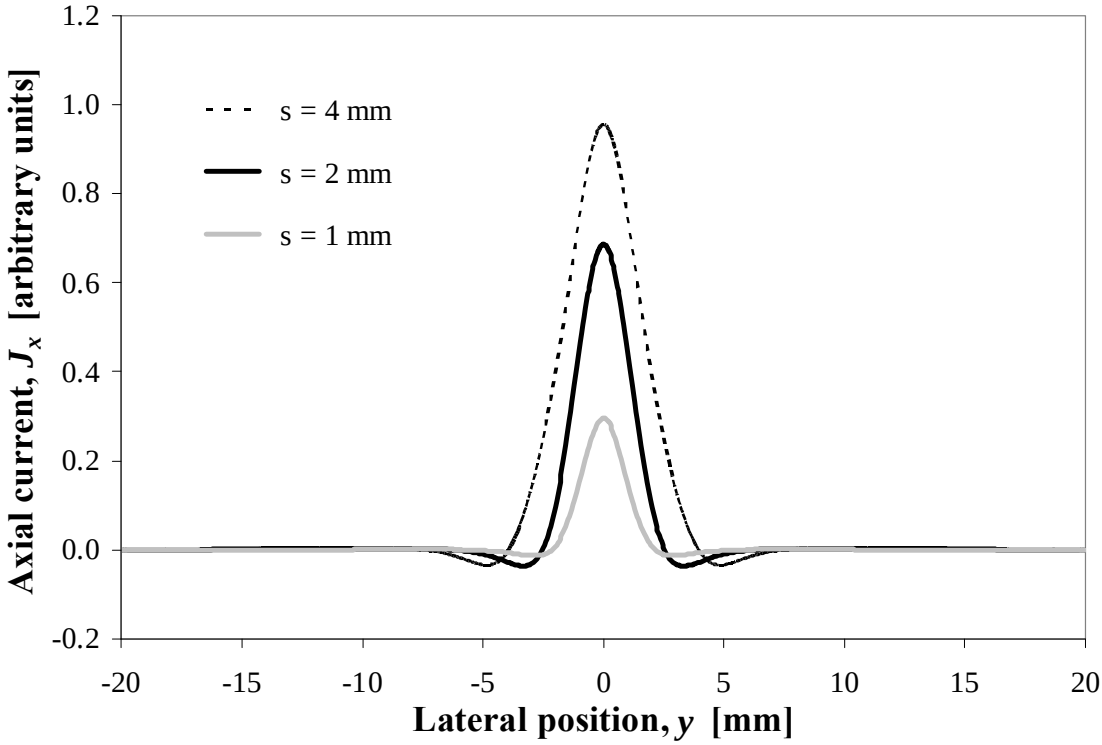

Figure 7.9: *Current distribution along the centreline of array probes with various spacings s between consecutive electrode pairs, for focusing with three pairs of electrodes, optimised for DC.*

On the basis of these results, it was therefore decided to build a second-generation linear array probe, where the distance between the inner (injecting) electrodes was reduced to $2b = 5$ mm, whereas the spacing between two consecutive pairs was kept at $s = 2$ mm and the separation between the outer (sensing) electrodes at $2a = 60$ mm. This newer probe was used for all the tests whose results are reported in the following Section, unless otherwise specified.

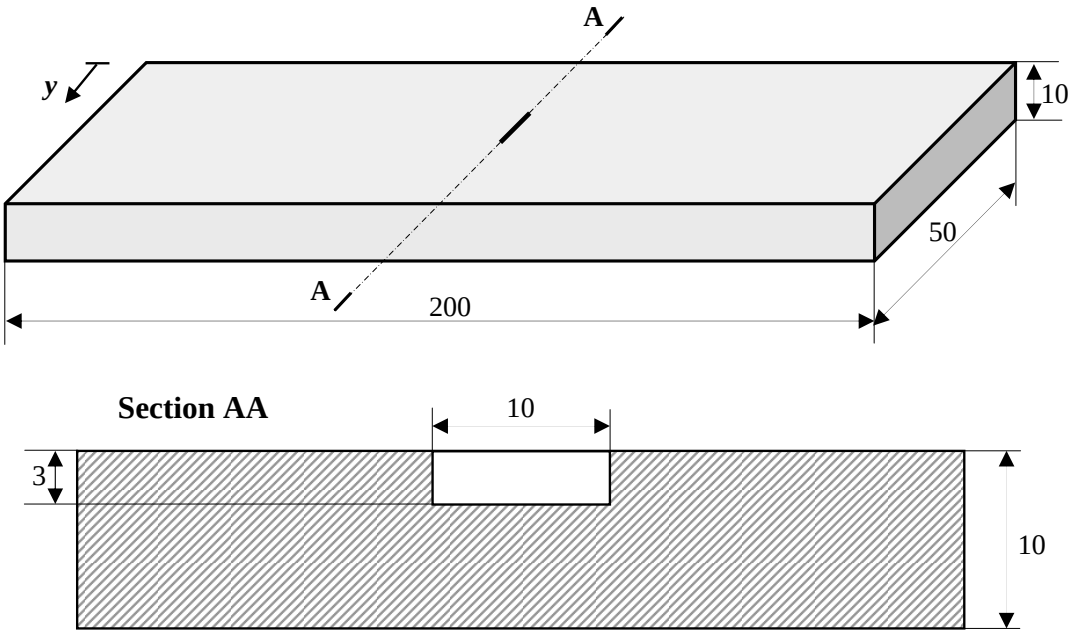

Figure 7.10: *Example of a specimen used in the tests.*

7.4 Reconstruction of notch profiles using a focused array

7.4.1 Notches of different shape

Tests were run on 200-mm long, 50-mm wide, 10-mm thick blocks of SS304; one of them was kept intact to serve as a reference (baseline), whereas notches of different shapes and sizes were machined on the other specimens, using EDM (Electrical Discharge Machining). As an example, a block with a 10-mm long, 3-mm deep rectangular notch is drawn in Fig. 7.10. The frequency of the currents used in the experiments was $f = 10.3$ Hz; as the standard penetration depth δ for SS304 at this frequency is larger than the thickness of the specimens, numerical simulations with the FE model were run on the unmodified geometry.

Fig. 7.11 shows the results of FE simulations and experimental measurements on the baseline and on three specimens with notches of different shapes (rectangular, triangular, circular arc) but identical length and maximum depth; it should be noted

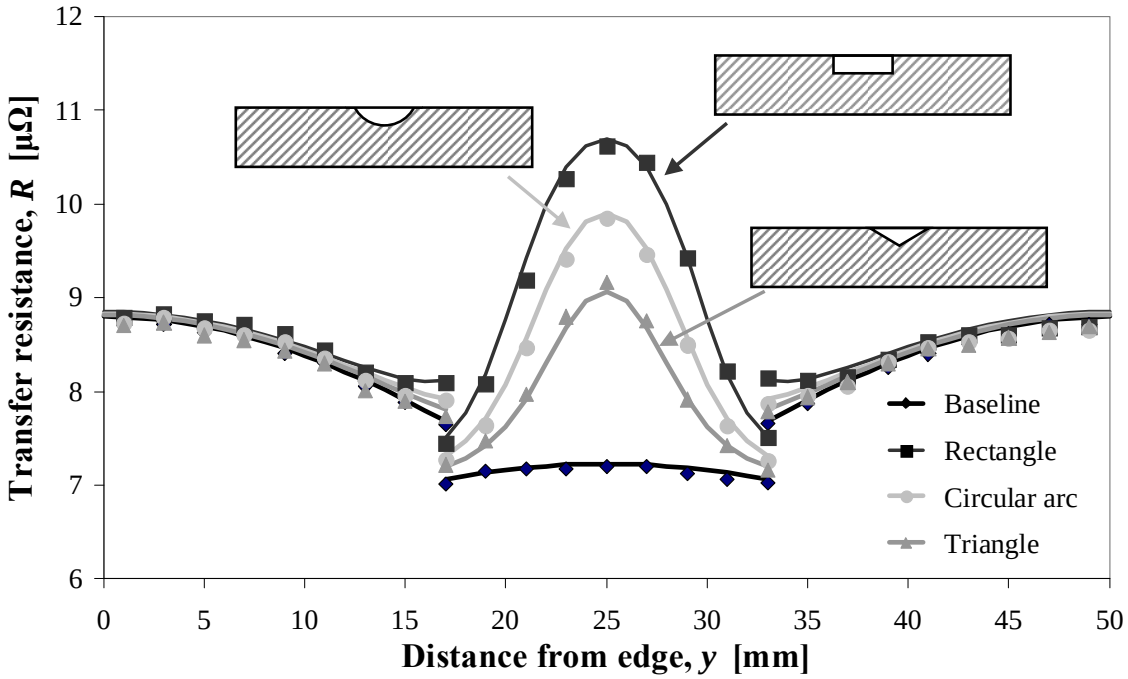

Figure 7.11: *FE predictions (lines) and measurements (symbols) at 10.3 Hz on a notch-free specimen and on specimens with 10-mm long, 3-mm deep notches of different shapes.*

that no focusing has been applied at this stage. Three array positions were required to cover the full block width, which explains the three groups of points in the graph for each specimen; the sudden jumps in the values are also due to the change in the position of the probe, and in particular of the outer electrode pair. Some variation would be expected across the array even in an infinitely wide undamaged plate, because the outer electrodes are fixed and only directly in line with the central pair of the array. This effect is predicted satisfactorily by the FE model, as is the much larger variation towards the edges of the specimen; both effects are removed once results relative to the baseline are considered.

As an example, the reconstructed profile of the triangular notch is shown in Fig. 7.12. At each measuring point the estimated depth is given by

$$d = T \cdot \frac{R - R_0}{R} \tag{7.4}$$

where T is the block thickness and R and R_0 are the transfer resistances measured on the notched specimen and on the baseline, respectively. This formula is easily derived assuming that at low frequency the potential drop (or equivalently the resistance) is

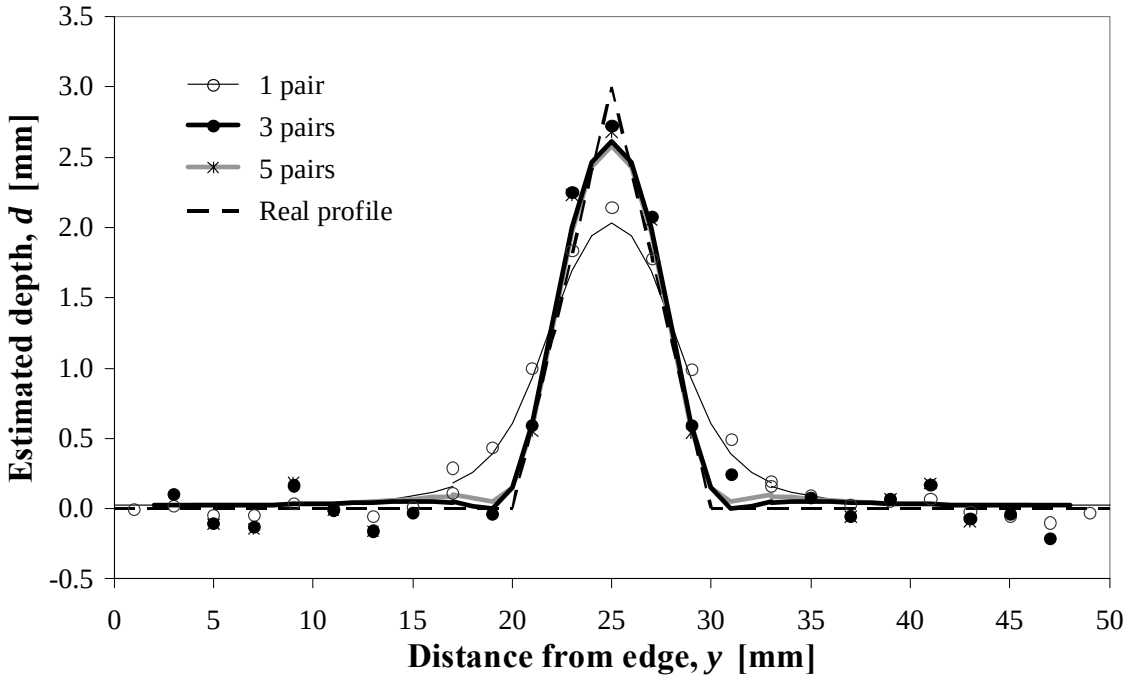

Figure 7.12: *Reconstructed profiles of a 10-mm long, 3-mm deep triangular notch using 1, 3 and 5 pairs of electrodes to focus currents. FE predictions (solid lines) and measurements (symbols) compared with the real profile (dashed line).*

inversely proportional to the remaining local thickness $T-d$ 'seen' by the current. It is therefore important that the lateral spreading of the current be small, as achieved by focusing. The results of Fig. 7.12 show that focusing the currents synthetically does in fact yield a very good reconstruction of the depth profile even for three electrode pairs. Note that both R and R_0 must be evaluated by using the same number of electrodes in Eq. 7.3 if focusing is used.

The reconstruction of the rectangular notch (see Fig. 7.13) is less satisfactory: focusing, while sharpening the representation of the step at the extremities of the notch, causes an overestimation of the maximum depth. Defects of such shape, however, are very unlikely to occur in practice; in fact, previous studies on this subject often made the assumption that cracks have a semi-circular or semi-elliptical shape (see for example [40] and [89]). A circular arc is therefore a fairer approximation of a real crack. The results for this notch are shown in Fig. 7.14: as for the triangular notch, the reconstruction is very good if focusing with three or five pairs.

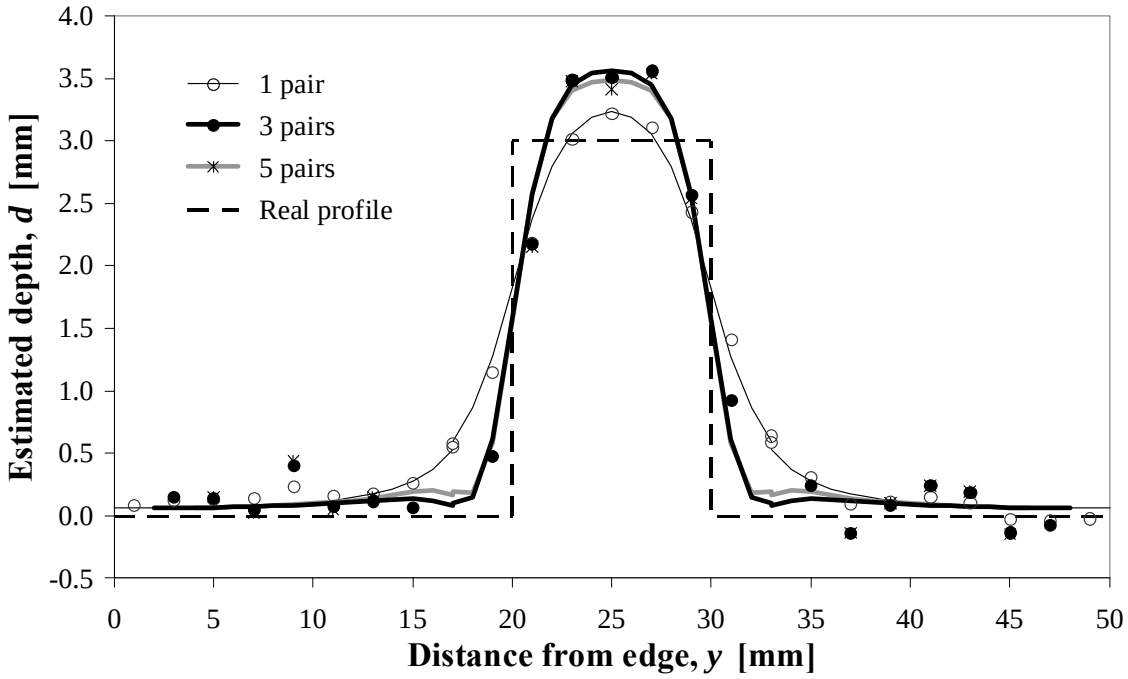

Figure 7.13: *Reconstructed profiles of a 10-mm long, 3-mm deep rectangular notch. FE predictions (solid lines) and measurements (symbols) compared with the real profile (dashed line).*

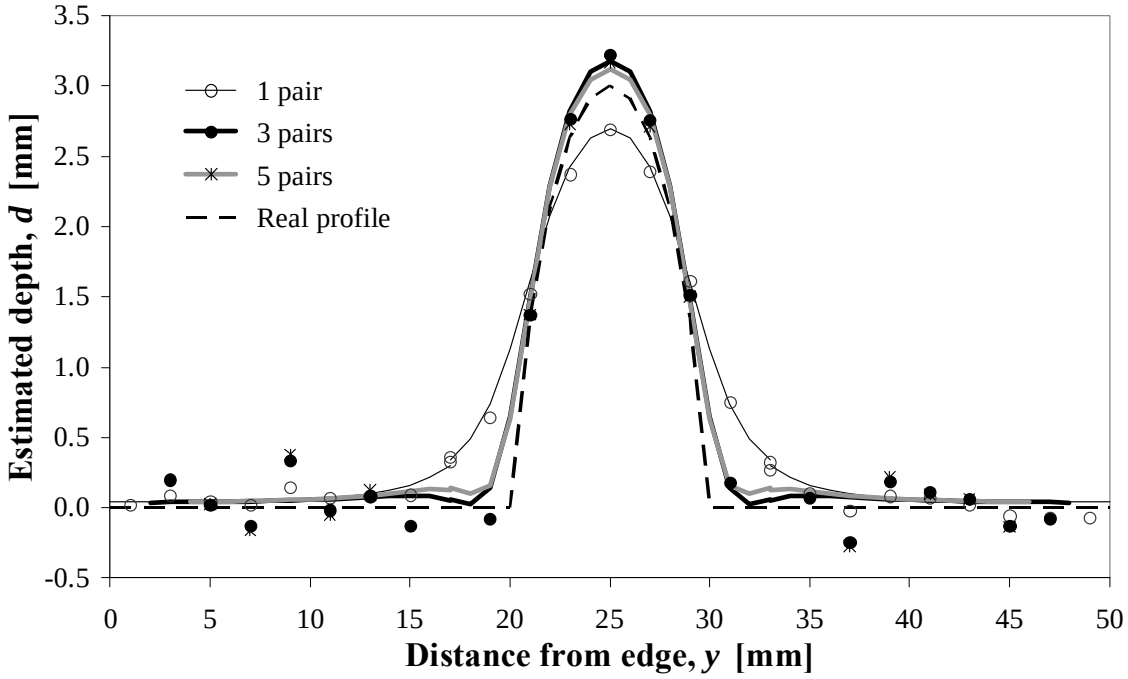

Figure 7.14: *Reconstructed profiles of a 10-mm long, 3-mm deep circular arc notch. FE predictions (solid lines) and measurements (symbols) compared with the real profile (dashed line).*

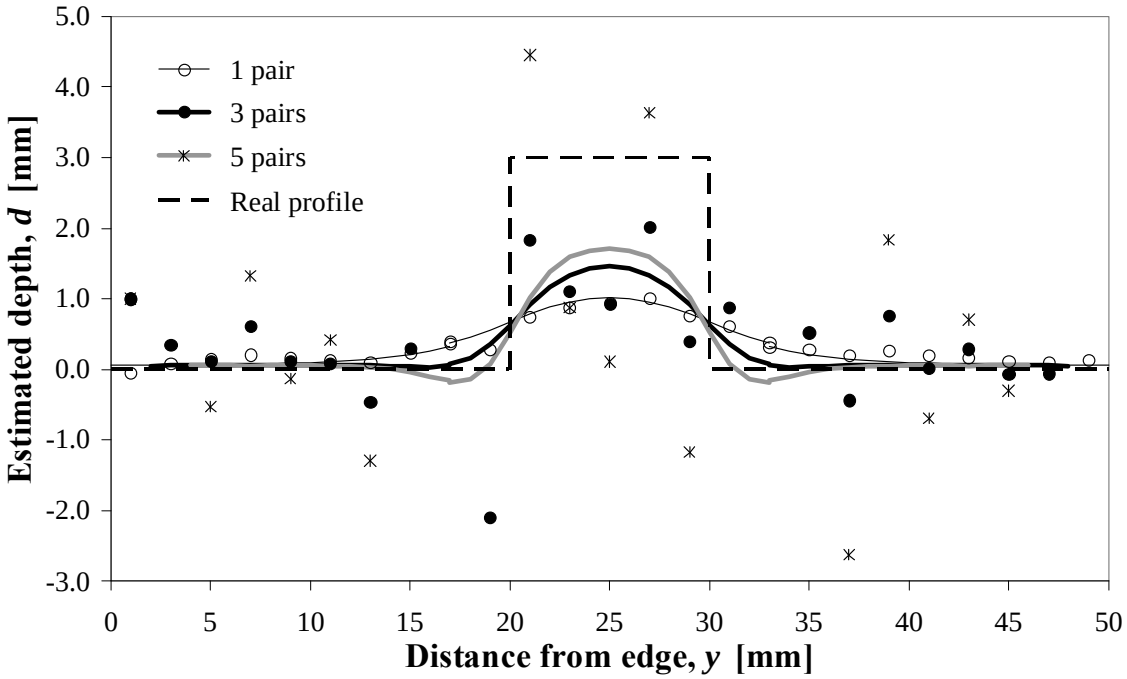

Figure 7.15: *Reconstructed profiles of a 10-mm long, 3-mm deep rectangular notch using a probe with larger distance between lines of inner electrodes ($2b = 10$ mm) and focusing with the current distributions of Fig. 7.6. FE predictions (solid lines) and measurements (symbols) compared with the real profile (dashed line).*

As a comparison, Fig. 7.15 shows the results obtained for the rectangular notch with the first-generation linear array probe, *i.e.* with a bigger spacing between the lines of sensing electrodes: it can be seen that the 'unfocused' reconstruction is of much lower quality than for the new probe with reduced spacing. Furthermore, the weightings of the injected currents used for the focusing in this case were those calculated for the normalised current densities of Fig. 7.6: the much larger scatter introduced by using these values for focusing is apparent.

7.4.2 Notches of different aspect ratio

Further tests were run on specimens having notches of similar shape and identical area but different aspect ratio. In particular, the triangular notch of Fig. 7.12 was compared with a shorter but deeper notch (6×5 mm as opposed to 10×3) and a longer but shallower one (15×2 mm); the results are shown in Fig. 7.16 and Fig. 7.17,

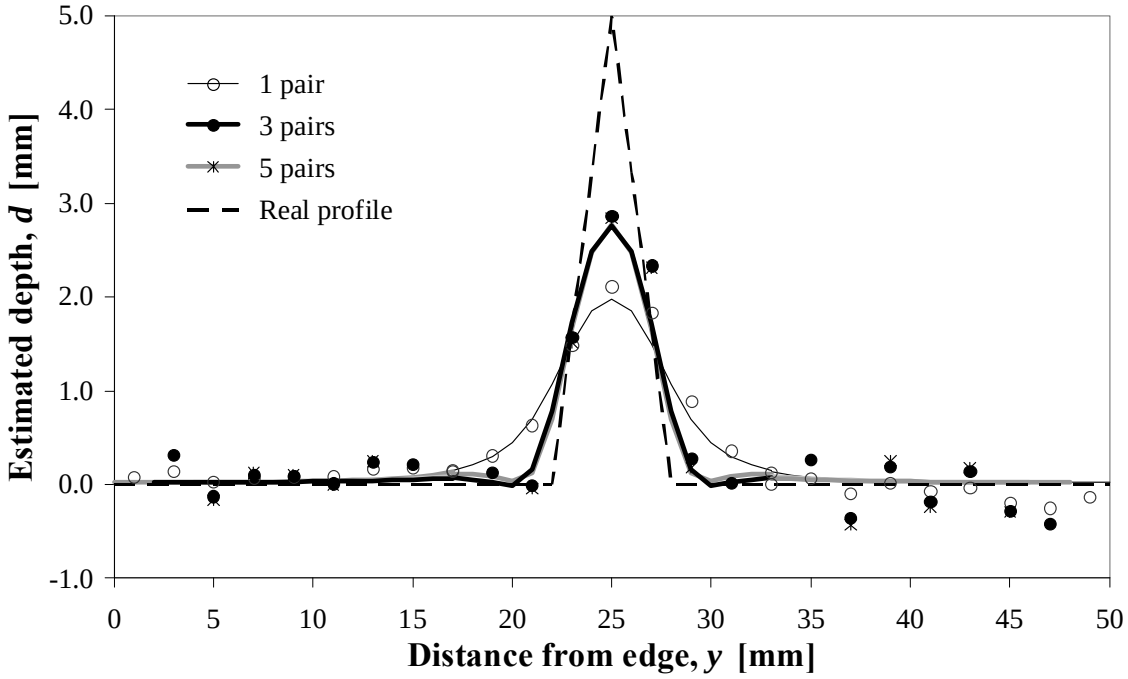

Figure 7.16: *Reconstructed profiles of a 6-mm long, 5-mm deep triangular notch. FE predictions (solid lines) and measurements (symbols) compared with the real profile (dashed line).*

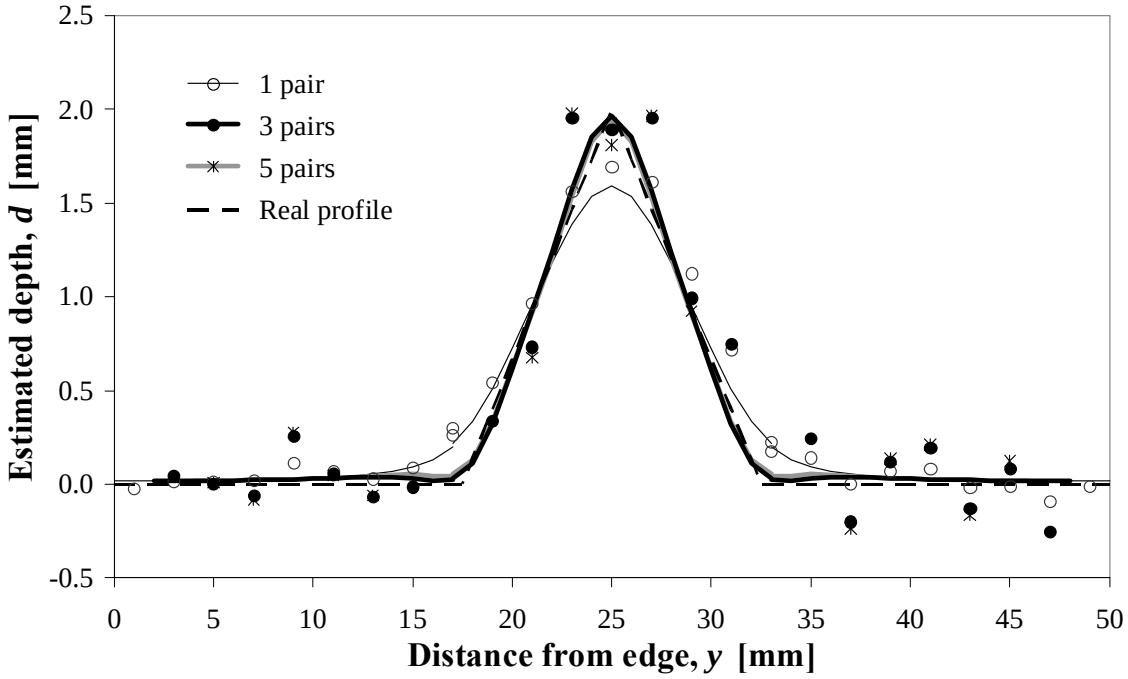

Figure 7.17: *Reconstructed profiles of a 15-mm long, 2-mm deep triangular notch. FE predictions (solid lines) and measurements (symbols) compared with the real profile (dashed line).*

respectively. The maximum depth of the deeper notch is underestimated by ∼40% even if focusing is used. Defects whose depth is almost equal to their length (or even larger) cannot be sized accurately by Potential Drop methods because currents will flow around their sides, rather than below them: this is an intrinsic limitation of PD techniques, but it should be mentioned that the geometry of real cracks is unlikely to be so sharp. On the other hand, focusing gives an excellent reconstruction of the depth profile of the shallower notch, whose aspect ratio is closer to those encountered in practice.

7.5 Conclusions

A linear array probe was developed which allows faster acquisition of Potential Drop data. Tests were run on EDM notches of various shapes and sizes; the agreement between the results of experimental measurements and numerical simulations with a FE model is excellent. The data thus obtained is then processed using a simple inversion formula which has been shown to give a good reconstruction of the notch depth profiles. It is important to note that no *a priori* assumption is made on the geometry of the defect; the reconstruction was found to work particularly well for shapes that approximate more closely the profile of real cracks.

In addition, it has been shown that synthetic focusing of the injected currents improves the results, as it sharpens the representation of rapid variations in the depth profile. The improvement can be noticed already when focusing with three pairs of electrodes, whereas extending the process to more pairs does not give any significant further contribution to the quality of the reconstruction.

Chapter 8

Potential Drop mapping

8.1 Introduction

In addition to the sizing of surface-breaking cracks as discussed in the previous Chapter, Potential Drop techniques can be used for the monitoring of corrosion and erosion on the inner surface of pipes, containers, pressure vessels, etc. [28, 63, 64, 66, 67, 97]. An array of electrodes is used to inject currents and measure voltages at multiple locations on the outer surface of the inspected region; the data are then combined to produce maps which give information on the position and size of defects. In order to achieve penetration of the currents through the entire thickness of the structure to be tested, the skin depth must be larger than the thickness of the specimen; therefore, the currents used for this application are low-frequency or even DC.

The DCPD systems by CorrOcean and by Rowan Technologies which were presented in Chapter 4 are examples of commercially available setups for remnant wall thickness monitoring that have been employed in the power generation industry. Unfortunately, very little quantitative information on the performance of these systems has been published. In [64] it is reported that corrosion in boilers at a power plant was successfully monitored over a period of 2.5 years, at the end of which the remaining wall thickness had decreased by about 30% in the most damaged areas;

the estimated spatial variations were slow, typically in the range of 1 mm/m.

In this Chapter an attempt will be made at assessing more systematically the capabilities of PD systems for such applications. In particular, the aim is to determine how accurately the maximum depth of a defect (or minimum remaining thickness) can be estimated as a function of the size and shape of the defect itself and of the geometry of the probe. An alternative formulation of the problem is to determine the minimum size of a defect whose depth can be estimated within a given degree of accuracy, and the probe configuration required to obtain this.

8.2 *Ad hoc* approximation for data inversion

Corrosion, like erosion, will be modelled as a loss of material, thus neglecting the presence of any products of chemical reactions, whose electrical conductivity is usually much smaller than that of the remaining tested material. Estimating the depth of an area of corrosion/erosion is then equivalent to determining the remnant thickness of the piece being inspected.

As mentioned in Chapter 5, an analytical expression for the voltage V between the measuring electrodes of a four-point probe when DC currents are injected on an infinite plate of uniform thickness t and conductivity σ was recently derived by Bowler [70]. For example, for an in-line probe with separation $2a$ between the outer electrodes and $2b$ between the inner electrodes, the voltage is

$$V = \frac{I}{\pi\sigma} \sum_{n=0}^{\infty} \epsilon_n \left[\frac{1}{\sqrt{(a-b)^2 + (2nt)^2}} - \frac{1}{\sqrt{(a+b)^2 + (2nt)^2}} \right], \tag{8.1}$$

where $\epsilon_0 = 1$ and $\epsilon_n = 2$ for $n \neq 0$.

As the thickness t of the plate increases, the potential drop between the two measuring electrodes tends to a constant value, determined by the distances between the electrodes:

$$V_{thick} = \frac{I}{\pi\sigma} \left[\frac{1}{a-b} - \frac{1}{a+b} \right] = \frac{I}{\pi\sigma} k_1. \tag{8.2}$$

This asymptotic value can be derived from Eq. 8.1 by taking the limit for $t \to \infty$. Bowler also showed that Eq. 8.1 has another asymptote for very thin plates:

$$V_{thin} = \frac{I}{\pi\sigma t} \ln \frac{a+b}{a-b} = \frac{I}{\pi\sigma} \frac{k_2}{t}. \tag{8.3}$$

Note that, in Eqs. 8.2 and 8.3, k_1 and k_2 are constants whose values depend exclusively on the geometry of the probe: two particular cases will be examined in the next Section.

An extension of these asymptotes allows us to write an approximate expression for V in the general case of a plate of finite thickness t:

$$V \approx [V_{thick}^{\beta} + V_{thin}^{\beta}]^{\frac{1}{\beta}} = \frac{I}{\pi\sigma} \left[k_1^{\beta} + \left(\frac{k_2}{t} \right)^{\beta} \right]^{\frac{1}{\beta}}, \tag{8.4}$$

where β is a parameter that can be fitted (*e.g.* with the least squares method) to minimise the difference between the approximate values calculated with this equation and the exact values given by Eq. 8.1.

As an example, Fig. 8.1 shows the voltage that would be measured for the injection of a unit current on an infinite plate of stainless steel 304 when using an in-line four-point probe in which all the electrodes are equally spaced by $s = 20$ mm. The two asymptotes are also shown on the same chart. It can be seen that the values given by Eq. 8.4 are indeed a very good approximation of those obtained with Eq. 8.1, as the two curves almost coincide: the difference between the two, plotted in Fig. 8.2 as a function of the plate thickness t, does not exceed 3% for $\beta = 3$. It is worth mentioning that here it was deliberately chosen to assign an integer value to β for simplicity; if this parameter were allowed to assume real values, then the maximum error could be reduced to just over 1% by setting $\beta = 3.33$ (determined by minimising the area under the curve of Fig. 8.2 with the least squares method).

The advantage over Eq. 8.1 offered by Eq. 8.4 is that the latter can be easily inverted to give

$$t = \frac{k_2}{\left[\left(\frac{\pi\sigma V}{I} \right)^{\beta} - k_1^{\beta} \right]^{\frac{1}{\beta}}} : \tag{8.5}$$

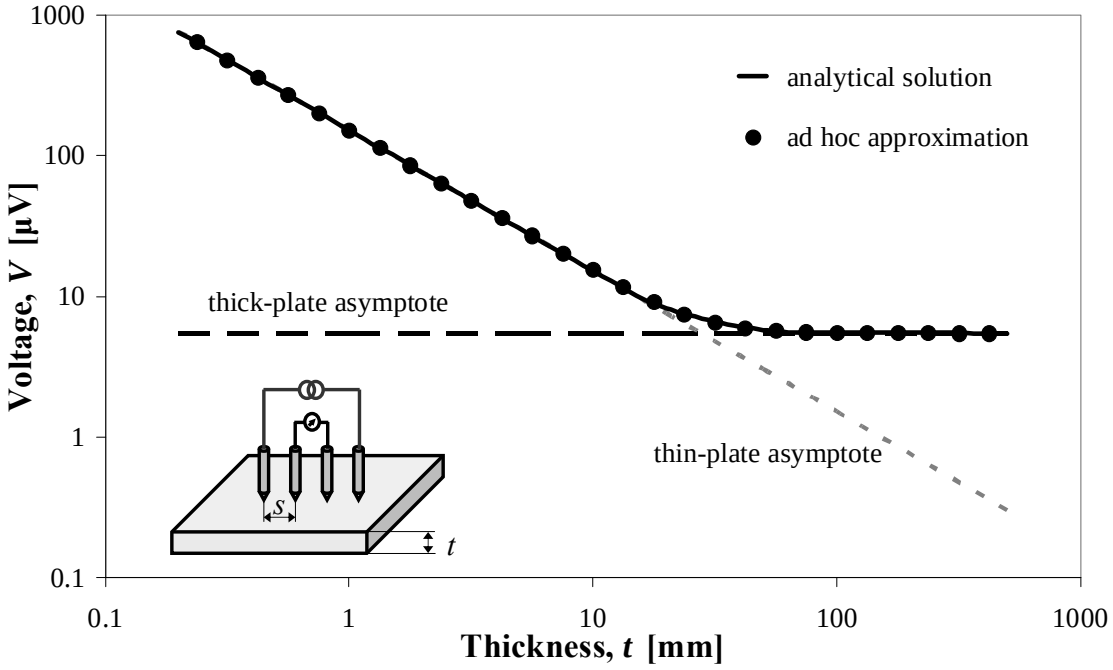

Figure 8.1: *Voltage between the measuring electrodes of an equispaced in-line four-point probe, with spacing $s = 20$ mm, for the injection of a unit current on an infinite SS304 plate of variable thickness t: predictions with the analytical formula of Eq. 8.1 (line) and with the approximation of Eq. 8.4 (symbols).*

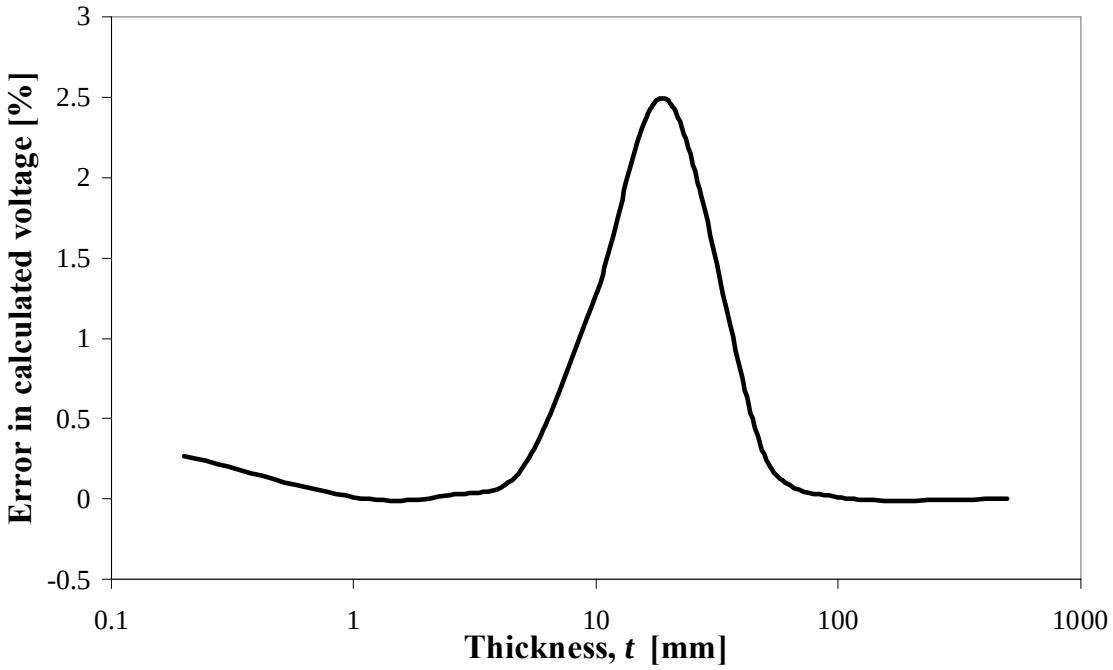

Figure 8.2: *Difference between the voltage calculated with Eq. 8.4 and the exact values given by Eq. 8.1 for an equispaced in-line four-point probe, as a function of plate thickness.*

this formula can be used for the inversion of Potential Drop data, *i.e.* to estimate the thickness t of a tested plate of known conductivity σ from measurements of the voltage difference V between two points on its surface. It is worth emphasising that k_1, k_2, and ultimately β, can be calculated in advance for a given arrangement of electrodes, as they depend only on the probe geometry. In the presence of an infinitely large corrosion/erosion region of uniform depth d on the bottom surface of the plate, Eq. 8.5 will give the estimated remaining thickness $(T - d_{est})$, where T is the thickness of the plate in its undamaged state; the defect depth can then by obtained simply by rewriting Eq. 8.5 as

$$d_{est} = T - \frac{k_2}{\left[\left(\frac{\pi\sigma V}{I}\right)^{\beta} - k_1^{\beta}\right]^{\frac{1}{\beta}}}. \tag{8.6}$$

However, in the practical case of a defect of finite length L and width W, the potential drop V will be smaller, since part of the current can flow around the defect; this will cause an underestimation of the defect depth. It is therefore necessary to correct for the finite size of the defect.

Numerical simulations with the FE model described in Chapter 6 and validated against the analytical solution for an undamaged plate given in [70] were run for this purpose, considering defects of various lengths L, widths W and depths d located at the centre of the bottom surface of a 360-mm long, 360-mm wide, 10-mm thick SS304 plate, as in the schematic of Fig. 8.3.

8.3 Geometry of the array probe

8.3.1 Standard configuration

The geometry of the array probe initially considered was a matrix of equally spaced electrodes, as shown in Fig. 8.4. A set of four horizontally, vertically or diagonally consecutive electrodes is used at a time; it will be assumed for simplicity that, in each set of four, currents are injected at the two outer electrodes and voltages

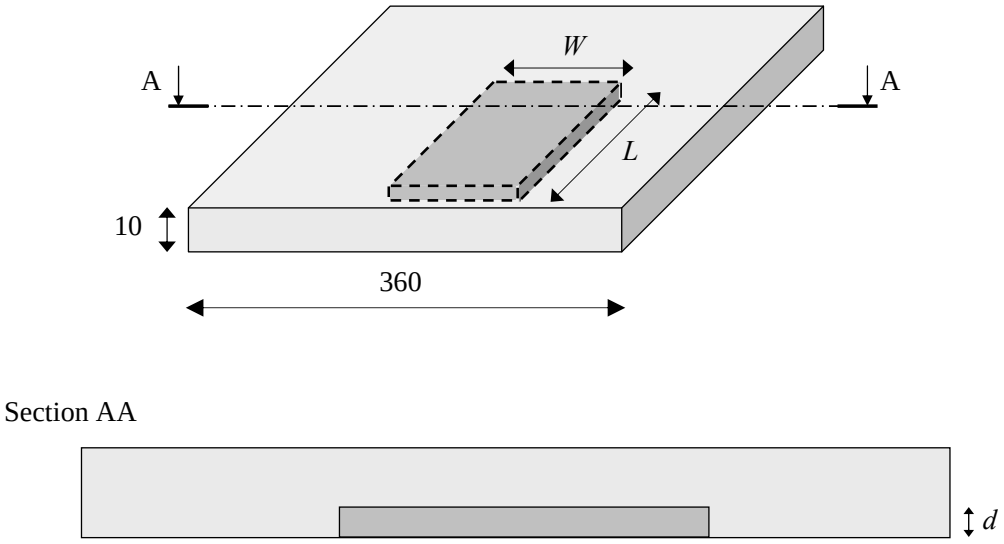

Figure 8.3: *Geometry of the SS304 plate modelled in the FE simulations. Note that the defect is centred on the bottom surface of the plate, not close to the edge as it may appear: this is only an optical effect due to the perspective.*

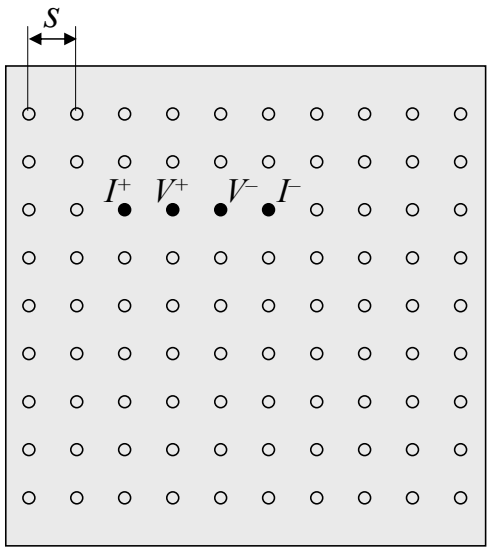

Figure 8.4: *Schematic of array probe using the standard configuration: each electrode can be used for current injection or voltage measurement.*

measured at the two inner ones, as in the example of Fig. 8.4, although, as discussed in Section 7.2, swapping the roles of the electrodes would give identical results. The voltages measured with each set are then combined to reconstruct a map of remaining thickness, or equivalently of defect depth. This arrangement of electrodes is employed in existing commercial systems (*e.g.* the system developed by Rowan Technologies, [33, 64]) and will be referred to as 'standard configuration'. Here the interest is to define the optimum spacing s between the electrodes.

For this configuration, substituting $2a = 3s$ and $2b = s$ in Eqs. 8.2 and 8.3, the expressions of the constants k_1 and k_2 assume a particularly simple form:

$$k_1 = \frac{1}{2s} \tag{8.7}$$

and

$$k_2 = \ln 2. \tag{8.8}$$

The exact optimum value of β, the remaining parameter in Eq. 8.6, depends on the probe spacing and should therefore be determined for each value of s; however, for all electrode spacings in the range considered here, setting $\beta = 3$ is a very good approximation.

In order to separate the effects of finite length and finite width of a defect, a first batch of FE simulations were run on infinitely wide defects of variable finite length L: the results obtained for 3-mm (= 30%) deep defects and different probe spacings are shown in Fig. 8.5. The depth of long defects is estimated accurately with Eq. 8.6 independent of the probe spacing s, whereas the underestimation of shorter defects is more pronounced for bigger values of s; on the other hand, a reduced spacing implies that a considerably larger number of electrodes would be required to cover a given area. A compromise could be reached with a spacing of about twice the plate thickness ($s = 2T$).

However, if infinitely long defects of finite width W are considered, then the voltage measured between the central pair of electrodes, and hence the depth estimated using Eq. 8.6, does not increase monotonically with the defect width. As shown in

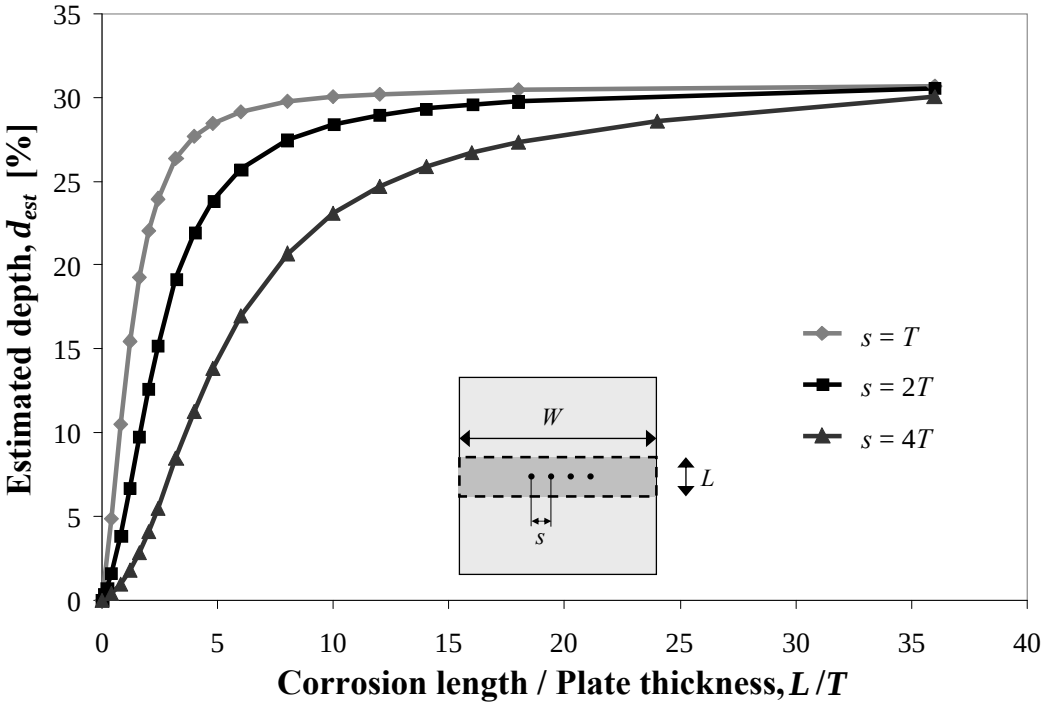

Figure 8.5: *Maximum estimated depth as a function of defect length for an infinitely wide, 30% deep defect, using the standard configuration with three different probe spacings, s.*

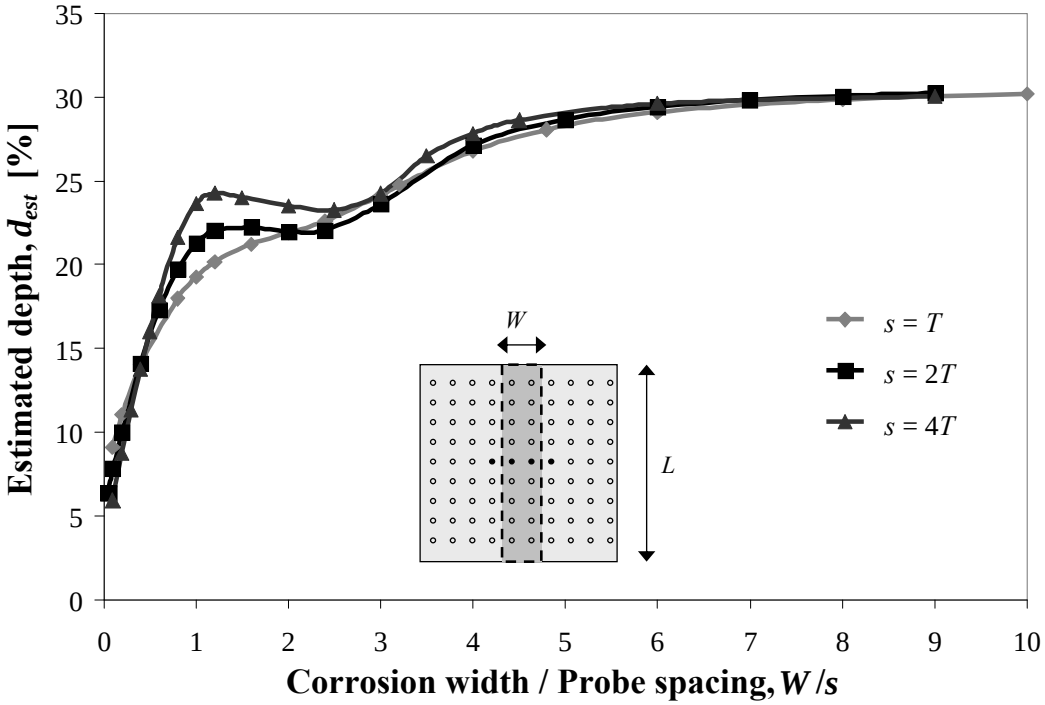

Figure 8.6: *Maximum estimated depth (as fraction of plate thickness) as a function of defect width (in multiples of the probe spacing) for an infinitely long, 30% deep defect, using the standard configuration with three different probe spacings, s.*

Fig. 8.6, the non-monotonic behaviour occurs for $s \leq W \leq 3s$, *i.e.* when the defect extends between the outer (current) and the inner (voltage) electrodes. The reason for this apparently surprising phenomenon is that the presence of an area of reduced thickness, and therefore higher electrical resistance, between the injecting electrodes alters the distribution of the currents, forcing them to spread out in the y direction (see the schematics of Fig. 8.7): the decrease in the density of current lines around the pair of electrodes aligned with the injection points (V^+ and V^- in Fig. 8.7*b*) translates in a reduction of the voltage measured between them; on the other hand, a slight increase can be observed in the potential drop between electrodes above or below the central pair (such as V_1^+ and V_1^-). This effect is less pronounced for smaller values of the probe spacing s, because the fraction of current flowing in the bottom part of the plate, and therefore affected by the presence of a defect, is relatively small if the distance between the injecting electrodes is comparable with the plate thickness T.

As a consequence of this, any defect narrower than about three times the electrode spacing (*i.e.* $W < 6T$ if using $s = 2T$) cannot be sized reliably using this probe configuration. Note that, while Fig. 8.6 suggests that a monotonic relationship between the measured voltage and the defect width could be obtained by using a

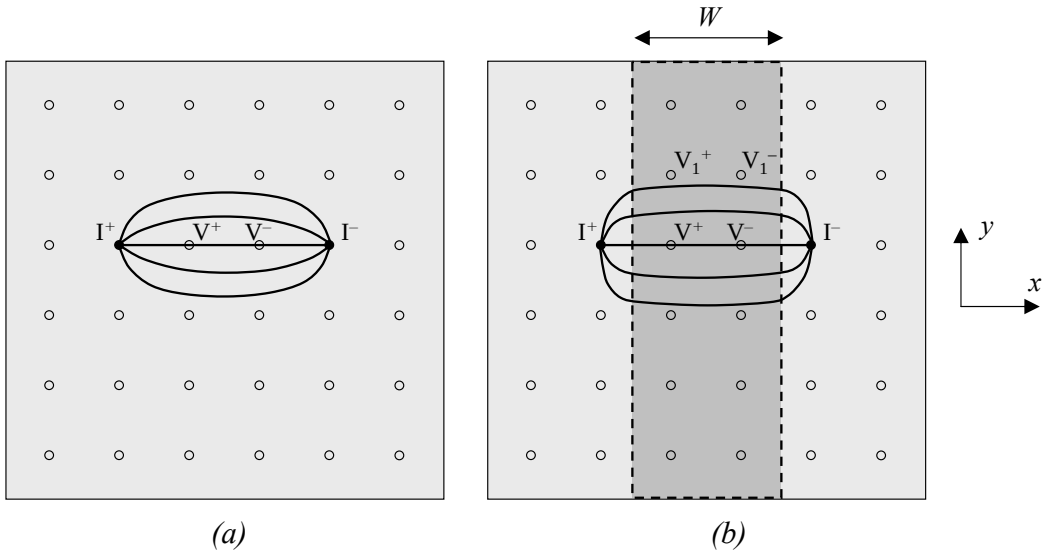

Figure 8.7: *Schematic of current distribution (a) in an intact plate, (b) in a plate with an infinitely long corrosion of width W.*

probe with a spacing $s \leq T$, this solution is in fact not viable, not only because of the large number of electrodes that would be needed, but also because the penetration of currents through the thickness, and therefore the sensitivity to corrosion/erosion on the far side, would be reduced.

8.3.2 Adjacent configuration

From the results just discussed it appears that bringing the voltage measurement electrodes closer to the current injection electrodes would be beneficial. The resulting arrangement, shown in Fig. 8.8, will be referred to as 'adjacent configuration'. In the following, the term 'pair' will be used to indicate one current electrode and its adjacent voltage electrode. As in the standard configuration, four electrodes at a time (two pairs in horizontal or vertical direction) are used to collect the data which will then be used for the reconstruction, and reciprocity ensures that the measured voltages do not change if the current and voltage electrodes are reversed.

The separation between the two electrodes in a pair was set to $\lambda = 2$ mm throughout this work, but it could be easily optimised; here the focus is rather on determining

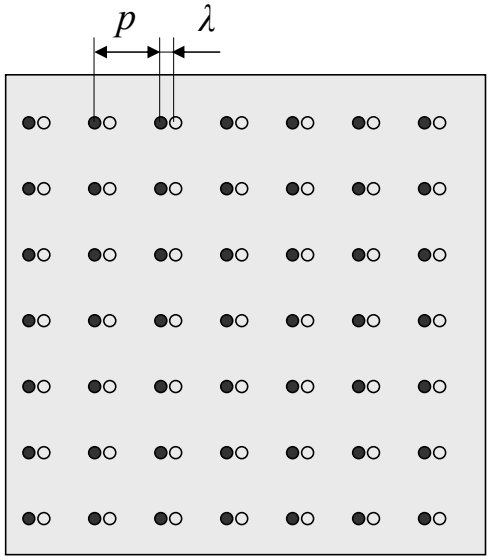

Figure 8.8: *Schematic of array probe using the adjacent configuration: solid and empty circles indicate current and voltage electrodes, respectively.*

an optimal value for the pitch p between any two current (or voltage) electrodes. From [70], the DC potential drop for this probe geometry on an undamaged infinite plate of thickness t is

$$V = \frac{I}{2\pi\sigma}\sum_{n=0}^{\infty}\epsilon_n\left[\frac{2}{\sqrt{\lambda^2+(2nt)^2}}+ \right. \\ \left. -\frac{1}{\sqrt{(p+\lambda)^2+(2nt)^2}}-\frac{1}{\sqrt{(p-\lambda)^2+(2nt)^2}}\right], \tag{8.9}$$

where $\epsilon_0 = 1$ and $\epsilon_n = 2$ for $n \neq 0$; this expression is different from Eq. 8.1 because of the different topology of the probe. The asymptotes are

$$V_{thick} = \frac{I}{\pi\sigma}\left[\frac{1}{\lambda}-\frac{p}{p^2-\lambda^2}\right], \tag{8.10}$$

$$V_{thin} = \frac{I}{\pi\sigma t}\ln\sqrt{\frac{p^2}{\lambda^2}-1}, \tag{8.11}$$

hence the values taken by the constants k_1 and k_2 in Eq. 8.6 are:

$$k_1 = \frac{1}{\lambda}-\frac{p}{p^2-\lambda^2}, \tag{8.12}$$

$$k_2 = \ln\sqrt{\frac{p^2}{\lambda^2}-1}. \tag{8.13}$$

The value of β, the other parameter in Eq. 8.6, also depends on p and λ; choosing $\beta = 2$, as was done to obtain the results presented here, gives a maximum error of less than 4% for all values of probe pitch considered in this work.

FE simulations showed that the voltage measured with this alternative array configuration (and thus the estimated depth) does increase monotonically not only with the length of the flaw, but also with its width, as shown in Fig. 8.9 for the same infinitely long, 3-mm (30%) deep defects of Fig. 8.6. The simple shape of these curves suggests that the underestimation of the depth of small defects can be corrected for if a reasonable estimate of the defect width could be obtained. As may be expected, this underestimation is more pronounced for probes with a larger pitch p; on the other hand, larger values of p also yield more accurate estimates of the depth of large defects, as confirmed in Fig. 8.10 for defects of infinite length and width and variable depth. A compromise must therefore be reached, depending on

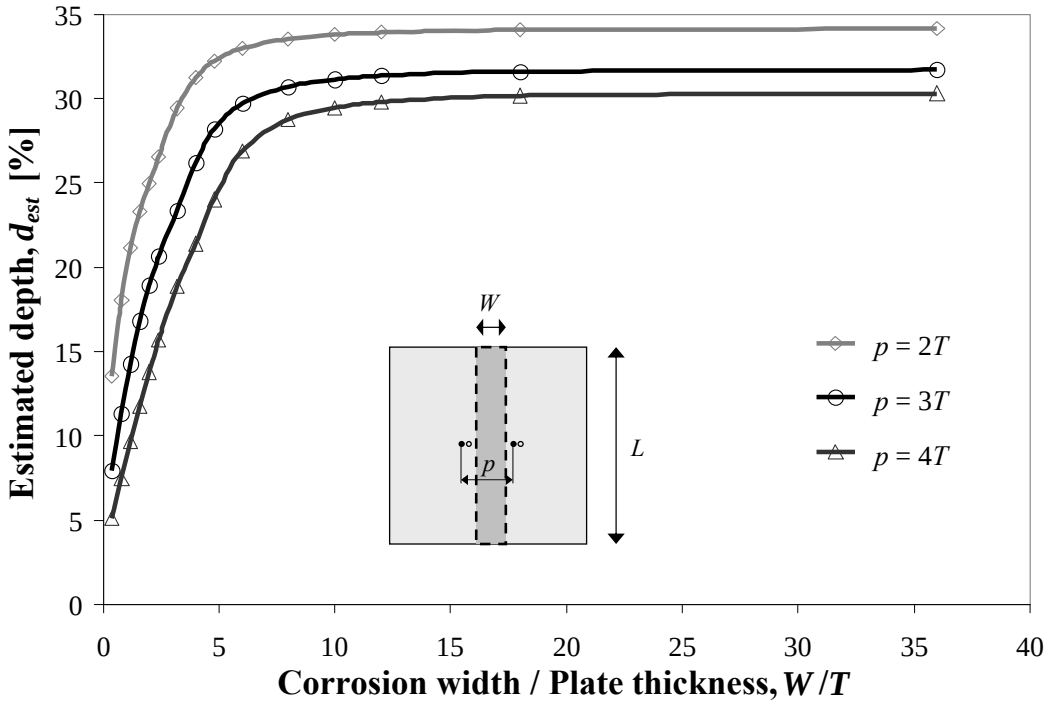

Figure 8.9: *Maximum estimated depth as a function of defect width for an infinitely long, 30% deep defect, using the adjacent configuration with three different probe pitches, p.*

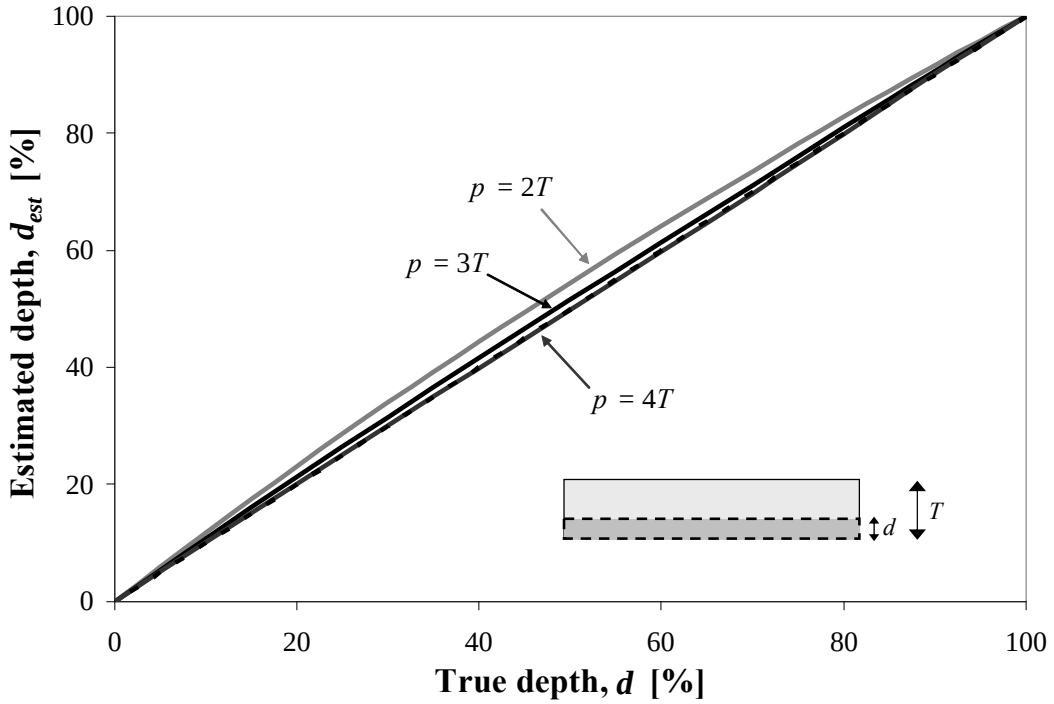

Figure 8.10: *Maximum estimated depth d_{est} versus true depth d for defects of infinite length and width, using the adjacent configuration with three different probe pitches, p. The dashed line (almost hidden behind the line for $p = 4T$) indicates the ideal case $d_{est} = d$.*

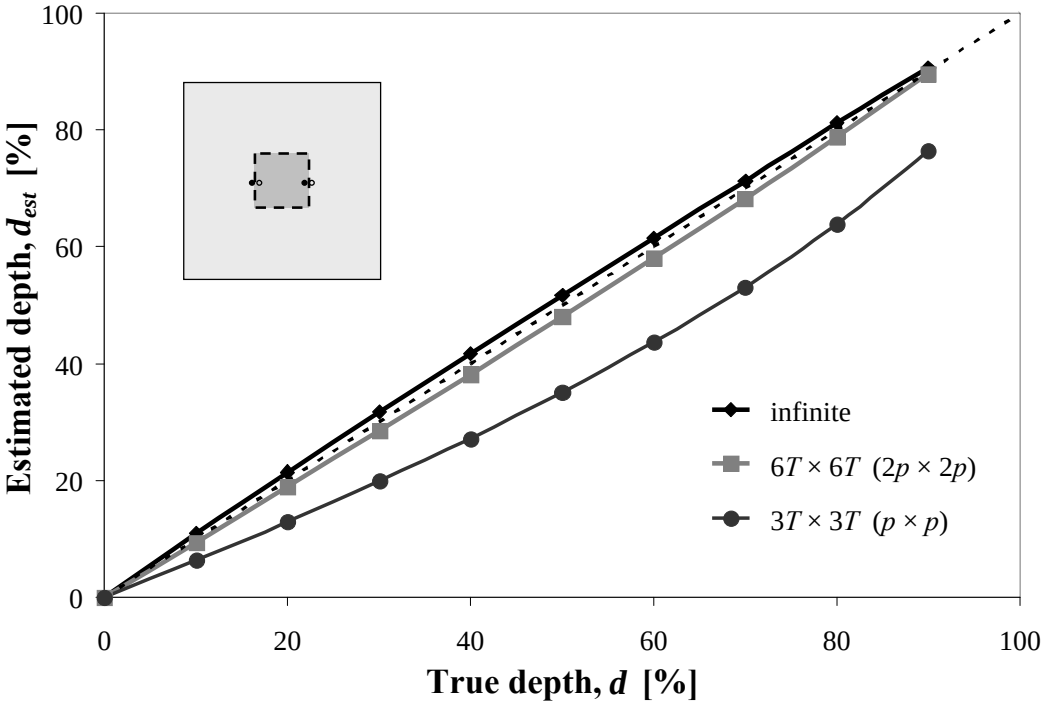

Figure 8.11: *Maximum estimated depth d_{est} versus true depth d for square defects of three different sizes, using the adjacent configuration with a probe pitch $p = 3T$. The dashed line indicates the ideal case $d_{est} = d$.*

the accuracy required and on the dimensions of the smallest defect that should be reliably sized; a probe pitch $p = 3T$ was chosen for the remainder of this work.

The combined effect of finite length and width can be seen in Fig. 8.11, which shows the estimated depth d_{est} (given by Eq. 8.6) for square defects of different side lengths as a function of the true depth d, for a probe with adjacent configuration and pitch $p = 3T$. The estimate is accurate for defects of plan size $6T$, or twice the probe pitch; for smaller defects, correction factors could be applied if the length and width of the defect could be estimated from the array data.

8.4 Maps of corrosion: numerical and experimental results

For the experimental tests, a flat-bottomed, 60-mm sided square defect of depth $d = 3$ mm was machined at the centre of a 500×500×10 mm SS304 plate. Based on the results of the FE simulations, it was decided to build an array probe exploiting the adjacent configuration with a pitch $p = 30$ mm. The probe, pictured in Fig. 8.12, had 16 pairs of electrodes arranged in four rows. The setup described in Chapter 3 was used, with the addition of four Stanford Research SIM925 octal four-wire multiplexers: two of these were in fact used as demultiplexers to drive the current electrodes, as explained in Section 7.2, while the other two were used to multiplex the voltages.

Low-frequency currents (10 Hz) were injected in the material. At this frequency the standard depth of penetration δ for stainless steel, calculated with Eq. 2.1, is much larger than the thickness T of the specimen, so it can be safely assumed that the hypothesis of a DC regime, under which Eq. 8.9 was derived, is satisfied to very good accuracy.

Data are acquired by injecting small currents (around 130 mA) between two hor-

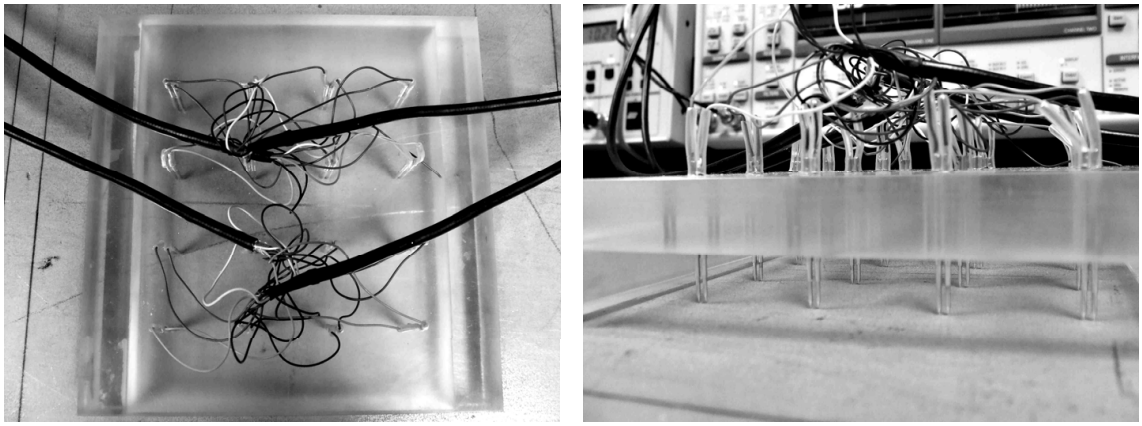

(a) *(b)*

Figure 8.12: *Photographs of the array probe used for the experiments: views (a) from the top and (b) from the side.*

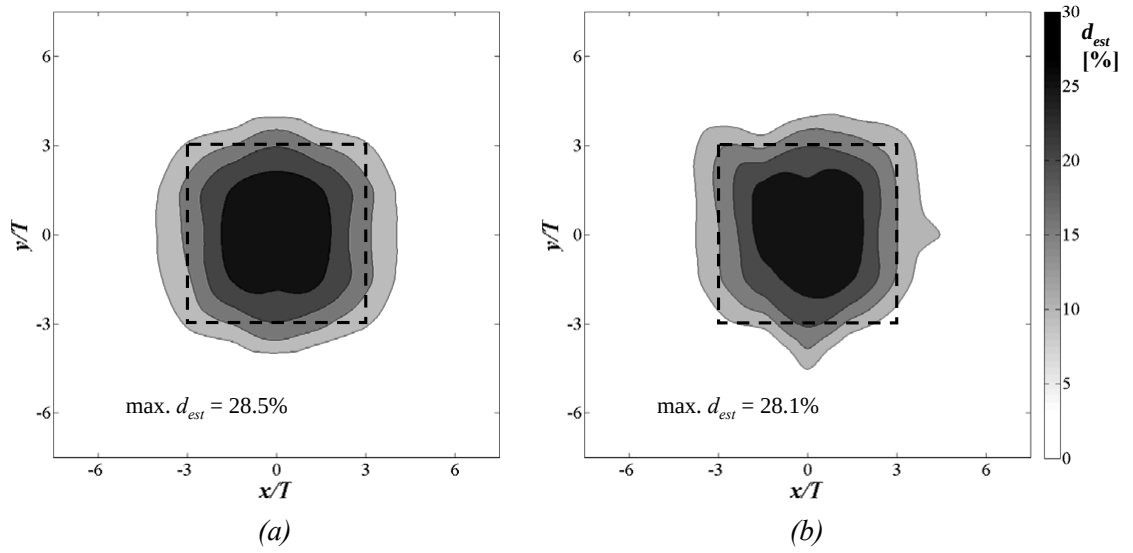

Figure 8.13: *Maps of estimated depth for a 30% deep, 60-mm sided square defect on a 500×500×10 mm SS304 plate, using the adjacent configuration with a probe pitch $p = 3T$. Probe in position (C) relative to defect centre (see Fig. 8.16). Reconstructions from (a) results of FE model, (b) experimental measurements. The dashed square indicates the real position of the defect.*

izontally or vertically consecutive current electrodes at a time and measuring the voltages between the electrodes adjacent to the injection points. The local estimated depth is then calculated for each set using Eq. 8.6, and interpolation between the reading points finally results in the map of Fig. 8.13*b*. This can be compared with the map of Fig. 8.13*a*, obtained from the results of the FE simulations. The agreement between numerical and experimental results is very good; the position of the defect is reconstructed correctly, and the maximum estimated depth (28.5% with the FE data, 28.1% with the experimental data) is encouragingly close to the real depth (30%), even though no correction factors have been applied for the finite size of the defect.

It is found that a quick, reasonable estimate of the defect length or width can be obtained simply with a 6-dB drop criterion, *i.e.* by taking a horizontal or vertical section through the map of Fig. 8.13 (not necessarily through the centre of the defect) and evaluating the distance between the two points at which the estimated depth is half of the maximum along that section, as shown in Figs. 8.14 and 8.15.

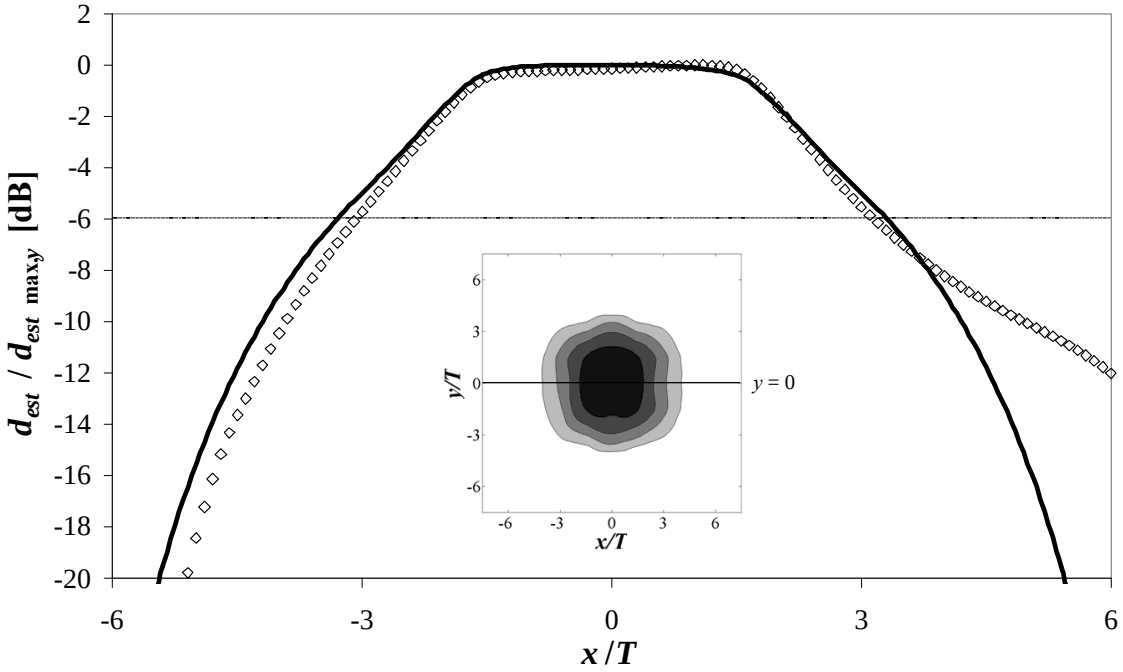

Figure 8.14: *Variation of estimated depth along section $y = 0$ of the maps of Fig. 8.13: numerical (lines) and experimental values (symbols), scaled to the respective maximum along the section.*

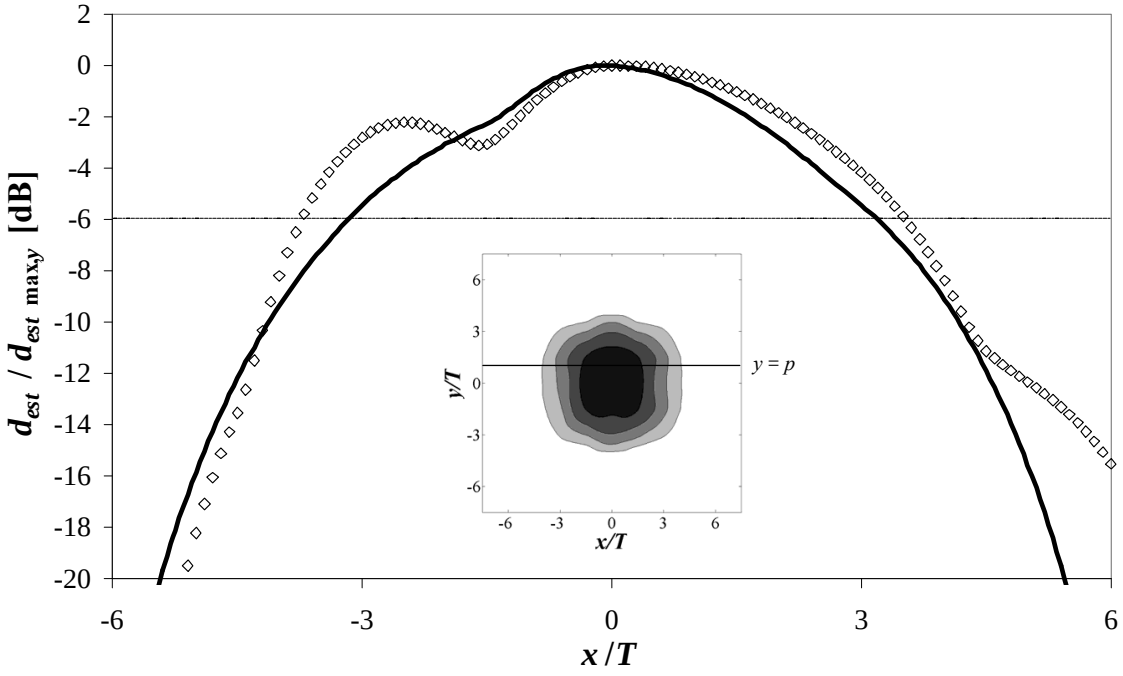

Figure 8.15: *Variation of estimated depth along section $y = p$ of the maps of Fig. 8.13.*

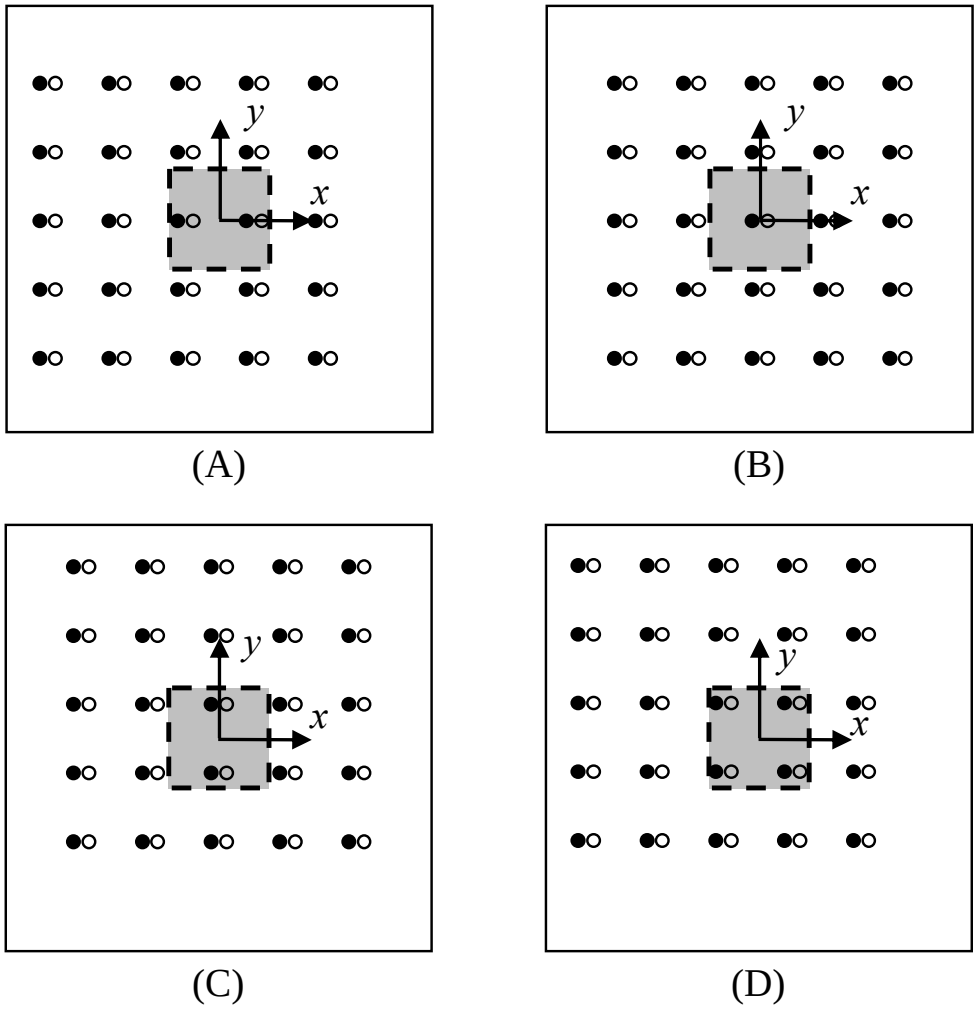

Figure 8.16: *Possible positions of the array probe relative to the defect centre.*

This suggests that the introduction of correction factors to compensate for the underestimation caused by the finite size of defects would be straightforward.

For a square defect such as the one considered here, the position of the array probe relative to the defect centre can vary between four extreme cases, represented in Fig. 8.16: the defect centre can coincide with (A) the centre of a horizontal set of electrodes, (B) an electrode pair, (C) the centre of a vertical set of electrodes, or (D) the centre of a diagonal set. The maps of Fig. 8.13 were obtained with the array in position (C), but the other positions give very similar results, as can be seen in Figs. 8.17–8.19. In all cases the maximum estimated depth is close to the actual value, varying between 26.2% and 28.6%. It can therefore be concluded that the quality of the results is not significantly affected by the position of the array

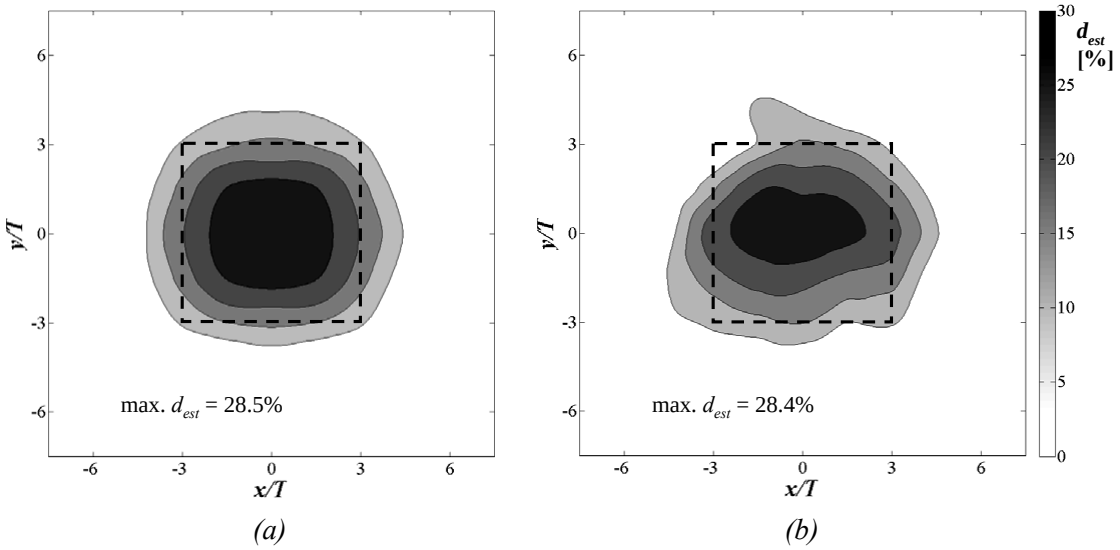

Figure 8.17: *Maps of estimated depth for a 30% deep, 60-mm sided square defect on a 500×500×10 mm SS304 plate, using the adjacent configuration with a probe pitch $p = 3T$. Probe in position (A) relative to defect centre (see Fig. 8.16). Reconstructions from (a) results of FE model, (b) experimental measurements.*

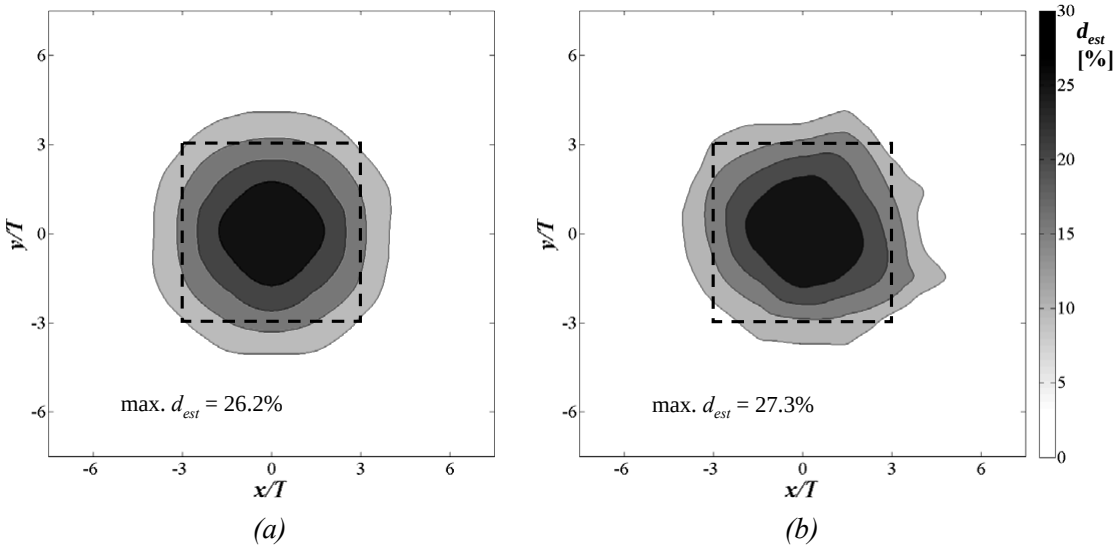

Figure 8.18: *Maps of estimated depth for a 30% deep, 60-mm sided square defect on a 500×500×10 mm SS304 plate, using the adjacent configuration with a probe pitch $p = 3T$. Probe in position (B) relative to defect centre (see Fig. 8.16). Reconstructions from (a) results of FE model, (b) experimental measurements.*

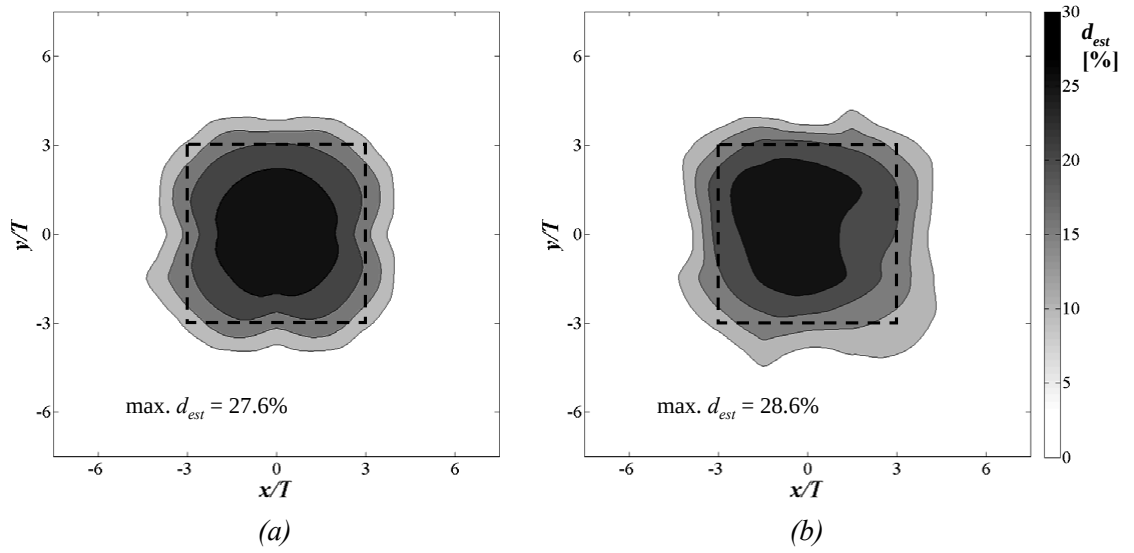

Figure 8.19: *Maps of estimated depth for a 30% deep, 60-mm sided square defect on a 500×500×10 mm SS304 plate, using the adjacent configuration with a probe pitch $p = 3T$. Probe in position (D) relative to defect centre (see Fig. 8.16). Reconstructions from (a) results of FE model, (b) experimental measurements.*

probe relative to the defect, which will generally be unknown in applications of this technique in the field.

A comparison of the corrosion maps reconstructed from the FE data obtained on the same damaged SS304 plate with the two array probe configurations discussed in this Chapter is shown in Fig. 8.20. It can be observed that the standard configuration, while giving a very good reconstruction of the shape of the defect, underestimates considerably its depth (the maximum value predicted is 22.1%, compared to 28.5% with the adjacent configuration and to the real value of 30%): as discussed in the previous Section, this is due to the non-monotonic variation of the measured voltage with defect width.

Finally, it should be mentioned that similar results were obtained when modelling scalloped rather than flat-bottomed defects. As an example, let us consider a corrosion region whose square plane size varies linearly between 66 mm at the bottom surface of the plate and 54 mm at the maximum defect depth of 3 mm, as shown in the schematic of Fig. 8.21: except for the case of pitting corrosion, the spatial

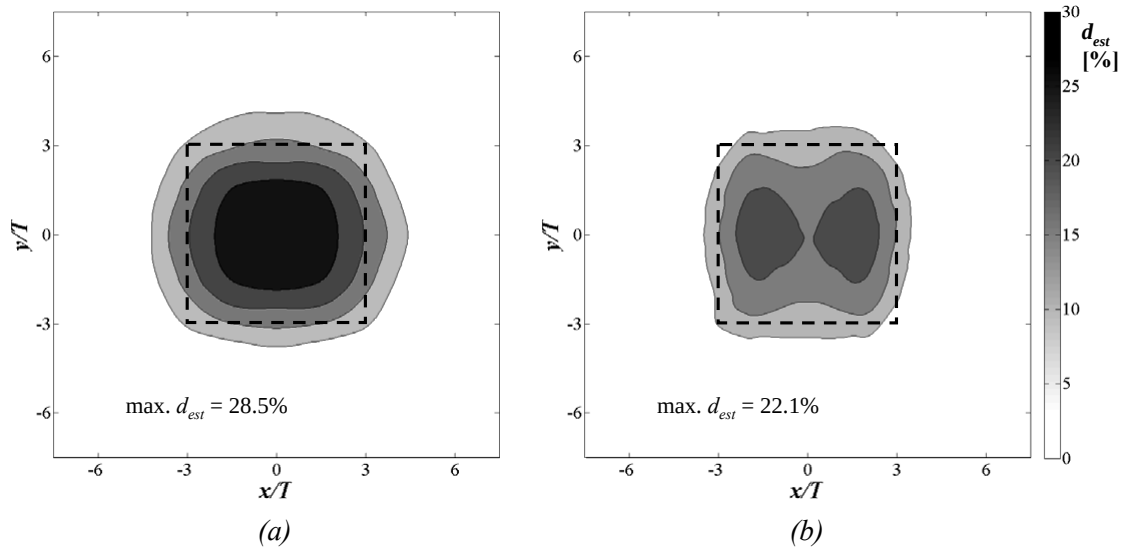

Figure 8.20: *Maps of estimated depth for a 30% deep, 60-mm sided square defect on a 500×500×10 mm SS304 plate. Reconstructions from results of the FE model using (a) the adjacent configuration with a probe pitch $p = 3T$, probe in position (A) relative to defect centre (see Fig. 8.16); (b) the standard configuration with a probe spacing $s = 2T$.*

variations occurring in practical applications are not expected to be significantly sharper than this. The reconstructed maps (obtained from FE data with the adjacent configuration for the four possible positions of the probe considered in Fig. 8.16) are shown in Fig. 8.22. It was found that the reconstruction of a scalloped defect is almost identical to that of a flat-bottomed defect having the same depth and a plane size equal to the average plane size of the scalloped defect (60 mm in the example), as can be noticed if the maps of Fig. 8.22 are compared with those of Figs. 8.13*a* and 8.17*a*–8.19*a*. Note also that the maximum estimated depth is close to the real depth in all cases.

8.5 Conclusions

A closed analytical expression for the estimation of remaining thickness from Potential Drop measurements was derived from an asymptotic extension of a formula given in the literature. This expression was used in the study of suitable array configurations for mapping of corrosion and erosion.

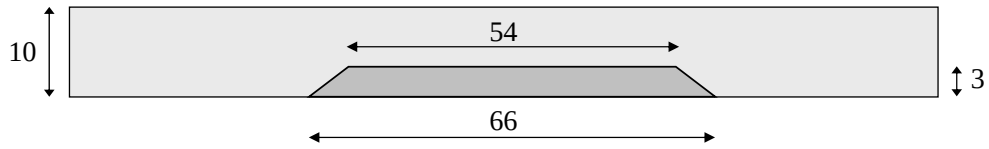

Figure 8.21: *Section of plate with a scalloped defect (compare with the section of Fig. 8.3).*

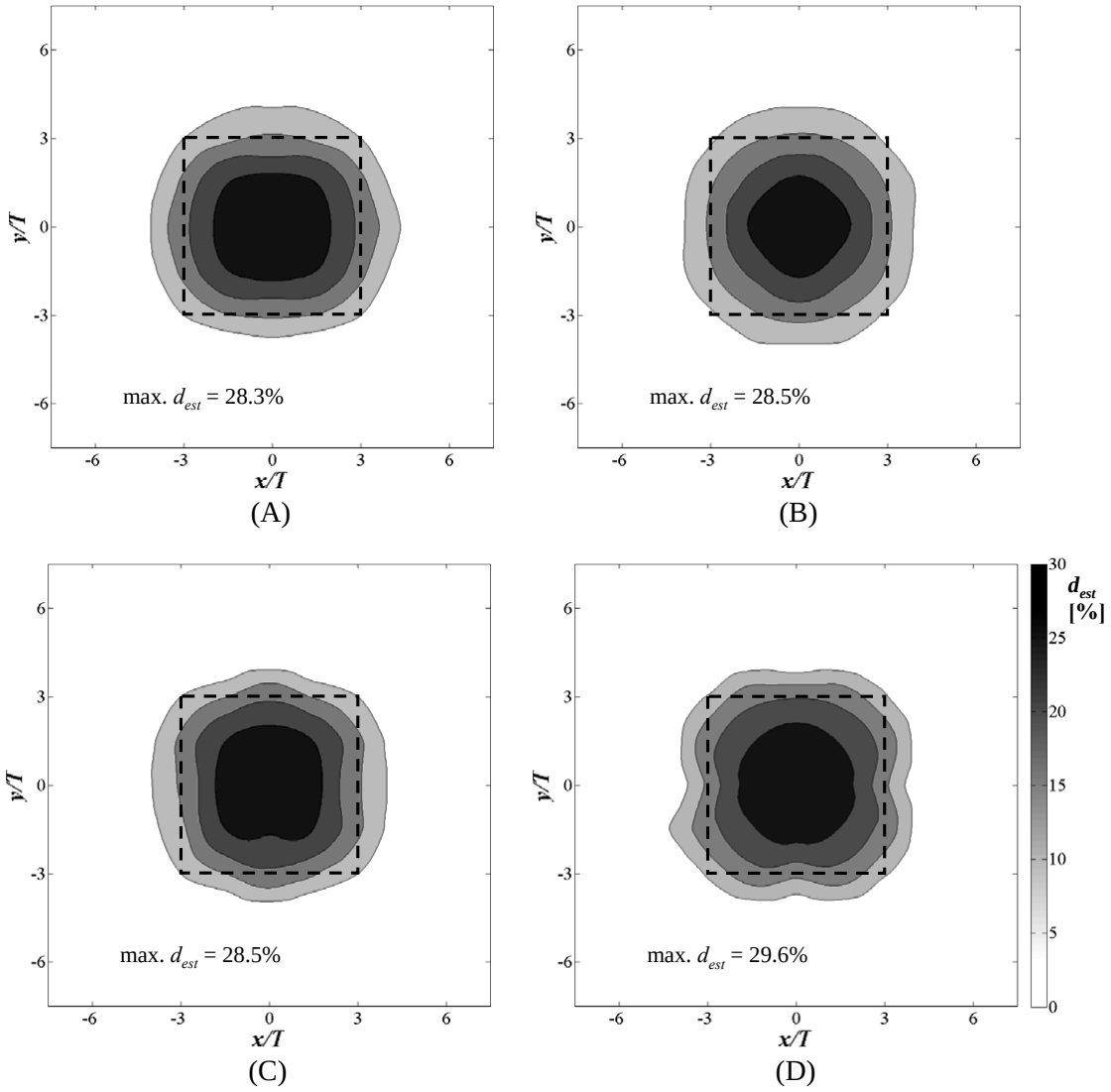

Figure 8.22: *Maps of estimated depth for a scalloped defect of average plane size 60 mm and maximum depth 3 mm (=30%) on a 500×500×10 mm SS304 plate, using the adjacent configuration with a probe pitch $p = 3T$, for four positions of the probe relative to defect centre (see Fig. 8.16). Reconstructions from results of the FE model.*

Numerical simulations with a FE model showed that the response of a conventional array probe used in commercially available DCPD systems may not increase monotonically with defect size, thus making the determination of depth unreliable for defects smaller than about three times the electrode spacing. This problem can be overcome by using instead a novel 'adjacent configuration'. This alternative arrangement of electrodes was shown to give good estimates of depth directly for defects whose size was twice the probe pitch, with excellent agreement between the experimental results and the predictions of the FE model. For smaller defects, simple correction factors can be used based on the defect length and width, which in turn can be easily estimated from the map of array data.

Chapter 9

Conclusions

9.1 Review of thesis

This thesis explored the possibility of using Potential Drop techniques for the characterisation of defects of various geometries; the subject of the research and the framework in which this project is set were introduced in Chapter 1. A summary of this work and of the results obtained is given here; for convenience, the main findings are again recapitulated in a more concise form in the next Section.

The fundamentals of the most widely used electromagnetic methods for Non-Destructive Testing were briefly described in Chapter 2, showing that Potential Drop techniques share some of the basic principles with other EM inspection methods. The advantages and disadvantages, practical applications and limitations of each technique were discussed, and reference was made to the available literature. From this review it emerged that, thanks to the recent advances in electronics and to the enormous, fast developments in computational capabilities, margins of improvement exist for Potential Drop techniques: the intensity of the currents injected in the material for the inspection can be significantly reduced; numerical simulations can be used to gain further insight on the interaction processes between the currents and any defects present in the tested structure, and also to improve the probe design; new methods for the processing and inversion of the acquired data can be developed. The

outcome of this review was therefore used to formulate an outline for the progress of the present work.

An initial, crucial part of this project was the development of an experimental setup for PD measurements, which was carried out under the guidance of Prof. P. B. Nagy. The setup was described in Chapter 3, where the characteristics of the instrumentation used were briefly discussed. The main advantage offered by this setup over existing laboratory or commercial systems is that currents of intensity as small as a few mA can be injected even for quasi-DC (low frequency) inspection, thanks to the high Common Mode Rejection Ratio offered by state-of-the-art amplifiers and preamplifiers, which allows very small differential signals to be recovered. Additionally, expedients such as repeating each measurement after switching the input channels of the preamplifier increase the effective CMRR of the system and thus reduce measurement uncertainties associated for instance with variations in the contact resistance between the probe and the surface of the tested structure.

Other concerns commonly raised when considering the employment of Potential Drop techniques in the field were addressed in Chapter 4: these issues also provided a benchmark for the comparison of the experimental setup with commercially available DCPD systems. The tests showed that stray current loops which may develop in large grounded structures do not significantly affect Potential Drop measurements: in fact, while the presence of 'short circuits' between points in the test area can alter the measured transfer resistance, this effect depends strongly on the quality of the electrical contacts and is likely to be negligible in realistic situations. On the other hand, changes in electrical resistivity due to temperature variations must be compensated for in long-term monitoring applications, but it was shown that a very simple algorithm based on the assumption of a linear dependence of resistivity on temperature is sufficient if the thermal variations are not too large or rapid. Furthermore, the tests showed that the performance of the low-current setup developed for the present work is similar to that of existing commercial systems which have been successfully used for industrial applications but which require the injection of much higher currents.

At an early stage in this research, the possibility was envisaged to develop a technique combining DCPD and ACPD, called Potential Drop Spectroscopy as it consists in taking measurements of voltage drop at several different frequencies over a broad spectrum spanning from the quasi-DC regime to the kHz range. As discussed in Chapter 5, the idea was that, at very low frequency, currents would flow deeply in the material and effectively form an envelope around branched cracks or other surface-breaking defects of complex geometry; as the inspection frequency is increased and the standard penetration depth becomes smaller, currents tend to follow more tightly the profile of the defect, and the increased path length results in a larger voltage difference between the measuring electrodes. Low-frequency data could then be used to obtain an estimate of the overall maximum depth of the defect, which is often a key parameter in calculations of structural integrity, whereas information on the complexity of the defect would be obtained from measurements at higher frequency, since flaws with a more articulated profile produce larger potential drops. Two-dimensional numerical simulations with a commercial Finite Element code confirmed this idea and gave a more detailed insight on the way the path followed by the injected currents is modified by the presence of defects and as a function of frequency. However, preliminary tests suggested that more research had to be undertaken before a quantitative evaluation of realistic defects of complex geometry, such as stress corrosion cracks, could be successfully attempted. In particular, it emerged that the three-dimensionality of real defects has to be taken into account.

A simple approximate model that allows three-dimensional ACPD problems to be simulated by running a DC analysis on a commercial Finite Element code was then developed and validated, as described in Chapter 6. The number of elements in the mesh required for a fully three-dimensional ACPD analysis can easily exceed the capabilities of most of today's computers; however, it was shown that the computational domain can be made significantly smaller by appropriately modifying the geometry of the specimen prior to the analysis. It was demonstrated that the thickness of the specimen should be reduced to about the standard penetration depth, taking into account any features such as surface-breaking defects; direct currents

can then be injected, since the frequency-dependent modified shape of the specimen will force them to flow along a path similar to that followed by alternating currents. Predictions obtained with this model were found to be in very good agreement with experimental results.

Having solved the direct problem of calculating the potential drop due to surface-breaking defects of simple, known geometry, the inverse problem of reconstructing the unknown depth profile of defects of finite length and arbitrary shape was examined in Chapter 7. For this study, a linear array probe was developed that allows faster acquisition of PD data along the defect's length, and low-frequency measurements were taken on EDM notches of various shapes and sizes. Excellent agreement was obtained between the experimental results and the predictions of the FE model discussed before. A simple formula, based on the assumption that, at least in the quasi-DC regime, the transfer resistance measured at each location is inversely proportional to the remaining thickness, was used for the inversion of the Potential Drop data. The reconstruction of the depth profile of the notches is generally good, especially for defects of more realistic shapes, although it should be emphasised that no *a priori* assumption is made on the geometry of the defect; on the other hand, the maximum depth of a defect may be severely underestimated when it is comparable to the length, but this case is infrequent in practice. It was also shown that the quality of the reconstruction can be improved by using a simple method for synthetic focusing of the injected currents, since this strengthens the validity of the assumption of a 'local' measurement: this is therefore particularly useful in the presence of rapid variations in the depth profile.

Finally, Chapter 8 considered another application of Potential Drop techniques, namely the monitoring of corrosion and erosion on the inner surface of pipes, containers, pressure vessels, etc. Using an array of electrodes to inject low-frequency currents and measure voltage differences at multiple locations on the outer surface of the inspected region, it is possible to combine the data to obtain maps which give information on the size and position of defects. For the inversion of PD data, a closed analytical expression was derived as an asymptotic extension of a formula

given in the literature. Finite Element simulations showed that voltages measured with the electrode arrangement traditionally used in commercially available DCPD systems, in which all electrodes are equally spaced, may not increase monotonically with defect size, and as a consequence the depth of defects smaller than about three times the electrode spacing can be severely underestimated. An alternative configuration of the array probe was therefore studied, in which the voltage electrodes are immediately adjacent to the current electrodes; it was shown that this overcomes the problem of non-monotonicity of the probe response, and that the depth of defects as small as about twice the probe pitch can be estimated with good accuracy. An array probe exploiting the novel configuration was then built, and maps of remnant depth were obtained for plates with machined defects: the experimental results confirmed the predictions of the FE model, and the depth and size of the defects was reconstructed with good accuracy independent of the relative position of the probe to the defect.

9.2 Brief summary of the main contributions

The main original contributions and findings of this thesis can be briefly summarised as follows:

- a low-current experimental setup for Potential Drop measurements was developed and benchmarked against commercially available DCPD systems that have been successfully used for industrial applications;
- the stability of these systems with respect to some difficulties encountered in applications of Potential Drop techniques in the field has been shown;
- a reduced-thickness model for Finite Element simulations of three-dimensional ACPD analyses was developed and validated;
- a simple, non-iterative formula which does not make *a priori* geometrical assumptions was used for the reconstruction of the depth profile of surface-breaking defects of finite length and arbitrary shape;

- it was shown that synthetic focusing of the injected currents in a linear array can improve the quality of the reconstruction of the depth profile;

- a novel geometry of an array probe for monitoring of corrosion/erosion on the far side of the inspected structure was shown to give better results than the configuration of electrodes commonly used in commercial systems.

Most of these results have been presented at international NDT conferences and published as proceedings [98–101], and papers are being prepared for submission to refereed journals.

9.3 Recommendations for practical applications of Potential Drop techniques

In the course of this study three main probe geometries have been identified for different applications of Potential Drop techniques. The exact values of parameters such as the spacings between the electrodes should be chosen carefully for each particular case, but the guidelines for the determination of their optimal values can be summarised as follows.

A simple four-point probe is sufficient for thickness gauging of metal plates. For this application, the only requirement on the probe geometry is that the separation between the injecting electrodes be sufficiently large (at least twice the estimated thickness) in order to ensure penetration of the current through the entire thickness of the specimen; for the same reason, direct or very low-frequency currents should be used. The same probe can also be used on plates of known thickness to measure their electrical conductivity; in this case, the advantage of using DC or quasi-DC is that the measured potential drop will not be affected by the magnetic permeability of the material.

For the sizing of surface-breaking cracks it is convenient to adopt a linear array probe such as that of Fig. 7.1. Using multiple inner pairs of electrodes allows data

to be taken at several locations along a crack without having to move the probe; furthermore, it gives the possibility to apply a simple synthetic focusing technique which improves the reconstruction of the defect profile. The separation $2b$ between the inner electrodes should be as small as possible to enhance the sensitivity to defects and to allow a more accurate sizing of short cracks; however, as the distance between the pins decreases, the errors associated with uncertainties in their positioning become more relevant. A distance $2b = 5$ mm seems a good compromise. As shown in Chapter 7, an optimal value for the distance between two consecutive electrode pairs is $s = 2$ mm. The separation $2a$ between the outer electrodes should be sufficiently large to ensure that the current distribution across the inner sensing electrodes is fairly uniform; in practice, its value will be chosen according to the number of inner pairs used (more pairs require a larger spacing) and to the dimensions of the specimen to be inspected. It should be borne in mind that the depth of any defect shorter than the spacing between the inner electrodes will be underestimated because a large fraction of current will flow around its sides; the same can be said of any defects whose depth is larger than their length, although cracks of such aspect ratios are unlikely to occur in practice.

An array probe is indicated for the monitoring of corrosion/erosion and to produce maps of remaining thickness. It was shown that the arrangement of electrodes of Fig. 8.8, in which the voltage electrodes are immediately adjacent to the current electrodes, can give a correct estimation of the depth of defects whose size is as small as about twice the probe pitch p; correction factors can be used for smaller flaws. A compromise must be reached between the smallest defect that needs to be accurately evaluated and the number of electrodes required to cover a given area of inspection; a probe pitch of about three times the initial thickness ($p = 3T$) seems a reasonable starting value.

For long-term monitoring of corrosion/erosion on critical parts, the electrodes of the array could be permanently or semi-permanently attached (*e.g.* welded or clamped) to the inspection area; in general, however, all these probes can be simply pressed onto the surface to be tested, as they use spring-loaded pins both to inject currents

and to pick up the resulting potential drops. The resistances to be measured in the tested material are typically much smaller than the contact resistances between the electrodes and the specimen surface, and therefore the instrumentation used for the measurements must have a Common Mode Rejection Ratio of at least 100 dB over the frequency range of interest. Currents of small intensity (around 100 mA) can be injected even at very low frequency if voltage differences in the nV range can be measured accurately: it is then advisable to use a lock-in amplifier, which is capable of recovering small signals from large background noise.

The small currents required for the inspection open up the possibility for the development of a portable, battery-powered system. This poses a challenge for the design of electronics of smaller dimensions than the instruments used in the experimental setup described in this work, but capable of achieving the same performance, if not better. When array probes are employed, care should also be taken in multiplexing a large number of cables carrying very small signals.

9.4 Future work

Experimental data have been taken on a few specimens with artificial stress corrosion cracking produced by SERCO. The specimens were 150-mm long, 50-mm wide, 10-mm thick blocks of stainless steel 304, and they were tested using the linear array probe described in Chapter 7; estimated depth profiles have been obtained with the inversion formula of Eq. 7.4, using the synthetic focusing technique introduced in the same Chapter. Unfortunately, these results could not be included in the present work because SERCO have not yet supplied data on the real depth of the defects, which is to be obtained from sectioning. Once available, these data will be compared with the predicted values and thus provide a significative test of the capabilities of Potential Drop techniques when trying to reconstruct the depth profile of cracks of more realistic, complex geometry.

It would also be useful to take numerical and experimental measurements of potential drop across notches of various shapes in specimens of different thicknesses and

materials (*e.g.* ferritic steel, aluminium, etc.), in order to verify the general validity of the inversion algorithm.

Still with respect to surface-breaking defects, it would be worth investigating the extent to which the ability of Potential Drop techniques to estimate the depth of short cracks could be improved by reducing the separation between the inner electrodes of the probe. In the presence of a deep, short defect, currents tend to flow laterally around it, rather than below it, so that the measured voltage difference is practically independent of the defect depth: this is therefore to be considered an intrinsic limitation of PD techniques. However, in such cases it could be beneficial to bring the electrodes closer to the crack (and hence to each other) in order to increase the sensitivity to the defect, although this would also inevitably increase the sensitivity to errors and uncertainties in the positioning of the pins.

The next step in the mapping of corrosion/erosion should be the study of smoothly scalloped defects, which would represent more realistically the geometry of defects encountered in practice. The defects considered in Chapter 8 had a homogeneous depth, or presented at most a 'bathtub-shaped' section (see Fig. 9.1*a*), with depth increasing relatively sharply at the edges and staying exactly constant over most of the defect's length and width; it would be desirable to study defects with a more rounded profile, as in Fig. 9.1*b*. However, it should be noted that the modelling of

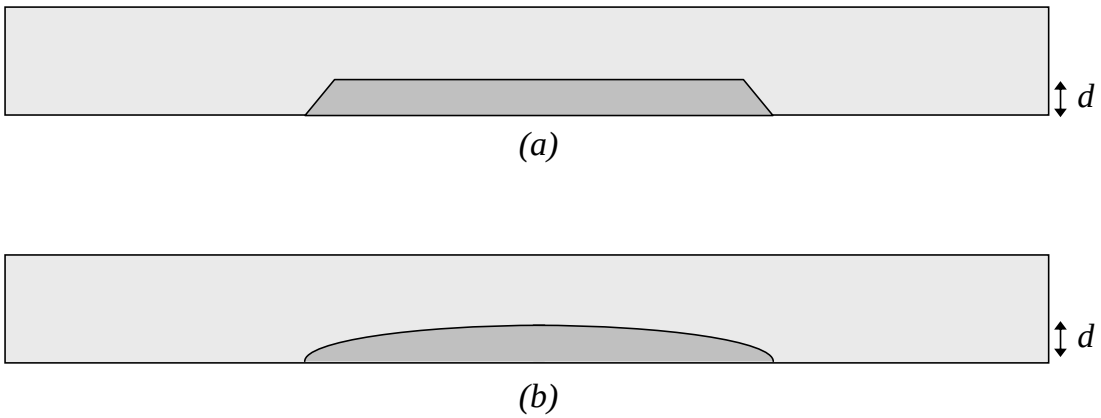

Figure 9.1: *Sections of plates with (a) 'bathtub-shaped' or (b) smoothly scalloped defect of maximum depth d.*

such geometries is not straightforward, because of the size and shape of the elements used for the FE simulations. In fact, the numerical results presented in Chapter 8 were obtained using 1-mm long, 1-mm wide, 0.5-mm thick brick-shaped elements, which can only give an approximate description of the defect profile, discretised in steps; in order to reproduce more accurately curved features, it would be necessary to reduce the element size, which in turn would significantly increase the memory and time required for the calculations. It is expected that the quality of the reconstruction, in terms of the estimation of the maximum depth, would still be satisfactory.

Another immediate extension of this study will be the determination of the correction factors that, as discussed in Chapter 8, need to be applied when evaluating defects smaller than about twice the probe pitch, whose depth would otherwise be underestimated. The correction factors can be modelled as a function of the length and width of the defect, so it becomes important to be able to determine these dimensions with a certain degree of accuracy. It was shown that a quick estimate of the length and width of a defect can be obtained from corrosion maps by applying a simple 6-dB drop criterion; however, this is only a first guess, and analyses on defects of different sizes and aspect ratios should be run in order to verify the general validity of this simple method, and possibly to refine it, or to replace it if appropriate with a more accurate estimate.

Finally, as mentioned in the previous Section, the experimental setup developed in the present work has shown potential for its use as a battery-operated system, thanks to the low currents injected. It is recommended that, for long-term monitoring applications, future developments of the probe include the possibility of measuring the surface temperature of the structure being tested, maybe exploiting the voltage electrodes as thermocouples.

Appendix A

Evaluation of the edge effect in PD measurements

A.1 Introduction

Correct positioning of the probe is important in practical applications of Potential Drop techniques: if discontinuities such as plate edges or welded joints are too close to the injecting electrodes, they can affect the spreading of currents in the tested material, and the transfer resistance measured between the voltage electrodes may be altered.

This Appendix reports the results of an investigation carried out to evaluate the so-called edge effect and to estimate the minimum distance from the edge of a plate at which the probe can be positioned without the measured voltages being significantly affected. The predictions of an analytical procedure are compared with experimental results.

The author is aware that results of a similar study, developed independently, have been recently presented by Lu *et al.* [102].

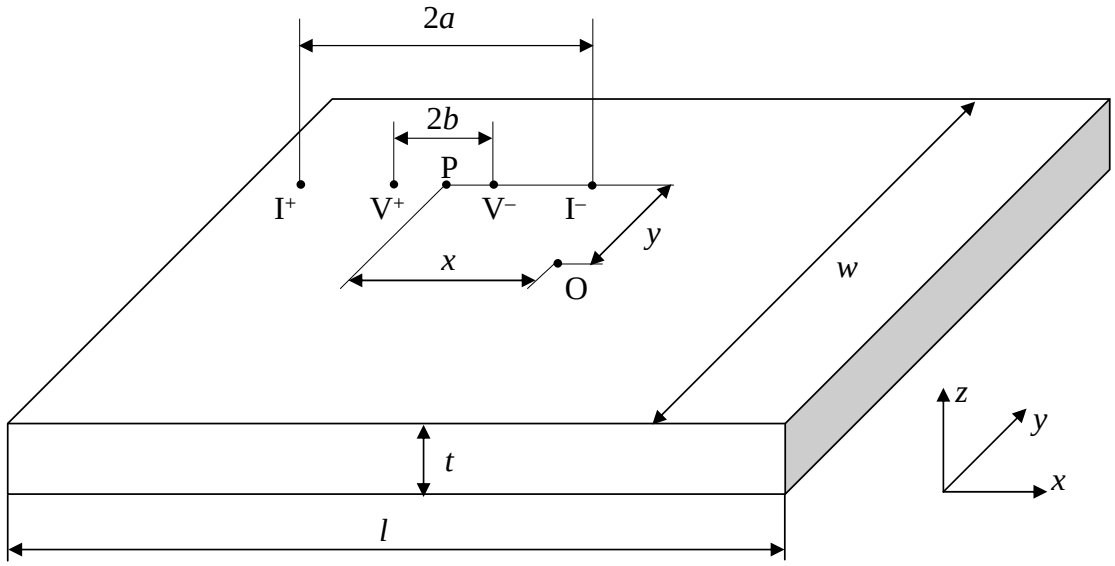

Figure A.1: *Geometry of finite plate for Potential Drop calculations.*

A.2 Analytical derivation of DC potential drop in a finite plate

It is possible to derive an analytical expression for the potential drop ΔV, and hence for the resistance R, between two points V^+ and V^- on a fully three-dimensional finite plate. Reference will be made to Fig. A.1, which shows a plate of length l, width w and thickness t; on this plane, electrodes inject and extract a direct current I at the points marked I^+ and I^-, respectively, while a second pair of electrodes measures the potential drop between the points V^+ and V^-. The four points are aligned parallel to the x direction and located symmetrically from the centre P of the probe, as shown in Fig. A.1; the separation between the current electrodes is $2a$, whereas the distance between the measuring points is $2b$. The expression derived in the following will account for the general case in which the centre P of the probe does not coincide with the centre O of the plate: offset in the x direction, *i.e.* parallel to the alignment direction of the four electrodes, will be referred to as the *axial displacement*, whereas the offset in the y direction will be called the *lateral displacement*.

The analytical expression for the potential drop in a finite plate can be derived by following a four-step procedure common to many mathematical physics problems (see *e.g.* [103]):

1. starting from the fundamental expression of the electric field in an infinite three-dimensional space, the voltage drop due to the injection and extraction of a current I from a half-space (see the schematic of Fig. A.2) is calculated;

2. in order to simulate an infinite plate of finite thickness t it is necessary to impose the closure of the current loops in the z direction. If a second half-space is added at a distance $2t$ from the first along the z direction, and the same currents are injected in it, then the resulting symmetric boundary condition at a depth t forces the current lines to close as desired. Closure of the currents originating from the additional electrodes can be obtained by adding a third half-space at a distance $2t$ from the second, and so on; the process is repeated until a sufficiently large (in theory, infinite) number of half-spaces stacked on top of each other is obtained, as sketched in Fig. A.3. The potential drop between the voltage electrodes on one plate is given by the sum of the potential drops caused by the currents injected and extracted on each of the half-spaces;

3. similarly, a strip of finite width w and thickness t and infinite length can be simulated by closing the current loops in the y direction, too: this is done by ideally aligning a large number of infinite plates along that direction at a distance $2w$ from each other, as in Fig. A.4. The potential drop in one strip is calculated by adding the contributions of all the plates;

4. finally, a plate of finite length l is obtained by imposing the closure of the current loops also in the last direction, and this is achieved mathematically by considering a large number of strips at a distance $2d$ from each other along the x direction, as in Fig. A.5. The potential drop in the plate of interest is calculated as the sum of the voltage differences induced by the currents injected in each of the strips.

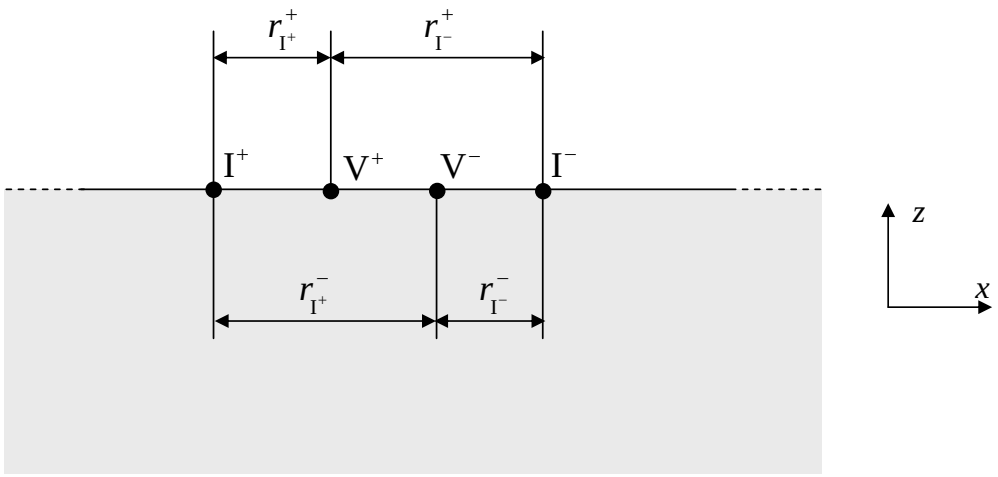

Figure A.2: *Distances between the electrodes for calculations of potential drop in a half-space.*

A.2.1 Half-space

In an infinite medium of uniform conductivity σ, the electrical field E generated by a direct current I at a distance r is

$$E(r) = \frac{I}{4\pi\sigma r^2}, \tag{A.1}$$

and the potential V, defined up to a constant C, is therefore

$$V(r) = -\int E(r)\,\mathrm{d}r = \frac{I}{4\pi\sigma r} + C. \tag{A.2}$$

Let us consider now the four-electrode configuration represented in Fig. A.2. Throughout the following, the superscripts $^+$ and $^-$ will be used to refer to the voltage electrodes, whereas the current electrodes will be indicated by the subscripts $_{I^+}$ and $_{I^-}$. Hence, for example, $r^-_{I^+}$ will indicate the distance between the positive current electrode I^+ and the negative voltage electrode V^-. Furthermore, currents will be considered positive if injected, negative if extracted.

The potential drop $\Delta V(I^+)$ due to the current injected in I^+ is, from Eq. A.2,

$$\Delta V(I^+) = V^+_{I^+} - V^-_{I^+} = \frac{I}{4\pi\sigma}\left(\frac{1}{r^+_{I^+}} - \frac{1}{r^-_{I^+}}\right), \tag{A.3}$$

whereas the potential drop $\Delta V(\mathrm{I}^-)$ due to the current extracted in I^- is

$$\Delta V(\mathrm{I}^-) = V^+_{\mathrm{I}^-} - V^-_{\mathrm{I}^-} = \frac{-I}{4\pi\sigma}\left(\frac{1}{r^+_{\mathrm{I}^-}} - \frac{1}{r^-_{\mathrm{I}^-}}\right). \tag{A.4}$$

These values must be doubled if it is assumed that currents are injected into (and extracted from) a conductive half-space rather than an infinite medium. The transfer resistance between V^+ and V^- in a half-space is then given by

$$R = \frac{\Delta V}{I} = \frac{\Delta V(\mathrm{I}^+) + \Delta V(\mathrm{I}^-)}{I} = \frac{1}{2\pi\sigma}\left(\frac{1}{r^+_{\mathrm{I}^+}} - \frac{1}{r^-_{\mathrm{I}^+}} + \frac{1}{r^-_{\mathrm{I}^-}} - \frac{1}{r^+_{\mathrm{I}^-}}\right); \tag{A.5}$$

substituting the values of the various distances r yields

$$R = \frac{1}{\pi\sigma}\left(\frac{1}{a-b} - \frac{1}{a+b}\right). \tag{A.6}$$

A.2.2 Infinite plate of finite thickness

Adding a series of fictitious pairs of injection and extraction points at a distance $2t$ from each other along the z direction, as shown in Fig. A.3, ensures that current paths originating from the existing current electrodes, for symmetry reasons, cannot spread further than t in that direction; the physical closure of the current loops due to the finite thickness of the plate is thus simulated. The current loops originating from the additional electrodes are closed in their turn by adding extra electrode pairs further away, and so on.

If the electrode pairs are numbered progressively from $n = -\infty$ to $n = +\infty$, with $n = 0$ indicating the 'real' current electrodes (as in Fig. A.3), then Eq. A.5 can be generalised by summing the contributions from all the current electrode pairs to yield the resistance between the voltage electrodes on an infinite plate of thickness t:

$$R = \frac{1}{2\pi\sigma}\sum_{n=-\infty}^{+\infty}\left(\frac{1}{r^+_{\mathrm{I}^+_n}} - \frac{1}{r^-_{\mathrm{I}^+_n}} + \frac{1}{r^-_{\mathrm{I}^-_n}} - \frac{1}{r^+_{\mathrm{I}^-_n}}\right). \tag{A.7}$$

Here the distances between the generic n-th current electrodes and the voltage electrodes are given by

$$\begin{cases} r^+_{\mathrm{I}^+_n} = r^-_{\mathrm{I}^-_n} &= \sqrt{(a-b)^2 + 4n^2t^2} \\ r^-_{\mathrm{I}^+_n} = r^+_{\mathrm{I}^-_n} &= \sqrt{(a+b)^2 + 4n^2t^2} \end{cases}. \tag{A.8}$$

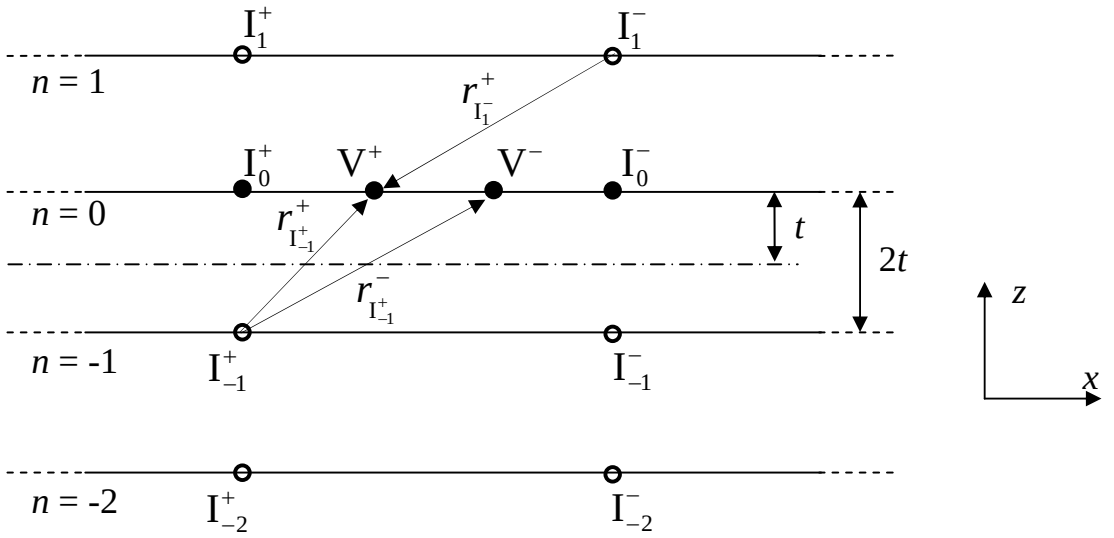

Figure A.3: *Additional half-spaces and current electrodes are considered above and below the plane containing the voltage electrodes, at distances* $2t$ *from each other, to simulate a plate of finite thickness* t*.*

The contributions of the fictitious current sources to the calculated resistance become smaller as the distance from the voltage electrodes increases, so that in practice it is possible to consider only a finite number of terms in the sum.

A.2.3 Infinite strip of finite width and thickness

As a third step, fictitious electrode pairs are added along the y direction. Fig. A.4 shows the general case in which the electrodes are offset by a distance y from half the width w of the specimen. Currents can be constrained within a width w by considering initially a strip of double width $2w$ and then adding a second pair of current electrodes Iy^+ and Iy^- positioned symmetrically from the centreline, as in Fig. A.4. This configuration is then repeated infinitely along the y and z directions, with a progressive index m numbering the 'double strips' in the y direction ($m = 0$ for the strip containing the voltage electrodes).

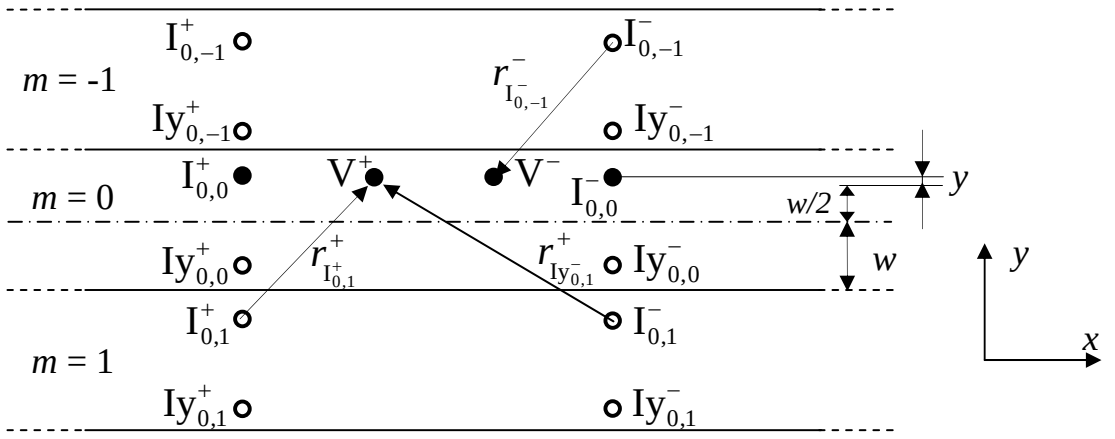

Figure A.4: *Additional current electrodes* Iy *are positioned symmetrically to the centre-line of the plane containing the voltage electrodes, and this configuration is repeated along the y direction to simulate a plate of finite width w.*

Eq. A.7 is then expanded as follows to include the new terms:

$$R = \frac{1}{2\pi\sigma} \sum_{m=-\infty}^{+\infty} \sum_{n=-\infty}^{+\infty} \left(\frac{1}{r^{+}_{\mathrm{I}^{+}_{n,m}}} - \frac{1}{r^{-}_{\mathrm{I}^{+}_{n,m}}} + \frac{1}{r^{-}_{\mathrm{I}^{-}_{n,m}}} - \frac{1}{r^{+}_{\mathrm{I}^{-}_{n,m}}} + \right. \\ \left. + \frac{1}{r^{+}_{\mathrm{Iy}^{+}_{n,m}}} - \frac{1}{r^{-}_{\mathrm{Iy}^{+}_{n,m}}} + \frac{1}{r^{-}_{\mathrm{Iy}^{-}_{n,m}}} - \frac{1}{r^{+}_{\mathrm{Iy}^{-}_{n,m}}} \right); \tag{A.9}$$

the distances are

$$\begin{cases} r^{+}_{\mathrm{I}^{+}_{n,m}} = r^{-}_{\mathrm{I}^{-}_{n,m}} = \sqrt{(a-b)^2 + 4m^2w^2 + 4n^2t^2} \\ r^{-}_{\mathrm{I}^{+}_{n,m}} = r^{+}_{\mathrm{I}^{-}_{n,m}} = \sqrt{(a+b)^2 + 4m^2w^2 + 4n^2t^2} \\ r^{+}_{\mathrm{Iy}^{+}_{n,m}} = r^{-}_{\mathrm{Iy}^{-}_{n,m}} = \sqrt{(a-b)^2 + [(2m+1)w + 2y]^2 + 4n^2t^2} \\ r^{-}_{\mathrm{Iy}^{+}_{n,m}} = r^{+}_{\mathrm{Iy}^{-}_{n,m}} = \sqrt{(a+b)^2 + [(2m+1)w + 2y]^2 + 4n^2t^2} \end{cases} . \tag{A.10}$$

A.2.4 Finite plate

The same procedure is finally used to impose closure of currents within a length l along the x direction. A plate of double length $2l$ is initially considered, and electrode pairs are repeated symmetrically with respect to the centre of the 'double plate', as shown in Fig. A.5 for a probe with an axial displacement x from the centre O of the plate. The configuration is then repeated in all directions, with an index

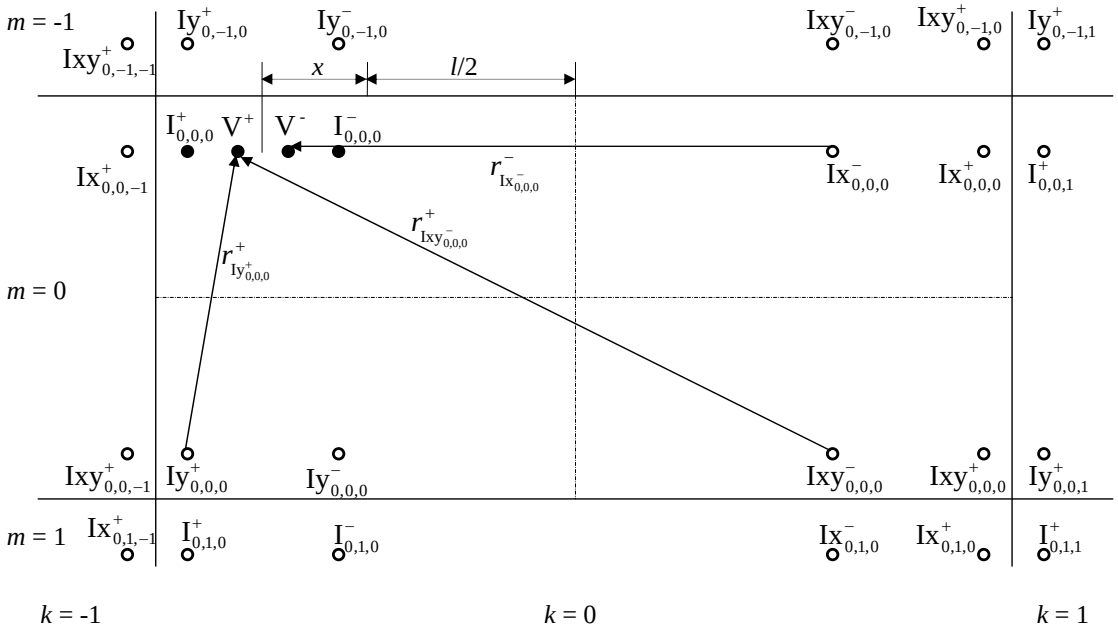

Figure A.5: *Additional current electrodes* Ix *and* Ixy *are positioned symmetrically to the centreline of the plane containing the voltage electrodes, and this configuration is repeated along the x direction to simulate a plate of finite length l.*

k numbering the 'double plates' in the x direction. The formula for the transfer resistance becomes then

$$R = \frac{1}{2\pi\sigma} \sum_{k=-\infty}^{+\infty} \sum_{m=-\infty}^{+\infty} \sum_{n=-\infty}^{+\infty} \left(\frac{1}{r^{+}_{\mathrm{I}^{+}_{n,m,k}}} - \frac{1}{r^{-}_{\mathrm{I}^{+}_{n,m,k}}} + \frac{1}{r^{-}_{\mathrm{I}^{-}_{n,m,k}}} - \frac{1}{r^{+}_{\mathrm{I}^{-}_{n,m,k}}} + \right.$$
$$+ \frac{1}{r^{+}_{\mathrm{Iy}^{+}_{n,m,k}}} - \frac{1}{r^{-}_{\mathrm{Iy}^{+}_{n,m,k}}} + \frac{1}{r^{-}_{\mathrm{Iy}^{-}_{n,m,k}}} - \frac{1}{r^{+}_{\mathrm{Iy}^{-}_{n,m,k}}} +$$
$$+ \frac{1}{r^{+}_{\mathrm{Ix}^{+}_{n,m,k}}} - \frac{1}{r^{-}_{\mathrm{Ix}^{+}_{n,m,k}}} + \frac{1}{r^{-}_{\mathrm{Ix}^{-}_{n,m,k}}} - \frac{1}{r^{+}_{\mathrm{Ix}^{-}_{n,m,k}}} + \tag{A.11}$$
$$\left. + \frac{1}{r^{+}_{\mathrm{Ixy}^{+}_{n,m,k}}} - \frac{1}{r^{-}_{\mathrm{Ixy}^{+}_{n,m,k}}} + \frac{1}{r^{-}_{\mathrm{Ixy}^{-}_{n,m,k}}} - \frac{1}{r^{+}_{\mathrm{Ixy}^{-}_{n,m,k}}} \right),$$

where the various distances, with reference to Fig. A.5, are given in Table A.1.

Table A.1: *Distances between electrodes in Eq. A.11.*

$$
\begin{aligned}
r^{+}_{\mathrm{I}^{+}_{n,m,k}} &= \sqrt{(-a+b+2kl)^2+4m^2w^2+4n^2t^2} \\
r^{-}_{\mathrm{I}^{+}_{n,m,k}} &= \sqrt{(-a-b+2kl)^2+4m^2w^2+4n^2t^2} \\
r^{+}_{\mathrm{I}^{-}_{n,m,k}} &= \sqrt{(a+b+2kl)^2+4m^2w^2+4n^2t^2} \\
r^{-}_{\mathrm{I}^{-}_{n,m,k}} &= \sqrt{(a-b+2kl)^2+4m^2w^2+4n^2t^2} \\
r^{+}_{\mathrm{Iy}^{+}_{n,m,k}} &= \sqrt{(-a+b+2kl)^2+[(2m+1)w+2y]^2+4n^2t^2} \\
r^{-}_{\mathrm{Iy}^{+}_{n,m,k}} &= \sqrt{(-a-b+2kl)^2+[(2m+1)w+2y]^2+4n^2t^2} \\
r^{+}_{\mathrm{Iy}^{-}_{n,m,k}} &= \sqrt{(a+b+2kl)^2+[(2m+1)w+2y]^2+4n^2t^2} \\
r^{-}_{\mathrm{Iy}^{-}_{n,m,k}} &= \sqrt{(a-b+2kl)^2+[(2m+1)w+2y]^2+4n^2t^2} \\
r^{+}_{\mathrm{Ix}^{+}_{n,m,k}} &= \sqrt{[a+b+(2k+1)l+2x]^2+4m^2w^2+4n^2t^2} \\
r^{-}_{\mathrm{Ix}^{+}_{n,m,k}} &= \sqrt{[a-b+(2k+1)l+2x]^2+4m^2w^2+4n^2t^2} \\
r^{+}_{\mathrm{Ix}^{-}_{n,m,k}} &= \sqrt{[-a+b+(2k+1)l+2x]^2+4m^2w^2+4n^2t^2} \\
r^{-}_{\mathrm{Ix}^{-}_{n,m,k}} &= \sqrt{[-a-b+(2k+1)l+2x]^2+4m^2w^2+4n^2t^2} \\
r^{+}_{\mathrm{Ixy}^{+}_{n,m,k}} &= \sqrt{[a+b+(2k+1)l+2x]^2+[(2m+1)w+2y]^2+4n^2t^2} \\
r^{-}_{\mathrm{Ixy}^{+}_{n,m,k}} &= \sqrt{[a-b+(2k+1)l+2x]^2+[(2m+1)w+2y]^2+4n^2t^2} \\
r^{+}_{\mathrm{Ixy}^{-}_{n,m,k}} &= \sqrt{[-a+b+(2k+1)l+2x]^2+[(2m+1)w+2y]^2+4n^2t^2} \\
r^{-}_{\mathrm{Ixy}^{-}_{n,m,k}} &= \sqrt{[-a-b+(2k+1)l+2x]^2+[(2m+1)w+2y]^2+4n^2t^2}
\end{aligned}
$$

A.3 Experimental results

Measurements were taken on a stainless steel 304 plate of length $l = 100$ mm, width $w = 100$ mm and thickness $t = 1$ mm, using the instrumentation described in Chapter 3. The distance between the current electrodes was $2a = 20$ mm, while the separation between the voltage electrodes was $2b = 10$ mm.

The resistance between the voltage electrodes was measured first with the probe positioned at the centre of the plate; measurements were then repeated after moving the probe in the y direction towards the edge of the plate in steps of 2 mm until

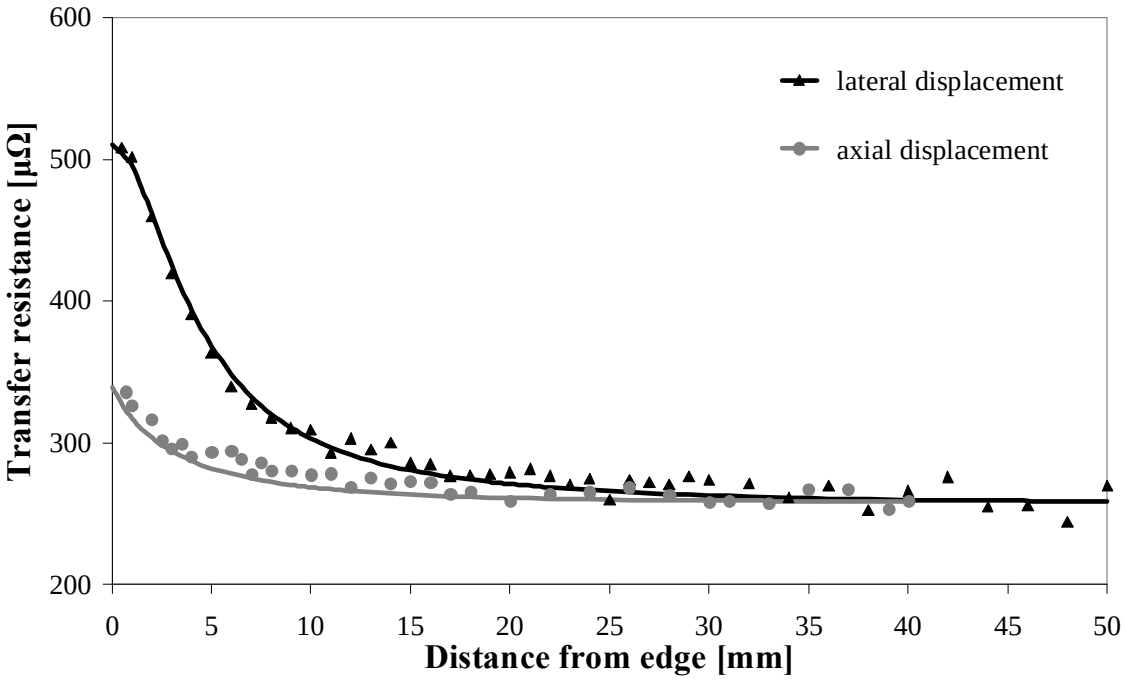

Figure A.6: *Predicted (lines) and measured (symbols) transfer resistance as a function of the distance of the probe from the edge of a 100-mm long, 100-mm wide, 1-mm thick SS304 plate, for axial or lateral displacement. Separation is* $2a = 20$ *mm between the current electrodes and* $2b = 10$ *mm between the voltage electrodes.*

the displacement from the centre reached 20 mm, then in steps of 1 mm; the last reading was taken with the electrodes positioned less than 1 mm from the edge, at the minimum distance that allowed stability of the probe. The probe was then positioned again at the centre of the plate, and the procedure was repeated moving the probe in the x direction; in this case, the last measurement was taken when one of the outer (injecting) electrodes was less than 1 mm from the edge: the maximum axial displacement of the probe was therefore almost 40 mm.

The graph in Fig. A.6 shows very good agreement between the measured data and the predictions obtained with the analytical model, in which a conductivity value of $\sigma = 2.4\%\text{IACS} = 1.39 \cdot 10^5\ \Omega^{-1}\text{m}^{-1}$ was assumed. The transfer resistance remains fairly constant (within experimental errors) over many different positions of the probe; it starts increasing significantly for probe displacements greater than about 30 mm or, in other words, when the distance between the centre of the probe and the nearest edge becomes smaller than about 20 mm, a distance corresponding to the

separation $2a$ between the injection points. For lateral displacements of the probe, the resistance calculated when the electrodes are sitting on the edge of the plate is double the value obtained at the centre, as might be expected considering that the space over which currents can spread is halved.

A.4 Conclusions

An analytical model was developed to calculate the potential drop due to the injection of direct currents on a homogeneous plate of finite length, width and thickness. The results were verified experimentally and indicate that Potential Drop measurements are not significantly affected by the presence of geometrical discontinuities in the tested structure, provided that the distance between the centre of the probe and the discontinuity is larger than the separation between the outer electrodes.

Appendix B

Current distribution in a linear array probe

Let us consider a linear array probe such as that introduced in Chapter 7; for convenience, a schematic is shown in Fig. B.1. Note that the (outer) sensing electrodes have not been drawn in Fig. B.1 because their position does not affect the distribution of currents. Assuming that currents are injected at selected pairs of inner electrodes, the resulting current density distribution in the material along the centreline of the probe can be calculated analytically for the two extreme cases of DC and very high frequency currents, which will now be considered separately.

B.1 Low-frequency case

If a direct current of intensity I is injected in a homogeneous and isotropic material, it spreads uniformly in all directions, so that the lines of equipotential are hemispherical surfaces. In the case of plates of finite thickness T, this is true for distances from the injection point not larger than T[(1)]. The current density J at a

[(1)]For the geometry of the linear array probes introduced in Chapter 7 ($2b$ = 5 or 10 mm, s = 2 mm), the distance between the furthest electrode pair used for focusing and the focal point itself was always smaller than the thickness of the specimens used in the experiments (T = 10 mm).

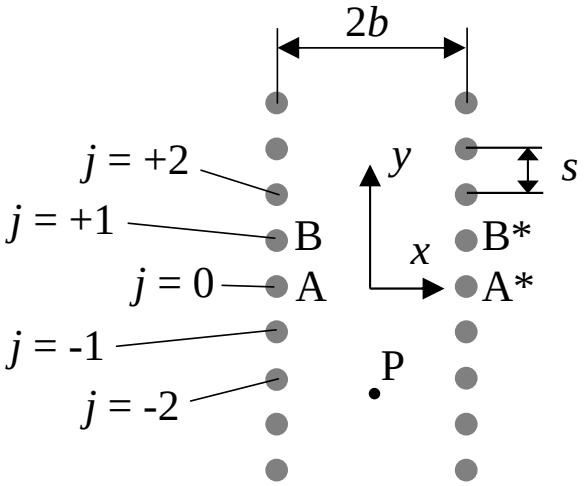

Figure B.1: *Schematic of linear array probe.*

distance r from the injection point is then given by

$$J = \frac{I}{2\pi r^2}. \tag{B.1}$$

In particular, with reference to Fig. B.1, the axial component (*i.e.* the component along the x direction) of the current density at a point $\mathrm{P}(0, y)$ on the surface due to the injection of a current I_0 at the electrode A will be

$$J_x^{(A)} = \frac{I_0}{2\pi(y^2 + b^2)} \cdot \frac{b}{\sqrt{y^2 + b^2}}. \tag{B.2}$$

It should be noted that if a current of the same amplitude and opposite sign is injected at the electrode A* facing A, the resulting current in P will have no component in the y direction, whereas the component in the x direction will double, so that from Eq. B.2 it is possible to write

$$J_x^{(0)} = \frac{I_0}{\pi b^2} \cdot \frac{1}{\left[\left(\frac{y}{b}\right)^2 + 1\right]^{\frac{3}{2}}}. \tag{B.3}$$

Similarly, let us consider another pair of electrodes $j = +1$ (also indicated as B, B* in Fig. B.1) at an offset s from the previous one; if a current I_1 is injected through this pair (more precisely, injected at B and extracted at B*), the current density in

P due to this will be

$$J_x^{(1)} = \frac{I_1}{\pi b^2} \cdot \frac{1}{\left[\left(\frac{y+s}{b}\right)^2 + 1\right]^{\frac{3}{2}}}. \tag{B.4}$$

Extending this concept to all other pairs of current electrodes, the total current density at the generic point P on the centreline of the array probe due to the injection of a combination of currents $I_0, I_{\pm 1}, I_{\pm 2}, \ldots$ at the various pairs is given by

$$J_x(y) = \frac{1}{\pi b^2} \cdot \sum_j \frac{I_j}{\left[\left(\frac{y+js}{b}\right)^2 + 1\right]^{\frac{3}{2}}}. \tag{B.5}$$

B.2 High-frequency case

Asymptotically for very high frequencies, it is possible to make the assumption that an alternating current I spreads just below the surface of the material because of the skin effect. Under this approximation, the current density at a distance r from the point of injection can be written as

$$J = \frac{I}{2\pi r \delta}, \tag{B.6}$$

where δ is the skin depth for that material at the given frequency.

This means that the axial component of the current density in P due to the injection of a high-frequency current I_0 at the electrode A in Fig. B.1 is

$$J_x^{(A)} = \frac{I_0}{2\pi\delta\sqrt{y^2+b^2}} \cdot \frac{b}{\sqrt{y^2+b^2}}, \tag{B.7}$$

and considering also the extraction of the same current I_0 from the other electrode A* of the pair, one has

$$J_x^{(0)} = \frac{I_0}{\pi\delta b} \cdot \frac{1}{\left(\frac{y}{b}\right)^2 + 1}. \tag{B.8}$$

With the same considerations made for the low-frequency case, it is possible to write the current density in P due to the injection (and extraction) of a current I_1 at the

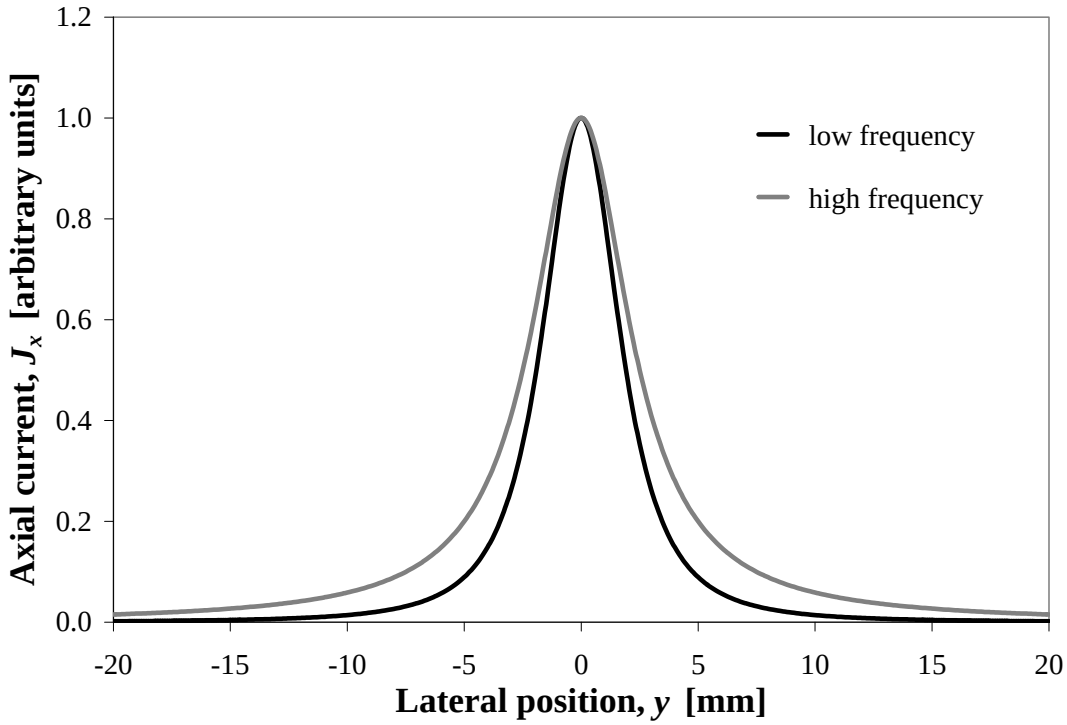

Figure B.2: *Current distribution along the centreline of an array probe with spacing* $2b = 5$ *mm for the injection of a low- or high-frequency unit current* I_0 *at the central pair.*

pair of electrodes $j = +1$ in Fig. B.1

$$J_x^{(1)} = \frac{I_1}{\pi\delta b} \cdot \frac{1}{\left(\frac{y+s}{b}\right)^2 + 1} \tag{B.9}$$

and the total current density given by the simultaneous injection of currents I_0, $I_{\pm1}$, $I_{\pm2}$, ... at the various pairs:

$$J_x(y) = \frac{1}{\pi\delta b} \cdot \sum_j \frac{I_j}{\left(\frac{y+js}{b}\right)^2 + 1}. \tag{B.10}$$

The current density distributions resulting from the injection of a current I_0 at the central pair ($j = 0$) only, calculated with Eq. B.3 and Eq. B.8 respectively for low and high frequency and for a probe with spacing $2b = 5$ mm, are plotted in Fig. B.2: the broader peak at high frequency is due to the fact that currents spread only in a thin layer rather than in all three dimensions. Examples of distributions resulting from the simultaneous injection of currents at multiple pairs, as calculated with Eq. B.5 for low frequency, can be found in Chapter 7.

References

[1] http://www.rcnde.ac.uk.

[2] M. G. Silk. Sizing crack-like defects by ultrasonic means. In R. S. Sharpe, editor, *Research Techniques in Non-Destructive Testing*, volume III, pages 51–99. Academic Press, London, 1977.

[3] M. G. Silk. The use of diffraction-based time-of-flight measurements to locate and size defects. *British Journal of Non-Destructive Testing*, 26(4):208–213, 1984.

[4] L. W. Schmerr, Jr., A. Sedov, and C. P. Chiou. A unified constrained inversion model for ultrasonic flaw sizing. *Research in Nondestructive Evaluation*, 1:77–97, 1989.

[5] L. W. Schmerr, Jr., S. J. Song, and A. Sedov. Ultrasonic flaw sizing inverse problems. *Inverse Problems*, 18:1775–1793, 2002.

[6] H. J. Kim, S. J. Song, and Y. H. Kim. Quantitative approaches to flaw sizing using ultrasonic testing models. In D. O. Thompson and D. E. Chimenti, editors, *Review of Progress in Quantitative Nondestructive Evaluation*, volume 22A, pages 703–710. American Institute of Physics, Melville, NY, 2003.

[7] G. Baskaran, K. Balasubramaniam, C. V. Krishnamurthy, and C. Lakshmana Rao. Ultrasonic TOFD flaw sizing and imaging in thin plates using embedded signal identification technique (ESIT). *Insight*, 46(9):537–542, 2004.

[8] R. C. McMaster, P. McIntire, and M. L. Mester, editors. *Electromagnetic Testing*, volume 4 of *Nondestructive Testing Handbook*. American Society for Nondestructive Testing, Columbus, OH, 2nd edition, 1986.

[9] R. C. McMaster and S. S. Udpa. Basic concepts and theory of eddy current testing. In R. C. McMaster, P. McIntire, and M. L. Mester, editors, *Electromagnetic Testing*, volume 4 of *Nondestructive Testing Handbook*, pages 25–51. American Society for Nondestructive Testing, Columbus, OH, 2nd edition, 1986.

[10] R. C. McMaster. Introduction to electromagnetic testing. In R. C. McMaster, P. McIntire, and M. L. Mester, editors, *Electromagnetic Testing*, volume 4 of *Nondestructive Testing Handbook*, pages 1–23. American Society for Nondestructive Testing, Columbus, OH, 2nd edition, 1986.

[11] M. J. Maulucci. Magnetic saturation techniques. In R. C. McMaster, P. McIntire, and M. L. Mester, editors, *Electromagnetic Testing*, volume 4 of *Nondestructive Testing Handbook*, pages 212–214. American Society for Nondestructive Testing, Columbus, OH, 2nd edition, 1986.

[12] D. L. Atherton, D. D. Mackintosh, S. P. Sullivan, J. M. S. Dubois, and T. R. Schmidt. Remote-field eddy current signal representation. *Materials Evaluation*, 51(7):782–789, 1993.

[13] J. R. Bowler and M. Johnson. Pulsed eddy-current response to a conducting half-space. *IEEE Transactions on Magnetics*, 33(3):2258–2264, 1997.

[14] S. K. Burke, G. R. Hugo, and D. J. Harrison. Transient eddy-current NDE for hidden corrosion in multilayer. In D. O. Thompson and D. E. Chimenti, editors, *Review of Progress in Quantitative Nondestructive Evaluation*, volume 17A, pages 307–314. Plenum, New York, 1998.

[15] S. Giguère, B. A. Lepine, and J. M. S. Dubois. Pulsed eddy current (PEC) characterization of material loss in multi-layer structures. *Canadian Aeronautics and Space Journal*, 46(4):204–208, 2000.

[16] R. A. Smith, D. Edgar, J. Skramstad, and J. Buckley. Enhanced transient eddy current detection of deep corrosion. *Insight*, 46(2):88–91, 2004.

[17] M. S. Safizadeh, B. A. Lepine, D. S. Forsyth, and A. Fahr. Time-frequency analysis of pulsed eddy current signals. *Journal of Nondestructive Evaluation*, 20(2):73–86, 2001.

[18] R. E. Beissner, J. H. Rose, and N. Nakagawa. Pulsed eddy current method: An overview. In D. O. Thompson and D. E. Chimenti, editors, *Review of Progress in Quantitative Nondestructive Evaluation*, volume 18, pages 469–475. Plenum, New York, 1999.

[19] D. D. Mackintosh, D. L. Atherton, and S. P. Sullivan. Remote-field eddy current signal analysis in small-bore ferromagnetic tubes. *Materials Evaluation*, 51(4):492–495, 1993.

[20] D. L. Atherton. Remote field eddy current inspection. *IEEE Transactions on Magnetics*, 31(6):4142–4147, 1995.

[21] D. E. Russell, D. D. Mackintosh, and A. A. Shatat. Remote field testing. In S. S. Udpa and P. O. Moore, editors, *Electromagnetic Testing*, volume 5 of *Nondestructive Testing Handbook*, pages 207–226. American Society for Nondestructive Testing, Columbus, OH, 3rd edition, 2004.

[22] S. S. Udpa and R. K. Stanley. Magnetic flux leakage testing. In S. S. Udpa and P. O. Moore, editors, *Electromagnetic Testing*, volume 5 of *Nondestructive Testing Handbook*, pages 227–245. American Society of Nondestructive Testing, Columbus, OH, 3rd edition, 2004.

[23] J. T. Schmidt, K. Skeie, and P. McIntire, editors. *Magnetic Particle Testing*, volume 6 of *Nondestructive Testing Handbook*. American Society for Nondestructive Testing, Columbus, OH, 2nd edition, 1989.

[24] N. N. Zatsepin and V. E. Ščerbinin. Calculation of the magnetostatic field of surface defects. *Soviet Journal of Nondestructive Testing*, 5:385–399, 1966.

[25] F. Förster. On the way from the know-how to know-why in the magnetic flux leakage field method of nondestructive testing. *Materials Evaluation*, 43:1154–1162; 1398–1404, 1985.

[26] D. L. Atherton. From high-resolution MFL signals to accurate defect sizing. *Pipes and Pipelines International*, 90(1):9–13, 1995. NDT Lab Library.

[27] R. K. Stanley. Diverted flux theory. In R. C. McMaster, P. McIntire, and M. L. Mester, editors, *Electromagnetic Testing*, volume 4 of *Nondestructive Testing Handbook*, pages 607–630. American Society for Nondestructive Testing, Columbus, OH, 2nd edition, 1986.

[28] R. C. McMaster. Electric current test principles. In R. C. McMaster, editor, *Nondestructive Testing Handbook*, pages 35.1–35.11. American Society for Nondestructive Testing, Columbus, OH, 1st edition, 1959.

[29] A. R. Jack and A. T. Price. The initiation of fatigue cracks from notches in mild steel plates. *International Journal of Fracture Mechanics*, 6(4):401–409, 1970.

[30] M. D. Halliday and C. J. Beevers. The DC electrical potential method for crack length measurement. In C. J. Beevers, editor, *Measurement of crack length and shape during fracture and fatigue*, pages 85–103. Engineering Materials Advisory Services, Warley, UK, 1980.

[31] M. Andersson, C. Persson, and S. Melin. Experimental and numerical investigation of crack closure measurements with electrical potential drop technique. *International Journal of Fatigue*, 28(9):1059–1068, 2006.

[32] http://www.roxar.com/fsm.htm.

[33] http://www.rowantechnologies.co.uk/monitoring_of_industrial_plant.htm.

[34] http://www.matelect.com/products.html.

[35] F. M. G. Wong. *Fatigue, Fracture, and Life Prediction Criteria for Composite Materials in Magnets.* PhD thesis, Massachussetts Institute of Technology, Cambridge, MA, USA, 1990.

[36] R. A. Cláudio, J. Maia, J. M. Dias Pereira, R. Baptista, C. M. Branco, and J. Byrne. Development of a DC potential drop system controlled by computer. In *9th Portuguese Conference on Fracture*, Setúbal, Portugal, 2004.

[37] I. S. Hwang and R. G. Ballinger. A multi-frequency AC potential drop technique for the detection of small cracks. *Measurement Science and Technology*, 3:62–74, 1992.

[38] R. J. Ditchburn, S. K. Burke, and C. M. Scala. NDT of welds: State of the art. *NDT&E International*, 29(2):111–117, 1996.

[39] N. Bowler and Y. Huang. Model-based characterization of homogeneous metal plates by four-point alternating current potential drop measurements. *IEEE Transactions on Magnetics*, 41(6):2102–2110, 2005.

[40] D. H. Michael, R. T. Waechter, and R. Collins. The measurements of surface cracks in metals by using a.c. electric fields. *Proceedings of the Royal Society of London A*, 381:139–157, 1982.

[41] M. C. Lugg, H. M. Shang, R. Collins, and D. H. Michael. The measurement of surface crack inclination in metals using AC electric fields. *Journal of Physics D: Applied Physics*, 21:1814–1821, 1988.

[42] M. C. Lugg. An introduction to ACPD. Technical Report TSC/MCL/1146, TSC (Technical Software Consultants Ltd), February 2002.

[43] T. V. Venkatasubramanian and B. A. Unvala. An AC potential drop system for monitoring crack length. *Journal of Physics E: Scientific Instruments*, 17:765–771, 1984.

[44] W. D. Dover, R. Collins, and D. H. Michael. The use of AC-field measurements for crack detection and sizing in air and underwater. *Philosophical Transactions of The Royal Society of London A: Mathematical Physical and Engineering Sciences*, 320:271–283, 1986.

[45] O. Buck. Recent advances in fracture mechanics testing. In S. V. Nair, J. K. Tien, R. C. Bates, and O. Buck, editors, *Fracture Mechanics: Microstructure*

and Micromechanisms, pages 31–86. ASME International, Metals Park, OH, 1989.

[46] M. C. Lugg. Data interpretation in ACPD crack inspection. *NDT International*, 22(3):149–154, 1989.

[47] J. R. Bowler and N. Bowler. Theory of four-point alternating current potential drop measurements on conductive plates. *Proceedings of the Royal Society of London A*, 463:817–836, 2007.

[48] http://www.tscinspectionsystems.co.uk/indexacfm.htm.

[49] M. C. Lugg. Alternating Current Field Measurement. In S. S. Udpa and P. O. Moore, editors, *Electromagnetic Testing Handbook*, volume 5 of *Nondestructive Testing Handbook*, pages 247–268. American Society for Nondestructive Evaluation, Columbus, OH, 3rd edition, 2004.

[50] A. M. Lewis, D. H. Michael, M. C. Lugg, and R. Collins. Thin-skin electromagnetic fields around surface-breaking cracks in metals. *Journal of Applied Physics*, 64(8):3777–3784, 1988.

[51] R. LeTessier, R. W. Coade, and B. Geneve. Sizing of cracks using the alternating current field measurement technique. *International Journal of Pressure Vessels and Piping*, 79:549–554, 2002.

[52] M. Smith and R. Sutherby. The detection of pipeline SCC flaws using the ACFM technique. *Insight*, 47(12):765–768, 2005.

[53] C. K. Low and B. S. Wong. Defect evaluation using the alternating current field measurement technique. *Insight*, 46(10):598–605, 2004.

[54] M. Smith and C. Laenen. Inspection of nuclear storage tanks using remotely deployed ACFMT. *Insight*, 49(1):17–20, 2007.

[55] W. D. Dover, R. Collins, and D. H. Michael. Review of developments in ACPD and ACFM. *British Journal of NDT*, 33(3):121–127, 1991.

[56] C. Laenen and A. Raine. Additional applications with the Alternating Current Field Measurement (ACFM) technique. *Insight*, 40(12):860–863, 1998.

[57] M. C. Lugg, C. Laenen, and G. Salazar. Alternating current field measurement testing of storage tank floor welds. *Materials Evaluation*, 65(12):1191–1196, 2007.

[58] W. D. Dover, F. D. W. Charlesworth, K. A. Taylor, R. Collins, and D. H. Michael. AC field measurement — theory and practice. In C. J. Beevers, editor, *The Measurement of Crack Length and Shape During Fracture and Fatigue*, pages 222–260. Engineering Materials Advisory Service, Warley, UK, 1980.

[59] http://www.tscinspectionsystems.co.uk/indexacpd.htm.

[60] V. Deutsch, P. Ettel, M. Platte, and H. Cost. Rißtiefenmessung: Zeitgemäße Meßtechnik für ein bewährtes Verfahren. *Materialprüfung*, 38(7-8):306–310, 1996.

[61] http://www.karldeutsch.de/fs_products_en.htm.

[62] R. O. Ritchie, G. G. Garrett, and J. F. Knott. Crack-growth monitoring: Optimisation of the electrical potential technique using an analogue method. *International Journal of Fracture Mechanics*, 7:462–467, 1971.

[63] D. M. Farrell and B. J. Robbins. On-line monitoring of furnace wall and superheater corrosion in power generation boilers. In *39th Corrosion Science Symposium*, Newcastle, 1998.

[64] D. M. Farrell, B. J. Robbins, P. Sikka, and M. Seaman. On-line monitoring and control of furnace wall corrosion in PF-fired boilers. *Power Plant: Operation, Maintenance and Material Issues*, 3(2), 2004.

[65] D. M. Farrell, B. J. Robbins, J. Stallings, S. Cardoso, and W. Bakker. Crack growth monitoring on industrial plant using established electrical resistance 'scanner' technology. *Insight*, 50(12):690–694, 2008.

[66] R. D. Strommen, H. Horn, and K. R. Wold. New technique monitors pipeline corrosion, cracking. *The Oil and Gas Journal*, 91(52):88–93, 1993.

[67] D. Corbin and E. Willson. New technology for real-time corrosion detection. In *Tri-Service Corrosion Conference*, Denver, CO, 2007.

[68] T. Kuroiwa, S. Hamada, Y. Ogawa, H. Iida, M. Kuroki, and M. Hayakawa. Application of potential drop technique to the inspection of welded boiler high temperature and pressure parts. In *11th International Conference on Fracture*, Turin, Italy, 2005.

[69] R. A. Serway and R. J. Beichner. *Physics for Scientists and Engineers with Modern Physics*. Saunders College Pub., London, 5th edition, 2000.

[70] N. Bowler. Theory of four-point direct-current potential drop measurements on a metal plate. *Research in Nondestructive Evaluation*, 17(1):29–48, 2006.

[71] K. Sieradzki and R. C. Newman. Stress corrosion cracking. *Journal of Physics and Chemistry of Solids*, 48(11):1101–1113, 1987.

[72] J. Heldt and H. P. Seifert. Stress corrosion cracking of low-alloy, reactor-pressure-vessel steels in oxygenated, high-temperature water. *Nuclear Engineering and Design*, 206(1):57–89, 2001.

[73] G. Van Boven, W. Chen, and B. Rogge. The role of residual stress in neutral pH stress corrosion cracking of pipeline steels. Part I: Pitting and cracking occurrence. *Acta Materialia*, 55:29–42, 2007.

[74] R. A. Smith. The wheel-rail interface - Some recent accidents. *Fatigue and Fracture of Engineering Materials and Structures*, 26(10):901–907, 2003.

[75] R. Pohl, A. Erhard, H. J. Montag, H. M. Thomas, and H. Wüstenberg. NDT techniques for railroad wheel and gauge corner inspection. *NDT&E International*, 37:89–94, 2004.

[76] U. Zerbst, K. Mädler, and H. Hintze. Fracture mechanics in railway applications: An overview. *Engineering Fracture Mechanics*, 72(2):163–194, 2005.

[77] B. A. Auld and J. C. Moulder. Review of advances in quantitative eddy current nondestructive evaluation. *Journal of Nondestructive Evaluation*, 18(1):3–35, 1999.

[78] L. Udpa, P. Ramuhalli, J. Benson, and S. S. Udpa. Automated analysis of eddy current signals for steam generator tube inspection. In *16th World Conference on NDT*, Montreal, 2004.

[79] N. Yusa, L. Janousek, M. Rebican, Z. Chen, K. Miya, N. Dohi, N. Chigusa, and Y. Matsumoto. Caution when applying eddy current inversion to stress corrosion cracking. *Nuclear Engineering and Design*, 236:211–221, 2006.

[80] V. Vitek. Plane strain stress intensity factors for branched cracks. *International Journal of Fracture*, 13(4):481–501, August 1977.

[81] M. P. Connolly, D. H. Michael, and R. Collins. The inversion of surface potential measurements to determine crack size and shape. *Journal of Applied Physics*, 64(5):2638–2647, 1988.

[82] M. O. Lai and C. K. Ng. Measurement of crack profiles using AC field measurement method. *Journal of Nondestructive Evaluation*, 13(4):155–163, 1994.

[83] D. Mirshekar-Syahkal, R. Collins, and D. H. Michael. The influence of skin depth on crack measurement by the ac field technique. *Journal of Nondestructive Evaluation*, 3(2):65–76, 1982.

[84] D. Mirshekar-Syahkal, D. H. Michael, and R. Collins. Parasitic voltages induced by artificial flaws when measured using the ac field technique. *Journal of Nondestructive Evaluation*, 2(3-4):195–202, 1981.

[85] A. M. Lewis. Electromagnetic methods for NDE of metal fatigue cracks: Practical techniques and theoretical models. *Non-Destructive Testing and Evaluation*, 6:389–409, 1992.

[86] N. Bowler. Analytical solution for the electric field in a half space conductor due to alternating current injected at the surface. *Journal of Applied Physics*, 95(1):344–348, 2004.

[87] N. Bowler. Electric field due to alternating current injected at the surface on a metal plate. *Journal of Applied Physics*, 96(8):4607–4613, 2004.

[88] http://www.matweb.com.

[89] K. Ikeda, M. Yoshimi, and C. Miki. Electrical potential drop method for evaluating crack depth. *International Journal of Fracture*, 47:25–38, 1991.

[90] H. Okada, W. Zhao, S. N. Atluri, and S. G. Sampath. A computational approach to determining the depth of surface flaws by the ACPD technique. *Engineering Fracture Mechanics*, 43(6):911–921, 1992.

[91] M. McIver. Characterization of surface-breaking cracks in metal sheets by using AC electric fields. *Proceedings of the Royal Society of London A*, 421:179–194, 1989.

[92] J. R. Carson. A generalization of the reciprocal theorem. *Bell System Technical Journal*, 3(3):393–399, 1924.

[93] E. A. Guillemin. *Introductory Circuit Theory*. John Wiley & Sons, New York, 1960.

[94] P. D. Corl, P. M. Grant, and G. S. Kino. A digital synthetic focus acoustic imaging system for NDE. In *1978 Ultrasonics Symposium*, pages 263–268, 1978.

[95] M. Karaman, P. C. Li, and M. O'Donnell. Synthetic aperture imaging for small scale systems. *IEEE Transactions on Ultrasonics, Ferroelectrics, and Frequency Control*, 42(3):429–442, 1995.

[96] J. C. Curlander and R. N. McDonough. *Synthetic Aperture Radar - Systems and Signal Processing*. John Wiley & Sons, New York, 1991.

[97] P. G. Kaup, F. Santosa, and M. Vogelius. Method for imaging corrosion damage in thin plates from electrostatic data. *Inverse Problems*, 12:279–293, 1996.

[98] G. Sposito, F. Simonetti, P. Cawley, and P. B. Nagy. Potential Drop Spectroscopy for characterization of complex defects. In D. O. Thompson and D. E. Chimenti, editors, *Review of Progress in Quantitative Nondestructive Evaluation*, volume 25A, pages 407–414. American Institute of Physics, Melville, NY, 2006.

[99] G. Sposito, P. Cawley, and P. B. Nagy. Crack profile reconstruction by means of potential drop measurements. In D. O. Thompson and D. E. Chimenti, editors, *Review of Progress in Quantitative Nondestructive Evaluation*, volume 26A, pages 733–740. American Institute of Physics, Melville, NY, 2007.

[100] G. Sposito, P. Cawley, and P. B. Nagy. Potential drop data inversion for crack depth profiling. In D. O. Thompson and D. E. Chimenti, editors, *Review of Progress in Quantitative Nondestructive Evaluation*, volume 27A, pages 618–624. American Institute of Physics, Melville, NY, 2008.

[101] G. Sposito, P. Cawley, and P. B. Nagy. Potential drop mapping for corrosion monitoring. In D. O. Thompson and D. E. Chimenti, editors, *Review of Progress in Quantitative Nondestructive Evaluation*, volume 28. American Institute of Physics, Melville, NY, 2009, in press.

[102] Y. Lu, J. R. Bowler, C. Zhang, and N. Bowler. Edge effects in four point direct current potential drop measurement. In D. O. Thompson and D. E. Chimenti, editors, *Review of Progress in Quantitative Nondestructive Evaluation*, volume 28. American Institute of Physics, Melville, NY, 2009, in press.

[103] H. S. Carslaw and J. C. Jaeger. *Conduction of Heat in Solids*. Oxford University Press, Oxford, 2nd edition, 1959.